

EXPERIMENTAL VALIDATION OF BRACING RECOMMENDATIONS FOR LONG-SPAN
CONCRETE GIRDERS

By

MEGAN SALVETTI BEERY

A THESIS PRESENTED TO THE GRADUATE SCHOOL
OF THE UNIVERSITY OF FLORIDA IN PARTIAL FULFILLMENT
OF THE REQUIREMENTS FOR THE DEGREE OF
MASTER OF SCIENCE

UNIVERSITY OF FLORIDA

2012

© 2012 Megan Salvetti Beery

To my husband, Kevin Beery

ACKNOWLEDGMENTS

The work presented in this thesis could not have been completed without the unwavering support and guidance of a number of individuals.

I would like to express my deep and sincere gratitude to my advisor, Dr. Gary Consolazio, whose motivation, encouragement, knowledge, and attention to detail have been invaluable to me. I thank you for seeing my potential from the first day I set foot in your office and for providing valuable feedback that cultivated my own professional confidence and expertise. I also thank the co-chair on my committee, Dr. H.R. (Trey) Hamilton for bringing his vast design knowledge to the table, as well as bringing humor into the engineering equation. Both Dr. Consolazio and Dr. Hamilton were always available to answer my questions, and I thank you both for always teaching me (and questioning me) to the point of full understanding. I would also like to thank Dr. Ron Cook for serving on my supervisory committee.

Appreciation is extended to everyone at the FDOT M. H. Ansley Structures Research Center for their insight during the planning phase and exceptional work performed during the fabrication phase of the project. I thank you for your precision and patience, and for making me feel so welcome every time I visited the lab. I would like to especially thank David Wagner for being such a fantastic co-project manager and friend. I could not have asked for a better research partner, turning the testing plans into reality through his selfless commitment to this project.

My officemates ensured that I was constantly engaged and entertained along the way, and for that I am very grateful. In particular, I can't thank Daniel Getter enough, for his friendship and for always offering his expertise and advice whenever asked of him.

I would also like to thank my family members for the support and love they continuously provide me. I thank my mother, Lynda Salvetti, for instilling in me a drive to succeed at an early age, and for supporting my decisions since I was old enough to pick my own outfit. I thank my

father, Joseph Salvetti, and step-mom, Cindy Salvetti, for being proud of me no matter what. I thank my grandpa, Joseph Strenk, for sparking and cultivating my interest in engineering. I thank my brother, Danny Salvetti, and step-sister, Kimberly Goss Stuetzer, for reminding me to have fun during my studies. Perhaps most importantly, I am eternally grateful to my husband, Kevin Beery, for his unconditional love and understanding throughout this journey.

TABLE OF CONTENTS

| | <u>page</u> |
|---|-------------|
| ACKNOWLEDGMENTS | 4 |
| LIST OF TABLES | 9 |
| LIST OF FIGURES | 10 |
| LIST OF ABBREVIATIONS..... | 15 |
| ABSTRACT..... | 16 |
| CHAPTER | |
| 1 INTRODUCTION | 18 |
| Objective..... | 19 |
| Scope..... | 19 |
| Literature Review | 20 |
| Bearing Pad Properties | 20 |
| Girder Buckling..... | 21 |
| 2 ISOLATED BEARING PAD ROLL STIFFNESS TESTS..... | 25 |
| Experimental Test Setup..... | 25 |
| Instrumentation | 26 |
| Test Procedure | 27 |
| Positioning Stage | 27 |
| Clamping Stage | 28 |
| Rolling Stage | 28 |
| Test Program..... | 29 |
| Repeated Axial Compression | 32 |
| Variation of Axial Compression Load | 32 |
| Results..... | 33 |
| Location of Pressure Resultants on Bearing Pads | 34 |
| Data Trends..... | 35 |
| Effect of Skew and Slope Combined..... | 36 |
| Effect of Skew | 36 |
| Effect of Slope..... | 36 |
| 3 INTRODUCTION TO GIRDER BUCKLING TESTS | 46 |
| Scope of Test Program..... | 46 |
| Experimental Constraints..... | 47 |
| Length of Test Girder | 47 |
| Loading Conditions | 47 |

| | | |
|---|---|-----|
| | Elastic Buckling..... | 49 |
| 4 | BUCKLING ANALYSIS..... | 52 |
| | Overview..... | 52 |
| | Finite Element Model of Experimental Test Setup..... | 52 |
| 5 | DEVELOPMENT OF TEST-GIRDER CROSS-SECTIONS..... | 59 |
| | Precast Segment Cross-Section Design..... | 60 |
| | Design of Girder Cross-Section..... | 60 |
| | Design of Closure Strip Cross-Section..... | 62 |
| | Design of End Block Cross-Section..... | 63 |
| 6 | CONSTRUCTION OF TEST GIRDER..... | 72 |
| | Precast Segments..... | 72 |
| | Closure Strips..... | 73 |
| | End Blocks..... | 74 |
| | Material Tests and Properties..... | 75 |
| | Girder Post-Tensioning and Grouting..... | 76 |
| 7 | GRAVITY LOAD SIMULATOR..... | 97 |
| | Gravity Load Simulator Design..... | 98 |
| | UF/FDOT Gravity Load Simulators..... | 99 |
| | Effect of Gravity Load Simulator Self Weight Equilibrium..... | 100 |
| 8 | EXPERIMENTAL BUCKLING TESTS PROGRAM..... | 114 |
| | Buckling Test Setup..... | 114 |
| | Test Matrix..... | 114 |
| | Test Procedure..... | 115 |
| | Setting Skew and Slope Angles..... | 115 |
| | Placing the Test Girder..... | 116 |
| | Buckling Test Procedure..... | 117 |
| | Instrumentation..... | 117 |
| | Displacement Transducers..... | 118 |
| | Load Cells..... | 119 |
| | Strain Gages..... | 119 |
| 9 | RESULTS..... | 131 |
| | Experimental Buckling Test Results..... | 131 |
| | Measured Load-Displacement Curves..... | 131 |
| | Data Curve Fitting..... | 132 |
| | Calculation of Buckling Capacity..... | 133 |
| | Buckling Capacity Results..... | 134 |

| | |
|---|-----|
| Buckling Finite Element Model..... | 135 |
| Moment-Rotation Curves from Roll Stiffness Tests | 135 |
| Scaling of Moment-Rotation Curves from Isolated Tests | 137 |
| Elastic Modulus Used in Finite Element Buckling Model | 139 |
| Finite Element Buckling Model Results..... | 140 |
| 10 CONCLUSIONS | 155 |
| APPENDIX | |
| A BEARING PAD TEST DEVICE FABRICATION PLANS..... | 157 |
| B FULL SCALE TEST GIRDER FABRICATION PLANS..... | 163 |
| C COMPRESSIVE STRENGTH AND ELASTIC MODULUS TEST RESULTS | 174 |
| D DYWIDAG JACK CALIBRATION FORM | 177 |
| E GRAVITY LOAD SIMULATOR FABRICATION PLANS | 180 |
| F CATCH FRAMES FABRICATION PLANS | 199 |
| G BUCKLING TESTS INSTRUMENTATION PLAN | 207 |
| LIST OF REFERENCES | 219 |
| BIOGRAPHICAL SKETCH | 222 |

LIST OF TABLES

| <u>Table</u> | | <u>page</u> |
|--------------|--|-------------|
| 2-1 | Bearing pad dimensions, shear modulus, durometer hardness, and configurations tested for each specimen | 38 |
| 2-2 | Mean roll stiffness and reduction in roll stiffness due to non-ideal (skewed, sloped) conditions | 38 |
| 5-1 | Section properties of precast segments | 65 |
| 5-2 | Section properties of closure strips | 65 |
| 5-3 | Section properties of end blocks | 65 |
| 6-1 | Summary of cylinder material tests performed within one week of buckling testing for each girder component | 79 |
| 6-2 | Compressive strength and modulus of elasticity of cylinders tested within one week of buckling testing | 79 |
| 6-3 | Sequence of incremental post-tensioning forces applied to girder during stressing | 80 |
| 6-4 | Grout cube strength test results | 80 |
| 8-1 | Test matrix | 121 |
| 8-2 | Placement method, per test basis | 121 |
| 9-1 | Buckling capacity results | 142 |
| 9-2 | Sigmoid curve functional parameters for each test configuration | 142 |
| 9-3 | Experimental and finite element buckling capacities for each test configuration | 142 |

LIST OF FIGURES

| <u>Figure</u> | <u>page</u> |
|---|-------------|
| 1-1 Description of physical system | 23 |
| 1-2 Plan view of girder, pad, and support with skew angle defined | 23 |
| 1-3 Elevation view of girder, pad, and support with slope angle defined | 24 |
| 2-1 Bearing pad test device | 39 |
| 2-2 Elevation view of test device: imposing slope (positioning stage) and applying axial load (clamping stage) | 39 |
| 2-3 Imposing skew during the positioning stage | 40 |
| 2-4 Applying loads to outriggers during rolling stage | 40 |
| 2-5 Identification of bearing pad dimensions | 41 |
| 2-6 Representative moment-rotation curves | 41 |
| 2-7 Moment-rotation curves for all tests, grouped by pad specimen | 42 |
| 2-8 Pressure distributions and axial load resultant positions on bearing pad: beginning, intermediate, and end of rolling stage | 43 |
| 2-9 Bulging of the internal elastomer layers during roll stiffness test | 44 |
| 2-10 Bearing pad roll stiffnesses for all configurations tested | 45 |
| 2-11 Mean bearing pad roll stiffnesses for all configurations tested | 45 |
| 3-1 Overview of test setup | 50 |
| 3-2 Physical length and span length defined | 50 |
| 3-3 Moment diagrams for simply supported beam with various loading conditions | 51 |
| 4-1 Test setup overview | 55 |
| 4-2 Test girder buckling system model | 56 |
| 4-3 Eccentricities of load application point and bearing pad relative to center of gravity of test cross-section | 57 |
| 4-4 Load application on test girder buckling analysis | 57 |

| | | |
|------|--|----|
| 4-5 | Load procedure for buckling analysis..... | 58 |
| 5-1 | Exploded view of test girder with prestressing shown | 66 |
| 5-2 | Test cross-section design flowchart..... | 67 |
| 5-3 | Iterative process of precast segment cross-section design..... | 68 |
| 5-4 | Typical shipping of bridge girders..... | 68 |
| 5-5 | Final precast segment cross-section..... | 69 |
| 5-6 | Final closure strip cross-section..... | 70 |
| 5-7 | End block width, controlled by bearing pad size and skew angle | 70 |
| 5-8 | Final end block cross-section..... | 71 |
| 6-1 | Casting dates for girder components and final orientation of girder in FDOT laboratory | 81 |
| 6-2 | Precast segments formwork aligned on single pretensioning bed at Dura-Stress | 81 |
| 6-3 | Placing concrete in the precast segment formwork | 82 |
| 6-4 | Unstressed post-tensioning bars placed in ducts to keep ducts straight during placing of concrete..... | 82 |
| 6-5 | Tarp covers applied to each segment during curing | 83 |
| 6-6 | Precast segments after formwork removed at Dura-Stress..... | 83 |
| 6-7 | Precast segment arrival at the FDOT laboratory..... | 84 |
| 6-8 | Duct couplers located within closure strips in bottom flange of girder..... | 84 |
| 6-9 | Duct couplers in closure strips, sealed with tape prior to concrete placement | 85 |
| 6-10 | Closure strip formwork..... | 85 |
| 6-11 | Placing concrete into the closure strip formwork | 86 |
| 6-12 | Embedded steel plate at top surface of closure strip..... | 86 |
| 6-13 | Finished closure strip with formwork removed | 87 |
| 6-14 | Concrete used in closure strip and end block concrete mix, showing presence of Propex Fibermesh® 150 reinforcing fibers | 87 |

| | | |
|------|--|-----|
| 6-15 | Open end block formwork revealing mild reinforcement and lifting loops | 88 |
| 6-16 | Anchorage zone mild steel reinforcement in end blocks | 89 |
| 6-17 | Completed end block formwork | 90 |
| 6-18 | Placement of concrete in north end block formwork | 90 |
| 6-19 | End block after removal of formwork | 91 |
| 6-20 | Leveling plates and anchor plates at bottom of end block | 91 |
| 6-21 | Moist cured cylinders submerged in a tank of lime water | 92 |
| 6-22 | Typical cylinder failure types observed during compressive strength testing | 92 |
| 6-23 | Bar identification numbers used during post-tensioning | 93 |
| 6-24 | Test girder during post-tensioning, braced against steel catch frames using timber blocking | 93 |
| 6-25 | Post-tensioning jack setup | 94 |
| 6-26 | Post-tensioning jack and pressure gage | 94 |
| 6-27 | Camber measurement at midspan of test girder immediately after completion of post-tensioning | 95 |
| 6-28 | Grout mixer and high capacity air compressor | 95 |
| 6-29 | Lifting the test girder into testing position, prior to end block fabrication | 96 |
| 7-1 | Undesirable horizontal restraining component that develops in an anchored loading system | 104 |
| 7-2 | Dimensions, defined | 104 |
| 7-3 | Instantaneous center | 105 |
| 7-4 | UF/FDOT gravity load simulator | 106 |
| 7-5 | Spherical roller bearing | 107 |
| 7-6 | Hydraulic jack connection to simulator center pin | 107 |
| 7-7 | Gravity load simulator displaced shape | 108 |
| 7-8 | Knife edge at load application point at top of test girder | 109 |

| | | |
|------|---|-----|
| 7-9 | UF/FDOT gravity load simulator and load frame in testing position..... | 109 |
| 7-10 | Definition of percent of simulator load applied laterally..... | 110 |
| 7-11 | Gravity load simulator model..... | 110 |
| 7-12 | Results of simulator analysis: theoretical percent of load applied laterally to the beam at the load application point (self weight excluded in model)..... | 111 |
| 7-13 | Results of simulator analysis: theoretical percent of load applied laterally to the beam at the load application point (self weight included in model)..... | 111 |
| 7-14 | Effect of simulator self weight and counterweights on verticalness of load line of action..... | 112 |
| 7-15 | Counterweight system..... | 113 |
| 8-1 | Overall test setup..... | 122 |
| 8-2 | Roll stiffness results..... | 123 |
| 8-3 | Bearing pad skew angle orientation in buckling tests..... | 123 |
| 8-4 | Beveled plate used to impose slope angle on bearing pads..... | 123 |
| 8-5 | Beveled plate and bearing pad positioned between end block and end support..... | 124 |
| 8-6 | Bearing pad orientation and initial pressure distributions during buckling tests..... | 124 |
| 8-7 | Final bearing pad pressure distributions during buckling tests..... | 125 |
| 8-8 | Sweep of test girder..... | 125 |
| 8-9 | Jack used to straighten test girder..... | 126 |
| 8-10 | Typical load time history..... | 126 |
| 8-11 | Naming convention for buckling test instrumentation..... | 127 |
| 8-12 | Midspan displacement transducers..... | 128 |
| 8-13 | South end block displacement transducers..... | 129 |
| 8-14 | Load cells, located at gravity load simulator locations..... | 129 |
| 8-15 | Vibrating wire strain gages, cast into closure strips..... | 130 |
| 9-1 | Test girder in buckled configuration..... | 143 |

| | | |
|------|---|-----|
| 9-2 | Definition of applied load (P) | 143 |
| 9-3 | Measured absolute load-displacement data | 144 |
| 9-4 | Measured incremental load-displacement data | 144 |
| 9-5 | Southwell hyperbola fit..... | 145 |
| 9-6 | Data curve fitting procedure | 145 |
| 9-7 | Best fit hyperbolas for each configuration..... | 146 |
| 9-8 | Hyperbolic curve fit and Southwell buckling load for test A-45-0-1 | 146 |
| 9-9 | Definition of buckling capacity | 147 |
| 9-10 | Description of “in-situ” roll test..... | 147 |
| 9-11 | Moment-rotation data from in-situ tests | 148 |
| 9-12 | Data curve fitting procedure, in-situ case shown..... | 149 |
| 9-13 | Moment-rotation curves, from isolated and in-situ roll stiffness tests..... | 150 |
| 9-14 | Moment-rotation curves, test configuration A-0-0, from isolated bearing pad tests (BPTD) and in-situ tests..... | 150 |
| 9-15 | Bearing pad contact areas during testing | 151 |
| 9-16 | Bearing pad contact areas during both isolated roll stiffness tests and buckling tests | 151 |
| 9-17 | Moment-rotation curves, from isolated roll stiffness tests (scaled and original) and in-situ roll stiffness tests | 152 |
| 9-18 | Moment-rotation curves, scaled from isolated bearing pad tests..... | 153 |
| 9-19 | Comparison of experimental and FE buckling curves..... | 153 |
| 9-20 | Buckling curves from experimental tests and finite element models | 154 |

LIST OF ABBREVIATIONS

| | |
|----------------|--|
| A | cross-sectional area (in ²) |
| C.G. | center of gravity |
| I _x | strong axis moment of inertia (in ⁴) |
| I _z | weak axis moment of inertia (in ⁴) |
| J | torsional constant (in ⁴) |
| O.C. | on center |
| OD | outer diameter |
| M _y | end moment about y-axis |
| y | height of centroid (in) |
| α | vertical asymptote |
| β | horizontal asymptote |
| φ | diameter |
| γ ₀ | functional parameter |
| γ ₁ | functional parameter |
| γ ₂ | functional parameter |

Abstract of Thesis Presented to the Graduate School
of the University of Florida in Partial Fulfillment of the
Requirements for the Degree of Master of Science

EXPERIMENTAL VALIDATION OF BRACING RECOMMENDATIONS FOR LONG-SPAN
CONCRETE GIRDERS

By

Megan Salvetti Beery

May 2012

Chair: Gary Consolazio
Cochair: H. R. (Trey) Hamilton
Major: Civil Engineering

During the construction process, flexible support conditions provided by steel reinforced neoprene bearing pads supporting precast, prestressed girders may allow the girders to become unstable, rolling about an axis parallel to the span of the girders. Imposed skew and/or slope angles significantly reduce bearing pads roll stiffness, which reduces girder buckling capacity due to gravity loading.

In this thesis, roll stiffnesses for bearing pads under skew and slope conditions are determined from experimental data gathered using a test device designed to measure such values. The test device reproduces the forces and deformations that act on a bearing pad in the field while simultaneously permitting axial load, skew angle, and slope angle to be controlled independently, so that the effect of each on bearing pad roll stiffness can be quantified. In total, 108 bearing pad tests were performed on three different standard bearing pads, with varying severities of imposed skew and slope angle.

Documentation of full scale girder buckling tests designed and conducted to experimentally quantify the influence of bearing pad roll stiffness on girder buckling capacity is also included in this thesis. The pads used to support each end of the test girder during the

buckling tests were the same pads previously tested to determine roll stiffness. In total, nine buckling tests were conducted, with various skew and slope conditions imposed on the bearing pads. Validation of analytical models (corresponding to the test setup) was carried out by comparing the buckling capacity predictions from analytical simulations to experimental test results.

CHAPTER 1 INTRODUCTION

Precast, pretensioned concrete bridge girders in simple span construction are typically supported on reinforced neoprene bearing pads (Figure 1-1A). Neoprene bearing pads transfer vertical load from the girder to the support and allow lateral movement of the girder, due to thermal expansion and contraction. During girder erection, the self weight of the girder is gradually applied to the bearing pad as the cables from the crane supports are removed. Before diaphragm or deck installation, the girder may become unstable and rotate about an axis parallel to the span of the girder (Figure 1-1B). Bearing pad roll stiffness combined with the effects of bracing stiffness and torsional buckling dictates the point of girder instability under girder self-weight (gravity) loading. In the case of girders supported by reinforced neoprene bearing pads, the roll stiffness of the end restraints can be severely reduced by skew angle (Figure 1-2) and slope angle (Figure 1-3). According to the Precast Concrete Institute (PCI) Bridge Design Manual (2003), skew angle is defined as the angle between the centerline of a support and a line normal to the roadway centerline (Figure 1-2). Slope angle is defined as the vertical angle between the bottom surface of the girder and the top surface of the bearing pad (Figure 1-3), and may be produced by camber (induced by eccentric prestressing of the girder), construction tolerances, bridge grade, or a combination of all three. Previous analytical research (Consolazio et al. 2007) has been conducted to quantify the roll stiffness of bearing pads under various angles of skew and slope. It was found that the roll stiffness of bearing pads—and therefore the buckling capacity of bridge girders—is significantly reduced by the imposition of skew and slope angles.

Objective

The research presented in this thesis is to experimentally expand upon the previous analytical research (Consolazio et al. 2007) conducted to determine the effect of imposed skew and slope angles on the roll stiffness of bearing pads and the buckling capacity of girders supported on these bearing pads. There were two distinct phases of the work presented in this thesis: isolated roll stiffness tests and girder buckling tests. In the isolated roll stiffness tests, roll stiffnesses for bearing pads under skew and slope conditions are derived from the experimental data gathered from a test device designed to measure such values. In the second phase, a full scale girder buckling test program was designed and conducted to experimentally quantify the influence of bearing pad roll stiffness on girder buckling capacity. The pads used to support each end of the test girder were the same pads previously tested—to determine roll stiffness—in the first (roll stiffness) phase of this study.

Scope

In the first phase of the current study, an experimental test device was developed to enable determination of bearing pad roll stiffness under the types of loading conditions that arise during bridge construction. The test device reproduces the forces acting on a bearing pad in the field while simultaneously permitting axial load, skew angle, and slope angle to be controlled independently, so that the effect of each on bearing pad roll stiffness is quantified. A total of 108 tests were performed on three different standard bearing pads, with varying severity of imposed skew and slope angle.

In the second phase of the current study, the scope of the experimental test program included the design and construction of a full scale test girder; a vertical loading system; and end supports that enabled various combinations of slope and skew to be imposed on the supporting bearing pads. In total, nine (9) buckling tests were conducted, with various skew and slope

conditions imposed on the supporting bearing pads. Analytical models corresponding to the test setup were developed and used to simulate the experimental buckling tests. Validation of the models was then carried out by comparing the buckling capacity predictions from the analytical simulation to experimental test results.

Literature Review

Although roll stiffness of a bearing pad is important regarding girder instability during the construction process, most research to date has focused on bearing pad stiffnesses that relate to the final constructed configuration of the bridge. The roll stiffness of bearing pads regarding girder instability during the construction stage has not been adequately explored. Similarly, several research programs have conducted experimental tests to investigate girder instability, primarily focusing on lateral torsional buckling. The effect of reduced roll stiffness—due to skew and slope angles—on girder buckling capacity has not yet been quantified.

Bearing Pad Properties

Isolated experimental bearing pad tests have been conducted to quantify bearing pad stiffness parameters, such as the effect of shear strain rate on the shear modulus of bearing pads (Allen et al., 2010), stress capacities and stress-strain limits of cotton duck bridge bearing pads in shear, compression, and rotation (Lehman et al., 2005), and long term load effects on bearing performance (Doody and Noonan, 1999). Muscarella and Yura (1995) also experimentally analyzed isolated bearing pads to determine the shear, compressive, and rotational stiffnesses, with emphasis on the difference in behavior of flat and tapered bearings. However, the rotational stiffness they calculated was about an axis perpendicular to the span of the girder, or a rotation induced by service loads, as opposed to girder instability during construction. Similarly, Vidot-Vega et al. (2009) experimentally determined the rotational stiffness of multiple bearing pads resisting moment in series due to rotation about an axis perpendicular to the span of the

girder, using a test device comprised of a continuous span over the support, pertaining to the final constructed configuration of the bridge.

Using analytical modeling, Yazdani et al. (2000) computed bearing pad shear, axial, and roll stiffnesses to determine the effect of neoprene bearing pads on the performance of fully constructed precast prestressed concrete bridges. Green et al. (2001) focused on the effect of skew angle on the performance of the final constructed bridge, examining the deflection and tensile stresses in girders with varying severity of skew, also through the use of analytical models. The current study, therefore, is unique in that it focused on experimentally evaluating the influence of imposed skew and slope angles on the roll stiffness—about an axis parallel to the girder span—of bearing pads as related to girder instability during the construction process.

Girder Buckling

As previously stated, several experimental tests have been conducted to investigate girder instability, including lateral torsional buckling testing of steel I-shapes (Yura and Phillips, 1992), lateral-torsional buckling behavior of fiber reinforced polymer I-shaped cross-sections (Stoddard, 1997), and lateral stability of slender rectangular reinforced concrete beams (Kalkan, 2009). Deaver (2003) investigated torsional bracing by simulating buckling of a two-beam system with midspan bracing. Mast examined the lateral bending stability of prestressed concrete beams when they are suspended from lifting loops (1989) and supported below by elastomeric bearing pads and on trucks and tractors (1993). Lateral-torsional buckling and rollover instability of prestressed girders supported on bearing pads was investigated by Hurff (2010). However, Hurff focused on the instability due to girder self-weight eccentricity caused by fabrication imperfections (prestress eccentricity, cracking, solar radiation) and support conditions (uneven bearing surface). The current study, therefore, is unique in that experimental tests were performed to quantify the buckling capacity of a test girder supported on bearing pads with

known roll stiffnesses under skewed and sloped conditions. Additionally, the experimental buckling tests were used to validate finite element buckling models, which incorporated the roll stiffness results from the isolated roll stiffness tests.

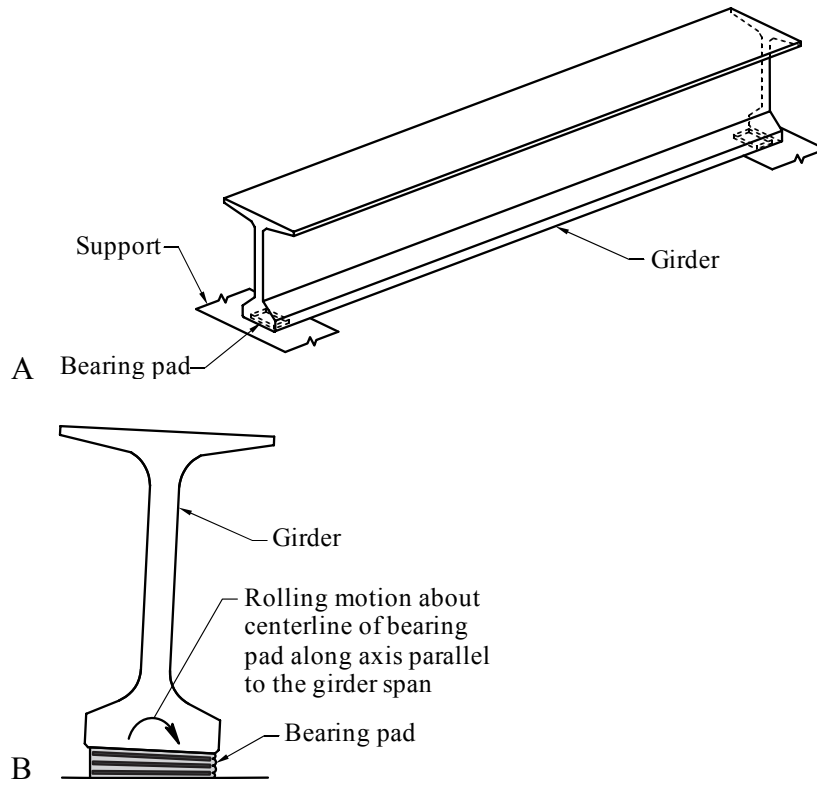


Figure 1-1. Description of physical system. A) Girder supported on bearing pads during bridge construction. B) Rolling motion of girder that occurs during instability (buckling).

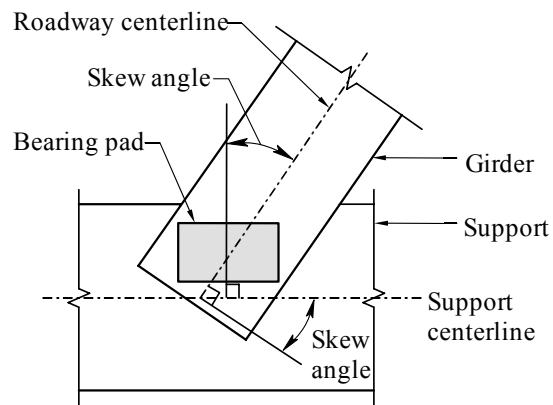


Figure 1-2. Plan view of girder, pad, and support with skew angle defined

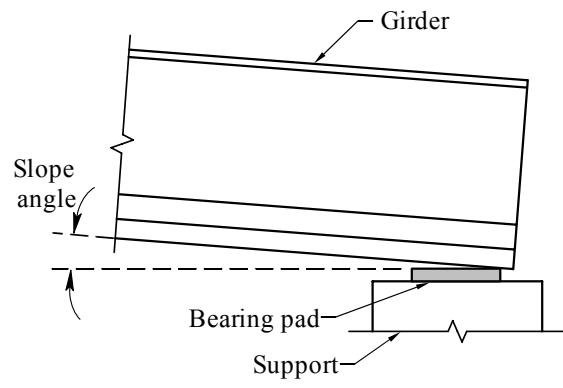


Figure 1-3. Elevation view of girder, pad, and support with slope angle defined

CHAPTER 2 ISOLATED BEARING PAD ROLL STIFFNESS TESTS

Experimental Test Setup

An experimental test device (Figure 2-1) was developed to enable determination of bearing pad roll stiffness under the types of loading conditions that arise during bridge construction. A key aspect in the design of the test device was the need to maintain a constant axial load on the bearing pad (to simulate constant gravity-induced girder reactions) as roll rotation of the pad occurred. Equally important, the test device was designed to be capable of simulating girder support conditions in which skew, slope, or combined skew and slope are present. A structural tube within the device represents the bridge girder axis and is used to impose, and hold constant, the slope angle (Figure 2-2) and the axial load on the pad. Two 5 in. thick steel bearing plates at the center of the test device, which were effectively rigid in comparison to the stiffness of the bearing pad, represent the bottom surface of the girder and the top surface of the bridge abutment, respectively. Simulating a skewed alignment between girder and bearing pad was achieved by positioning the pad at the desired skew angle (relative to the axis of the tube, Figure 2-3) between the steel bearing plates. As constructed, the test device was capable of imposing desired combinations of axial load, skew angle, and slope angle on the bearing pad for the purpose of evaluating pad roll stiffness. Fabrication plans for the bearing pad test device can be found in Appendix A.

Each bearing pad test conducted in this study consisted of three stages: positioning, clamping, and rolling. In the positioning stage, the bearing pad and test device were configured to impose the desired skew and slope angles on the pad. Subsequently, the pad was clamped within the test device such that a target axial load on the pad was achieved. Holding the axial load constant, a moment was then applied to the test device—through application of vertical

loads acting at the ends of the outriggers (Figure 2-1)—to produce a roll rotation on the pad, thereby simulating the unrestrained rolling motion of a girder during instability (buckling) in the field. For each test thus performed, bearing pad roll stiffness was quantified by determining the slope of the linear relationship between moment imposed on the pad, and the resulting measured roll angle.

Instrumentation

Axial load cells (Interface, model 1232, 100 kip capacity), which were used to measure total axial load applied to the bearing pad, were located below the steel bearing plates and were arranged in a statically determinate “tripod” configuration (Figure 2-1) to ensure that contact between load cells and bearing plates was maintained at all times. Using a tripod configuration also enabled the location of the bearing pad pressure resultant to be determined, relative to the center of the bearing pad, at any point during a roll stiffness test. Washer load cells (Interface, model LW25100, 30 kip capacity) were used to measure vertical roll loads applied to the ends of the outriggers and to compute roll moments imposed on the bearing pad. As the roll loads (and corresponding moments) were applied, an inclinometer (FRABA Posital CanOPEN, +/- 0.087 rad. range, 17 μ rad. resolution) measured the roll angle imposed on the bearing pad. Redundancy in roll angle measurement was achieved by using displacement transducers (TML model CDP-50 and CDP-100, 50 mm and 100 mm (2 in. and 4 in.) stroke, respectively) to measure relative vertical displacements between the steel bearing plates. Knowing the horizontal distance between the displacement transducers, the roll angle imposed on the bearing pad could be calculated from the relative displacement measurements and used to confirm the inclinometer reading. Displacement transducers were also used to monitor horizontal movements of the bearing plates to confirm that shear deformations generated in the bearing pad remained negligibly small during testing.

Test Procedure

As noted earlier, each bearing pad roll stiffness test conducted in this study involved three distinct stages: positioning, clamping, and rolling. Rotations and loads imposed on the pad during each of these stages are identified using coordinate axes defined in Figure 2-1. Examining the global x-y-z coordinate system, both the x- and y-axes are level (horizontal), have their origins at the top surface of the undeformed bearing pad, and are aligned with the centerlines of the outriggers and tube, respectively. The global z-axis is aligned vertically; positive upward.

Positioning Stage

Each test began by positioning the test device on the bearing pad so as to produce the desired slope and skew angles. Slope angle was defined as the vertical angle (Figure 2-2) between the \hat{y} -axis (aligned with the sloped tube) and the y-axis (defined previously). Slope was imposed on the bearing pad by rotating the upper portion test device (the portion above the bearing pad) about the global x-axis of the system. In non-sloped tests, the tube was positioned level (horizontal) and the y- and \hat{y} -axes were identical.

Once the desired slope angle was imposed, the elevations of the y-positive and y-negative ends of the tube (Figure 2-2) were “locked-off” at the correct heights, such that they remained constant throughout the test. Note that the line passing through the y-positive and y-negative hinges was sloped, and aligned with the \hat{y} -axis, ensuring that the top portion of the test device rolled about the \hat{y} -axis, thereby mimicking girder motion during a buckling/overturning event.

Skew angle was imposed, during insertion of the bearing pad between the bearing plates, by rotating the bearing pad about the z-axis (Figure 2-3). Skew angle was defined as the angle between the long axis of the bearing pad and the x-axis of the test device. When positioning the bearing pad at the desired skew angle, the bearing pad was also centered at the z-axis as illustrated in Figure 2-3.

Clamping Stage

During the clamping stage, axial load was gradually applied to the bearing pad by applying clamp loads to the top surfaces of both ends of the tube (Figure 2-2). At the beginning of the clamping stage, the piston of the hollow core hydraulic jack (Figure 2-1) on the y-positive end was fully retracted, and the y-negative end of the tube was “locked-off”. As the piston was subsequently extended, the y-positive end of the tube moved in the negative z-direction (downward), while the movement of the y-negative end of the tube remained restrained. This caused the load produced by the hydraulic jack on the y-positive end of the tube to be mirrored on the y-negative end. In applying the clamp loads through restrained movement, a slight increase of the slope on the pad occurred but was accounted for in advance such that the tube was at the correct slope at the end of the clamping stage. Full application of the target axial load signified the end of the clamping stage, after which the load was held constant for the remainder of the test (to within an acceptable deviation from the target axial load of +/-5% of the target axial load).

Since the clamp loads were applied perpendicular to the top surface of the tube (Figure 2-2), the potential existed for inducing a shear load on the bearing pad (in the y-direction) when the test device was configured with a non-zero slope angle. Therefore, to properly simulate field conditions (where no shear load would be induced), a shear restraint rod (Figure 2-2) was used to prevent the top frame from moving in the y-direction relative to the bottom bearing plate.

Rolling Stage

Girder roll in the field, as would occur during buckling, was simulated in the laboratory by rolling the test device about an axis parallel to the longitudinal axis of the bottom of the tube, aligned with the center of the bearing pad, referred to as the \hat{y} -axis (Figure 2-2). When performing a non-sloped test, the tube was level and the \hat{y} -axis was aligned to the y-axis. Equal

and opposite vertical roll loads were applied to the ends of the outriggers to impose moment about the centerline of the bearing pad (Figure 2-4). At the beginning of the rolling stage, no roll loads were applied to the ends of the outriggers. As the rolling stage progressed, moment and corresponding roll rotation were increased in a step-wise manner, allowing the change of roll rotation to be measured at each load increment.

The individual roll loads were applied iteratively to create the moment on the bearing pad, first gradually increasing the upward load to the x-negative outrigger until a specific target was reached, and then by increasing the downward load to the x-positive outrigger until the loads being read by both roll load cells were equal. Throughout the roll stage of each test, the method of roll load application was load-controlled. A hydraulic jack provided the upward load to the x-negative outrigger, which was increased gradually until a specific load difference was read between the two roll load cells. With the hydraulic jack locked off, the displacement of the x-negative end of the outrigger was maintained while load was applied to the x-positive end of the outrigger. A nut was threaded downward to bear against the end of the x-positive outrigger; the downward displacement produced was dependent upon the number of turns of the nut. By turning the nut until both roll load cells read equal loads (to within an acceptably small tolerance), a pure moment was induced on the bearing pad about its centerline. Multiple sets of moment and roll angle were achieved using this iterative process, allowing moment to be measured as a function of roll rotation, to ultimately determine the roll stiffness of a bearing pad.

Test Program

Composite bearing pad details for prestressed concrete girder cross-sections are specified in the Florida Department of Transportation (FDOT) *Design Standards, Index No. 20500* (2010). The three different pad sizes (denoted A, B, and C; Figure 2-5) tested for roll stiffnesses in this study were those typically used in conjunction with the American Association of State Highway

and Transportation Officials (AASHTO) Type V and VI sections as well as the Florida Bulb-T sections (FDOT 2010). Basing the standard bearing pad sizes on girder cross section, the AASHTO Type V and VI and Florida Bulb-T sections are often used in long span configurations, making them more prone to girder instability than the smaller sections. Two specimens of each pad type were tested, for a total of six specimens (denoted A1, A2, B1, B2, C1, and C2), so that the repeatability of the test results could be evaluated.

Although the FDOT *Design Standards* (2010) specify required shear moduli for the standard bearing pads, the AASHTO *LRFD Bridge Design Specifications Table 14.7.5.2-1* (2004) provides a relationship between shear modulus and durometer hardness. To determine whether the bearing pads acquired for this study were manufactured in accordance with the FDOT requirements, the durometer hardness of each specimen was measured. The measured values were then compared to the equivalent durometer hardnesses that were determined to match the shear moduli specified by FDOT. It was found that each specimen had a measured durometer hardness equal to or exceeding the FDOT requirements (Table 2-1), except specimen C2. In addition to confirming durometer hardness, prior to the end of the test program, external elastomer cover material around the edges of bearing pads C1 and C2 was trimmed off to visually confirm the thicknesses of the internal elastomer layers. Both of the bearing pads modified through this trimming process—referred to as pads C1mod and C2mod to distinguish from the original, unchanged pads C1 and C2—had internal elastomer layers of uniform thickness, to within the tolerance suggested by the National Cooperative Highway Research Program (NCHRP) *Report 449* (Yura et al. 2001) revisions to the AASHTO *M251 Specification*, of +/-3 mm (+/-0.12 in.).

Each bearing pad specimen was first tested under non-skewed, non-sloped conditions and then tested under different combinations of skew and slope to determine the effect of each on bearing pad roll stiffness. Maximum slope angle tested was 0.04 rad. (based on camber, construction tolerance, and bridge grade) and the maximum skew angle tested was 45 deg. At the extreme, a combination of both 0.04 rad. of slope and 45 deg. of skew was tested. Intermediate slope angles of 0.02 rad. and 0.03 rad. were also included in the study to quantify roll stiffness reduction as a function of slope severity.

The naming system used to identify each *configuration* tested was T-x-y, where x=skew angle (deg.), and y=slope angle (rad.). For example, test configuration T-45-04 refers to a test performed at a 45 deg. skew angle and a 0.04 rad. slope angle. Bearing pad specimen identifiers (A1, A2, B1, B2, C1, C2) were also combined with configuration indicators to identify specific tests. For example, A1-45-04 refers to a test performed on bearing pad specimen A1 at a 45 deg. skew angle and a 0.04 rad. slope angle. When discussing an averaged value—such as roll stiffness—between two specimens, A-45-04 refers to the average value of all of the tests performed on A1-45-04 and A2-45-04.

Using this naming convention, the skewed and sloped test conditions that were conducted on each bearing pad are presented in Table 2-1, in which an “X” indicates that tests were performed in that given configuration. Multiple test repetitions were performed in each configuration and on each specimen to ensure repeatability of the test device and results. Individually determined axial load levels were assigned to each bearing pad type (A, B, C) to ensure similar bearing pad axial pressures, regardless of bearing pad size. Also, while all pad configurations were tested under high axial load (pressure), for cases B1-0-0, B2-0-0, and C1-0-0, additional low load (pressure) tests were also performed.

Repeated Axial Compression

Prior to conducting this study, it was not known whether repeated loading, which is known to cause softening of neoprene when loaded in shear (Gent 2001), would affect the roll stiffness results obtained. Cyclic softening of neoprene under shear loading is called the Mullins effect and is recognized by the American Society for Testing and Materials (ASTM) as a phenomenon that must be accounted for when experimentally determining the shear modulus of a bearing pad (2003). Although there is no ASTM requirement for testing a bearing pad cyclically in compression, it was deemed necessary to do so in this study to determine if a similar effect occurred when testing for the roll stiffness. Multiple tests were performed on each bearing pad specimen, and in each configuration, however significant softening of the bearing pad was never observed. Therefore, it was concluded that no axial softening phenomenon, similar to the Mullins effect for shear, was present at the load levels used in the test program.

Variation of Axial Compression Load

As noted previously, selected roll stiffness tests were performed at both low and high axial loads to determine whether variations in axial load would affect bearing pad roll stiffness. The low and high loads assigned to each bearing pad type were chosen to approximate the self weight end reactions of the Florida Bulb-T 72 and 78 sections, at the longest length reasonable for current design practice (Consolazio et al. 2007). At the maximum practical span length of 43 m (140 ft.), the end reaction of the Florida Bulb-T 72 was used as the low axial load, whereas the end reaction of a Florida Bulb-T 78 with a span of 49-55 m (160-180 ft.) was used as the high axial load. Roll stiffness test results indicated that, over an axial load range that is typical of field conditions, bearing pad roll stiffness was not significantly affected by axial load level (average roll stiffness at low load was approximately 22% smaller than roll stiffness at high load).

Ultimately, the high axial load level was chosen for the remainder of the test program, to represent the self weight of a long span Florida Bulb-T 78.

Results

For a given girder cross-section, span length, and bearing pad, girder stability is greatest when bearing pad roll stiffness is maximized. Ideal conditions for maximizing bearing pad roll stiffness correspond to the T-0-0 (non-skewed, non-sloped) configuration included in the test program. Confirming the ideal nature of the non-skewed, non-sloped configuration, the T-0-0 test results for each pad always had a higher initial roll stiffness than pads tested in the most severe non-ideal configuration, T-45-04 (45 deg. skew, 0.04 rad. slope). In Figure 2-6, a representative set of moment-rotation results, obtained from testing pad B2 in the T-0-0 and T-45-04 configurations, illustrates the extent to which roll stiffness may be reduced by the introduction of non-ideal conditions. Performed on the same bearing pad specimen and at the same axial load level, the tests that generated the results shown in Figure 2-6 differed only in skew and slope. As will be demonstrated later, intermediate configurations (e.g. T-45-0, skewed but not sloped) had, on average, roll stiffnesses that fell between the two extreme cases (ideal: T-0-0 and severe: T-45-04).

As shown in Figure 2-6, data from the ideal case exhibit an initial, linear roll stiffness that is followed by an apparent softening (reduction in stiffness) at larger roll angles. This stiffness reduction corresponds to the upper bearing plate of the test device gradually losing contact with the pad and eventually “rolling off” the pad. With regard to the calculation of girder buckling capacity, it is the initial, linear roll stiffness of the bearing pad—and therefore the slope of the initial, linear portion of the moment-rotation (roll) curve—that is of primary importance. An algorithm was established to consistently determine the number of points contained within the initial, linear portion of each moment-rotation data set obtained, through which a linear

regression line was generated. The roll stiffness (k_r) of each bearing pad was defined as the slope of the linear regression line through the initial, linear portion of the moment-rotation curve (Figure 2-6).

Moment-rotation curves obtained for all roll stiffness test performed in this study, grouped by bearing pad specimen, are presented in Figure 2-7. Generally, the moment-rotation curves for the intermediate cases fell between the two extreme cases (T-0-0 and T-45-04), with good repeatability of the data within each specimen and configuration. Whereas tests with zero slope generally exhibited both linear and nonlinear portions of the moment-rotation curve, most of the tests with non-zero slope exhibited moment-rotation curves that remained essentially linear throughout the entire test.

Location of Pressure Resultants on Bearing Pads

Initial roll stiffness, as well as whether a bearing pad exhibited linear or non-linear behavior, depended upon the location of pressure resultants on the bearing pad. Under conditions of combined skew and slope, significant reductions in roll stiffness were clearly evident from the test data. Such reduction of stiffness occurs due to the eccentricity of the pressure resultant of the axial load on the bearing pad. As a girder (or the bearing pad test device) rolls on a bearing pad, the pressure distribution on the pad becomes more concentrated on the side of the pad that corresponds to the direction of roll. This causes the location of the pressure resultant to move as well, becoming increasingly eccentric from the centerline of the girder with increasing roll angle.

Figure 2-8 presents pressure distributions and pressure resultant locations at various stages of roll angle leading ultimately to girder instability. In the non-skewed configurations (Figure 2-8A and Figure 2-8B) a large eccentricity between the girder centerline and the pressure resultant is available to resist overturning moment applied during girder roll. In contrast, although the skewed, non-sloped case (Figure 2-8C) begins with a concentric loading similar to the non-

skewed, non-sloped case (Figure 2-8A), a smaller eccentricity develops during girder roll, thereby decreasing the roll stiffness. The smallest available eccentricity occurs under the skewed, sloped configuration (Figure 2-8D), which also produces the least roll stiffness. For configurations in which the moment-rotation curves are non-linear, the eccentricity is most important at intermediate roll angles where the response transitions from linear to non-linear. At the point of girder instability, the instantaneous eccentricity is an indicator of the secant stiffness at the corresponding roll angle, which is why the non-skewed cases (with larger eccentricities) exhibit larger overall stiffnesses than do the skewed cases (recall Figure 2-7). The presence of an eccentric pressure distribution at the end of the rolling stage of tests conducted in the non-skewed, non-sloped configuration (Figure 2-8A) is evidenced by bulging at the edge of the pad, as shown in Figure 2-9.

Linearity of the moment-rotation curve is controlled by the portion of the bearing pad that remains in contact with the girder as it becomes unstable. In sloped configurations, a larger portion of the bearing pad—opposite the direction of girder roll—remains in contact with the girder than in the non-sloped configurations. Losing contact with the girder on the side of the pad opposite the direction of girder roll causes nonlinearity in the moment-rotation curve.

Data Trends

Individual roll stiffnesses, determined from each test conducted in this study, are shown in Figure 2-10, together with mean values computed for each combination of bearing pad type, skew, and slope. For convenience, the mean roll stiffness for each combination of pad type, skew, and slope are also reproduced in Figure 2-11. Table 2-2 also presents corresponding roll stiffness reductions due to combinations of skew and slope as compared to the ideal T-0-0 configuration. Excluding the A-0-02 mean results, within each bearing pad type, the ideal case (T-0-0) had the largest roll stiffness, and the extreme skew and slope case (T-45-04) had the

smallest roll stiffness, with intermediate configurations producing roll stiffnesses falling between the two. Examining Figure 2-11, the roll stiffness of the type C bearing pads was generally decreased after the modification of the bearing pads (C-0-0 to Cmod-0-0), which can be attributed to the trimming of the outer layer of rubber.

Effect of Skew and Slope Combined

The combination of skew and slope produced the most severe reduction of roll stiffness. When slope is combined with skew, the average reductions of roll stiffness—relative to the ideal T-0-0 case— for configurations T-45-02 and T-45-04 were 81% and 85%, respectively. This indicates that reducing the slope angle from 0.04 rad. to 0.02 rad. has little benefit if skew is also present. Furthermore, comparisons of results from test configurations T-45-02 and T-45-04 for each pad type (i.e., A-45-02 vs. A-45-04, B-45-02 vs. B-45-04, C-45-02 vs. C-45-04) reveal that the roll stiffness decreases only slightly in going from the T-45-02 to the T-45-04 condition.

Effect of Skew

Comparing test results for configurations T-0-0 to T-45-0 in Figure 2-11, it is evident that significant reductions in bearing pad roll stiffness resulted from the presence of skew only, regardless of specific bearing pad type (A, B, C). Average roll stiffness reduction due to skew alone for all of the bearing pad types was 49%, with little variation in percent reduction when comparing different pad types.

Effect of Slope

There was an inconclusive trend in the roll stiffness reduction due to imposed slope angle alone. Decreasing roll stiffness due to increasing slope was observed in the type B bearing pads (i.e. roll stiffness decrease from B-0-0 to B-0-02, and from B-0-02 to B-0-03). However, for the modified type C bearing pads, when comparing the ideal (Cmod-0-0) configuration to sloped configurations (Cmod-0-02 and Cmod-0-03), an insignificant reductions of stiffness resulted

from imposed slope angle. [Note that roll stiffness reductions due to slope alone as produced by configurations Cmod-0-02 and Cmod-0-03 are calculated in comparison to Cmod-0-0 (as opposed to C-0-0)]. Roll stiffness reduction due to slope was also inconclusive due to results obtained from the type A bearing pads, where the roll stiffness increased from A-0-0 to A-0-02, but decreased from A-0-0 to A-0-04. However, this apparent anomaly may be related to the fact that the range of scatter in the data obtained for configuration A-0-02 was greater than that of any other configuration tested on the type A bearing pads (Figure 2-10).

Table 2-1. Bearing pad dimensions, shear modulus, durometer hardness, and configurations tested for each specimen

| | Bearing pad type | | | | | |
|---------------------------------------|------------------|----|--------|-----|--------|----|
| | A | | B | | C | |
| Bearing pad length, L (in.) | 11 | | 14 | | 12 | |
| Bearing pad width, W (in.) | 24 | | 24 | | 23 | |
| Bearing pad height, H (in.) | 1-29/32 | | 2-9/16 | | 2-9/16 | |
| Number of internal plates | 3 | | 4 | | 4 | |
| Shear modulus (psi) | 110 | | 110 | | 150 | |
| Equivalent durometer hardness (Grade) | 50 | | 50 | | 60 | |
| Bearing pad specimen | A1 | A2 | B1 | B2 | C1 | C2 |
| Measured durometer hardness (Grade) | 53 | 50 | 53 | 52 | 61 | 53 |
| Low axial load level (kip) | - | - | 67 | 67 | 69 | - |
| High axial load level (kip) | 92 | 92 | 101 | 101 | 97 | 97 |
| Test Configuration T-0-0 | X | | X | | X, X* | |
| Test Configuration T-0-02 | X | | X | | X* | |
| Test Configuration T-0-03 | | | X | | X* | |
| Test Configuration T-0-04 | X | | | | | |
| Test Configuration T-45-0 | X | | X | | X | |
| Test Configuration T-45-02 | X | | X | | X | |
| Test Configuration T-45-04 | X | | X | | X | |

* Test configuration performed on modified bearing pad.

Table 2-2. Mean roll stiffness and reduction in roll stiffness due to non-ideal (skewed, sloped) conditions

| Configuration | Roll stiffness, kip-ft./rad. | | | |
|---------------|------------------------------|---------------|---------------|----------------|
| | [Roll stiffness reduction] | | | |
| | Pad A | Pad B | Pad C | Pad Cmod |
| T-0-0 | 7004 [0%] | 11427 [0%] | 9737 [0%] | 6079 [38%]* |
| T-0-02 | 8597 [-23%] | 7282 [36%] | - | 5810 [4%] |
| T-0-03 | - | 5291 [54%] | - | 5490 [10%] |
| T-0-04 | 5360 [23%] | - | - | - |
| T-45-0 | 4067 [42%] | 5661 [50%] | 4490 [54%] | - |
| T-45-02 | 1740 [75%] | 1610 [86%] | 1764 [82%] | - |
| T-45-04 | 1339 [81%] | 1416 [88%] | 1372 [86%] | - |

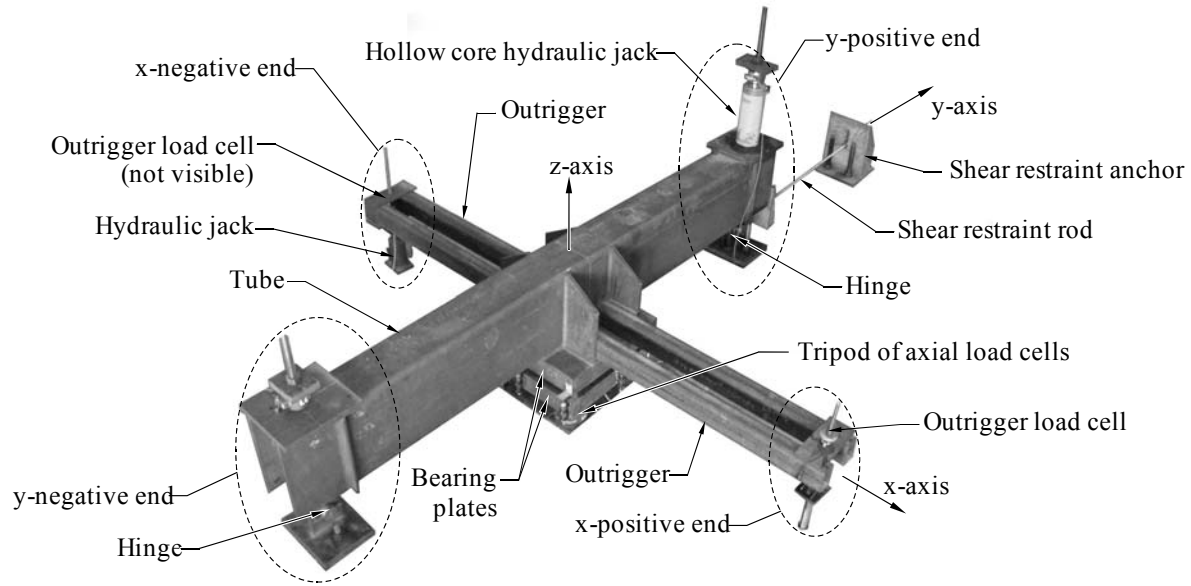


Figure 2-1. Bearing pad test device (photo courtesy of University of Florida, Department of Civil and Coastal Engineering)

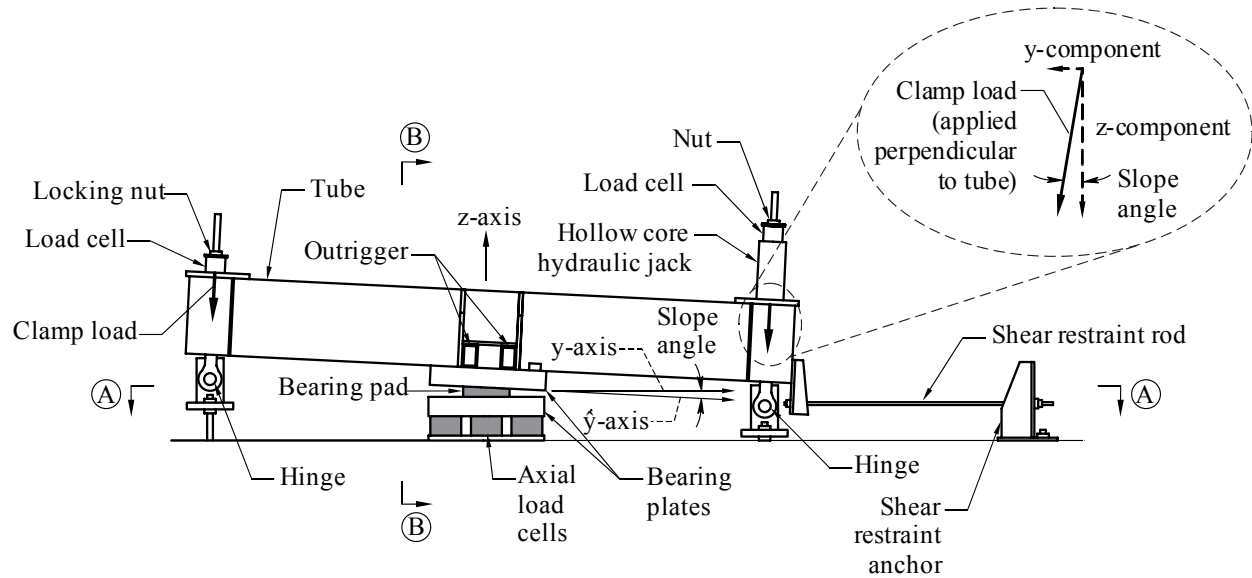


Figure 2-2. Elevation view of test device: imposing slope (positioning stage) and applying axial load (clamping stage)

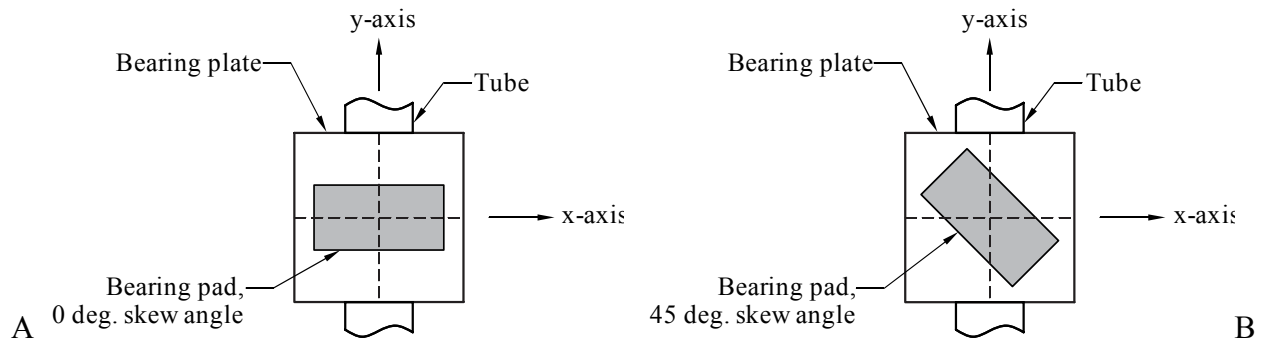


Figure 2-3. Imposing skew during the positioning stage, 0 deg. and 45 deg. skew shown (see Section A-A, Figure 2-2)

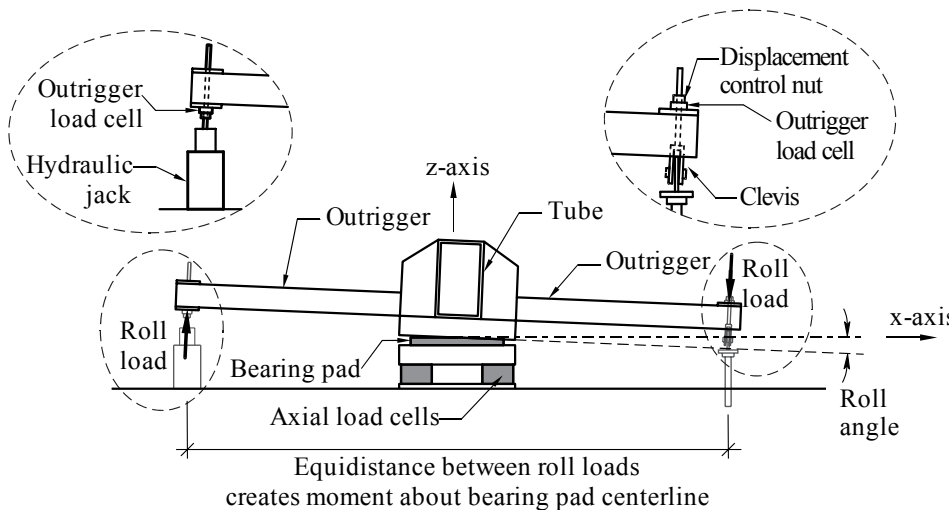


Figure 2-4. Applying loads to outriggers during rolling stage (see Section B-B, Figure 2-2)

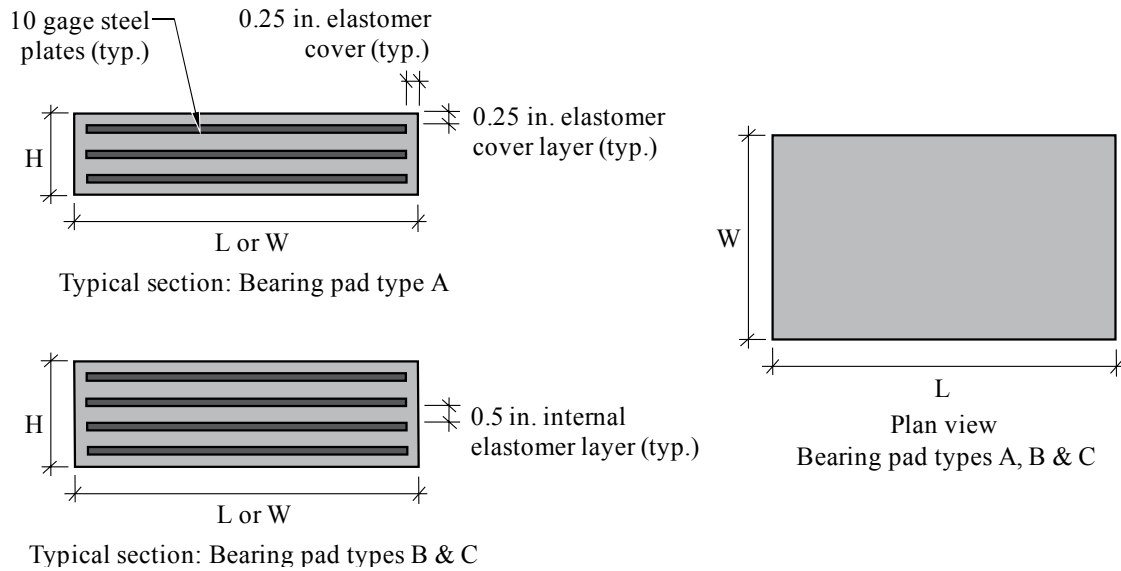


Figure 2-5. Identification of bearing pad dimensions (see Table 2-1 for actual dimensional values)

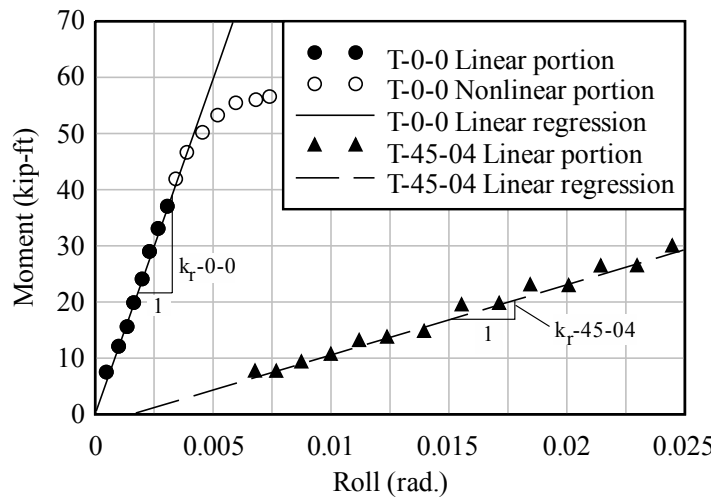


Figure 2-6. Representative moment-rotation curves, configurations T-0-0 and T-45-04 (obtained from testing bearing pad B2)

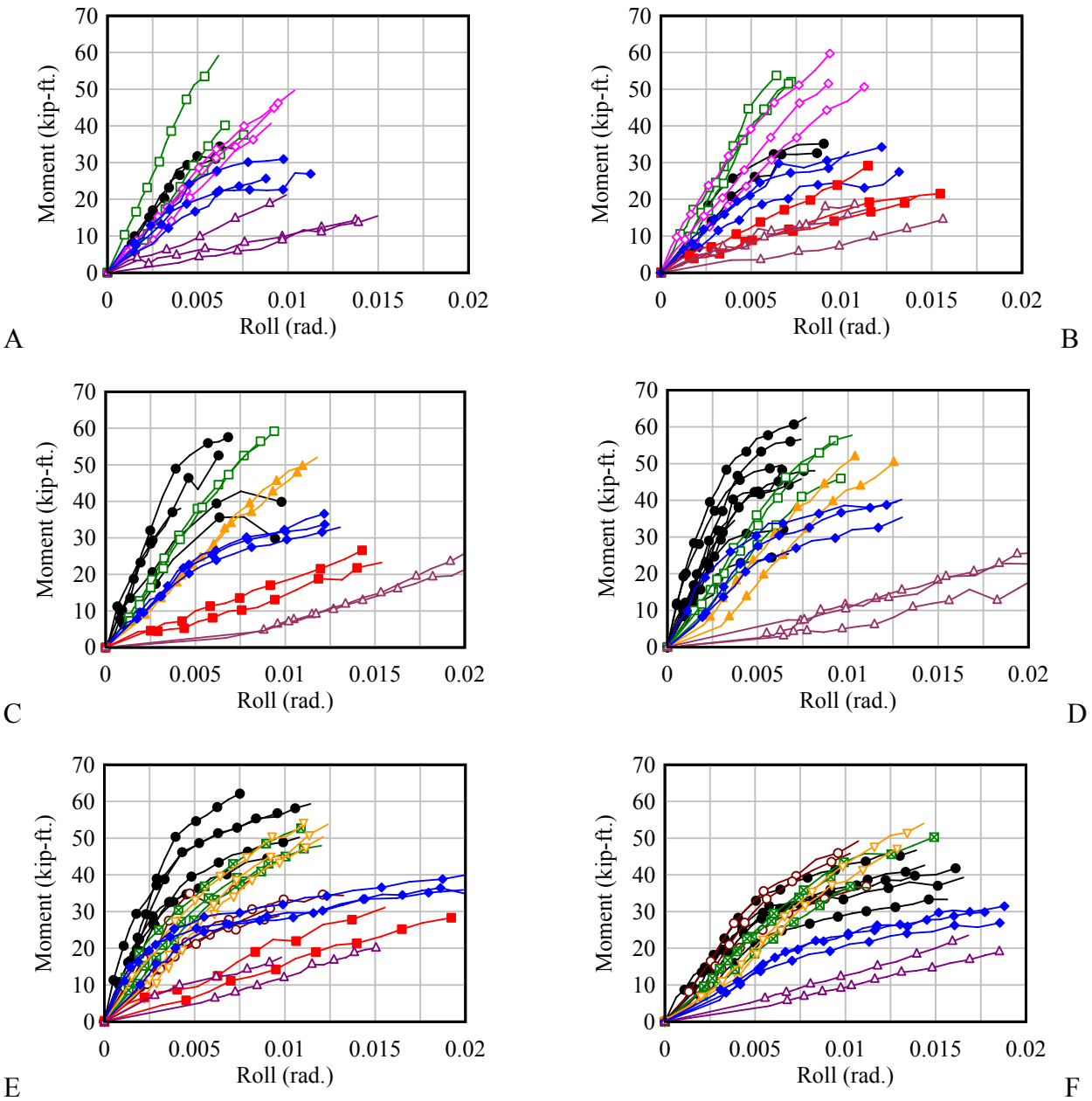


Figure 2-7. Moment-rotation curves for all tests, grouped by pad specimen.
 A) Pad A1. B) Pad A2. C) Pad B1. D) Pad B2. E) Pad C1. F) Pad C2.

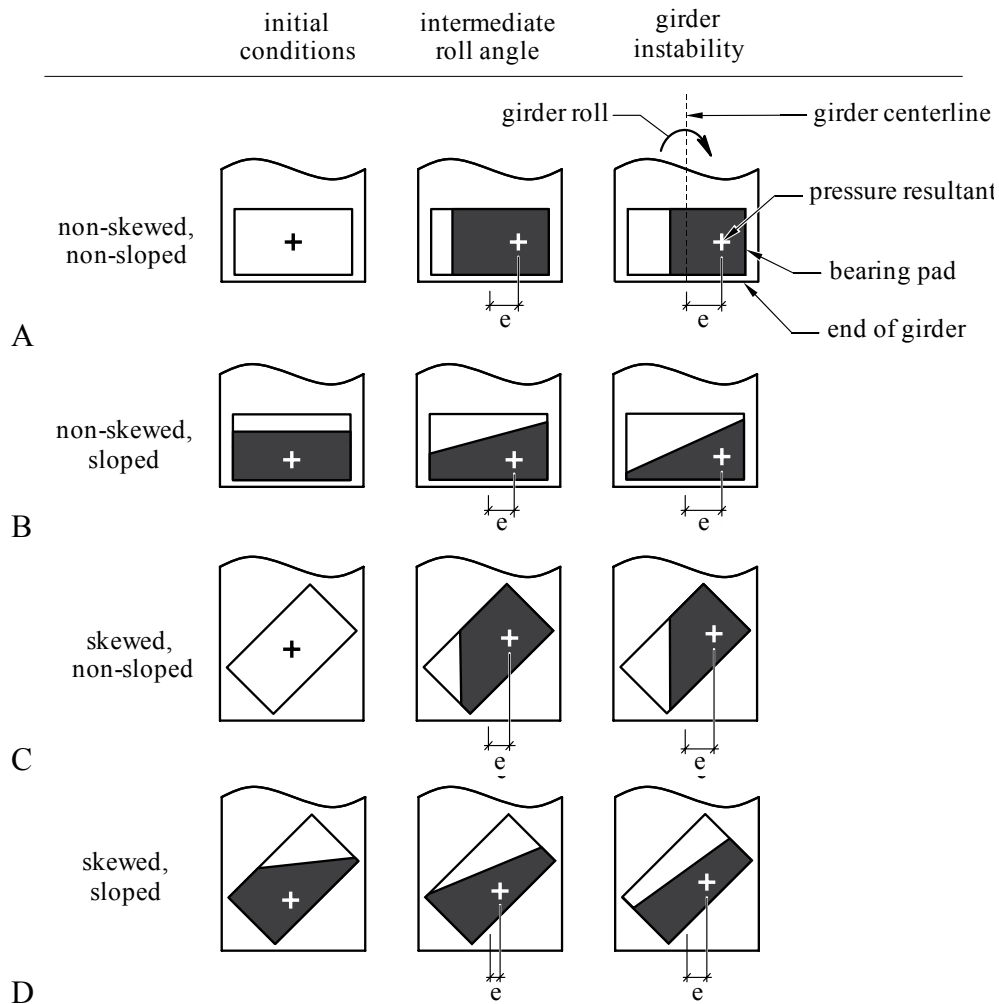


Figure 2-8. Pressure distributions and axial load resultant positions on bearing pad: beginning, intermediate, and end of rolling stage. Configurations: A) Non-skewed, non-sloped. B) Non-skewed, sloped. C) Skewed, non-sloped. D) Skewed, sloped.

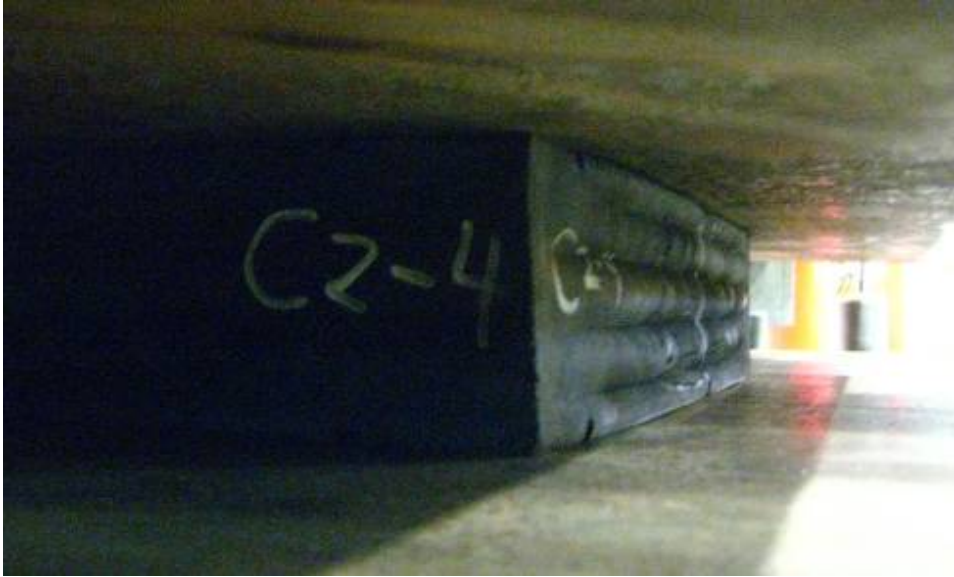


Figure 2-9. Bulging of the internal elastomer layers during roll stiffness test (photo courtesy of University of Florida, Department of Civil and Coastal Engineering)

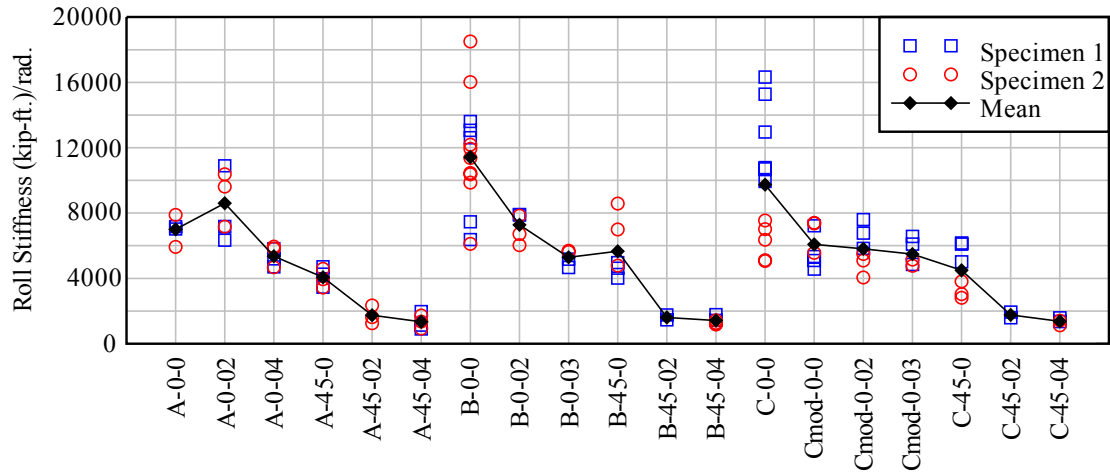


Figure 2-10. Bearing pad roll stiffnesses for all configurations tested

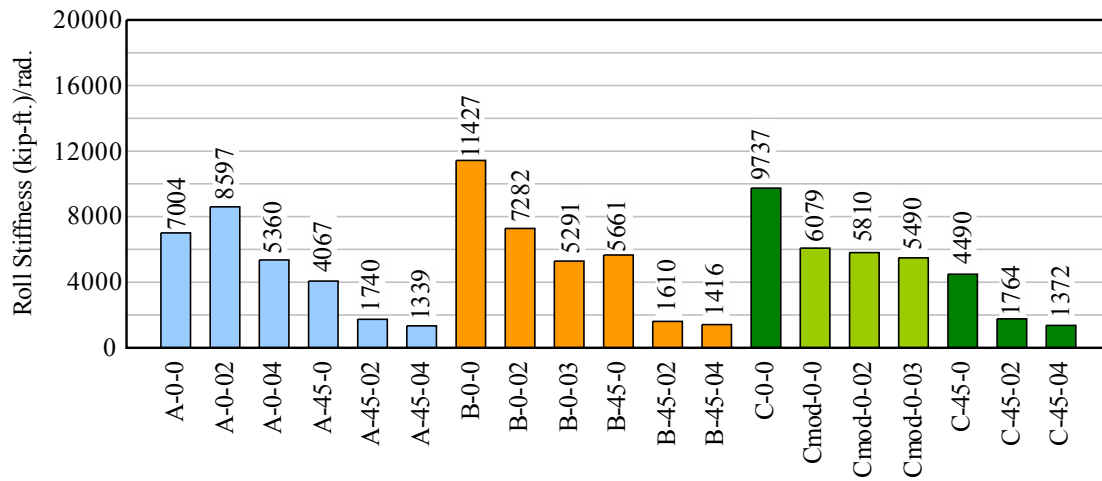


Figure 2-11. Mean bearing pad roll stiffnesses for all configurations tested

CHAPTER 3 INTRODUCTION TO GIRDER BUCKLING TESTS

The point at which a girder may reach instability in the field, during construction of a bridge, is dictated by several factors, including cross-sectional properties of the girder, span length, geometric imperfections such as sweep, and bearing pad roll stiffness. As discussed previously in Chapter 2, bearing pad roll stiffness is significantly reduced when skew, slope, or a combination of the two is imposed on a pad. In a previous analytical study (Consolazio et al. 2007), it was shown that imposition of skew and/or slope—resulting in reduced bearing pad roll stiffness—leads to decreased girder buckling capacity. In the phase of the present study that is described in this and following chapters, a full scale girder buckling test program was designed and conducted to experimentally quantify the influence of bearing pad roll stiffness on girder buckling capacity.

Scope of Test Program

The scope of the experimental test program included the design and construction of: a full scale test girder; a vertical loading system (consisting of gravity load simulators); and end supports that enabled various combinations of slope and skew to be imposed on the supporting bearing pads (Figure 3-1). The pads used to support each end of the test girder were the same pads previously tested—to determine roll stiffness—in the first phase of this study. Rigid end supports elevated the test girder approximately 8 ft. above the lab floor to provide vertical clearance for gravity load simulators that were positioned beneath the beam (Figure 3-1). Each gravity load simulator (described in detail later) applied vertical load to the test girder in a manner that did not introduce any lateral stiffness. In total, nine (9) buckling tests were conducted, with various skew and slope conditions imposed on the supporting bearing pads. Analytical models corresponding to the test setup were developed and used to simulate the

experimental buckling tests. Validation of the models was then carried out by comparing the buckling capacity predictions from the analytical simulation to experimental test results.

Experimental Constraints

Length of Test Girder

Buckling tests were performed inside the FDOT M. H. Ansley Structures Research Center laboratory where the available length the strong floor permitted a maximum physical test girder length of 102 ft. With the overall (end to end) girder length limited to 102 ft., the effective girder span length—as measured from center of bearing pad to center of bearing pad—had to be a few feet shorter to accommodate pad skew at each end of the girder (Figure 3-2). For each pad skew angle tested, both bearing pads had to be completely contained within the footprint of the girder end blocks (i.e., no part of the pad was permitted to protrude beyond the end of the physical length of girder). For reasons that will be discussed in detail later, the type A bearing pads (described previously in Chapter 2) were used to support the ends of the girder during the buckling tests. Rotating the type A bearing pad to the maximum skew angle of 45 deg. and allowing 5/8 in. clearance between the corner of the pad and edge of the girder end block (Figure 3-1), required that the center of the bearing pad be located 13 in. from the edge of the test girder, making the span length 99 ft.-10 in., or approximately 100 ft.

Loading Conditions

Under field loading conditions, girder buckling is induced by the self weight of the girder, which consists of a uniformly distributed vertical load acting through the center of gravity of the girder cross-section. To emulate such field loading conditions in the laboratory, ideally a uniform load would be applied, with no lateral restraint, through the center of gravity of the girder. In this study, devices called ‘gravity load simulators’ (described in detail later) were designed, fabricated, and used to apply vertical loads—without lateral restraint—to the test girder. Since

such devices apply point loads rather than uniformly distributed loads, the uniform field loading condition was approximated in the laboratory using two point loads located approximately at the third points of the girder span (Figure 3-1).

Originally, two possible loading conditions were investigated to determine the level of error that would be introduced by replacing the ideal uniform loading condition with point loads: a single concentrated load applied at midspan, and two equal concentrated loads applied at the third points. For each of the three loading conditions of interest (uniform load, midspan point load, and third point loads), moment diagrams for a simply supported beam, each with the same maximum moment, are presented in Figure 3-3. As shown, the shape of the uniformly loaded moment diagram is most closely matched by the pair of concentrated loads as opposed to the single concentrated load. In fact, the areas under the moment diagrams produced by uniform load and third point loads are exactly equal. Therefore, two point loads were applied to the test girder using gravity load simulators located approximately at the third points of the girder (applying loads at the precise third points was not practical due to laboratory strong floor embed locations).

Gravity induced self-weight loads on the girder act, by definition, through the center of gravity of the cross-section. Applying laboratory loads through the center of gravity, however, would have required the introduction of holes through the web of the test girder, creating issues such as the potential for localized crushing of the concrete in the web, or cracking. To avoid these concerns, the point loads were instead applied at the centerline of the top surface of the test girder (Figure 3-1). Finite element analyses of both the center of gravity loading scenario and the top surface loading scenario were conducted to determine if the buckling loads corresponding to each loading scenario were sufficiently in agreement. Analysis results indicated minimal

difference in buckling loads, therefore it was deemed acceptable to load the test girder at the top surface of the top flange.

Elastic Buckling

The buckling tests conducted in this study were performed for the purposes of experimentally demonstrating sensitivity of buckling capacity to changes in bearing pad roll stiffness, and to collect data for validation of numerical models. Furthermore, to establish confidence in the experimental data, it was desirable to demonstrate repeatability of the test results. Given these objectives, cracking of the concrete girder (particularly partial section cracking) was undesirable as it might have obscured the influence of the pad roll stiffness and would have been very challenging to reproduce analytically. Additionally, section cracking could have lead to differences in beam response from one test repetition to the next (for a fixed bearing pad configuration). ACI 318-11 Table R18.3.3 states that if a girder enters the transition zone (i.e., the zone between the uncracked and fully cracked conditions), then cracked section properties must be used to determine girder deflection. Since deflection was a key parameter measured during each laboratory buckling tests, it was desirable to design the test girder to buckle elastically so that partially cracked section properties would not need to be used in interpreting the test results. Elastic behavior also ensured repeatability of the tests (which will be clearly demonstrated later in this thesis) and ensured that the only factor influencing buckling capacity was bearing pad roll stiffness.

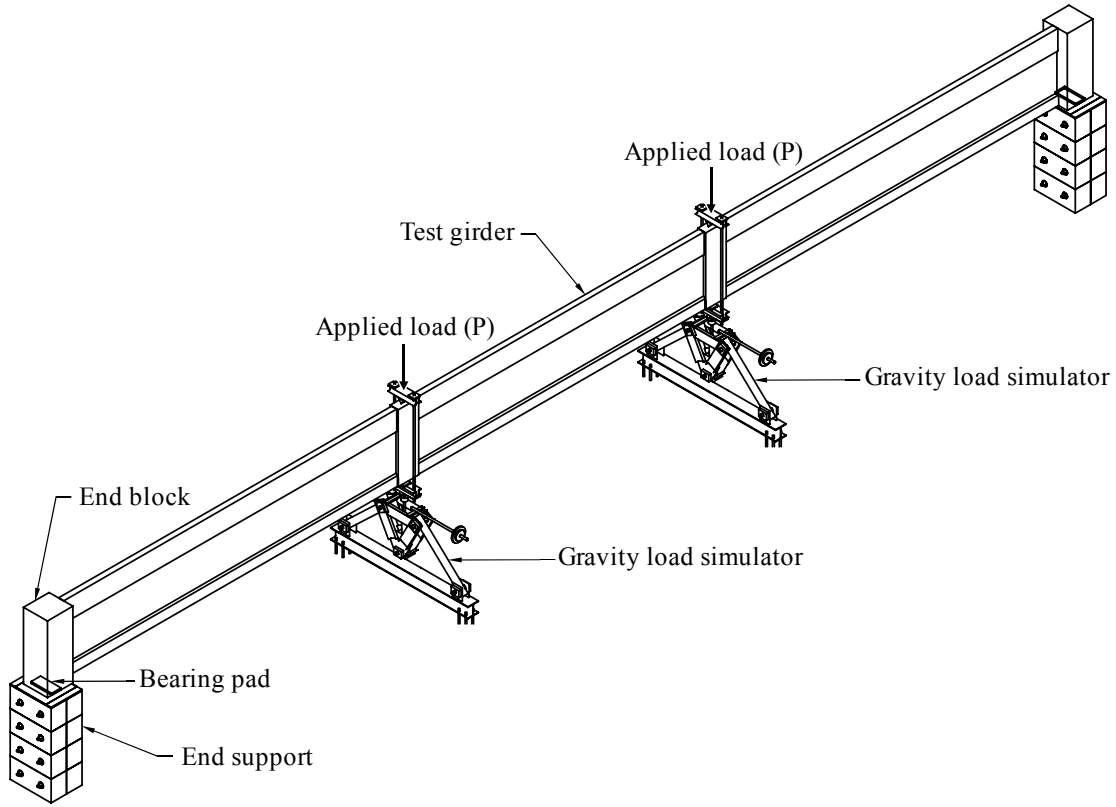


Figure 3-1. Overview of test setup

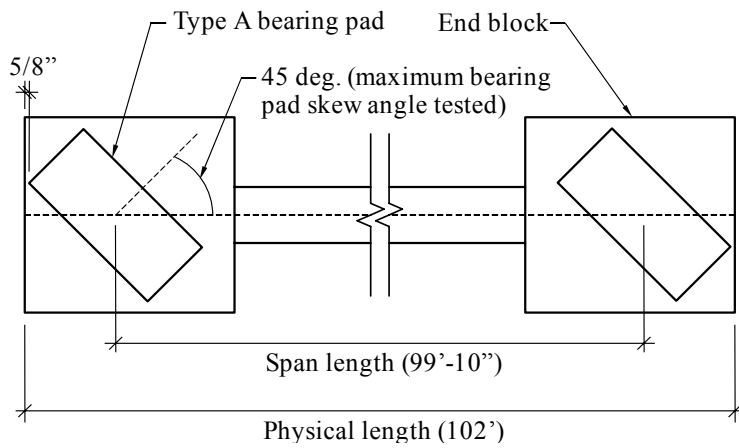


Figure 3-2. Physical length and span length defined

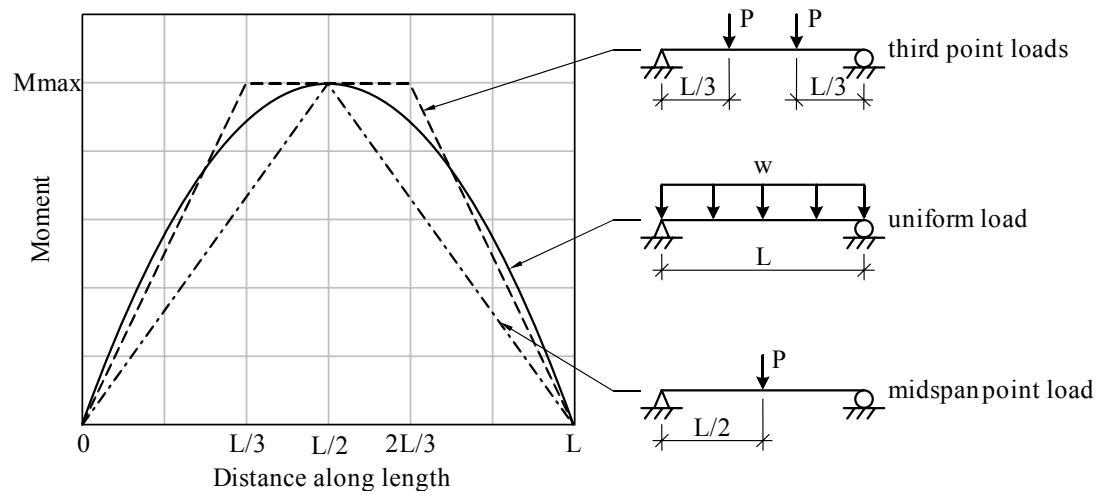


Figure 3-3. Moment diagrams for simply supported beam with various loading conditions

CHAPTER 4 BUCKLING ANALYSIS

Overview

To facilitate the design of a test girder cross section that would buckle elastically at a span length of approximately 100 ft., finite element models of the girder and support system were developed using the finite element code ADINA (ADINA 2010). Girder models employing a variety of different trial cross-sectional shapes were analyzed under the planned experimental test loading conditions to arrive at a cross-sectional shape that was expected to buckle elastically at a span length of 100 ft. This chapter describes the finite element models and the analysis procedures that were used to quantify girder buckling load and arrive at a suitable girder cross-sectional shape.

Finite Element Model of Experimental Test Setup

As noted previously, buckling tests were performed on a full scale test girder using a vertical loading system consisting of gravity load simulators and load frames. For reasons that will be discussed later in this thesis, it was necessary to construct the test girder in a segmental manner. Consequently, three component types, each with a distinct cross-sectional shape, were used to form the overall girder: precast segments, closure strips, and end blocks (Figure 4-1). Gravity load simulators were used to apply vertical load to the top of the test girder at the closure strip locations.

To determine a girder cross-sectional shape that would buckle elastically at a 100 ft span, buckling capacity analyses are carried out by conducting large displacement analyses on system-level models (Figure 4-2) that combined beam elements (representing the test girder) and spring elements (representing the bearing pad). In this approach, loads are incrementally applied to the structure, and at each level of loading, static equilibrium of the structure (stability) is solved for

in the deformed configuration of the structure (i.e., taking into account the changes of geometry that have occurred as a result of the loads). In order to use such an approach to solve buckling problems, member imperfections (e.g., sweep) must be introduced into the initial configuration of the structure. Sweep imperfection of the girder is introduced by superimposing a second order lateral parabolic shape on the girder with maximum sweep occurring at mid-span. Inclusion of sweep in the girder model accounts for construction imperfections and also aids in initiating girder instability under the applied loads.

Concrete components of the test girder are modeled using a linear elastic material model. During the test girder cross sectional shape development stage of this project, a representative elastic modulus of 4,770 ksi was used for the concrete. This modulus was later updated to reflect results of modulus tests on concrete cylinders from the test girder.

To achieve both computational efficiency and accuracy, a combination of standard Hermitian beam elements and warping beam elements are used to model the girder. Warping effects (resulting from torsion) are accounted for by means of an additional warping degree of freedom when using warping beam elements. In contrast, plane sections remain planar when using Hermitian beam elements. The slender precast segments and closure strips are modeled with warping beam elements to capture warping effects if necessary. The relatively rigid end blocks are modeled using Hermitian elements. Regardless of type of element (Hermitian or warping), resultant cross-sectional properties are varied along the length of the test girder, depending on the section (precast segment, closure strip, or end block) present at each location (Figure 4-2). The girder elements are geometrically located at the center of gravity (C.G.) of the test cross-section. The eccentricity between the bearing pad (described below) and the C.G. of the section is represented in the model using rigid links (Figure 4-3). Similarly, rigid elements

extend upward to loading points at the top surface of the physical beam. Vertical point loads are applied to these locations to simulate vertical loads applied by each gravity load simulator.

Each bearing pad in the system model is represented using a set of six (6) spring elements consisting of three translational springs and three rotational springs (Figure 4-2). Translational springs—representing the shear stiffness of the bearing pad (along the x-axis or y-axis) and axial stiffness (along the z-axis)—are linear and based on stiffness results from previous research (Consolazio et al. 2007). Similarly, rotational springs representing pad torsional stiffness (about the z-axis) and roll about an axis perpendicular to the span of the beam (about the x-axis) were modeled as linear springs, with stiffnesses determined from results of previous research (Consolazio et al. 2007). In contrast, rotational springs about the y-axis (i.e., the roll axis) are *nonlinear*, derived from roll stiffness results (moment-roll curves) quantified in Chapter 2, from the isolated bearing pad experiments.

Loads acting on the girder model include uniform self-weight (graving loading), which acts through the center of gravity of the section (Figure 4-4A), and concentrated vertical loads applied to the top of the section at the two closure strip locations (Figure 4-4B). To analyze the girder for the purpose of quantifying buckling capacity, loads are applied to the model in two stages (Figure 4-5). The uniform loading is increased in small steps (increments) from zero to the full self weight of the girder, then held constant while the magnitude of the applied point loads is incrementally increased. At each incremental load step, girder displacements are computed by numerically satisfying static equilibrium of the girder in the deformed geometric configuration. A buckling simulation is complete once equilibrium can no longer be established, indicating that structural instability (buckling) has occurred.

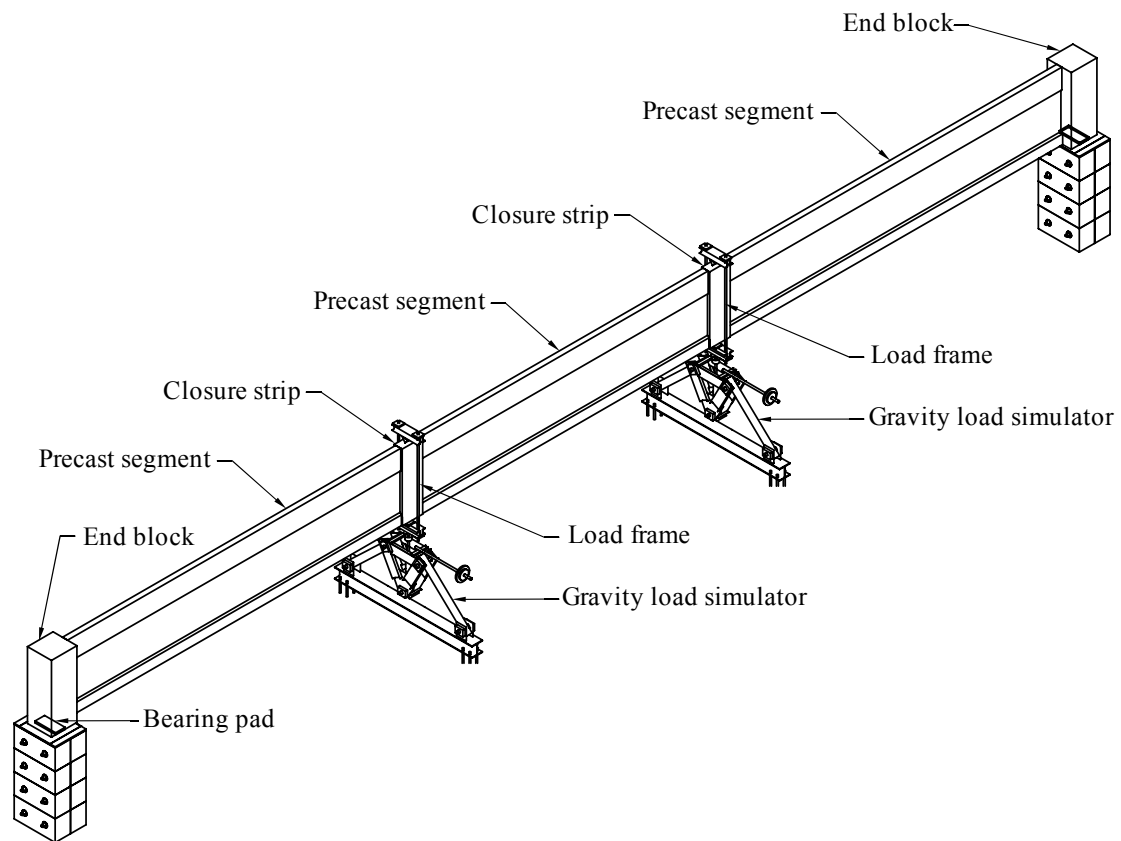


Figure 4-1. Test setup overview

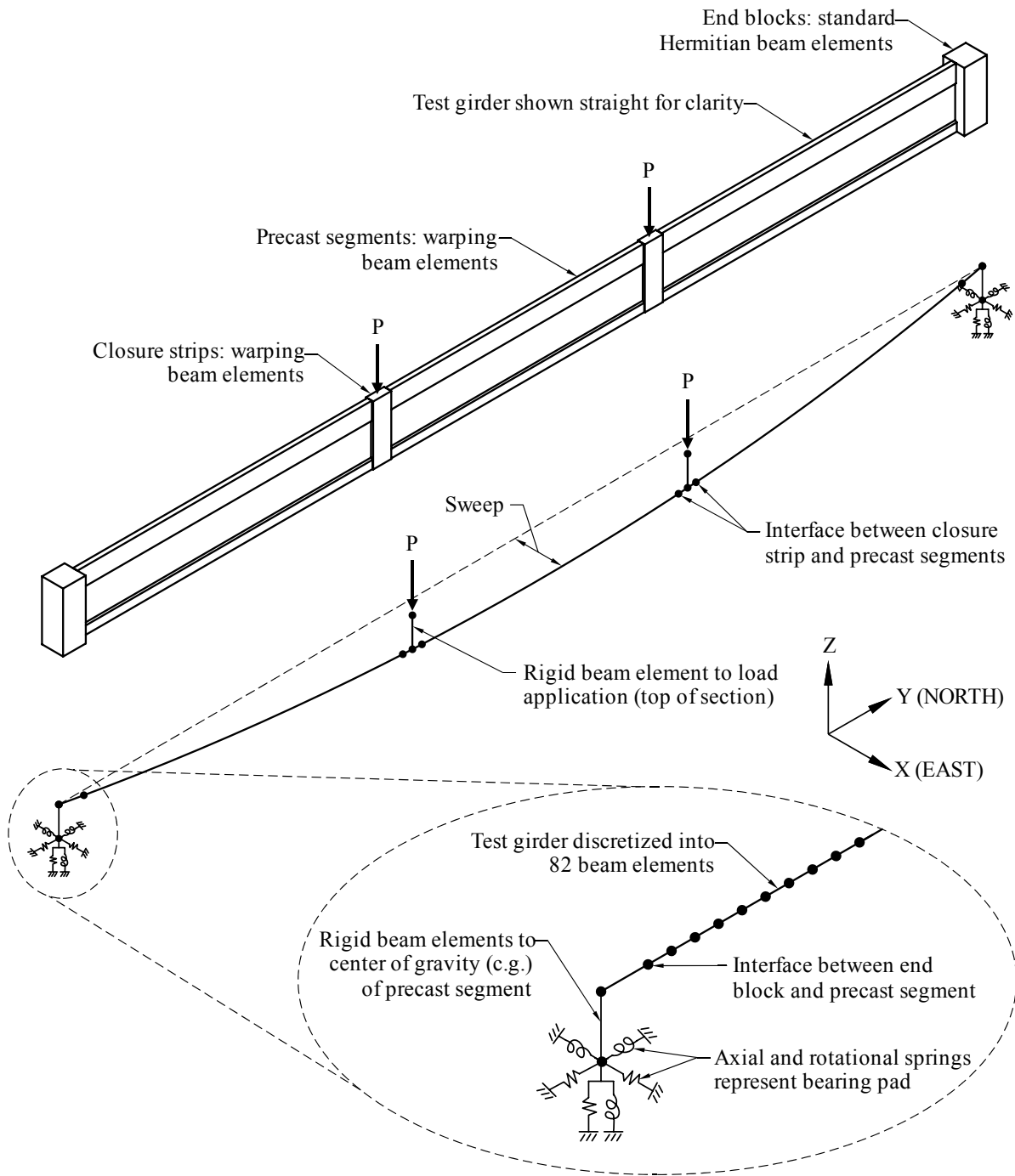


Figure 4-2. Test girder buckling system model

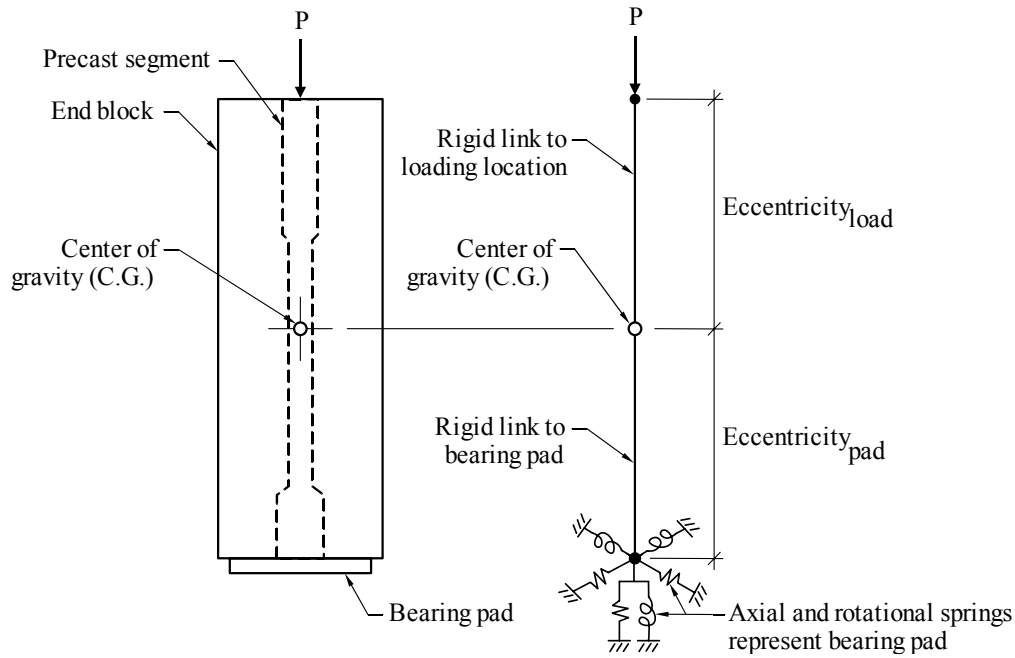


Figure 4-3. Eccentricities of load application point and bearing pad relative to center of gravity of test cross-section

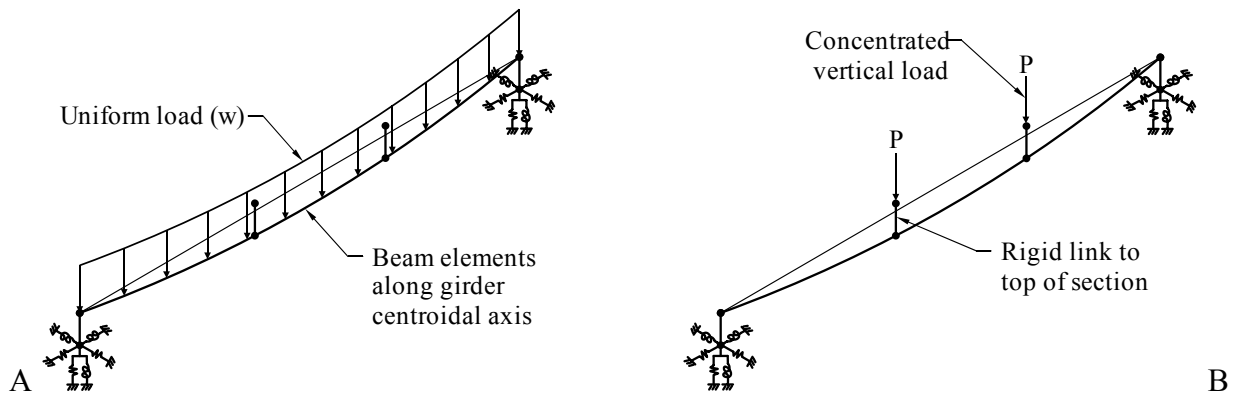


Figure 4-4. Load application on test girder buckling analysis. A) Uniform load. b) Concentrated vertical loads.

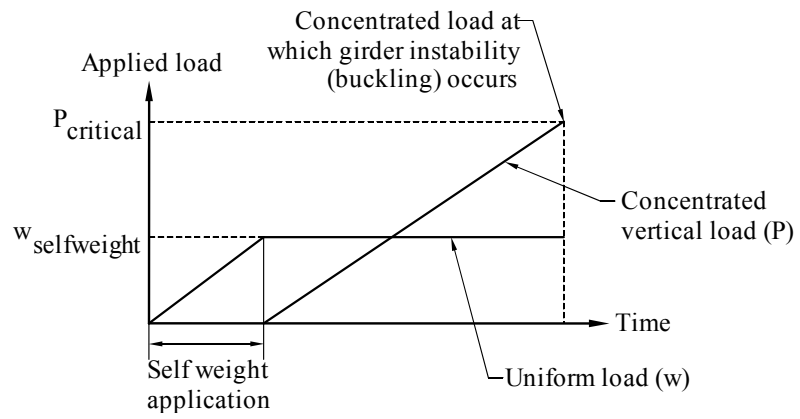


Figure 4-5. Load procedure for buckling analysis

CHAPTER 5 DEVELOPMENT OF TEST-GIRDER CROSS-SECTIONS

Under ideal circumstances, buckling tests would be performed on a typical section used in long-span girder construction. During the course of this project, the standard section for long-span construction was updated from the Florida bulb-tee (FBT) to the current Florida I-beam (FIB). Using the same pad types tested in the roll stiffness experiments, finite element buckling analyses were performed with the cross-sectional properties of several of the FBT and FIB sections. In the case of the non-skewed, non-sloped bearing pad orientations, the load required to buckle either type of section at the available test span length of 100 ft would cause significant cracking in the girder. To avoid violating one of the initial test setup constraints (the girder must remain in the uncracked zone), alternative cross-sections were explored that would buckle elastically in the laboratory at a 100 ft. span length. Preliminary analysis indicated that the resulting test cross-section would need to be significantly more slender than a typical FBT or FIB section. To limit stresses induced during transportation, the test girder was composed of three individual prestressed precast segments that were transported on a flatbed truck.

Using segmental construction, post-tensioning was used to form a continuous test girder of the prestressed precast segments, closure strips, and end blocks (Figure 5-1). At the junction between each precast segment was a closure strip, which served as a means of connecting the precast segments together and also served as the location at which concentrated point loads would be applied. End blocks were used to provide sufficient bearing surface areas for the bearing pads located at the ends of the test girder, and to provide an anchorage points for the post-tensioning. The remainder of this chapter details each component of the segmental test girder and summarizes the basis for design of each component. Complete construction drawings for the test girder can be found in Appendix B.

Precast Segment Cross-Section Design

Design of Girder Cross-Section

Several analytical tools were used in the test girder design process to determine cross-sectional properties of trial cross-sections (Mathcad), predict buckling loads (the finite element analysis software package ADINA), and calculate stresses throughout the test girder using the predicted buckling loads (Mathcad). The procedure for designing the test girder cross-section is summarized in Figure 5-2. Beginning with the standard Florida bulb-tee cross-section, a buckling analysis was performed. The strong and weak axis internal moments obtained from the buckling analysis (due to the predicted buckling loads) were used to calculate concrete stresses along the length of the test girder, which also accounted for stresses due to prestressing. These stress calculations were performed at various stages in the life of the test girder: during prestressing, during transport, and during testing. The calculated stresses at each stage were compared to the transition zone tensile and compressive stress limits required by the FDOT Structures Design Guideline (2012) §4.3.1.C.3 and ACI318-11 §18.3.3, §18.4.1, and §18.4.2. If the calculated stress at any point exceeded these stress limits, then the trial cross-section design was rejected and a new cross-section was developed. A separate cross-sectional analysis program was used to determine cross-section properties (e.g., moments of inertia, torsional constant, warping constant) of trial sections by specifying the cross-section geometry. The cross-section properties of the new trial section were subsequently incorporated into the buckling model, and the process of determining the internal moments and checking stresses was repeated.

Following this iterative process, several different test cross-sections were designed and evaluated to check for exceedance of permissible stress limits. For each iteration, the cross-section was altered to decrease the buckling capacity of the test girder, thereby decreasing

the stresses in the test girder. For long span slender flexural elements, buckling capacity is highly sensitive to the weak axis moment of inertia (I_z) and torsional constant (J), in that decreasing either property decreases the buckling load. Maintaining a large strong axis moment of inertia (I_x)—and therefore maintaining a large strong-axis moment capacity of the test girder—is necessary to avoid cracking under the applied buckling load.

The process of increasing slenderness and reducing buckling capacity was initiated with the standard FBT78 cross-section, where portions of the protruding top and bottom flanges were removed (Figure 5-3). An iterative trimming process, each subsequent section was designed to be less wide than the previous iteration, while the height remained unchanged, effectively reducing the buckling load while maintaining moment capacity. Once the flanges were completely removed and the cross-section was still predicted to crack under the applied buckling load, the web thickness was trimmed as well.

After several iterations, the slenderness of the cross-section became an issue in regard to limiting stresses during shipping. Typically, if a girder is 100 ft long, it is transported by spanning between a truck and a trailer thus acting as a simply supported beam (Figure 5-4). Braces are provided at the ends to tie the girder to the truck or trailer and to brace it against overturning. In this manner, long-span prestressed girders can be brought to a job site as one piece. However, the test girder cross-section in this project was designed to be very slender (relative to a typical bridge girder), and would have been damaged in transport if the test girder were cast and transported as a single 100 ft unit. Consequently, the girder was designed to consist of three segments of approximately equal length to facilitate shipping without damage.

To further optimize the section, the trimming approach was continued until only minimum concrete cover (as per ACI 318-11 §7.7.3) was provided to the post-tensioning in the bottom

flange. The final precast segment test cross-section (Figure 5-5) is thin (compared to a typical bridge girder) and as tall as a FBT78, with a small weak axis moment of inertia and torsional constant, coupled with a large strong axis moment of inertia to prevent cracking during buckling. Section properties for the final girder cross-section are summarized in Table 5-1. DYWIDAG galvanized steel duct (2.05 in. outer diameter) cast in each girder segment formed a conduit to accommodate DYWIDAG post-tensioned bar (1 in. diameter), extending through the full length of the test girder (Figure 5-1). Pretensioned strand (0.6 in. diameter) was cast in each precast segment, which provided additional compression at the bottom of the segments to prevent cracking during transport and testing. The pretensioned strand at the top of the section was lightly stressed, and served primarily to hang shear reinforcement hooks prior to casting the segments. Mild reinforcement running along the length of each segment was placed throughout the depth of the section.

Design of Closure Strip Cross-Section

The primary function of the closure strips was to provide adequate cover for post-tensioned bar couplers and bar coupler housings that were placed between each precast segment. Typically in segmental construction using post-tensioned bars (as opposed to strands), the maximum length of bar available is less than the span length, and it therefore becomes necessary to couple post-tensioned bars together to form longer continuous bars. This approach was required in the case of the project test girder, because the total girder length was 100 ft and the DYWIDAG post-tensioned bar was only available in mill lengths up to 60 ft. Acrylic bar coupler housings (3.2 in. outer diameter) were cast in the closure strips to form a conduit sufficiently large to accommodate DYWIDAG post-tensioned bar couplers (2 in. diameter). The width of the closure strip (9.5 in.) was controlled by minimum concrete cover requirements for the bar coupler housings, per ACI 318-11 §7.7.3 (Figure 5-6). Closure strip cross-section properties are

presented in Table 5-2. As noted earlier, concentrated vertical loads were applied to the top of the test girder using gravity load simulators, at locations corresponding approximately to the span length third points. In an effort to minimize localized cracking caused by the application of concentrated point loads, closure strips were located at these loading locations, which permitted the loads to be applied to a wider cross-section. Embedded steel plates also served to minimize localized cracking at the top of the closure strips. Grout tubes were provided for each post-tensioning duct at the closure strips.

Design of End Block Cross-Section

As noted previously, the end blocks were designed to allow sufficient bearing surface areas for the bearing pads located at the ends of the test girder, and to provide anchorage points for the post-tensioning. For each bearing pad skew angle tested, the bearing pads had to be completely contained within the footprint of the girder end blocks (i.e., no part of the pad was permitted to protrude beyond the width of the girder end block). Consequently, the width of the end blocks (Figure 5-7) was selected so that the bearing pads had a large enough area to bear completely against the end block even at the maximum skew angle tested—a 45 deg. skewed configuration. The end block cross-sectional shape is presented in Figure 5-8, with cross-section properties presented in Table 5-3.

Anchorage zone reinforcement required for the post-tensioning bars was cast into the end blocks. In post-tensioned members, the anchorage zone is defined as the portion of the member through which the concentrated prestressing force is transferred to the concrete and distributed across the section (ACI 318-11 §2.2), and is the general expression for combined general and local zones (FHWA 2004). In this project, DSI engineers supplied specifications for local zone reinforcement (mild steel), including the bar sizes and configuration, and concrete strength required before stressing the bars. Separately, general zone reinforcement, was designed by the

UF research team for the end blocks, and consisted of a cage of hoops and ties in both vertical and horizontal orientations. Leveling plates were cast into the concrete end blocks to provide a bearing surface for the anchor plates provided by DSI. Grout tubes for the post-tensioning duct protruded from the exterior of the end blocks. Lifting loops consisting of prestressing strand were cast in the end blocks and were designed to support and lift the test girder into place for testing after post-tensioning was complete.

Table 5-1. Section properties of precast segments

| Section property name | Section property value |
|----------------------------------|-----------------------------|
| Area A | 405.0 (in. ²) |
| Height of centroid y | 38.39 (in.) |
| Moment of inertia I _x | 246,400 (in. ⁴) |
| Moment of inertia I _z | 1,136 (in. ⁴) |
| Torsional constant J | 3,765 (in. ⁴) |

Table 5-2. Section properties of closure strips

| Section property name | Section property value |
|----------------------------------|-----------------------------|
| Area A | 741.0 (in. ²) |
| Height of centroid y | 39.0 (in.) |
| Moment of inertia I _x | 375,700 (in. ⁴) |
| Moment of inertia I _z | 5,573 (in. ⁴) |
| Torsional constant J | 20,640 (in. ⁴) |

Table 5-3. Section properties of end blocks

| Section property name | Section property value |
|----------------------------------|-------------------------------|
| Area A | 2,184 (in. ²) |
| Height of centroid y | 39.00 (in.) |
| Moment of inertia I _x | 1,107,000 (in. ⁴) |
| Moment of inertia I _z | 142,700 (in. ⁴) |
| Torsional constant J | 442,200 (in. ⁴) |

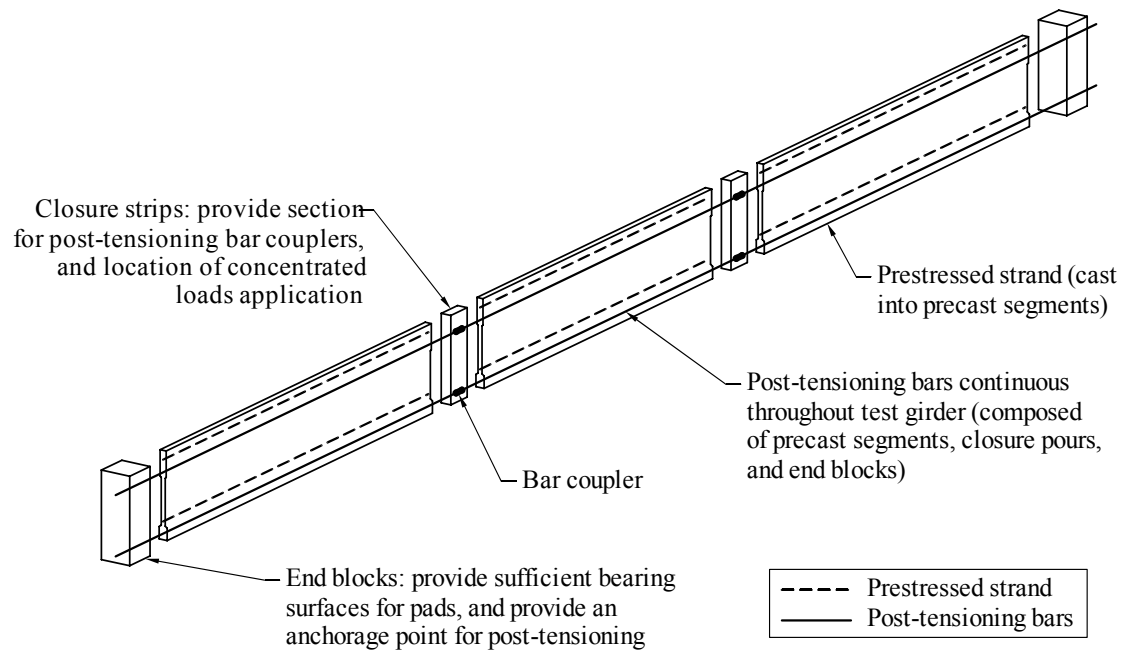


Figure 5-1. Exploded view of test girder with prestressing shown

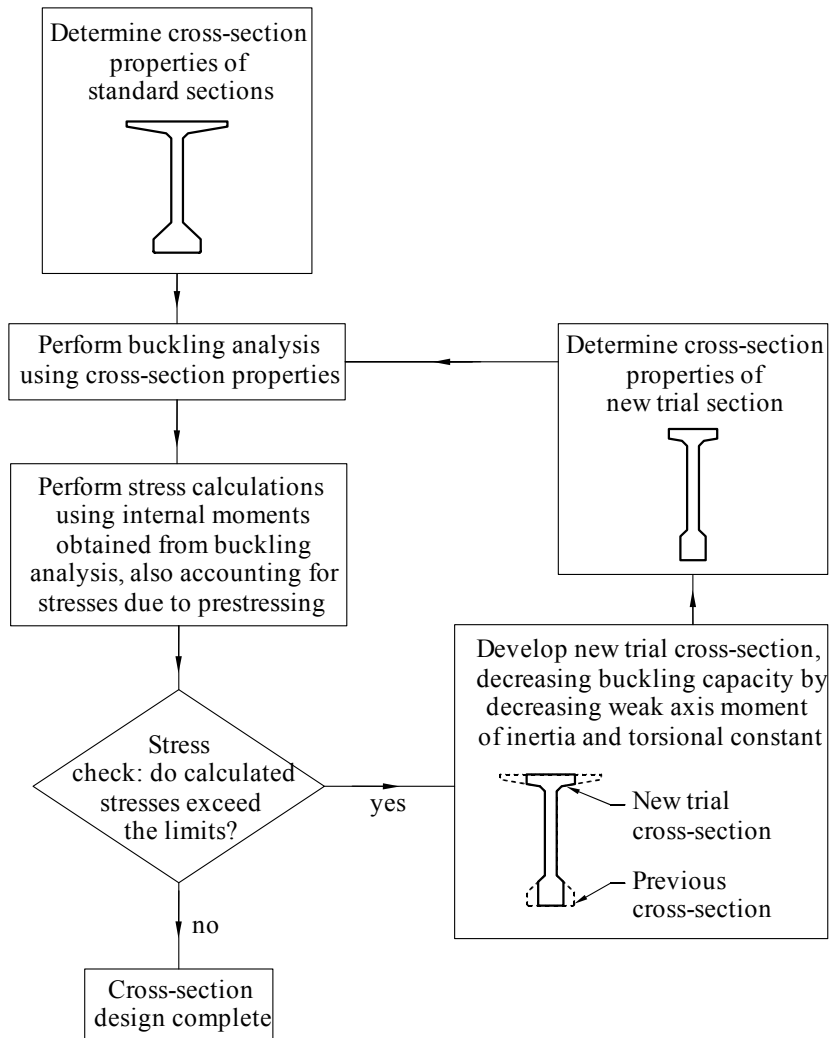


Figure 5-2. Test cross-section design flowchart

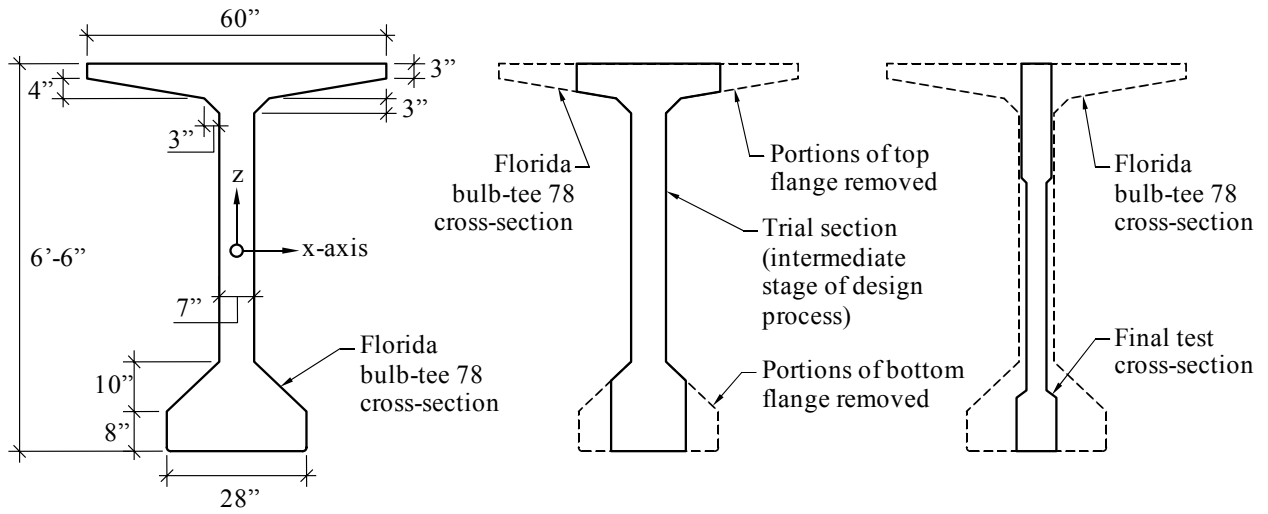


Figure 5-3. Iterative process of precast segment cross-section design



Figure 5-4. Typical shipping of bridge girders (photo courtesy of Dr. Robert I. Carr)

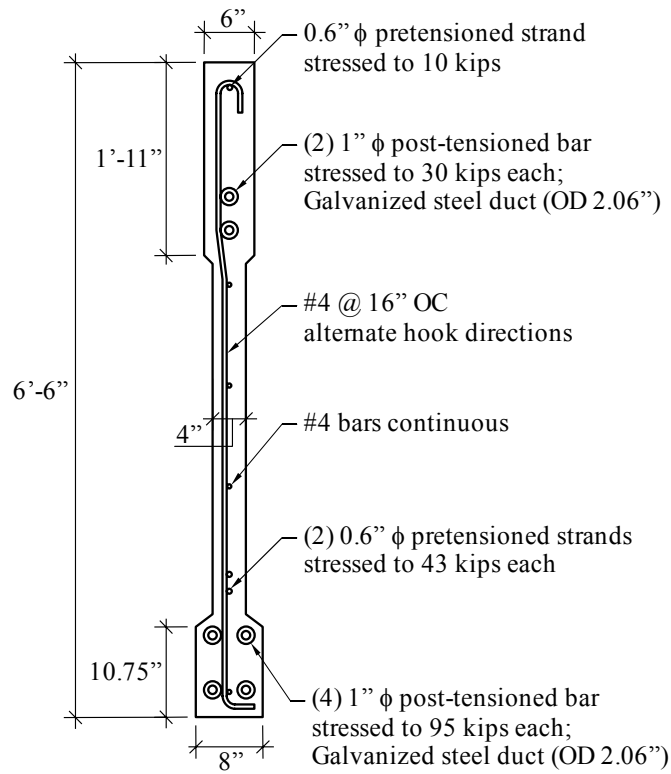


Figure 5-5. Final precast segment cross-section

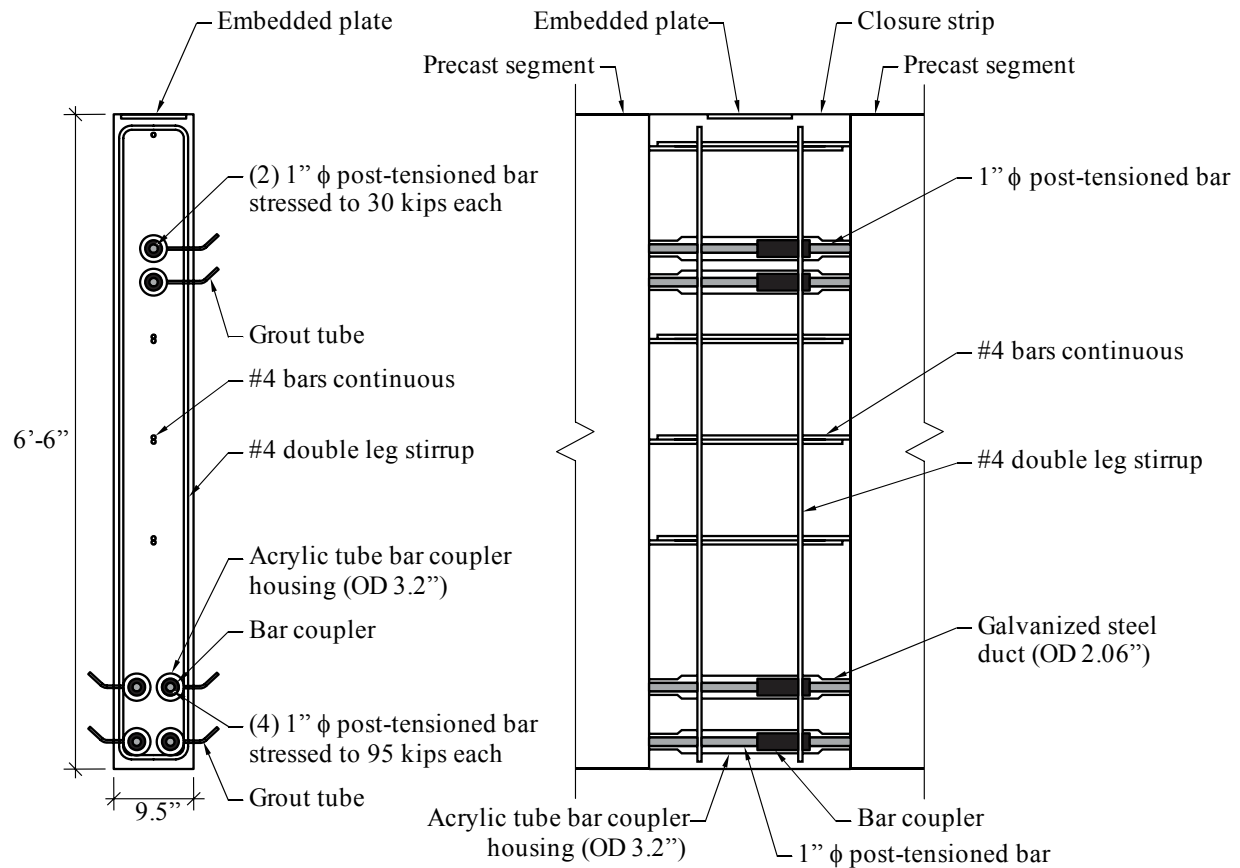


Figure 5-6. Final closure strip cross-section

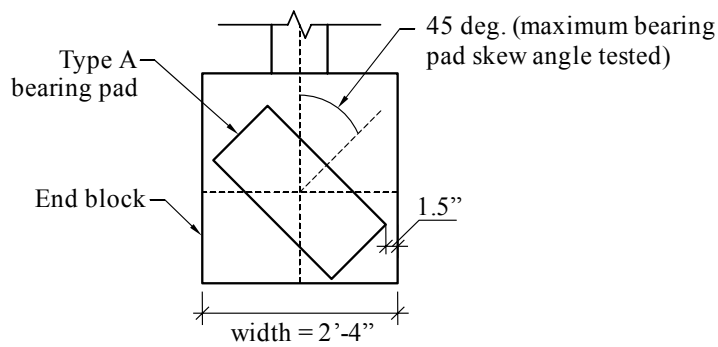


Figure 5-7. End block width, controlled by bearing pad size and skew angle

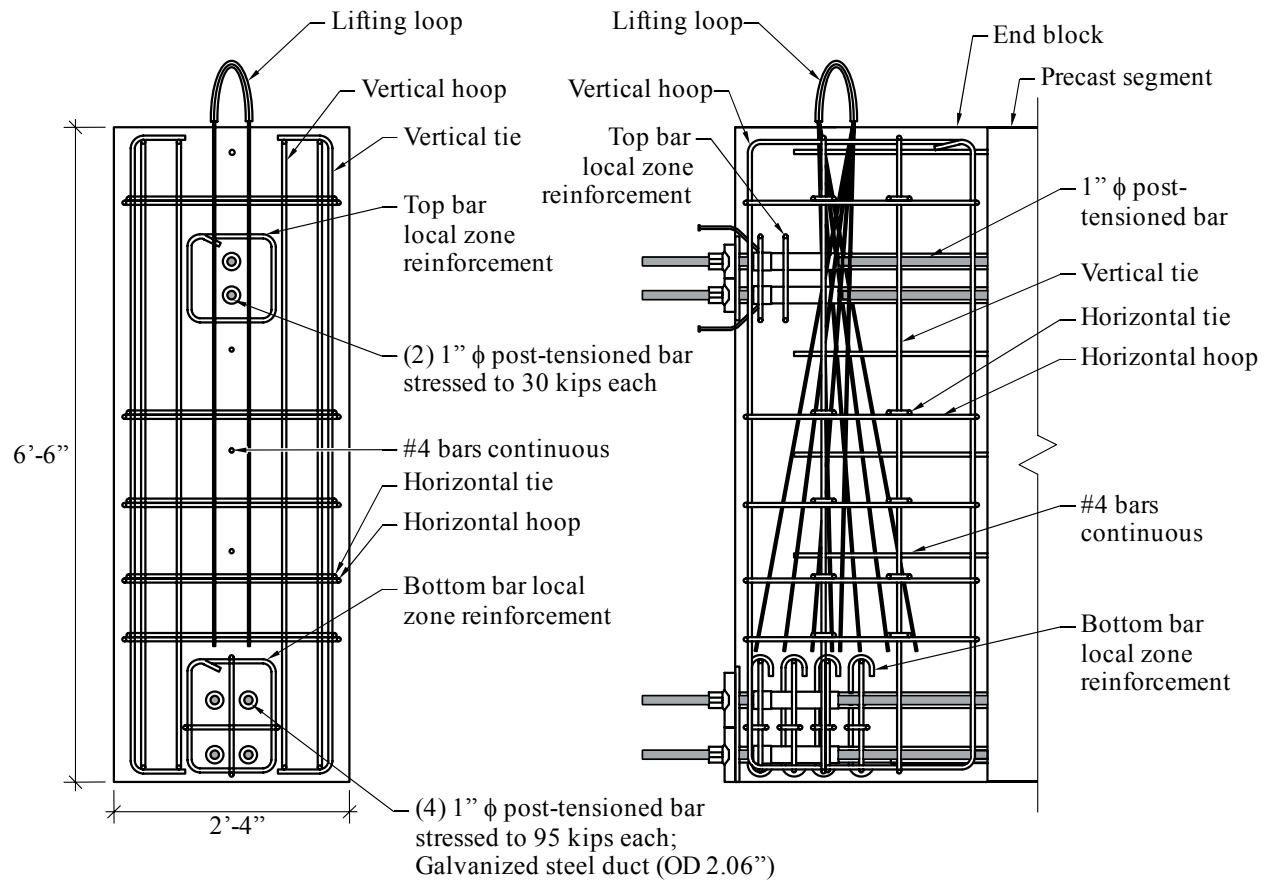


Figure 5-8. Final end block cross-section

CHAPTER 6 CONSTRUCTION OF TEST GIRDER

The test girder was constructed in a segmental manner, and consisted of three (3) precast prestressed segments, two (2) closure strips and two (2) end blocks. The precast segments were cast at Dura-Stress Inc. in Leesburg, FL and shipped to the FDOT M.H. Ansley Structures Research Center (referred to in this chapter as the FDOT laboratory) in Tallahassee, FL. Oriented as shown in Figure 6-1, the closure strips and end blocks were cast in place at the FDOT laboratory after which the test girder was post-tensioned and grouted. Cylinders cast from batches of concrete placed in the end blocks and closure strips were tested for compressive strength and modulus of elasticity. This chapter documents the construction of the test girder—including the casting of each section and post-tensioning—and summarizes the material tests performed on the cylinders cast from each batch of concrete.

Precast Segments

The precast segments were cast at Dura-Stress Inc. in Leesburg, FL. All three segments were cast on a single bed, with pretensioned strands spanning continuously throughout all three precast segments (Figure 6-2). Each segment was cast (Figure 6-3) on a separate day, within five days of each other (casting dates are indicated in Figure 6-1). Although different concrete batches were used for each segment, the mix design was the same for all segments, with specified 28-day concrete compressive strength of 6,500 psi. For each precast segment concrete batch, eleven 4 in. x 8 in. (diameter x height) cylinders were cast for later use in strength and modulus testing, to determine the material properties of the test girder at the time of buckling tests. Unstressed post-tensioning bars were temporarily placed in the post-tensioning ducts to increase the stiffness of the ducts while placing the concrete and to help maintain straight duct alignment (Figure 6-4). After concrete placement, tarps were draped over each segment during

the curing stage (Figure 6-5). Once the concrete reached the specified strength (verified by testing cylinders from corresponding batches) required for prestress transfer, the prestressed strands were cut and the segments were left to cure without a tarp (Figure 6-6). Approximately two weeks after casting the last of the three segments, Dura-Stress transported the segments on a flatbed trailer (Figure 6-7) to the FDOT laboratory.

Closure Strips

Closure strips located at approximately the third points of the span of the test girder were cast in place at the FDOT laboratory (casting dates are indicated in Figure 6-1). DYWIDAG bar couplers and bar coupler housings (larger diameter duct, to provide space for the bar coupler) were positioned within the closure strips (Figure 6-8). Bar coupler housings were fabricated from acrylic tube—cut in half lengthwise and clamped around transition pieces—to provide visual confirmation of the location of the couplers within the closure strips. Prior to placing the concrete, the bar coupler housings were taped to ensure that no concrete seeped into the void around the couplers (Figure 6-9). Mild reinforcing steel extending from the ends of the precast segments overlapped inside the closure strips, providing additional continuity to the test girder (Figure 6-9).

Formwork for the closure strips was fabricated at the FDOT laboratory (Figure 6-10), and the closure strips were cast in place (Figure 6-11) between the precast segments. The bottom of the formwork was built up to the same elevation as the bottom surface of the precast segments, to ensure a flat, continuous bottom surface of the test girder. To protect the concrete at the top of the closure strips against localized cracking (during subsequent girder testing during which time concentrated loads would be applied at the closure strip locations), a steel plate was cast at the top of each closure strip, embedded flush with the top surface of the concrete (Figure 6-12).

Grout tubes were connected to the coupler housings (Figure 6-9) and passed through holes in the formwork, allowing the tubes to be accessible after the concrete had cured and the formwork had been removed, as shown in Figure 6-13. Both closure strips were poured on the same day (2011-08-30), from the same batch of concrete. The concrete poured in the closure strips (and end blocks) had a specified 28-day concrete compressive strength of 8,000 psi and utilized Propex Fibermesh® 150 reinforcing fibers (Figure 6-14) to aid in preventing localized section cracking, particularly at the bottom of the girder. Ten 4 in. x 8 in. cylinders were cast from the closure strip batch of concrete for later use in strength and modulus testing.

End Blocks

One function of the girder end blocks was to provide a cross-section capable of accommodating post-tensioning anchorage zone reinforcement, anchor and leveling plates, and lifting loops. Like the closure strips, the end blocks were cast at the FDOT laboratory. Figure 6-15 shows the south end block formwork with one side wall removed to expose the interior details. Lifting loops (composed of prestressing strand) were cast into the end blocks and were designed to support and lift the completed test girder after it had been post-tensioned. Anchorage zone reinforcement (Figure 6-16), consisting of mild reinforcing steel, served to distribute the concentrated post-tensioning forces more uniformly over the concrete section. Embedded vertical leveling plates (Figure 6-16) were also cast into the end blocks to provide bearing surfaces for the post-tensioning anchor plates. Figure 6-17 shows the final configuration of the formwork for the end blocks, and Figure 6-18 shows concrete being placed in the north end block.

After formwork removal (Figure 6-19), grout tubes protruded from the faces of the end blocks so that they were accessible during the post-tensioning operation. Leveling plates cast flush with the surface of the end blocks are clearly visible in Figure 6-20A (prior to installation

of the post-tensioning anchor plates and anchor nuts). Each of the two end blocks was poured from a different batch of concrete, on different days (casting dates are indicated in Figure 6-1), however the mix design for both batches was the same: specified 28-day concrete compressive strength of 8,000 psi and Propex Fibermesh® 150 reinforcing fibers to aid in preventing localized cracking. For each end block concrete batch, a minimum of ten 4 in. x 8 in. cylinders were cast for later use in strength and modulus testing.

Material Tests and Properties

Each time a concrete component of the test girder was cast, 4 in. x 8 in. cylinders were also cast for the purpose of later quantifying material properties. Tests were performed to determine compressive strength (f'_c) and modulus of elasticity (E) of the cylinders at the time of the buckling tests. Approximately half of the cylinders were field cured and the other half moist cured. Field cured cylinders were cured in the casting yard with the test girder sections for precast segments and in the FDOT structures laboratory in the case of the closure strips and end blocks. Prior to removal of formwork from each cast girder component, the corresponding cylinders remained in plastic molds. After formwork removal, cylinders were demolded and cured in the open air (field cured) or fully submerged in a tank of lime water (moist cured, Figure 6-21). Several moist cured cylinders were tested for compressive strength at intermediate stages of the project (e.g., prior to post-tensioning, to ensure adequate strength before stressing), the results of which are documented in Appendix C. Compressive strength and elastic modulus tests were performed within one week of the girder buckling tests (cylinders tested between 2011-12-08 and 2011-12-12, buckling tests performed between 2011-12-12 and 2011-12-15) to provide data needed for subsequent finite element model validation. Table 6-1 provides a summary of the quantity of cylinders (field and moist cured) that were tested for compressive

strength and elastic modulus within one week of buckling testing. Specific dates on which each cylinder material test was performed are documented in Appendix C.

Compressive strength tests were conducted in accordance with the *Standard Test Method for Compressive Strength of Cylindrical Concrete Specimens* (ASTM C 39). Modulus of elasticity tests were conducted in accordance with the *Standard Test Method for Static Modulus of Elasticity and Poisson's Ratio of Concrete in Compression* (ASTM C 469). Compressive strength tests were conducted at the University of Florida (on 2011-12-08) and elastic modulus tests were conducted in the FDOT State Materials Office (SMO) laboratory in Gainesville, Florida (on 2011-12-09 and 2011-12-12). Average compressive strengths and elastic moduli measured for each component of the test girder are shown in Table 6-2. Specific results obtained for individual cylinder tests are documented in Appendix C. Qualitatively, the majority of cylinders tested for compressive strength (both moist cured and field cured) broke in either a Type 1 (cone) or Type 4 (shear) fracture mode (Figure 6-22).

Girder Post-Tensioning and Grouting

The final stage of the segmental construction process involved post-tensioning the various components of the girder (end blocks, precast segments, and closure strips) together to form a continuous girder and subsequently grouting the post-tensioning ducts. On 2011-09-20, the test girder was post-tensioned using a sequence of incremental post-tensioning force applications (21 in total) that were designed to ensure that the test girder would not crack during stressing. Each bar was assigned an identification code (Figure 6-23) and stressed incrementally in the sequence documented in Table 6-3. It should be noted that, because the precast segment cross-section was so slender, there was concern that even with the use of the stressing sequence indicated in Table 6-3, incremental eccentric stressing forces might cause the girder to deflect laterally and crack prior to achieving a final symmetric post-tensioned condition. Consequently, throughout

the post-tensioning and grouting operation, the test girder was braced against lateral movement at several locations along its length by inserting timber blocking between the girder and surrounding steel catch frames (Figure 6-24).

Each bar was stressed from the north end of the test girder using a DYWIDAG compact lightweight hydraulic jack (operated by a DSI technician). The jack fit over a pull rod that was threaded to the post-tensioning bar protruding from the anchor nut. The jack nose contained a ratchet device which allowed the anchor nut to be tightened (inside the jack) by turning a nut located on the exterior of the jack with a wrench (Figure 6-25). A pressure gage connected to the jack (Figure 6-26) was used to determine the force level in each bar, per the jack calibration form provided by DYWIDAG (Appendix D). Additionally, a Geokon load cell was aligned with the jack on the post-tensioned bar (Figure 6-25) with the intent of providing independent confirmation of the load level. However, the load cell readings were deemed inaccurate because the load was slightly eccentric on the load cell. Therefore, the hydraulic pressure gage (and associated calibration form) was the sole method of determining load level in each bar during the stressing sequence. Once the pressure gage indicated that the target prestress level had been attained, the anchor nut was tightened and the jack was moved onto the next bar in the sequence. Once all bars were fully stressed, the jack was moved to the south end of the beam and a series of bar liftoff tests were performed to confirm that the south end prestress levels were consistent with the north end prestress levels. These checks served two purposes: 1) to ensure that the bars and bar couplers had not snagged at any point along the length of the girder during stressing, and 2) to ensure that no bars lost any prestress force during the final increments in the stressing sequence. After all of bars were post-tensioned, the camber measured at midspan (Figure 6-27) was 11/16 in. which was in excellent agreement with the predicted camber of 3/4 in.

Upon completion of post-tensioning, the ducts surrounding the post-tensioning bars were pumped full of grout to mechanically bond the post-tensioning bars to the test girder. Grout was mixed with a CG550 single tub grout plant mixer provided by DYWIDAG (Figure 6-28) and pumped through the ducts. Grout cube samples were cast and subsequently tested in accordance with the *Standard Test Method for Compressive Strength of Hydraulic Cement Mortars* (ASTM C 109) at the FDOT State Materials Office (SMO) laboratory in Gainesville, Florida (on 2011-10-26). Grout strength measurements obtained from these tests are presented in Table 6-4. After post-tensioning and grouting, the test girder was lifted into testing position (Figure 6-29) using the lifting loops cast into each end block.

Table 6-1. Summary of cylinder material tests performed within one week of buckling testing for each girder component

| Date poured | Girder component concrete batch from which cylinders were cast | Moist cured cylinders | | Field cured cylinders | | Total cylinders |
|-------------|--|-----------------------|-----------------------|-----------------------|-----------------------|-----------------|
| | | Compressive Strength | Modulus of Elasticity | Compressive Strength | Modulus of Elasticity | |
| 2011-05-18 | Precast segment: exterior A | 2 | 3 | 3 | 3 | 11 |
| 2011-05-19 | Precast segment: exterior B | 2 | 3 | 3 | 3 | 11 |
| 2011-05-23 | Precast segment: interior | 2 | 3 | 3 | 3 | 11 |
| 2011-08-26 | South end block | 3 | 3 | 2 | 3 | 11 |
| 2011-08-30 | Closure strips | 3 | 3 | 1 | 3 | 10 |
| 2011-08-30 | North end block | 3 | 3 | 1 | 3 | 10 |

Table 6-2. Compressive strength and modulus of elasticity of cylinders tested within one week of buckling testing

| Date poured | Girder component concrete batch from which cylinders were cast | Moist cured cylinders | | Field cured cylinders | |
|-------------|--|----------------------------|-----------------------------|----------------------------|-----------------------------|
| | | Compressive Strength (psi) | Modulus of Elasticity (ksi) | Compressive Strength (psi) | Modulus of Elasticity (ksi) |
| 2011-05-18 | Precast segment: exterior A | 8200 | 5150 | 6340 | 4620 |
| 2011-05-19 | Precast segment: exterior B | 8520 | 5200 | 5830 | 4770 |
| 2011-05-23 | Precast segment: interior | 7910 | 5070 | 7140 | 4930 |
| 2011-08-26 | South end block | 9120 | 5380 | 7510 | 4850 |
| 2011-08-30 | North end block | 9440 | 5020 | 7080 | 4230 |
| 2011-08-30 | Closure strips | 7580 | 4750 | 5260 | 3630 |

Table 6-3. Sequence of incremental post-tensioning forces applied to girder during stressing

| Increment | Bar forces (kip) | | | | | |
|-----------|------------------|------|------|------|------|------|
| | ID 1 | ID 2 | ID 3 | ID 4 | ID 5 | ID 6 |
| 1 | 19 | — | — | — | — | — |
| 2 | 19 | — | — | 19 | — | — |
| 3 | 19 | — | 19 | 19 | — | — |
| 4 | 19 | 19 | 19 | 19 | — | — |
| 5 | 31 | 19 | 19 | 19 | — | — |
| 6 | 31 | 19 | 19 | 31 | — | — |
| 7 | 31 | 19 | 31 | 31 | — | — |
| 8 | 31 | 31 | 31 | 31 | — | — |
| 9 | 31 | 31 | 31 | 31 | 6 | — |
| 10 | 31 | 31 | 31 | 31 | 6 | 6 |
| 11 | 31 | 31 | 31 | 31 | 6 | 30 |
| 12 | 31 | 31 | 31 | 31 | 30 | 30 |
| 13 | 64 | 31 | 31 | 31 | 30 | 30 |
| 14 | 64 | 31 | 31 | 64 | 30 | 30 |
| 15 | 64 | 31 | 64 | 64 | 30 | 30 |
| 16 | 64 | 64 | 64 | 64 | 30 | 30 |
| 17 | 95 | 64 | 64 | 64 | 30 | 30 |
| 18 | 95 | 64 | 64 | 95 | 30 | 30 |
| 19 | 95 | 64 | 86 | 95 | 30 | 30 |
| 20 | 95 | 95 | 86 | 95 | 30 | 30 |
| 21 | 95 | 95 | 95 | 95 | 30 | 30 |

Table 6-4. Grout cube strength test results

| Specimen | Strength (psi) |
|----------|----------------|
| Cube 1 | 12,770 |
| Cube 2 | 13,510 |
| Cube 3 | 13,150 |
| Average | 13,140 |

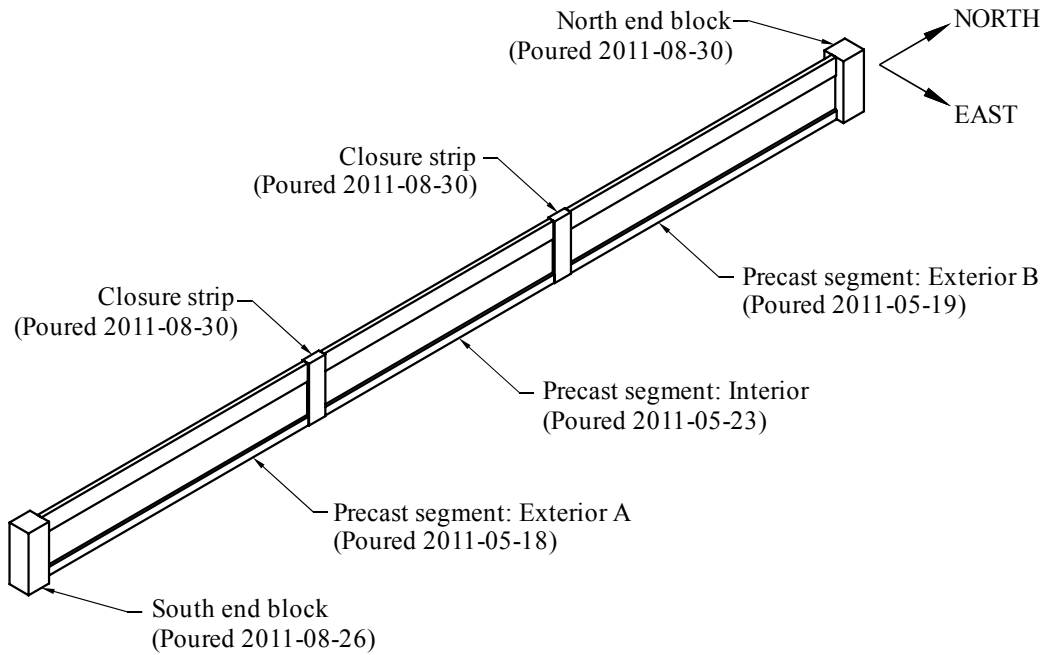


Figure 6-1. Casting dates for girder components and final orientation of girder in FDOT laboratory



Figure 6-2. Precast segments formwork aligned on single pretensioning bed at Dura-Stress (photo courtesy of University of Florida, Department of Civil and Coastal Engineering)



Figure 6-3. Placing concrete in the precast segment formwork (photo courtesy of University of Florida, Department of Civil and Coastal Engineering)



Figure 6-4. Unstressed post-tensioning bars placed in ducts to keep ducts straight during placing of concrete (photo courtesy of University of Florida, Department of Civil and Coastal Engineering)



Figure 6-5. Tarp covers applied to each segment during curing (photo courtesy of University of Florida, Department of Civil and Coastal Engineering)



Figure 6-6. Precast segments after formwork removed at Dura-Stress (photo courtesy of University of Florida, Department of Civil and Coastal Engineering)



Figure 6-7. Precast segment arrival at the FDOT laboratory (photos courtesy of University of Florida, Department of Civil and Coastal Engineering). A) Segments on flatbed trailer. B) End view of segments.

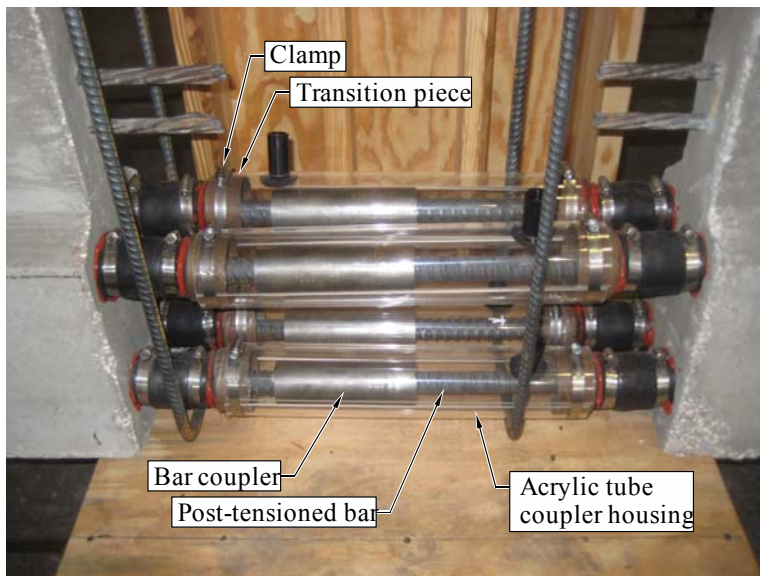


Figure 6-8. Duct couplers located within closure strips in bottom flange of girder (photo courtesy of University of Florida, Department of Civil and Coastal Engineering)



Figure 6-9. Duct couplers in closure strips, sealed with tape prior to concrete placement (photo courtesy of University of Florida, Department of Civil and Coastal Engineering)



Figure 6-10. Closure strip formwork (photo courtesy of University of Florida, Department of Civil and Coastal Engineering)



Figure 6-11. Placing concrete into the closure strip formwork (photo courtesy of University of Florida, Department of Civil and Coastal Engineering)



Figure 6-12. Embedded steel plate at top surface of closure strip (photo courtesy of University of Florida, Department of Civil and Coastal Engineering)



Figure 6-13. Finished closure strip with formwork removed (photo courtesy of University of Florida, Department of Civil and Coastal Engineering)



Figure 6-14. Concrete used in closure strip and end block concrete mix, showing presence of Propex Fibermesh® 150 reinforcing fibers (photo courtesy of University of Florida, Department of Civil and Coastal Engineering)



A



B

Figure 6-15. Open end block formwork revealing mild reinforcement and lifting loops (photos courtesy of University of Florida, Department of Civil and Coastal Engineering). A) Side view. B) Isometric view.

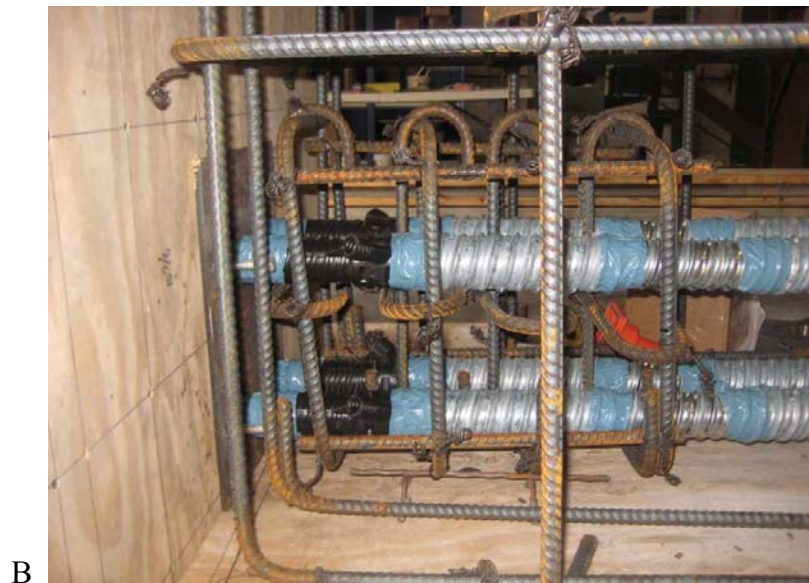


Figure 6-16. Anchorage zone mild steel reinforcement in end blocks (photos courtesy of University of Florida, Department of Civil and Coastal Engineering). A) Elevation view at top of cross section. B) Elevation view at bottom of cross section.



Figure 6-17. Completed end block formwork (photos courtesy of University of Florida, Department of Civil and Coastal Engineering). A) South end block. B) North end block.



Figure 6-18. Placement of concrete in north end block formwork (photo courtesy of University of Florida, Department of Civil and Coastal Engineering)



Figure 6-19. End block after removal of formwork (photo courtesy of University of Florida, Department of Civil and Coastal Engineering)



Figure 6-20. Leveling plates and anchor plates at bottom of end block (photos courtesy of University of Florida, Department of Civil and Coastal Engineering). A) Embedded leveling plates flush with surface of end block. B) Post tensioning anchor plates and anchor nuts installed.



Figure 6-21. Moist cured cylinders submerged in a tank of lime water (photo courtesy of University of Florida, Department of Civil and Coastal Engineering)



Figure 6-22. Typical cylinder failure types observed during compressive strength testing (photos courtesy of University of Florida, Department of Civil and Coastal Engineering).
A) Type 1 (cone failure). B) Type 4 (shear failure).

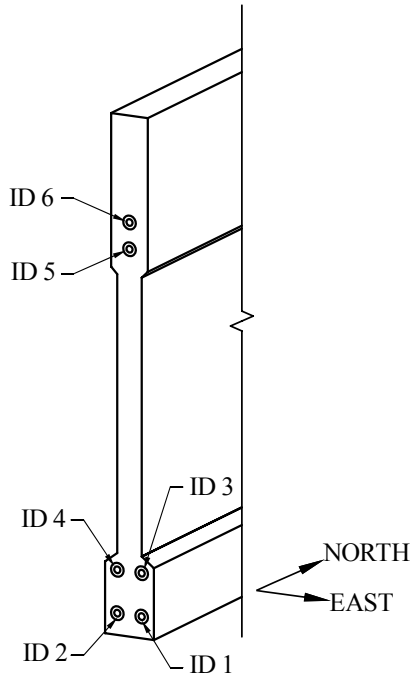


Figure 6-23. Bar identification numbers used during post-tensioning (south end of girder shown)

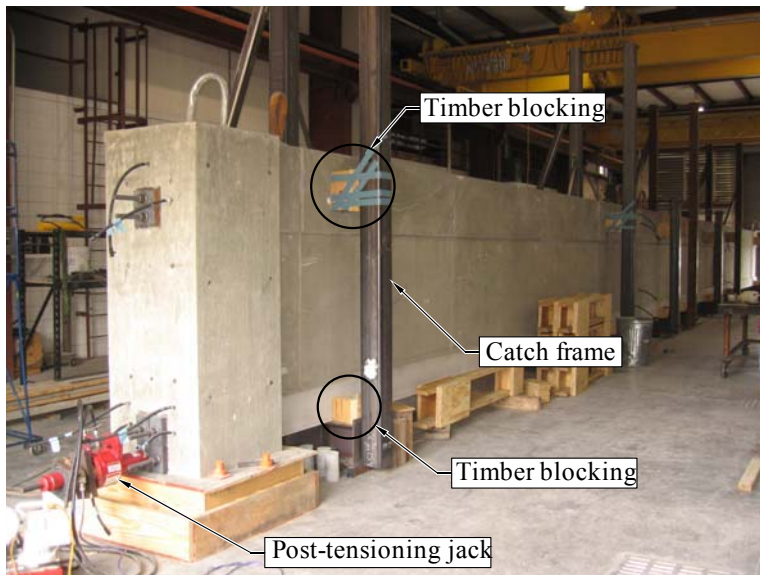


Figure 6-24. Test girder during post-tensioning, braced against steel catch frames using timber blocking (photo courtesy of University of Florida, Department of Civil and Coastal Engineering)



Figure 6-25. Post-tensioning jack setup (photo courtesy of University of Florida, Department of Civil and Coastal Engineering)



Figure 6-26. Post-tensioning jack and pressure gage (photo courtesy of University of Florida, Department of Civil and Coastal Engineering)



Figure 6-27. Camber measurement at midspan of test girder immediately after completion of post-tensioning (photo courtesy of University of Florida, Department of Civil and Coastal Engineering)



Figure 6-28. Grout mixer and high capacity air compressor (photo courtesy of University of Florida, Department of Civil and Coastal Engineering)



Figure 6-29. Lifting the test girder into testing position, prior to end block fabrication (photo courtesy of University of Florida, Department of Civil and Coastal Engineering)

CHAPTER 7 GRAVITY LOAD SIMULATOR

As previously discussed, concentrated vertical point loads were applied to the top of the test girder—through the use of gravity load simulators—to induce buckling (lateral deflection) of the girder in the experimental tests in a manner that did not introduce lateral stiffness into the system. Typically in experimental testing, a test specimen will deflect principally in the direction that the load is being applied in. For example, when a simply-supported beam is tested in flexure, a vertical point load can be applied at midspan and the beam will deflect vertically at the point of loading. In such a case, load application can be achieved through the use of a jack that is anchored to a stationary (effectively rigid) test frame which reacts against the test specimen. In contrast, in a buckling test of the type conducted in this study, the girder not only deflects in the direction of the applied load (vertically), but it also deflects laterally (perpendicular to the load direction). If a typical load application method—where the jack is anchored to a stationary position—were used in a buckling experiment, the load frame would resist lateral motion of the test specimen and a horizontal component of restraining force would develop (Figure 7-1). This condition is unacceptable, because the lateral load component would artificially increase the measured buckling capacity of the girder. To maintain vertical load and zero lateral restraining force as buckling occurs, a special type of load application frame (called a gravity load simulator) can be used that translates freely with the test girder as it buckles laterally. This chapter discusses the mechanics and design of the gravity load simulators designed and employed in this project, including a novel modification to previous designs by other researchers that improves the accuracy and performance of the system.

Gravity Load Simulator Design

The first gravity load simulator was developed by Yarmici and Yura (1967) to test structures permitted to sway. As designed, the simulator acts as a horizontally unstable truss structure (i.e., zero lateral stiffness) which provides vertical load application without horizontal restraint to the test specimen. As shown schematically in Figure 7-2, the simulator consists of two inclined arms that are connected to the ground and to a rigid triangle at the center of the simulator via pins. The source of load—a hydraulic jack—is attached at the base of the rigid triangle, also through a pinned connection. As is noted by Yarmici and Yura (1967), “For the type of mechanism shown, equilibrium requires that the line of action of the load passes through the instantaneous center, that is, the point of intersection of the two arms. The position of the instantaneous center changes as the mechanism is deflected.” With carefully chosen geometry (top width, arm length, load height, and base width; Figure 7-2), the load line of action will remain vertical and through the instantaneous center, regardless of the deflected position (Figure 7-3). Additional guidance for determining optimal geometry for the simulator can be found in Yarmici and Yura (1967).

The original simulators, at Lehigh University, had 80 kip load capacity and could translate laterally 16 in., for performing buckling tests on full scale building frames (Yarmici and Yura, 1967). Since then, several other researchers have constructed gravity load simulators for various test programs. Lateral torsional buckling tests of steel I-shapes were conducted at University of Texas at Austin (Yura and Phillips, 1992). At the University of Texas at Houston, two simulators (6 in. displacement capacity, 150 kip load capacity) were constructed to investigate torsional bracing by simulating buckling of a two-beam system with midspan bracing (Deaver, 2003). A gravity load simulator at the Georgia Institute of Technology (7.5 in. displacement capacity, 60 kip load capacity) was used to experimentally investigate lateral-torsional buckling behavior

of fiber reinforced polymer I-shaped cross-sections (Stoddard, 1997) and also to examine the lateral stability of slender rectangular reinforced concrete beams (Kalkan, 2009). Also at the Georgia Institute of Technology, a relatively large gravity load simulator (12.875 in. displacement capacity, 300 kip load capacity) was used to study the stability of prestressed concrete beams (Hurff, 2010). It should be noted that Hurff observed that the load line of action was not perfectly vertical when the simulator swayed from its original centered position. Postulating that self weight of the simulator caused this issue, a control mechanism was installed that forced the simulator to act as a stable mechanism, in which the position of the simulator was manually adjusted until the applied load was vertical. Further investigations into the simulator self weight issue were not conducted by Hurff.

UF/FDOT Gravity Load Simulators

A pair of gravity load simulators (one of which is shown in Figure 7-4) has been designed and fabricated for this project, with a maximum lateral deflection capacity of 16 in. and vertical load capacity of 50 kip each. The UF/FDOT simulators have the same geometry as the original simulator developed by Yarmici and Yura (1967). High-quality spherical roller bearings (Figure 7-5) are used to prevent binding (due to shaft bending or simulator geometry fabrication imperfections) and minimize friction at the pinned connections, thereby minimizing restraint of the simulator to lateral motion. The bearings used in the simulators are self-aligning—accommodating misalignment between the shaft and housing without increasing friction—which allows out of plane bearing rotation of ± 1.5 deg. The bearings are housed in thick plates that are bolted and welded to the simulators (Figure 7-4A). PVC end caps serve as bearing seals that prevent dust from entering the bearings and creating friction (Figure 7-4B). A hydraulic jack is connected to the center pin of each simulator (Figure 7-6), allowing the hydraulic jack to rotate freely about the pin and maintain vertical load application as the simulator displaces (Figure 7-

7). Two safety mechanisms are included in the design of the simulators: one temporary restraint and one permanent restraint (Figure 7-4). The temporary restraints are engaged when the simulators are not in use—removed during buckling tests—to keep each simulator from displacing laterally under its own weight. For safety during a buckling test, permanent restraint chains—which are slack during normal operation (Figure 7-4A)—connect the bottom of the rigid triangles to the base beams. The restraint chains allow full range of motion expected during a buckling test (expected deflection of 10 in. out of the maximum allowable displacement of 16 in.), but prevent the simulators from displacing further than desired (Figure 7-7).

The completed simulators were positioned below the test girder closure strips. Load frames were designed to transfer the vertical load from the gravity load simulator (below the test girder) to the load application point (at the top of the test girder). A threaded rod in line with the hydraulic jack connected the load frame to the simulator (Figure 7-7). A knife edge (Figure 7-8) was used to apply point loads to the top of the test girder, which allowed the girder to rotate freely about the y-axis within the load frame as it buckled (Figure 7-7). When loaded, the simulators could be pushed laterally by hand from the equilibrium position, and upon release, would float back to equilibrium. Figure 7-9 shows a photograph of one of the gravity load simulators and load frame in testing position. Full fabrication plans for the simulators can be found in Appendix E.

Effect of Gravity Load Simulator Self Weight Equilibrium

Prior to performing buckling experiments, the performance of each simulator was tested to ensure that the load line of action remained vertical. Restraining the test girder centered above the simulators, the loaded simulators maintained equilibrium as expected, and the direction of load was confirmed to be vertical using a carpenter's level. Subsequently, a trial buckling test was performed in which load was applied to the test girder, which was allowed to freely deflect

laterally. Both simulators reached equilibrium in a position such that the applied load was not perfectly vertical. Specifically, the middle pin of each simulator was displaced further than the load application point (at the top of the test girder). This condition caused a lateral load applied to the test girder in the direction of buckling (Figure 7-10). With the simulators floating in this manner of equilibrium, the simulators were pushed (by hand) until vertical alignment was reached. Upon release, each simulator floated back to the equilibrium position with a non-vertical load line of action. In the displaced configuration observed during this trial buckling test, the load line of action was not vertical as expected, indicating that additional forces (such as the weight of the simulator) affected the system during the test. As mentioned in the previous section, Hurff (2010) observed that the Georgia Tech simulator did not reach equilibrium with a vertical load orientation unless the simulator was in the undeformed (centered) position. Hurff fixed this problem by using a lateral control mechanism that caused the simulator to become a stable structure. While this solution proved effective for maintaining proper load orientation, the lateral restraint provided by the control mechanism is undesirable for buckling experiments. Ideally, the girder should be permitted to deflect laterally (buckle) without restraint, which is consistent with an un-braced field condition. Thus, an alternative solution was developed which allows unrestrained lateral motion and maintains vertical load orientation throughout the full range of motion.

To further investigate how the self weight of the gravity load simulator influences its equilibrium position, numerical models of the simulator were developed (Figure 7-11). In the initial simulator model, rigid beam elements represent the components of the simulator, the self weight of which (due to gravity) are neglected. The inclined arm beam elements are attached to hinges at the base of the system, with end moment (M_y) releases at the connection to the rigid

triangle. Moment transfer between the elements of the rigid triangle ensures that the rigid triangle acts as a single unit. The connection of the gravity load simulator at the middle pin and the load application point to the test girder (the knife edge) is represented in the model using a beam element. Releasing the end moment (M_y) of this element at the connection to the rigid triangle allows the element to rotate freely about the middle pin of the simulator. Initial strain is applied to this element, simulating the tension applied through the use of the jack during a buckling test. A prescribed displacement is applied at the load application point, representing the lateral deflection of the test girder. The load application point is modeled as a roller support (free to rotate about the y-axis and translate along the x-axis), representing the knife edge at the top of the test girder.

Yarmici and Yura (1967) describe that the theoretical load applied by a gravity load simulator is generally not truly vertical, and that a slight lateral load is applied to the test specimen as a result of this non-vertical orientation. Neglecting gravity, the results of the simulator analysis (Figure 7-12) are consistent with Yarmici and Yura (1967). The analysis indicates that—within the range of lateral deflections expected in the buckling experiments—the lateral load component is, at most, approximately -0.02% of the applied vertical load. Note that Yarmici and Yura's sign convention (Figure 7-10) states that a negative percentage corresponds to a lateral load that is restraining the beam, and a positive percentage corresponds to a lateral load that is driving the beam in the direction of buckling. For example, the simulator analysis results (Figure 7-12) show that, when the test girder has displaced 5 in., under zero-gravity conditions, the lateral force component is approximately -0.02%. Thus, if a 10 kip load is applied vertically, 0.002 kip would develop laterally at the top of the beam, restraining the beam slightly.

To determine the effect of self weight on simulator equilibrium, gravity is introduced into the simulator model via mass proportional body forces (and therefore taking the self weight of the simulator into account), and the analysis described above is repeated. The self weight causes much larger lateral loads to develop in the direction of buckling, and those loads increase with increasing displacement (Figure 7-13). This occurs because the self weight of the simulator is eccentric relative to the idealized instantaneous center—the point of intersection of the two inclined arms when neglecting gravity—as shown conceptually in Figure 7-14A.

Recall that Hurff (2010) corrected this problem by providing lateral restraint to the gravity load simulator. In this study, an alternative solution was employed that avoids restraining lateral motion. The system consists of weights placed eccentrically from the instantaneous center which counterbalance the eccentric self weight of the simulator (Figure 7-14B). With acceptable counterweight magnitude and eccentricity, the effect of the simulator self weight can be corrected, and the load line of action remains vertical. The counterweights are an excellent option because there is no addition stiffness added to the system (permitting unrestrained lateral motions), and the counterweights can be adjusted to maintain vertical load regardless of the displaced shape of the test girder. The physical counterweight system was fabricated using barbell weights of various sizes, slid onto a steel pipe that was mounted to the rigid triangle of the simulator (Figure 7-15). For each simulator, two (2) 25 lb weights and one (1) 45 lb weight were available for the counterweight system. Small clamps ensured that the weights did not slide unless physically pushed along the pipe. Details of the counterweight system are included in the gravity load simulator fabrication plans, found in Appendix E.

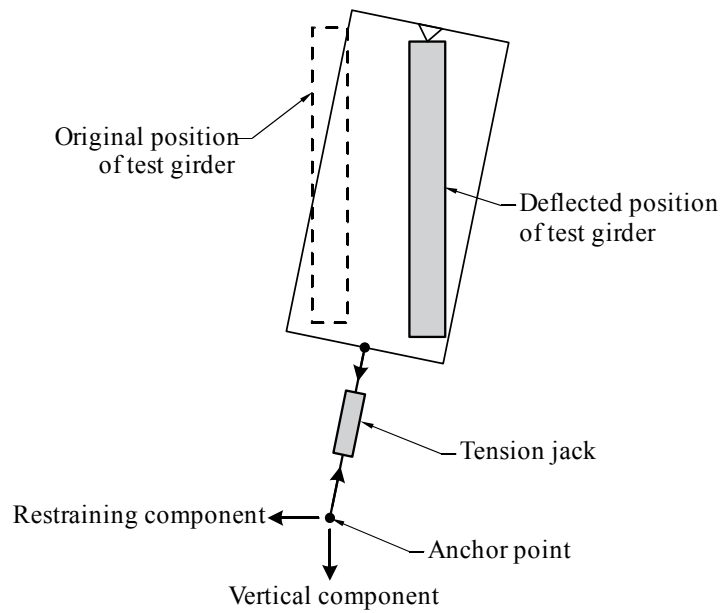


Figure 7-1. Undesirable horizontal restraining component that develops in an anchored loading system (After source: Yarmici and Yura, 1967)

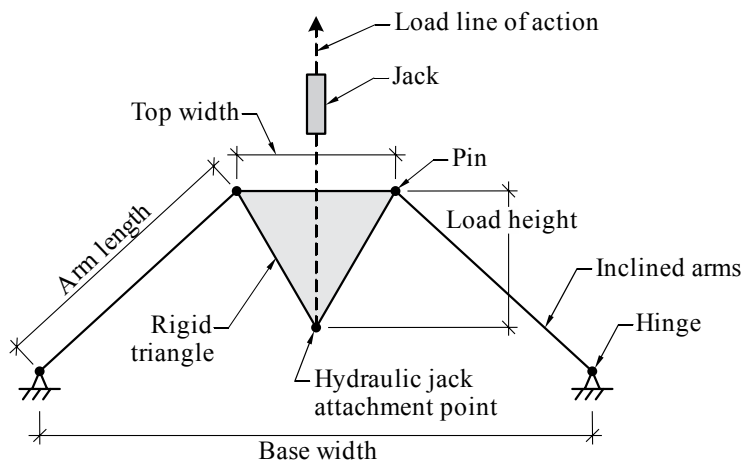


Figure 7-2. Dimensions, defined (After source: Yarmici and Yura, 1967)

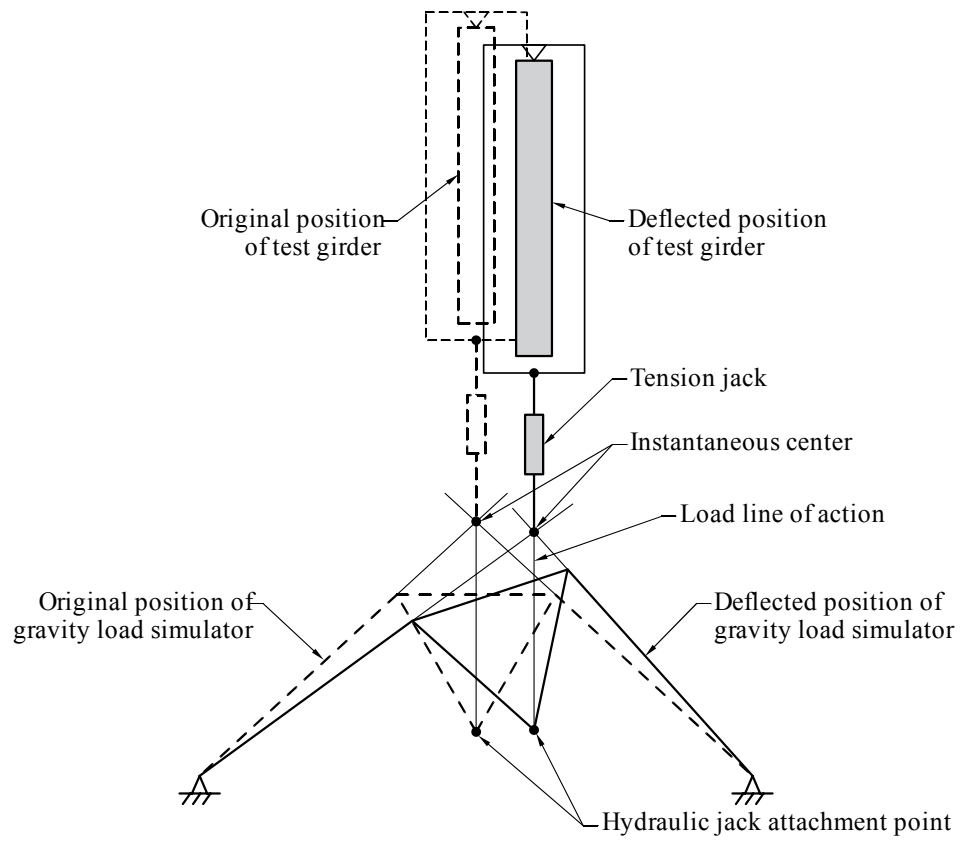


Figure 7-3. Instantaneous center (After source: Yarmici and Yura, 1967)

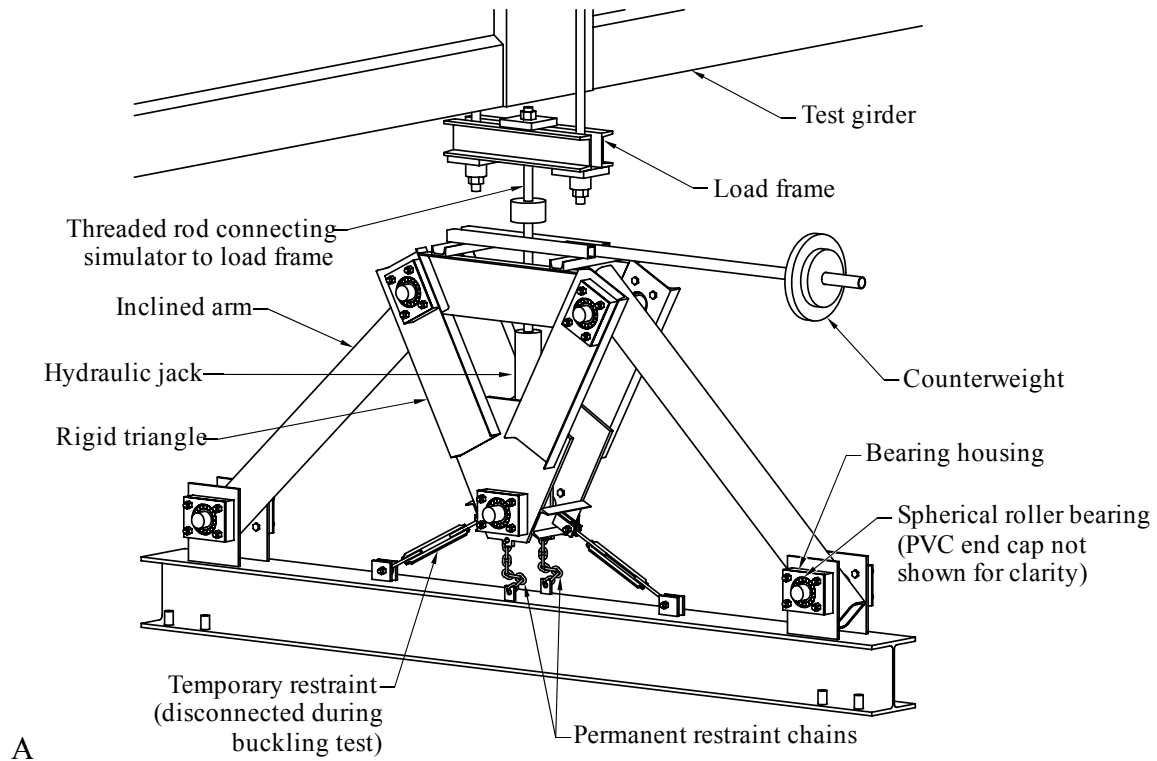


Figure 7-4. UF/FDOT gravity load simulator. A) Schematic view. B) Photograph (photo courtesy of University of Florida, Department of Civil and Coastal Engineering).



Figure 7-5. Spherical roller bearing (photo courtesy of SKF)



Figure 7-6. Hydraulic jack connection to simulator center pin (photo courtesy of University of Florida, Department of Civil and Coastal Engineering)

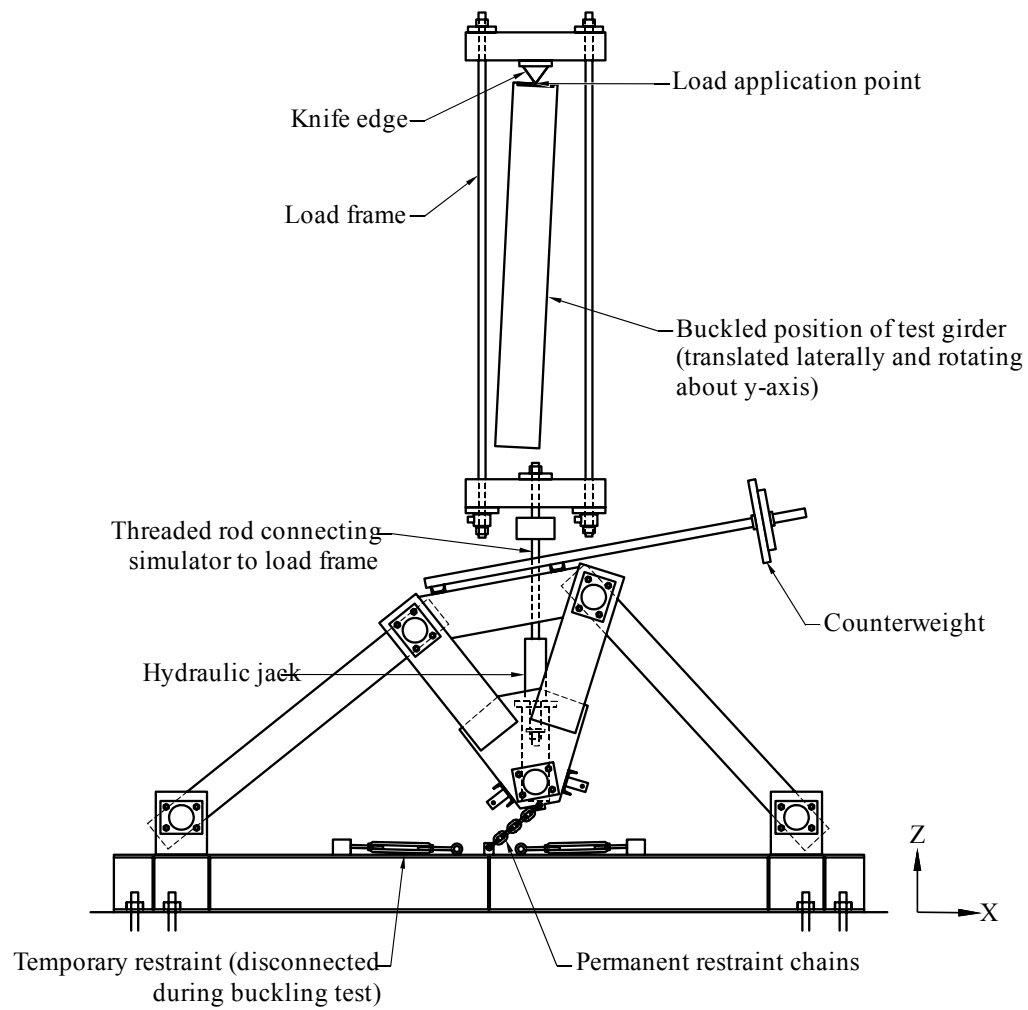


Figure 7-7. Gravity load simulator displaced shape



Figure 7-8. Knife edge at load application point at top of test girder (photo courtesy of University of Florida, Department of Civil and Coastal Engineering)



Figure 7-9. UF/FDOT gravity load simulator and load frame in testing position (photo courtesy of University of Florida, Department of Civil and Coastal Engineering)

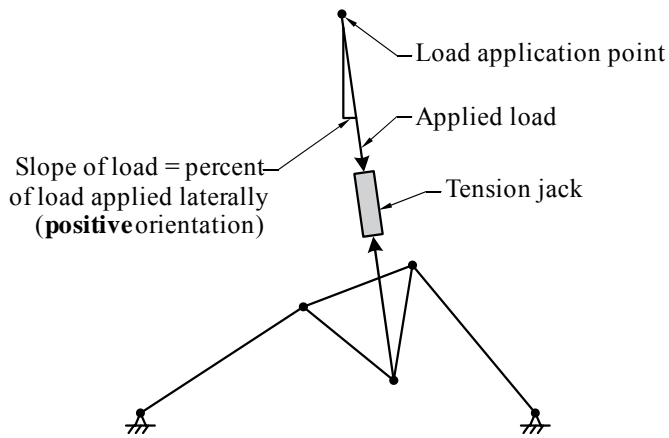


Figure 7-10. Definition of percent of simulator load applied laterally (After source: Yarmici and Yura, 1967)

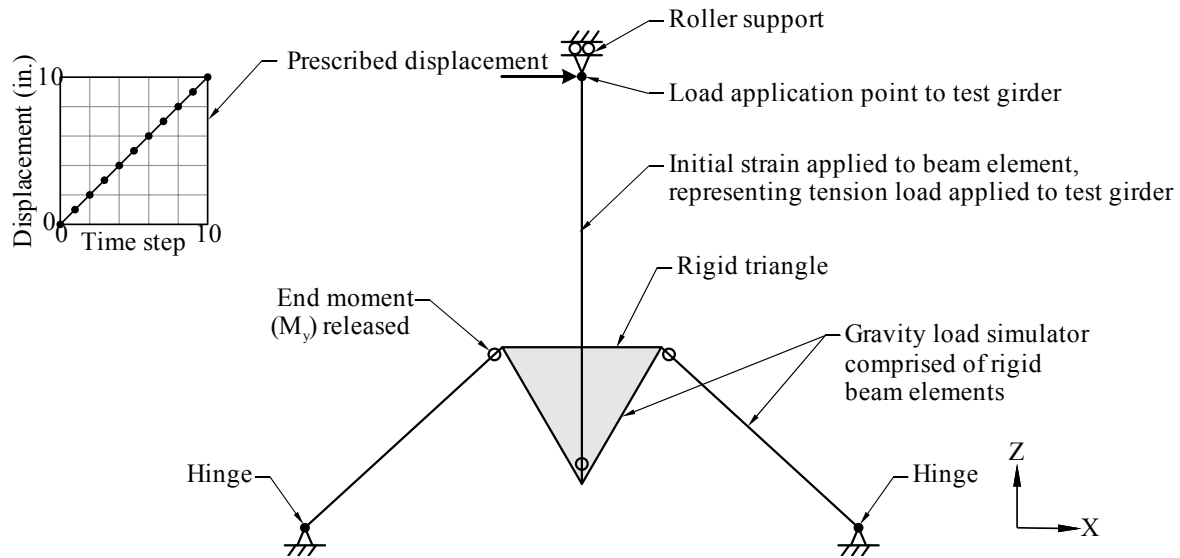


Figure 7-11. Gravity load simulator model

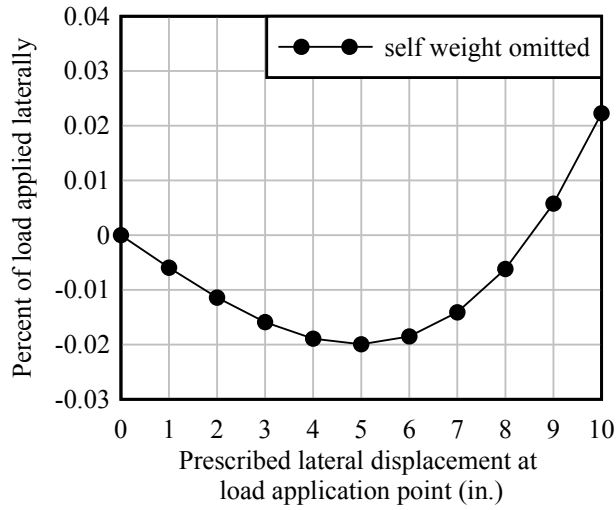


Figure 7-12. Results of simulator analysis: theoretical percent of load applied laterally to the beam at the load application point (self weight excluded in model)

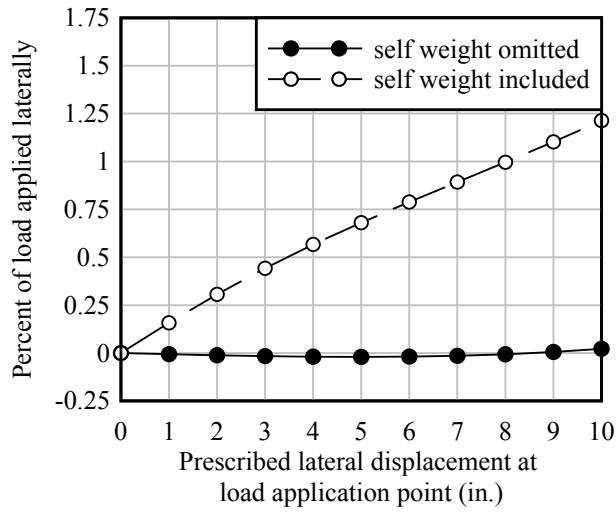


Figure 7-13. Results of simulator analysis: theoretical percent of load applied laterally to the beam at the load application point (self weight included in model)

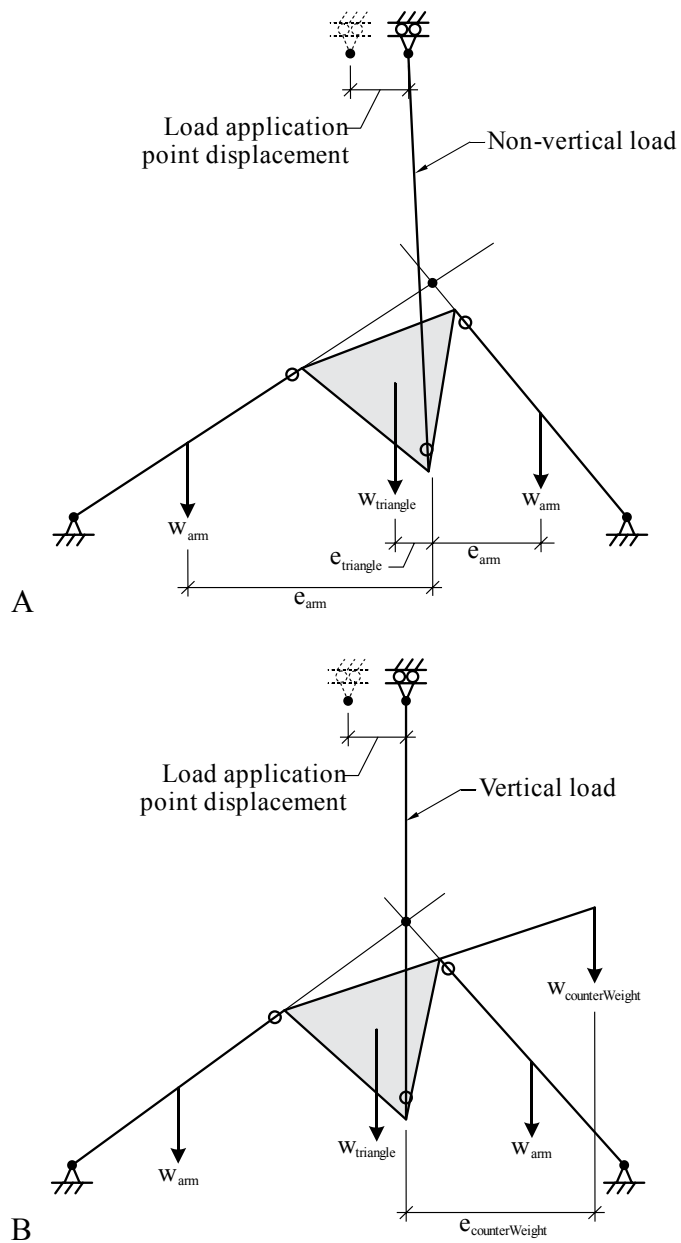


Figure 7-14. Effect of simulator self weight and counterweights on verticalness of load line of action. A) Counterweights omitted, load is skewed. B) Counterweights included, load is vertical.



Figure 7-15. Counterweight system (photo courtesy of University of Florida, Department of Civil and Coastal Engineering)

CHAPTER 8 EXPERIMENTAL BUCKLING TESTS PROGRAM

Buckling Test Setup

An overview of the test setup is shown in Figure 8-1. To accommodate the gravity load simulators, the test girder was elevated approximately 8 ft. above the lab floor and rested on rigid end supports. Because the test girder was elevated overhead, catch frames were designed to support the test girder should it become fully unstable during testing. Five catch frames were fabricated: two positioned at the ends, one positioned at midspan, and two positioned near the third points (Figure 8-1). The catch frames allowed the test girder up to 9 in. of lateral movement at midspan before the test girder came into contact with the catch frames. Full fabrication plans for the catch frames can be found in Appendix F. Each end support was fabricated with the test girder suspended in testing position, built up below the end blocks. Made of eight solid concrete blocks, the end supports were built up one level at a time and welded together to create a rigid support (Figure 8-1). A pad of Hydro-Stone® was poured at the base and at the top of the end supports, to ensure that the bearing surface for the end blocks on the ground was level and to provide a level surface for the bearing pad contact area, respectively.

Test Matrix

The bearing pads used to support the ends of the test girder were the same pads previously tested for roll stiffness in the first phase of this project. As shown in Chapter 2, among all bearing pad types tested, Type A bearing pads had the least amount of variation in individual roll stiffness results under all combinations of skew and slope angles (results reproduced in Figure 8-2). Therefore, pad Type A was chosen to support the ends of the girder during the buckling tests. To best illustrate the influence of roll stiffness on buckling capacity, the girder was to be tested with bearing pads oriented at the extreme values of skew and slope that were previously

investigated (A-0-0, A-45-0, A-0-04, and A-45-04). Recall that, in the abbreviated naming convention, the first letter denotes pad type, the following number denotes skew angle (in degrees), and the last number denotes slope angle (in 10^{-2} radians). However, during buckling testing in test configuration A-45-04, the test girder buckled under its own self weight (i.e., with no additional applied vertical load). Consequently, a configuration with an intermediate combination of skew and slope was required. Reducing skew from 45 deg. to 15 deg. increased buckling capacity enough to allow a test to be performed with applied load and with the pad in a skewed and sloped configuration. The test matrix for the buckling tests—with number of tests performed per configuration—is presented in Table 8-1.

Test Procedure

There were two main phases to the setup portion of the buckling tests: 1) imposing skew and slope angles on the bearing pad, and 2) placing the test girder on the bearing pads. After the setup portion each buckling test (setting the bearing pads and placing the girder on the pads) was completed, the buckling test was performed. This section documents the procedure for setting up and performing the buckling tests.

Setting Skew and Slope Angles

Prior to performing each buckling test, bearing pads—located between the end blocks and rigid end supports—were oriented at the desired skew and slope angle. Skew angle was set by rotating the bearing pad about the z-axis of the pad relative to the test girder (Figure 8-3). Slope angle was set by placing a beveled plate (Figure 8-4) between the bearing pad and rigid end support (Figure 8-5). Bearing pads were orientated in the buckling tests such that the pressure distributions during buckling testing matched that of the pressure distributions during roll stiffness testing (Chapter 2). Conceptually, Figure 8-6 shows the initial pressure distribution of each test configuration, and Figure 8-7 shows the final pressure distribution for each test

configuration. In the sloped tests, the thick ends of both beveled plates faced north, creating a pressure concentration on the north portion of the bearing pads. This scenario represents the pressure distribution on the pair of bearing pads that would be produced by girder grade (as opposed to girder camber).

Placing the Test Girder

As the skew and slope angles were set, the test girder was lifted—via lifting loops cast into the end blocks—to allow adjustments. Once the bearing pad skew and slope angles were set, the test girder was lowered onto the pads for a buckling test. As shown in Figure 8-8A, the beam swept naturally to the east. Measured at the centroid height, the sweep was found to be 2.87 in. under end configuration A-0-0. For most tests, a hydraulic jack was used to push the test girder toward the west at the centroid, effectively removing sweep from the system (i.e., pushing the girder straight) (Figure 8-8B). The jack used to straighten the test girder was mounted to the midspan catch frame, as shown in Figure 8-9. For comparison, two different methods for placing the test girder on the bearing pads were used:

- Method A: The test girder was straightened using the jack, lowered onto the bearing pads, and then allowed to sweep freely by slowly retracting the jack, and;
- Method B: The girder was set down on the pads in the swept position.

Method A is advantageous because the sweeping motion of the test girder could be directly recorded during a buckling test (as the jack is slowly retracted). However, when Method A was used, it was observed that as the test girder deflected into the swept position, torsion was introduced to the bearing pad about its z-axis. This outcome is undesirable because pad torsion is not present in the field, nor was not present in the roll stiffness tests. To determine the effect of torsion in the pad on the buckling capacity of the test girder, test configuration A-0-0 was tested under both conditions (using Method A and Method B). Examining the load-displacement curves

presented in Chapter 9 for test configuration A-0-0, the effect of torsion on the bearing pads is insignificant. Table 8-2 summarizes the placement method of each individual test performed per configuration (e.g., A-0-0-1 was the first test performed in configuration A-0-0, A-0-0-2 was the second test performed in configuration A-0-0, etc.).

Buckling Test Procedure

Similarly to the roll stiffness tests, load was applied iteratively to the test girder, first gradually increasing the applied load at the north simulator until a specific target was reached, and then increasing the load at the south simulator until the loads were equal in both locations (Figure 8-10). Once the loads were approximately equal at both simulators, the simulator counterweight system was adjusted at each location to ensure vertical load application. Load orientation was confirmed to be vertical using a carpenter's level. After the counterweights were adjusted, a data point was established (Figure 8-10), at which time the applied load and girder deflection was measured.

Instrumentation

Several types of instrumentation devices—displacement transducers (displacement sensors, lasers, and string potentiometers), load cells, and strain gages (both external and vibrating wire strain gages cast into the concrete)—were used in the buckling tests. A naming convention for the instrumentation was developed to reflect the instrument type and its specific location on the test girder. As summarized in Figure 8-11, each instrument name has the same format of T-LD-F-H, where “T” indicates the type of instrument, while “-LD-F-H” indicates the location of the measurement. For example, the instrument shown in Figure 8-11 is an external strain gage mounted to the east face of the test girder top flange. Therefore, the instrument shown in Figure 8-11 is named SG-N24-E-76, which means that the device is a strain gage, located 24 ft north of midspan, mounted to the east face, at a height of 76 in. from the bottom of the girder.

The full instrumentation plan (Appendix G) further describes the naming convention, as well as provides an overview of all of the instrumentation by name.

Displacement Transducers

Displacement sensors, string potentiometers and laser gages were used to measure girder deflection at various points along its length. All three types of displacement transducer were used at midspan, but only displacement sensors were used at the end blocks. Laser gages (Balluff model BOD 66M) measured lateral displacement at the centroid height near the gravity load simulator locations.

Because midspan lateral deflection was a key parameter measured in a buckling test, the midspan of the test girder was heavily instrumented with displacement transducers (Figure 8-12). Displacement transducers were mounted to the central catch frame and used to record midspan deflections along both the x-axis and z-axis. A laser gage (Balluff model BOD 66M) and a displacement sensor (TML model SDP-200D) were mounted next to one another at the centroid height to measure lateral displacement (along the x-axis). The laser gage (Dx-N0-W-38) was used as the primary lateral displacement measuring device during a buckling test, while the displacement sensor (Dx-S0-W-38) provided redundancy to the laser gage. String potentiometers (SpaceAge Control model 62-60-82E1) measured both lateral and vertical displacement of the test girder, providing additional redundancy to the lateral displacement measurement provided by the laser gage.

The end blocks were also heavily instrumented with displacement sensors, as shown in Figure 8-13. All displacement transducers monitoring the end blocks were TML model SDP-50, mounted to the rigid end supports. Vertical displacement transducers (along the z-axis, Dz) and horizontal displacement transducers (along the x-axis, Dx) were used to calculate the roll angle imposed on the bearing pad. Knowing the horizontal distance between the vertical (Dz)

displacement transducers and the vertical distance between the horizontal (D_x) displacement transducers, the roll angle imposed on the bearing pad at the end block could be calculated from the relative displacement measurements, and used to confirm each other. Horizontal displacement transducers along the y-axis (D_y) were used to calculate torsional rotation in the bearing pad.

Load Cells

Load cells measured the applied vertical load to the test girder at the gravity load simulator locations. An Interface load cell (model 1220, 50 kip capacity) was installed in line with the threaded rod connecting the gravity load simulator to the load frame. This cell directly measured the load applied to the test girder (Figure 8-14). Additionally, a pair of Geokon load cells (model 3000, 50 kip capacity) were mounted in line with the load frame rods that flank each side of the test girder (Figure 8-14). These cells provided load measurements that were redundant with the Interface load cell. The average of the Interface load cell readings on each gravity load simulator (named F-N15-C and F-S15-C, located at the north and south simulators, respectively) were used to monitor the load applied to the test girder and determine the buckling capacity of the test girder. These load cells (F-N15-C and F-S15-C) were also used to generate the load-time history presented in Figure 8-10.

Strain Gages

Strain gages (both external and cast into the concrete) were used to detect cracking, if it occurred. Several external strain gages (Kyowa 60mm and 120 ohm) were mounted to the test girder at locations most likely to crack, namely on the bottom of the precast segments close to the interface with each closure strip (see Appendix G for specific locations). The remaining external strain gages were placed at increments along the length of the beam on the east and west faces of both the top and bottom flanges, to capture the strain profile if necessary. A pair of

vibrating wire strain gages (Geokon model 4200) were cast into each closure strip, located vertically between the post-tensioning coupler housings (Figure 8-15). These gages were used to detect cracking should it occur in the closure strips. The vibrating wire strain gages were also used to measure true strain in the test girder over time, including during the post-tensioning stage, whereas the external strain gages measured incremental strain (caused by applied vertical load during a buckling test).

Table 8-1. Test matrix

| Test configuration | Skew angle (deg.) | Slope angle (rad.) | Number of tests performed |
|--------------------|-------------------|--------------------|---------------------------|
| A-0-0 | 0 | 0 | 3 |
| A-45-0 | 45 | 0 | 2 |
| A-0-04 | 0 | 0.04 | 3 |
| A-15-04 | 15 | 0.04 | 1 |

Table 8-2. Placement method, per test basis

| Test ID | Placement method |
|-----------|------------------|
| A-0-0-1 | A |
| A-0-0-2 | A |
| A-0-0-3 | B |
| A-45-0-1 | B |
| A-45-0-2 | B |
| A-0-04-1 | A |
| A-0-04-2 | A |
| A-0-04-3 | A |
| A-15-04-1 | A |

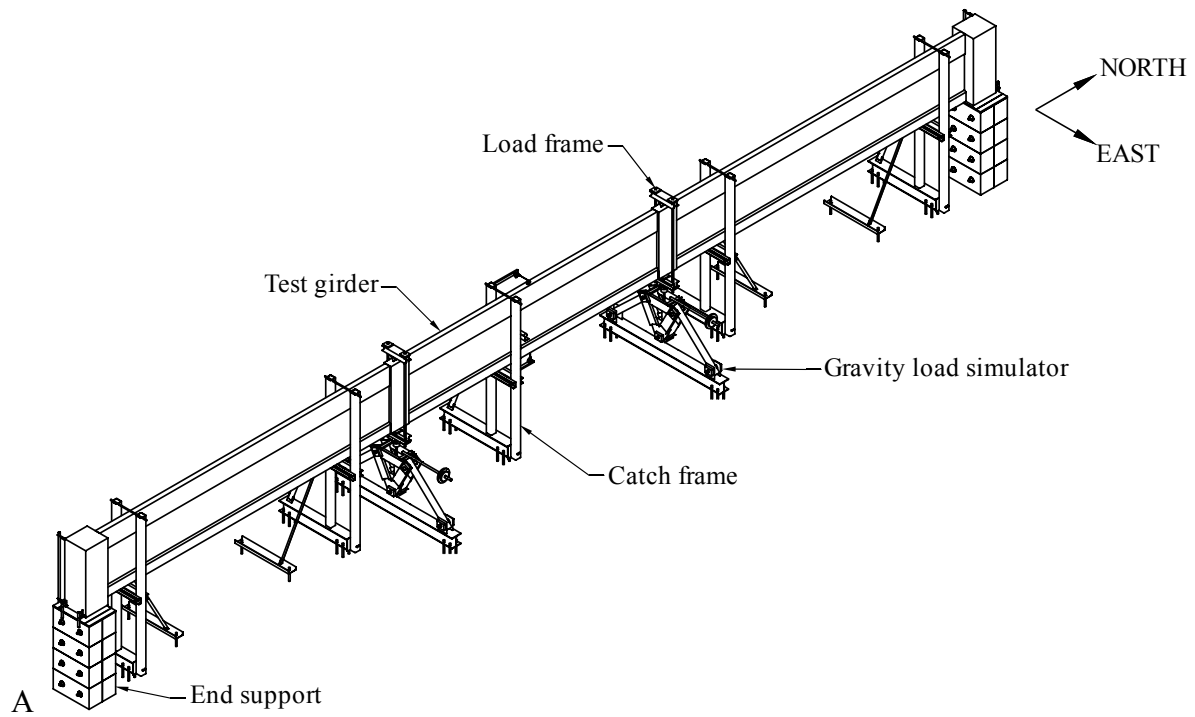


Figure 8-1. Overall test setup. A) Schematic. B) Photograph (photo courtesy of University of Florida, Department of Civil and Coastal Engineering).

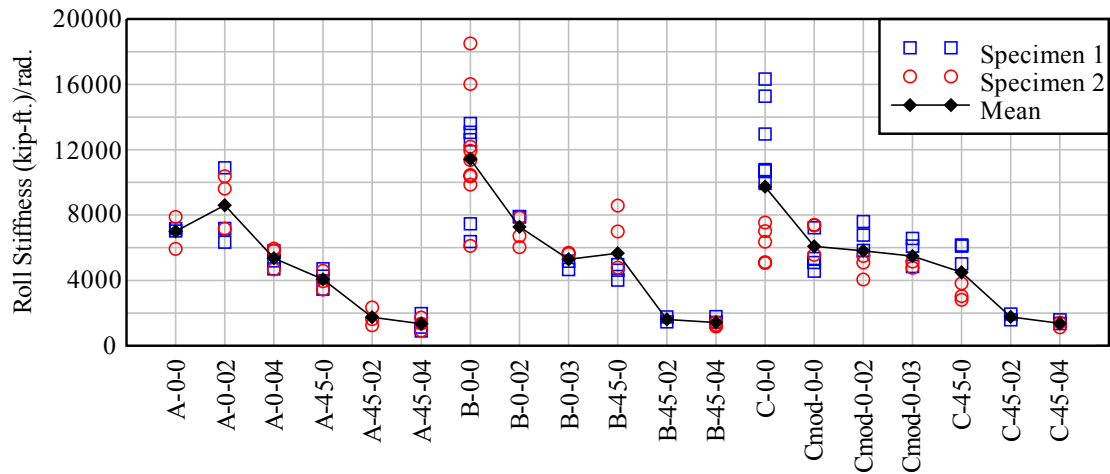


Figure 8-2. Roll stiffness results, reproduced from Chapter 2

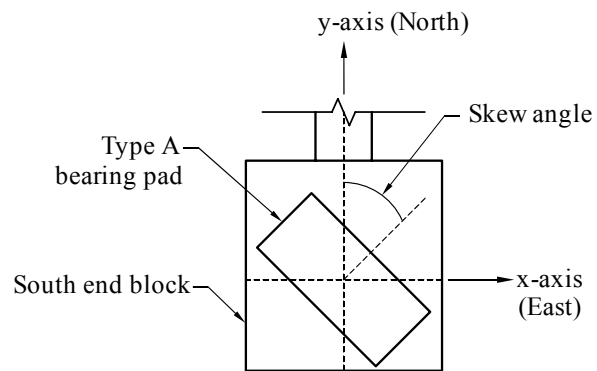


Figure 8-3. Bearing pad skew angle orientation in buckling tests



Figure 8-4. Beveled plate used to impose slope angle on bearing pads (photo courtesy of University of Florida, Department of Civil and Coastal Engineering)



Figure 8-5. Beveled plate and bearing pad positioned between end block and end support (photo courtesy of University of Florida, Department of Civil and Coastal Engineering)

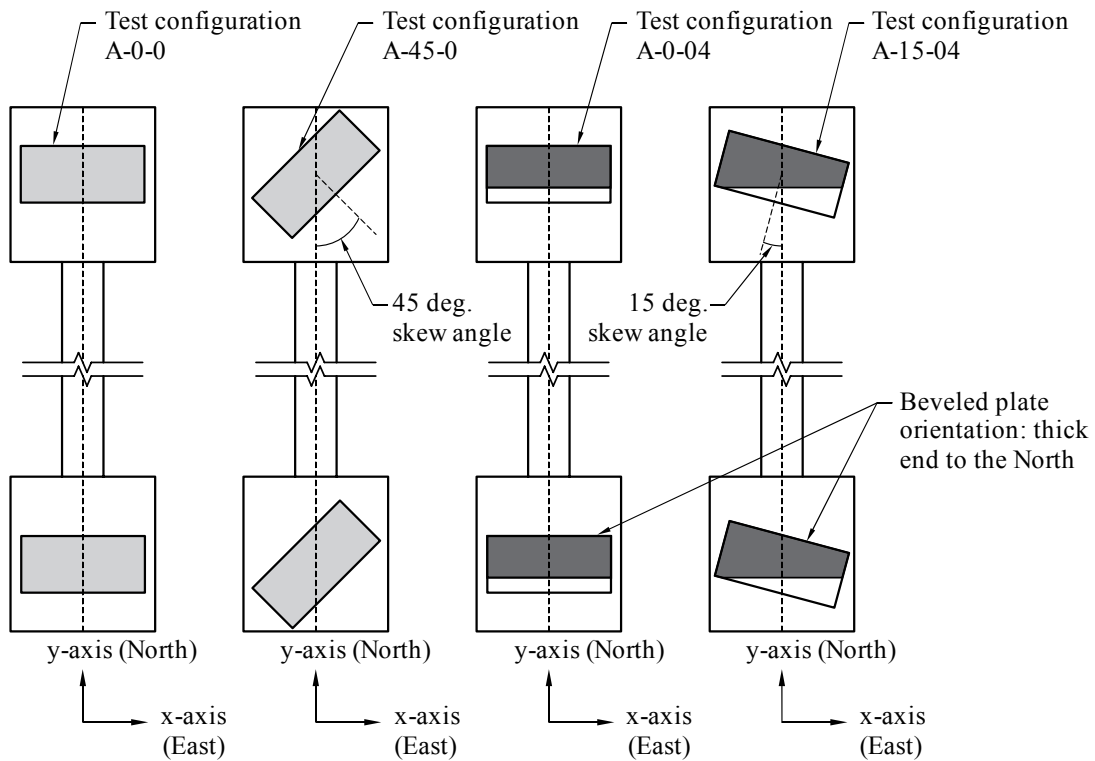


Figure 8-6. Bearing pad orientation and initial pressure distributions during buckling tests

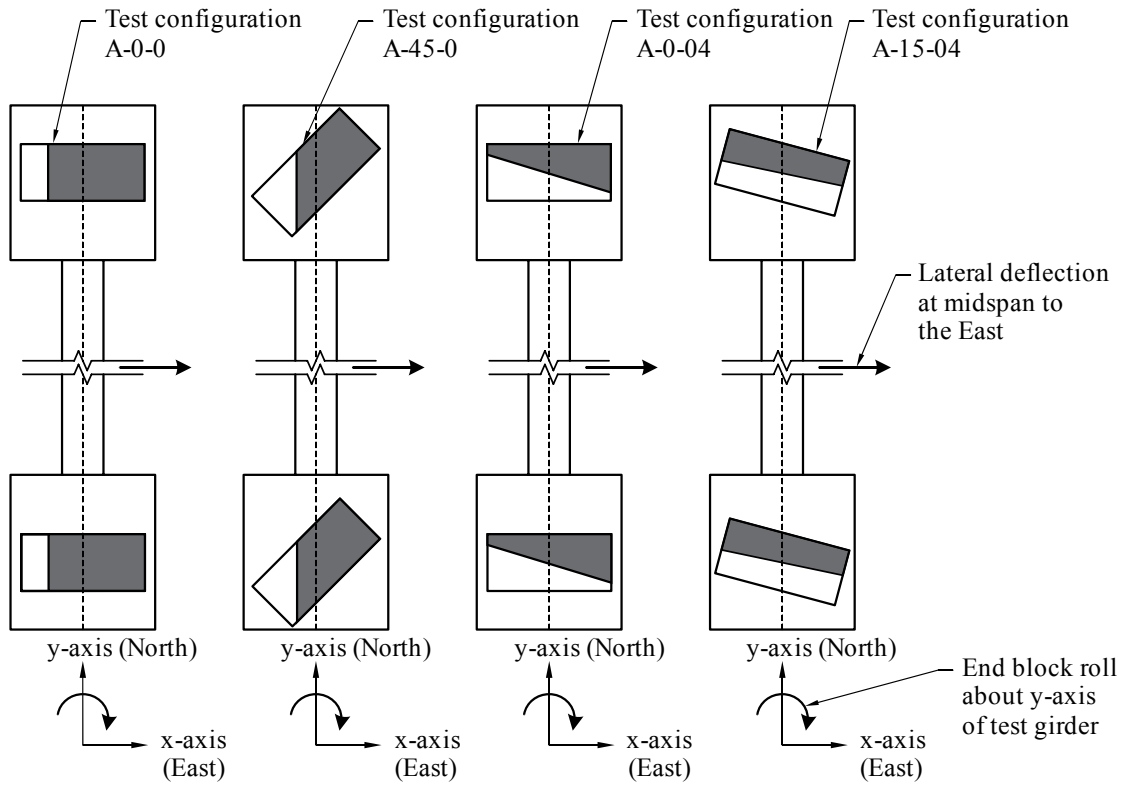


Figure 8-7. Final bearing pad pressure distributions during buckling tests

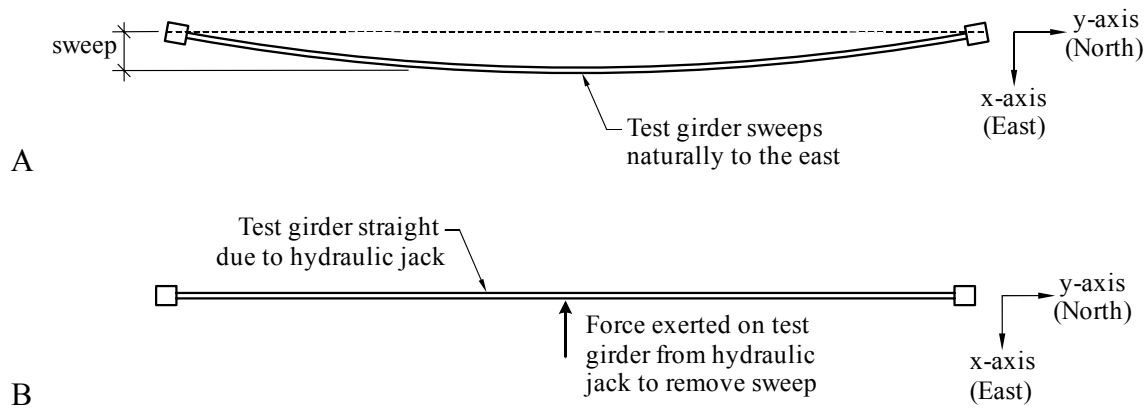


Figure 8-8. Sweep of test girder. A) Unrestrained position. B) After hydraulic jack applied.



Figure 8-9. Jack used to straighten test girder (photo courtesy of University of Florida, Department of Civil and Coastal Engineering)

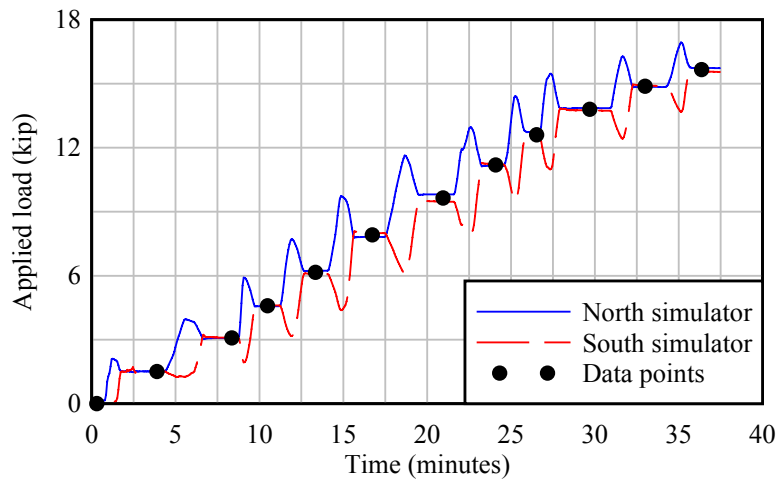


Figure 8-10. Typical load time history (test A-0-0-2 shown)

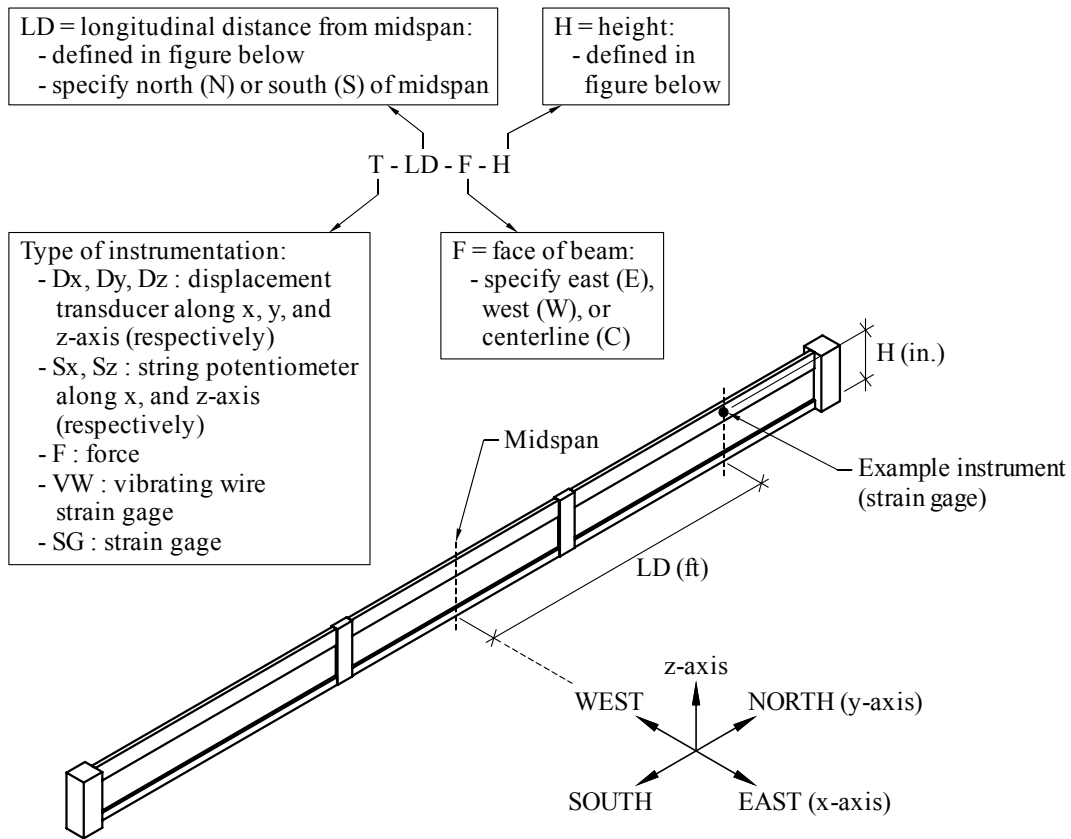


Figure 8-11. Naming convention for buckling test instrumentation

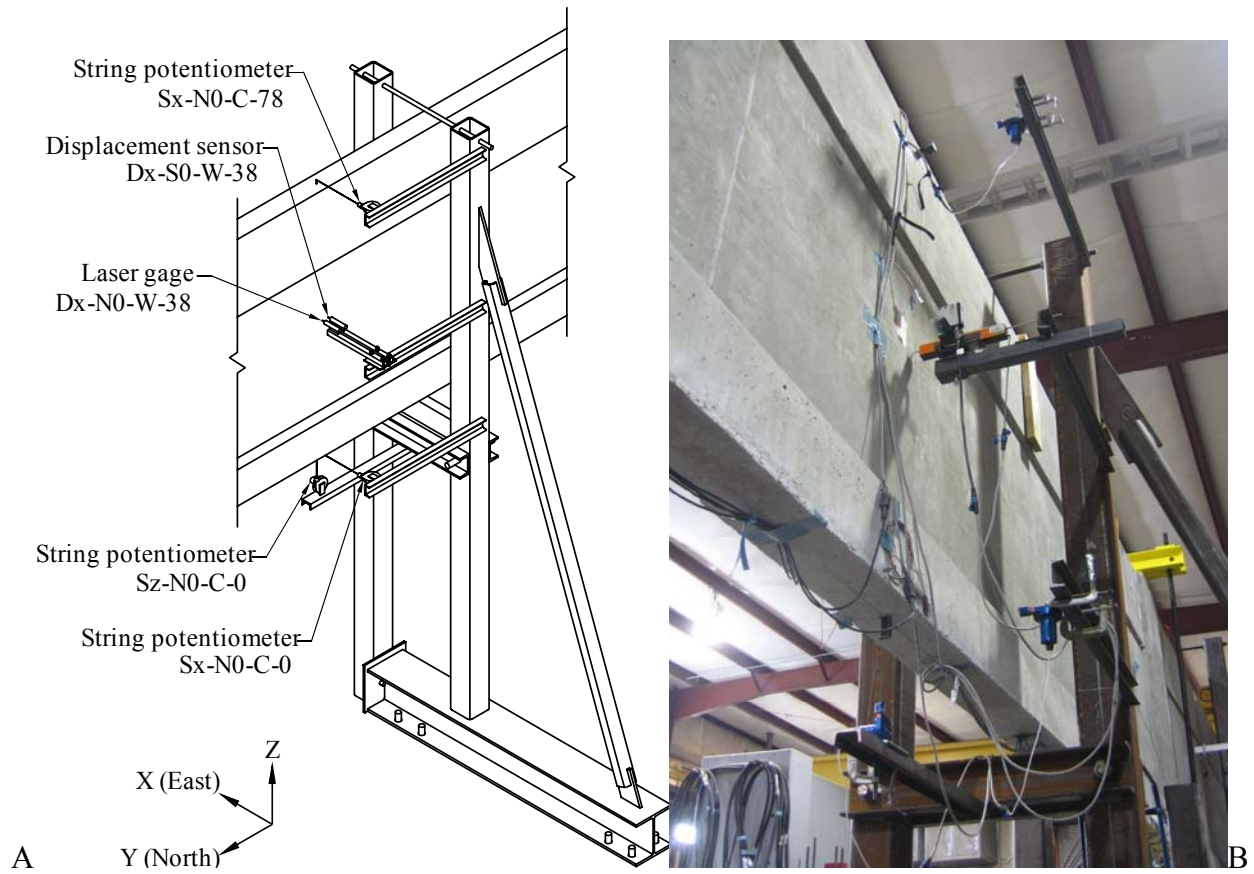


Figure 8-12. Midspan displacement transducers. A) Schematic. B) Photograph (photo courtesy of University of Florida, Department of Civil and Coastal Engineering).

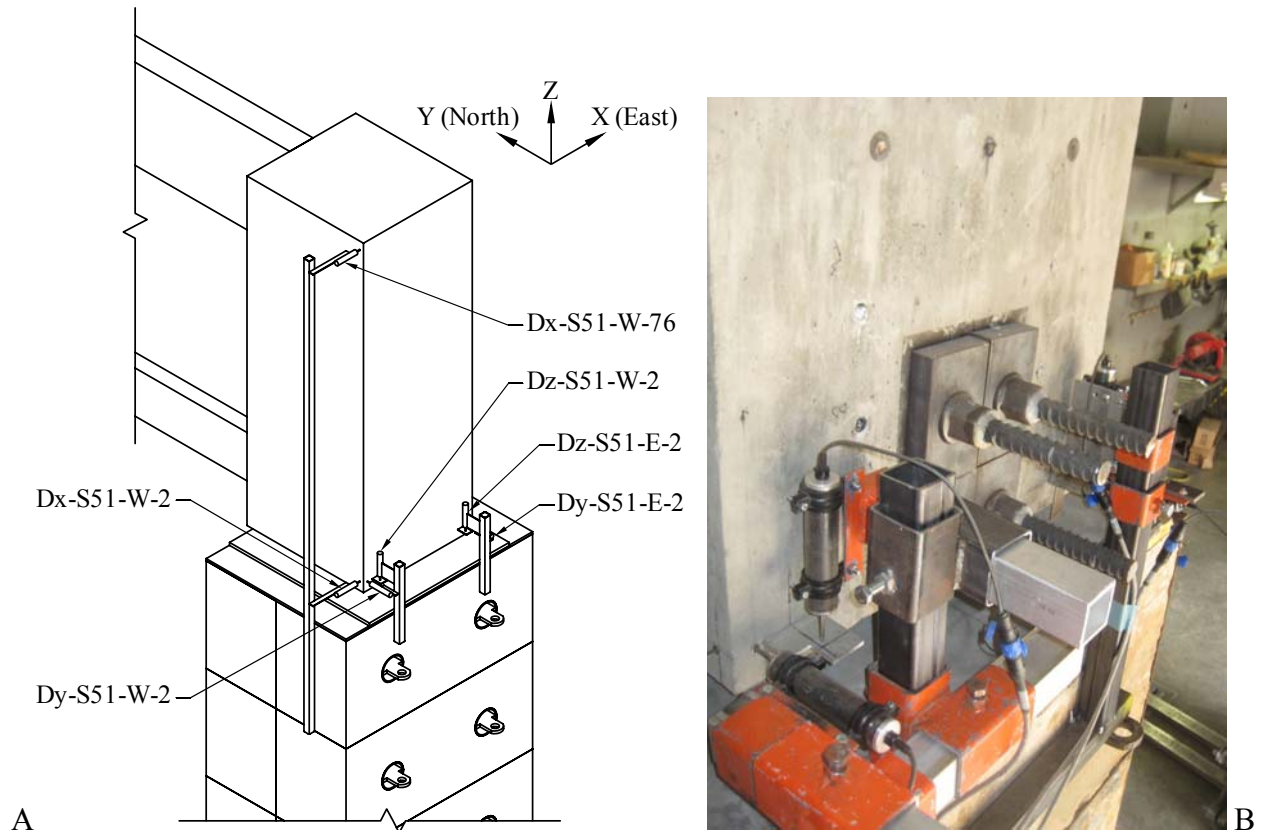


Figure 8-13. South end block displacement transducers. A) Schematic. B) Photograph (photo courtesy of University of Florida, Department of Civil and Coastal Engineering).

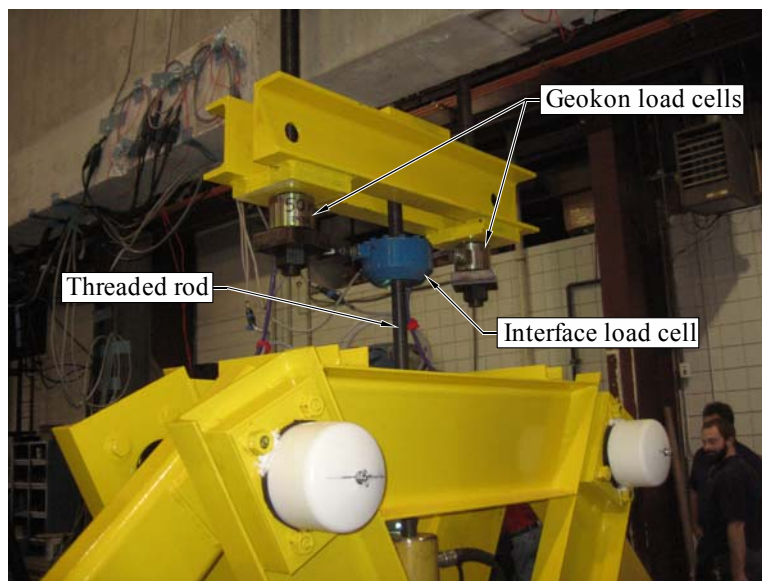


Figure 8-14. Load cells, located at gravity load simulator locations (photo courtesy of University of Florida, Department of Civil and Coastal Engineering)



Figure 8-15. Vibrating wire strain gages, cast into closure strips (photo courtesy of University of Florida, Department of Civil and Coastal Engineering)

CHAPTER 9 RESULTS

As discussed in Chapter 3, there were two primary goals of the second phase of the project. The first objective was to experimentally determine the buckling capacity of the test girder supported on bearing pads with various configurations of skew and slope angles. The second objective was to use these experimental results to validate and calibrate a finite element buckling model. The results of the experimental buckling tests are presented in this chapter, including the measured data, a data curve fitting scheme, a method for calculating buckling capacities, and the computed buckling capacities themselves. Additionally, the results of the experimental tests are compared to the finite element analysis results. Aspects of the validated finite element model—bearing pad roll stiffness, concrete elastic modulus specified, and load-displacement results—are also presented.

Experimental Buckling Test Results

It is important to note that, of the nine (9) individual buckling experiments performed and presented in this chapter, only one test (A-45-0-1) was carried out until buckling of the test girder occurred (Figure 9-1). The remaining tests were terminated before the test girder became fully unstable, to ensure cracking did not occur (and therefore maintain repeatability). Therefore, the last measured data point presented for an individual test does not indicate that buckling has occurred, but rather it indicates the load and displacement level at which the test was concluded.

Measured Load-Displacement Curves

For each test, vertical load was applied at the top of the test girder at the gravity load simulator locations (Figure 9-2), and midspan lateral (x-axis) displacement was measured roughly at the centroid of the test girder. Data points were established when the Interface load cell readings (F-N15-C and F-S15-C, located at the north and south simulators, respectively)

measured approximately the same applied load. In this chapter, the average of these load cell readings is defined as the applied load (P) (Figure 9-2). Midspan lateral displacements presented in this chapter were measured using displacement sensor Dx-N0-W-38. Measured load-displacement curves for each test are shown in Figure 9-3. For each curve, the displacement of the first data point indicates the sweep of the test girder under only its own self weight. Note that sweep was recorded using displacement sensor Dx-N0-W-38 for the tests conducted following method A (recall Chapter 8), whereas the sweep was measured using a tape rule for the tests conducted following method B. By shifting the displacement data along the x-axis to the origin (Figure 9-4)—corresponding to incremental midspan displacement caused by applied load—excellent repeatability is observed between tests with the same configuration.

Data Curve Fitting

A method developed by Southwell (1932) is commonly used to characterize the load-displacement behavior of buckling experiments and also to predict the buckling capacity without performing the experimental test until buckling occurs. Using the Southwell method, a rectangular hyperbola with asymptotes passing through the origin of coordinates is fitted to load-displacement data obtained from a buckling experiment using the equation:

$$x \cdot y - \beta \cdot x + \alpha \cdot y = 0 \quad (9-1)$$

where α and β are the asymptotes of the hyperbola (Figure 9-5). Rearranging the equation provides a more familiar form:

$$y = \frac{\alpha \cdot \beta \cdot x^2}{\alpha \cdot x^2 + \alpha^2 \cdot x} \quad (9-2)$$

To fit a curve through multiple sets of data, individual data sets are commonly averaged together to form a single data set and a curve is fit to the averaged data. This approach works best when each data set includes approximately the same number of points, and data are recorded at the

same interval. However, the data from the buckling tests were not recorded in this manner. As shown in Figure 9-4, data for individual tests within each configuration were measured at unequal intervals, and the range of each test was not equal. Thus, simply averaging the data for each configuration would bias the average toward tests in which data were captured at smaller intervals. To avoid this issue, the following procedure was used to process the data for each individual test and develop a characteristic fitted curve for each configuration:

- A hyperbola (Equation 9-2) was fit—by using least-squares error—to each individual test data set (Figure 9-6A)
- The hyperbolas within each test configuration were resampled at equal displacement intervals, specifically $1/20^{\text{th}}$ of the maximum displacement within a configuration (Figure 9-6B)
- A single hyperbola was fit to the cloud of resampled data for each configuration (Figure 9-6C)

This procedure was applied to each test configuration, with the final hyperbola results shown in Figure 9-7.

Calculation of Buckling Capacity

Using the Southwell method (1932), buckling capacity is approximately equal to the horizontal asymptote (β) of the best fit hyperbola. Recall that among the buckling experiments conducted, one test (A-45-0-1) was run until buckling occurred. Thus, this case can be used to test the accuracy of approximating the buckling load using the fitted value β . For this test, the buckling load was measured as 13.1 kip. However, as shown in Figure 9-8, the Southwell method estimates the buckling load (β) as 18.7 kip, overestimating by 43%. As stated by Southwell (1932), the “analysis may be expected to apply best to cases in which the initial deflection [sweep] was small.” In other words, the Southwell method works best when the primary instability is lateral torsional buckling. However, for the experiments conducted in this

study, the test girder initial sweep was large enough that the failure mode was a mixture of lateral torsional buckling and roll-over instability as opposed to pure lateral torsional buckling instability. Due to the slenderness and post-tensioning levels necessary to elastically buckle the test girder at 100 ft, the test girder had a sweep that was more than twice the acceptable level in practice.

As per the 2010 FDOT *Standard Specifications for Road and Bridge Construction* (FDOT 2010), maximum allowable girder sweep was limited to 1/8 in. of sweep per 10 ft of girder length, but not to exceed 1.5 in. for Florida Bulb T-beams and Florida-I Beams. The minimum sweep of the test girder—in test configuration A-0-0—was 2.8 in. Because of these large initial displacements, the asymptote of the hyperbola (β) is not the ideal definition of the buckling load for the experiments performed in this study. Instead, an alternative definition for buckling capacity is employed, still incorporating the Southwell hyperbola. Using the fitted hyperbola (Eqn. 9-2), the buckling load is defined as the point at which the slope drops to below 1/10th of its initial value (Figure 9-9). This rule agreed with the data set from the one test case that was carried out to buckling during testing (A-45-0-1, as noted in the following section).

Buckling Capacity Results

Using the 10% buckling rule, the ideal case, A-0-0 (non-skewed, non-sloped), had the largest buckling capacity, and the skewed, sloped case (A-15-04) had the lowest buckling capacity. The intermediate cases (A-45-0 and A-0-04) both had buckling capacities between the two extremes. Table 9-1 provides a summary of the buckling capacity for each test configuration, as well as the percent reduction in buckling capacity from the ideal (A-0-0) case. There was good agreement between the calculated buckling capacity of A-45-0 and the measured buckling capacity of test A-45-0-1, which buckling in the lab at a measured load of 13.1 kip. Using the

10% buckling rule, the buckling capacity for A-45-0 is calculated as 12.8 kip (2.3% error relative to test A-45-0-1).

In the case of test configuration A-15-04, determining the buckling capacity through the use of the 10% rule is not applicable, because the test girder had such a large sweep (5.7 in.) compared to what is acceptable in practice. This magnitude of initial lateral displacement (sweep) caused the test girder to purely overturn, as opposed to buckle. While a hyperbola can be fit through the data, the buckling load cannot be defined and will not be presented for the remainder of this thesis.

Buckling Finite Element Model

The results of the experimental buckling tests were used to validate the finite element buckling model. This section discusses the model and several of its components, including the development of the moment-rotation curves that were used to represent the bearing pad, the modulus of elasticity test girder concrete, and the results obtained from each test configuration.

Moment-Rotation Curves from Roll Stiffness Tests

Originally, the nonlinear roll stiffness of the bearing pads were to be modeled using the moment-rotation curves obtained from the isolated roll stiffness tests using the bearing pad test device (Chapter 2). However, axial (vertical) load levels on the pads were different between the isolated tests and the buckling tests. This difference altered the moment-rotation behavior during buckling tests as compared to the isolated tests. Therefore, additional roll stiffness tests were performed on the bearing pads under buckling testing conditions, with the bearing pads located beneath the test girder in test configuration A-0-0. Under these conditions, the bearing pads were tested “in-situ.” In this section, the in-situ test procedure and results are presented, and the results are compared to the isolated roll stiffness results obtained using the bearing pad test device (denoted “isolated” in this chapter).

For the in-situ tests, a lateral load was applied to the top flange of the test girder near each end block, and the girder was allowed to roll about the y-axis of the bearing pad (Figure 9-10A). The load was applied by a hydraulic jack mounted to the catch frames at each end of the test girder, and measured with an inline load cell (Figure 9-10B). Displacement sensors at the end blocks along the x-axis (Dx) measured the relative horizontal displacement between the top and bottom of the end blocks. Given the vertical distance between each pair of sensors (Dx-N51-W-2 and Dx-N51-W-76; Dx-S51-W-2 and Dx-S51-W-76), the end block roll angle was calculated. Three in-situ roll tests were performed (on 2011-12-19 and 2011-12-20). The measured data are shown in Figure 9-11.

In the finite element model, bearing pad rotational resistance is modeled using nonlinear rotational springs which are simply defined by a moment-rotation curve. Therefore, the measured moment-rotation data from the roll stiffness tests were averaged and subsequently fitted to a representative function for input into the finite element model. To maintain equal weight when averaging the curves, the measured load-displacement curves (Figure 9-12A) from individual tests were resampled at an equal interval of 0.0003 rad (Figure 9-12B), and the resampled curves were averaged (Figure 9-12C). The averaged data exhibit an initial, linear roll stiffness (slope of moment-rotation curve) that is followed by an apparent softening (reduction in stiffness), until the slope of the moment-rotation curve effectively equals zero and the moment-rotation curve plateaus. A sigmoid function, which has a shape that matches the average data closely, was chosen to represent the moment-rotation curves for the bearing pads. A basic sigmoid function takes the following functional form:

$$f(x) = \frac{1}{1 + e^{-x}} \quad (9-3)$$

However, to fit the moment-roll curves, the basic functional form must undergo a variety of transformations. Thus, the data were fit (by using least-squares error) with the following modified functional form:

$$f(x) = \gamma_0 + \frac{\gamma_1}{1 + e^{-\gamma_2 \cdot x}} \quad (9-4)$$

where γ_0 , γ_1 , and γ_2 are functional parameters.

This same process of resampling, averaging, and fitting the data was then applied to the moment-rotation curves obtained from the isolated roll stiffness tests using the bearing pad test device. Similarly to the in-situ roll stiffness tests, the measured data has an initial linear stiffness that gradually decreases, closely matching the modified sigmoid curve shape. The best fit sigmoid curves for the moment-rotation curves of the isolated and in-situ roll stiffness tests are shown in Figure 9-13. The functional parameters of the best fit sigmoid curve for each test configuration—both isolated and in-situ roll stiffness tests—are presented in Table 9-2 (data units: kip, in., and rad).

Scaling of Moment-Rotation Curves from Isolated Tests

The axial load applied to the type A bearing pads during the isolated roll stiffness tests was approximately 92 kip, which was chosen to be representative of the self weight end reactions of a realistic long span girder (Florida Bulb-T sections). However, during buckling testing, the test girder was constrained to a 100 ft span length, which required a more slender and therefore lighter girder cross-section to be used, resulting in a reduced axial load applied to the pad. During buckling testing, the axial load—due to the self weight of the slender test girder and applied vertical loads—was approximately 40 kip. Thus, the ratio of axial load during buckling testing to axial load during isolated roll stiffness testing was approximately 0.43. Under this reduced axial load, the in-situ moment-rotation behavior of the bearing pads was different than

measured during the isolated tests, as shown in Figure 9-14. Although both the in-situ and isolated moment-rotation data have similar initial roll stiffness, the plateau value differs significantly. As shown in Figure 9-14, the plateau of the moment-rotation curve occurs at a much lower moment than the in-situ tests.

The difference in moment-rotation behavior can be attributed to the difference in pre-compression, which affects the contact area between the pad with the end block (or test device) as it rolls. In non-sloped test configurations (A-0-0 and A-45-0), rotational stiffness is reduced as the end block (or test device) gradually loses contact as the test device rolls off the pad, hence the gradually nonlinear nature of the moment-rotation curve. Initially, under non-sloped conditions, the bearing pad is fully in contact with the bottom of the end block or test device, and thus the initial roll stiffness of the bearing pad is not affected by the magnitude of axial load. However, during the in-situ roll stiffness tests (and buckling tests)—in which pre-compression is reduced relative to the isolated tests—a smaller rotation is required for the end blocks to lose contact with the pads (Figure 9-15). Consequently, the in-situ plateau moment is reduced relative to the isolated tests. The plateau moment should then be proportional to the axial pre-compression. Thus, the roll capacity should differ by the ratio of axial load during testing (0.43 in this case).

A similar phenomenon also occurs for sloped cases. However, the *initial* contact area of the end block (or test device) with the bearing pad is approximately proportional to axial pre-compression (Figure 9-16). Thus, the initial roll stiffness is also proportional to the pre-compression. Like the non-sloped cases, the roll capacity is proportional to axial pre-compression. Therefore, for sloped cases, *both* the initial stiffness and plateau moment of the moment-rotation curve are decreased by the ratio of applied axial load (0.43 in this case).

For use in the buckling finite element model, moment-rotation curves obtained from the isolated roll stiffness tests were scaled by a factor of 0.43 (equal to the ratio of axial loads). In non-sloped test configurations (A-0-0 and A-45-0), the scale factor was applied to the plateau of the moment-rotation curve only, while maintaining the initial slope (Figure 9-17A and Figure 9-17B). However, for the sloped configuration (A-0-04), the scale factor was applied to both the initial slope and the moment plateau (Figure 9-17C). Examining the moment-rotation curves from test configuration A-0-0 (Figure 9-17A), the scaled curve closely matches the in-situ curve for both the initial stiffness and moment plateau. The final scaled curves for each test configuration—used in all subsequent finite element buckling analyses—are compared in Figure 9-18.

Elastic Modulus Used in Finite Element Buckling Model

Concrete components of the test girder were modeled using a linear elastic material model. As discussed in Chapter 6, the elastic modulus was determined for the precast segments using field cured and moist cured cylinders. The average elastic modulus for the field cured cylinders was 4,770 ksi, and the average of the moist cured cylinders was 5,140 ksi. Two separate finite element buckling analyses were performed in test configuration A-0-0 (using the scaled roll stiffness curves), each with an elastic modulus corresponding to the field cured or moist cured results. The buckling curves predicted by both models are presented in Figure 9-19, along with the best fit hyperbola generated from the experimental data. As shown, the model with the field cured elastic modulus more accurately represents the experimental results. This can be attributed to the web thickness of the precast segments, which matched the diameter of the concrete cylinders (4 in.). Therefore, the conditions imposed on the field cured cylinders (cured alongside the test girder) were more representative of the precast segments than the moist cured cylinders

(inside a tank of lime water). Thus, the field cured elastic modulus (4,770 ksi) is used in all subsequent finite element models.

Finite Element Buckling Model Results

A finite element buckling analysis was performed for each of the three test configurations, using the scaled roll stiffness curves and field cured elastic modulus as described in the previous sections. Using the same buckling rule used on the experimental results, the buckling capacity of a finite element analysis was defined as the point at which the slope of the load-displacement curve drops to below 1/10th of its initial value. The buckling curves and capacities of the finite element analyses are shown in Figure 9-20, along with the buckling curves and capacities generated using hyperbolas fitted to the experimental data. The buckling capacities calculated from the experimental tests and finite element analyses are also summarized in Table 9-3.

Generally, good agreement is observed between the shape of the curves—particularly in the non-sloped cases—and also between the predicted buckling capacities. In the non-sloped cases (A-0-0 and A-45-0), the finite element buckling capacity was lower than the experimental buckling capacity. However, in the sloped case (A-0-04), the initial slope and buckling capacity of the model are slightly larger than the experimental results. This disagreement can most likely be attributed to a difference in the theoretical initial contact area of the bearing pad, caused by the initial sweep during a buckling test. If, as a simplification, linear elastic bearing pad response is assumed, then the ratio of initial contact areas between buckling tests and isolated roll tests would be equal to the ratio of applied axial load. Thus, scaling the isolated roll stiffness curves by the ratio of the applied axial loads should accurately reflect this difference. However, because relatively large sweep was present in the test girder, the end blocks initially rolled about the bearing pad as the test girder was being placed. Therefore, the contact area in the buckling tests may actually have been less than the theoretical contact area accounted for by using the scale

factor. Thus, the initial slope and buckling load obtained from the experimental results would be smaller than the finite element prediction (as seen in the A-0-04 case).

Therefore, based on the acceptable levels of difference observed between the shape of the experimental buckling curves and the finite element analysis buckling curves, and based on a maximum difference of 15% between experimentally and analytically determined buckling capacities, the finite element modeling methods employed in this study are considered to be experimentally validated.

Table 9-1. Buckling capacity results

| Test configuration | Skew angle (deg.) | Slope angle (rad.) | Buckling capacity (kip) | Buckling capacity percent reduction from A-0-0 (%) |
|--------------------|-------------------|--------------------|-------------------------|--|
| A-0-0 | 0 | 0 | 15.4 | 0.0% |
| A-45-0 | 45 | 0 | 12.8 | 16.9% |
| A-0-04 | 0 | 0.04 | 11.8 | 23.4% |

Table 9-2. Sigmoid curve functional parameters for each test configuration

| Test configuration | γ_0 | γ_1 | γ_2 |
|--------------------|------------|------------|------------|
| A-0-0 (isolated) | -458.1 | 916.1 | 373.2 |
| A-0-0 (in-situ) | -156.7 | 313.5 | 1370.2 |
| A-45-0 (isolated) | -363.3 | 726.6 | 324.2 |
| A-0-04 (isolated) | -986.3 | 1972.5 | 143.8 |

Table 9-3. Experimental and finite element buckling capacities for each test configuration

| Test configuration | Experimental buckling load (kip) | Finite element model buckling load (kip) | Percent difference |
|--------------------|----------------------------------|--|--------------------|
| A-0-0 | 15.4 | 13.9 | -9.7% |
| A-45-0 | 12.8 | 10.9 | -14.9% |
| A-0-04 | 11.8 | 12.2 | 3.4% |

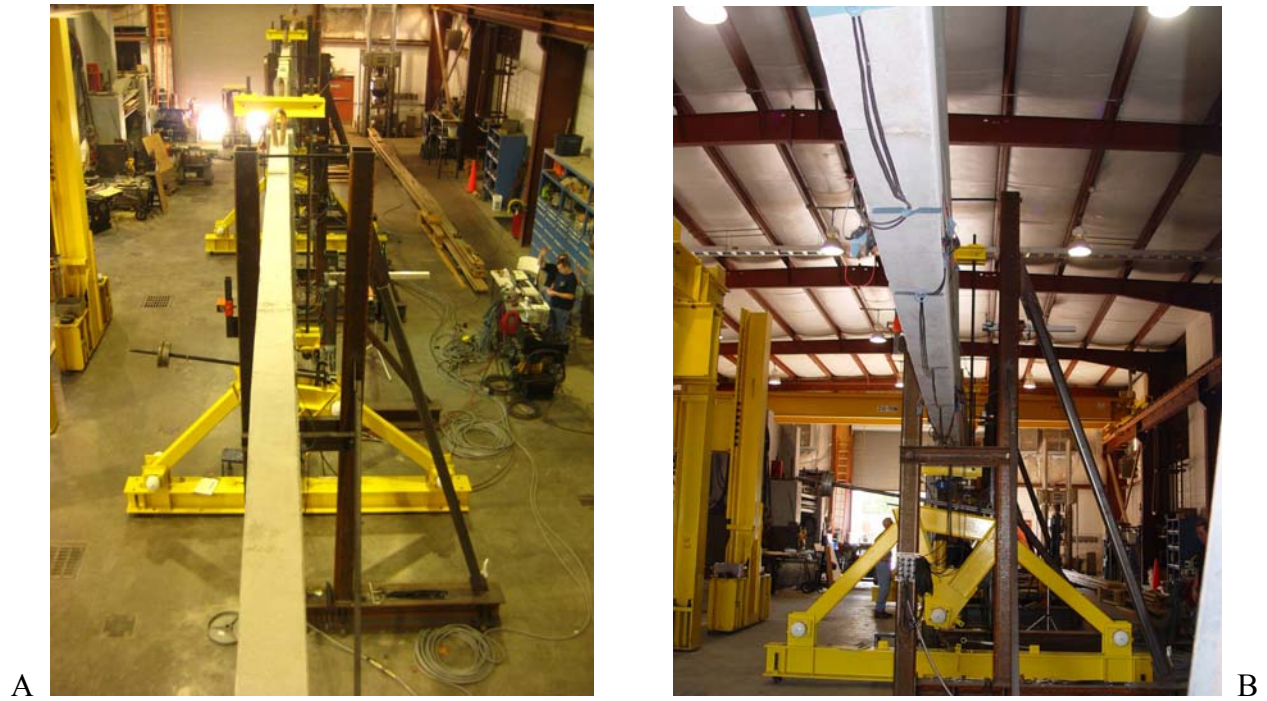


Figure 9-1. Test girder in buckled configuration, test A-45-0-1 (photos courtesy of University of Florida, Department of Civil and Coastal Engineering). A) Photograph taken above girder. B) Photograph taken below girder.

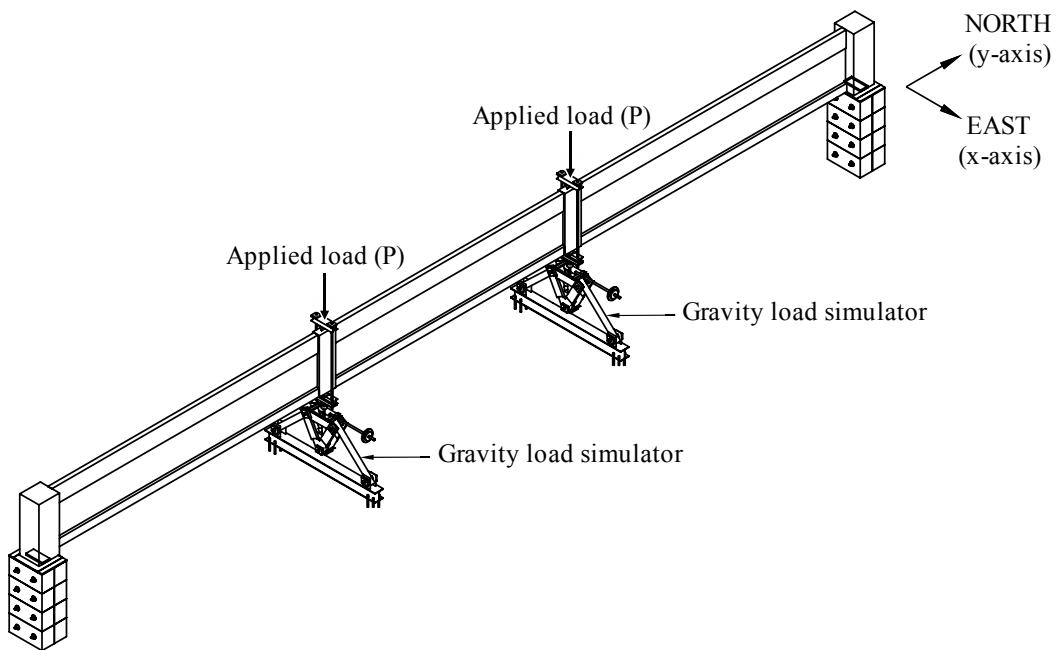


Figure 9-2. Definition of applied load (P)

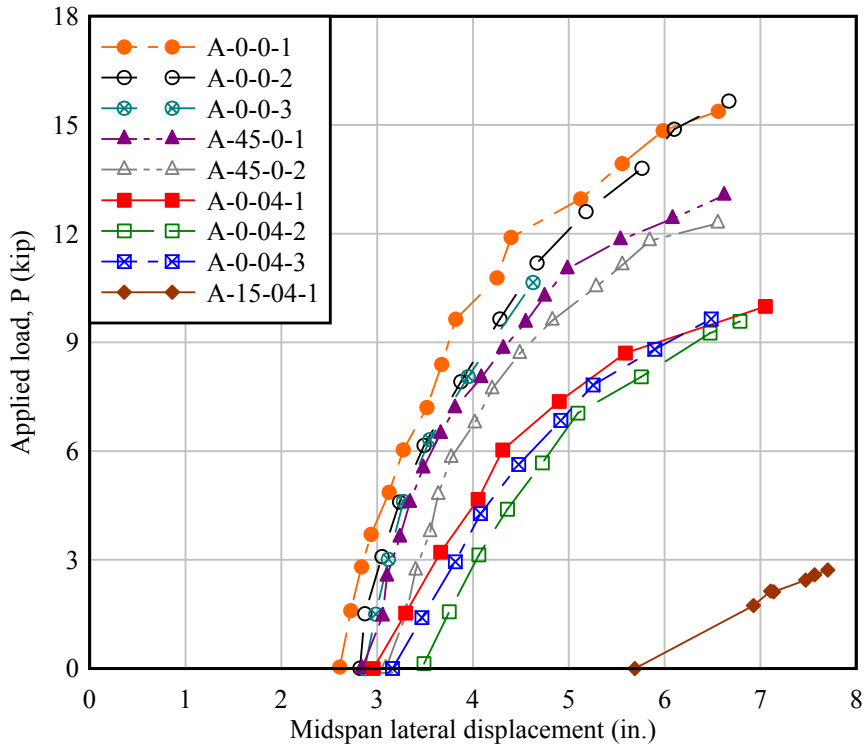


Figure 9-3. Measured absolute load-displacement data

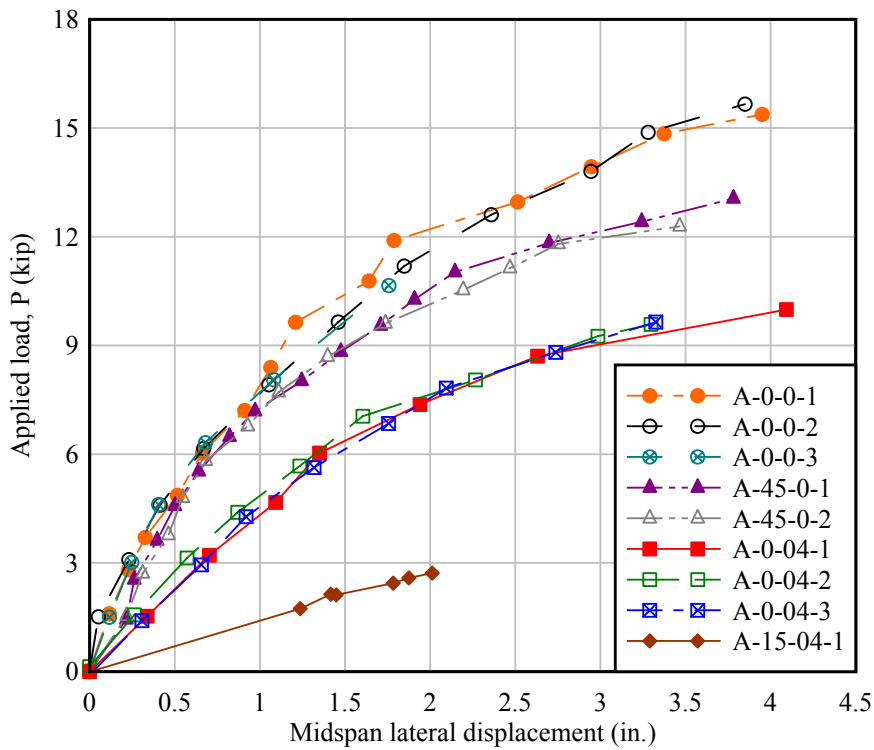


Figure 9-4. Measured incremental load-displacement data

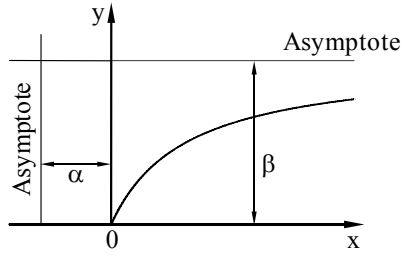


Figure 9-5. Southwell hyperbola fit

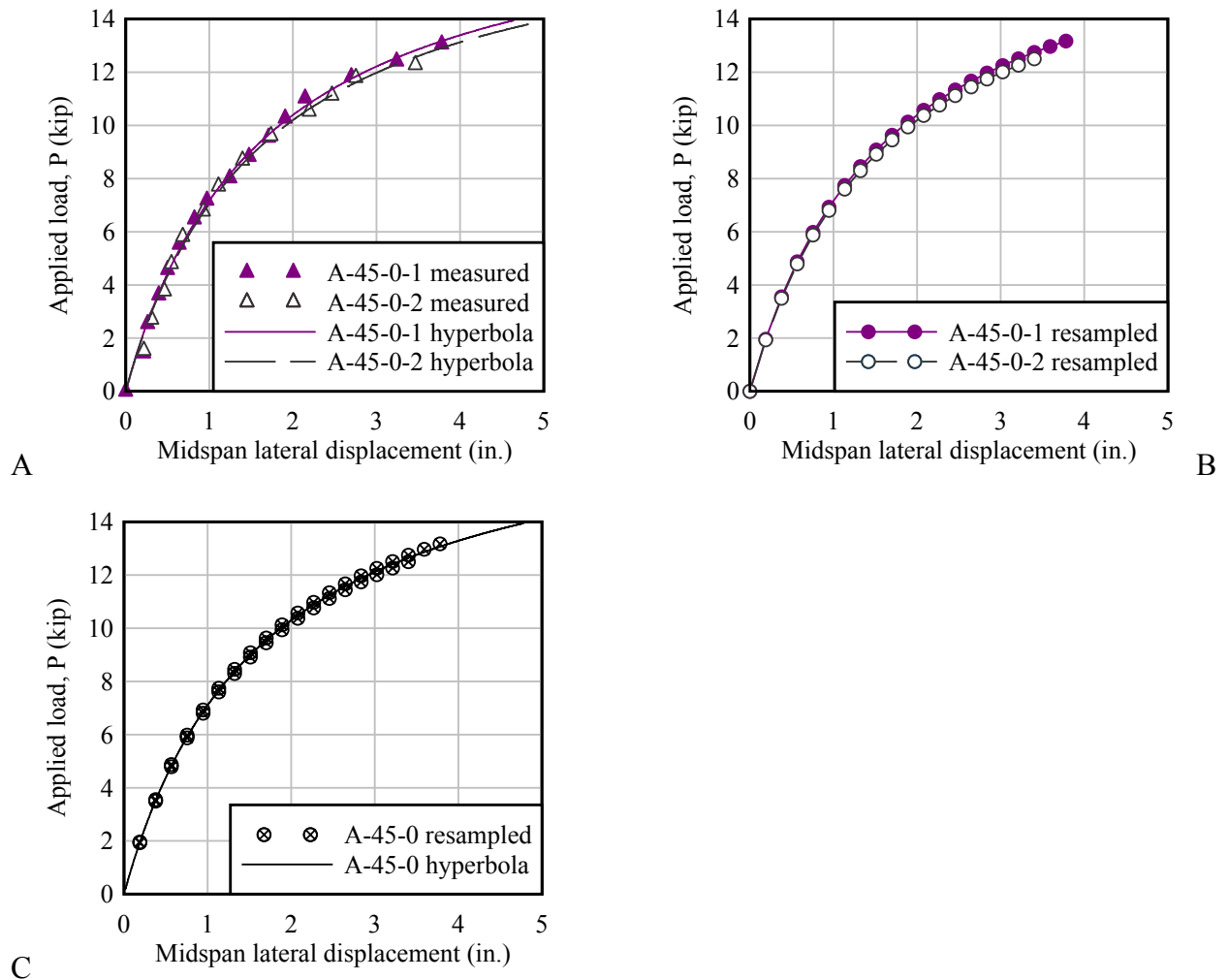


Figure 9-6. Data curve fitting procedure. A) Best fit hyperbolas for each individual test through measured data. B) Resampled data on hyperbola at regular interval. C) Test configuration hyperbola fit through resampled cloud of data.

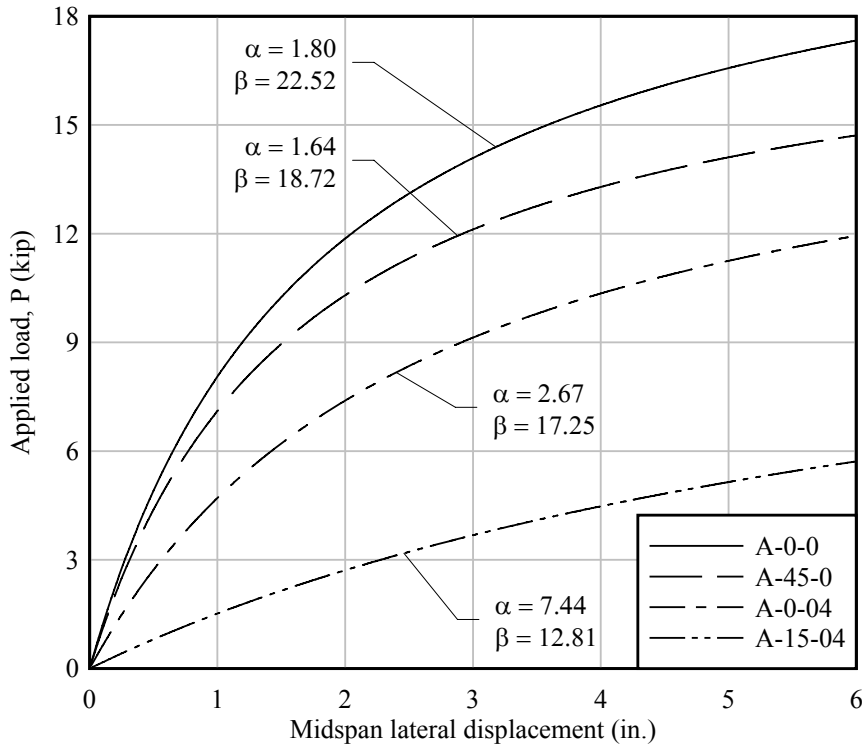


Figure 9-7. Best fit hyperbolas for each configuration

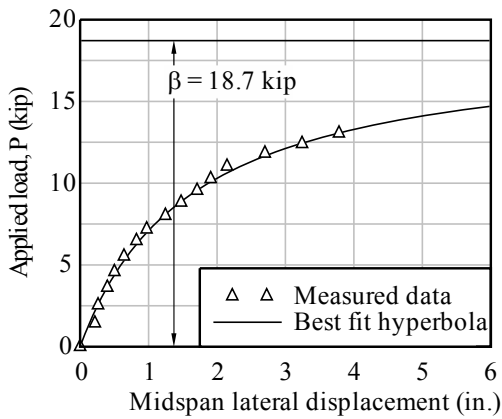


Figure 9-8. Hyperbolic curve fit and Southwell buckling load for test A-45-0-1

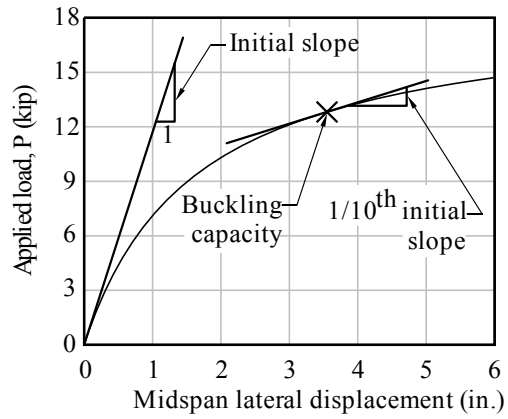


Figure 9-9. Definition of buckling capacity (A-45-0 configuration shown)

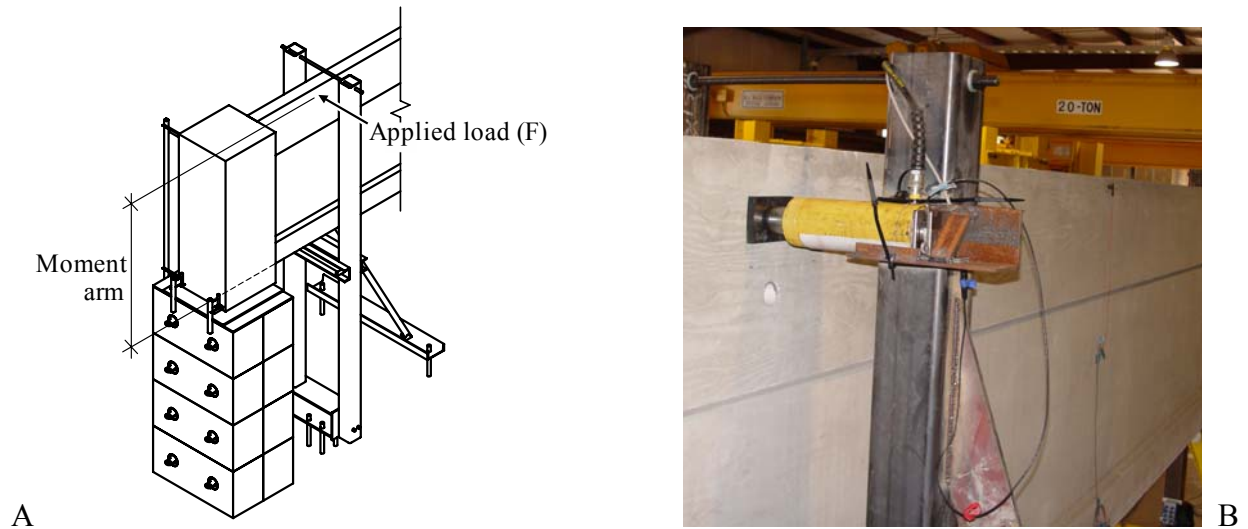


Figure 9-10. Description of “in-situ” roll test. A) Schematic of test. B) Loading setup, mounted to catch frame (photo courtesy of University of Florida, Department of Civil and Coastal Engineering).

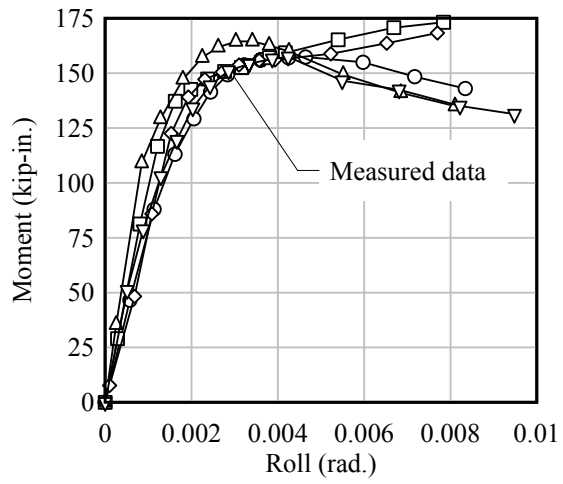


Figure 9-11. Moment-rotation data from in-situ tests (A-0-0)

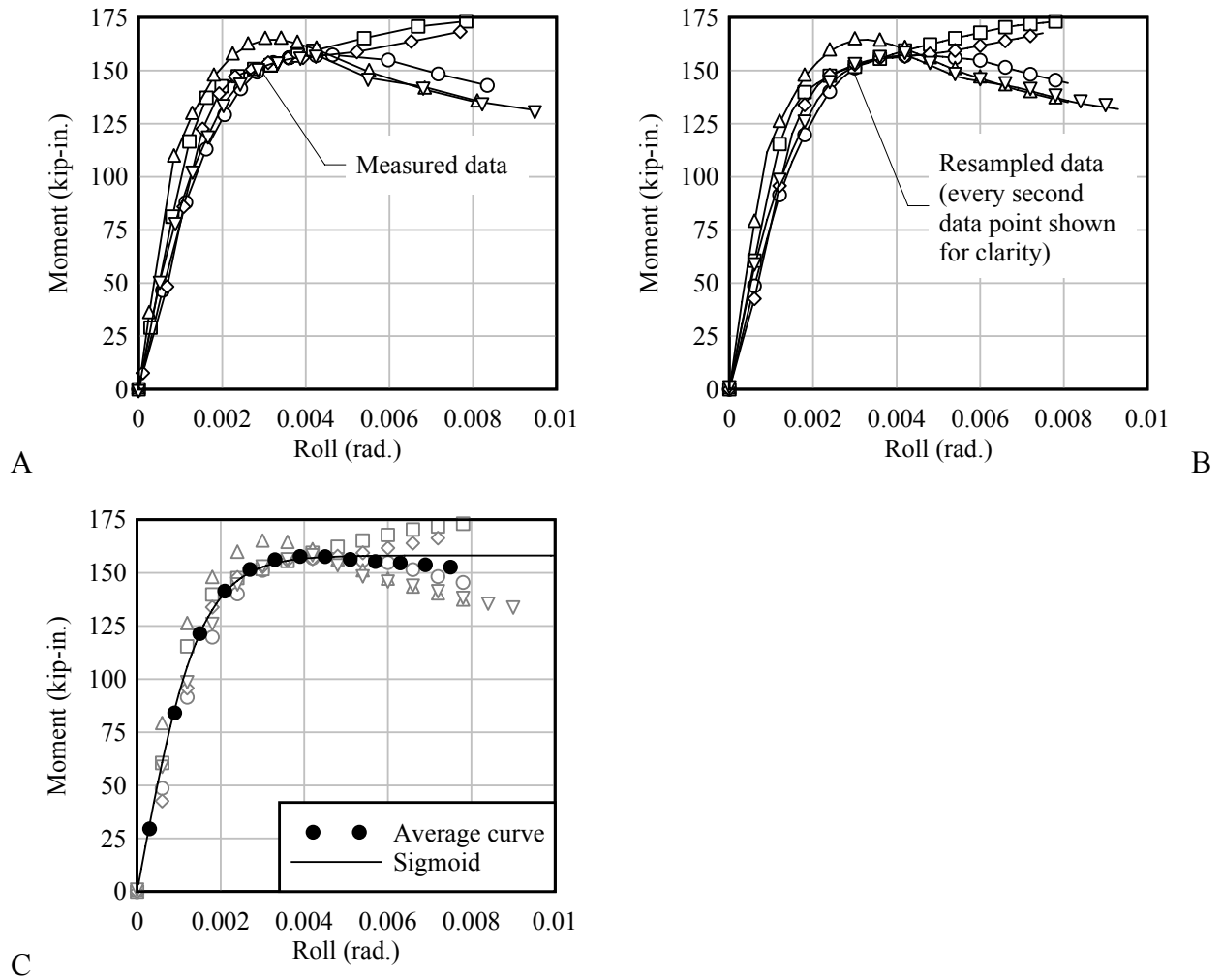


Figure 9-12. Data curve fitting procedure, in-situ case shown. A) Measured data. B) Resampled data. C) Average curve and best fit sigmoid curve.

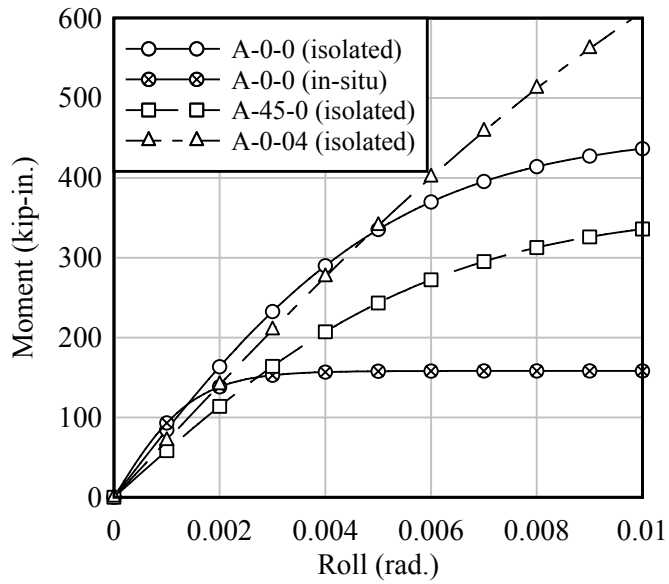


Figure 9-13. Moment-rotation curves, from isolated and in-situ roll stiffness tests

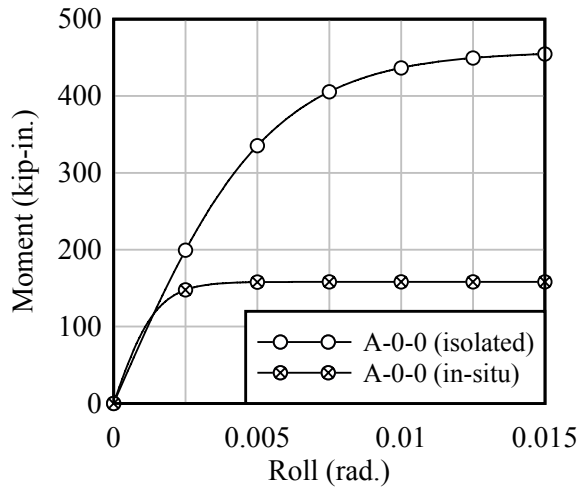


Figure 9-14. Moment-rotation curves, test configuration A-0-0, from isolated bearing pad tests (BPTD) and in-situ tests

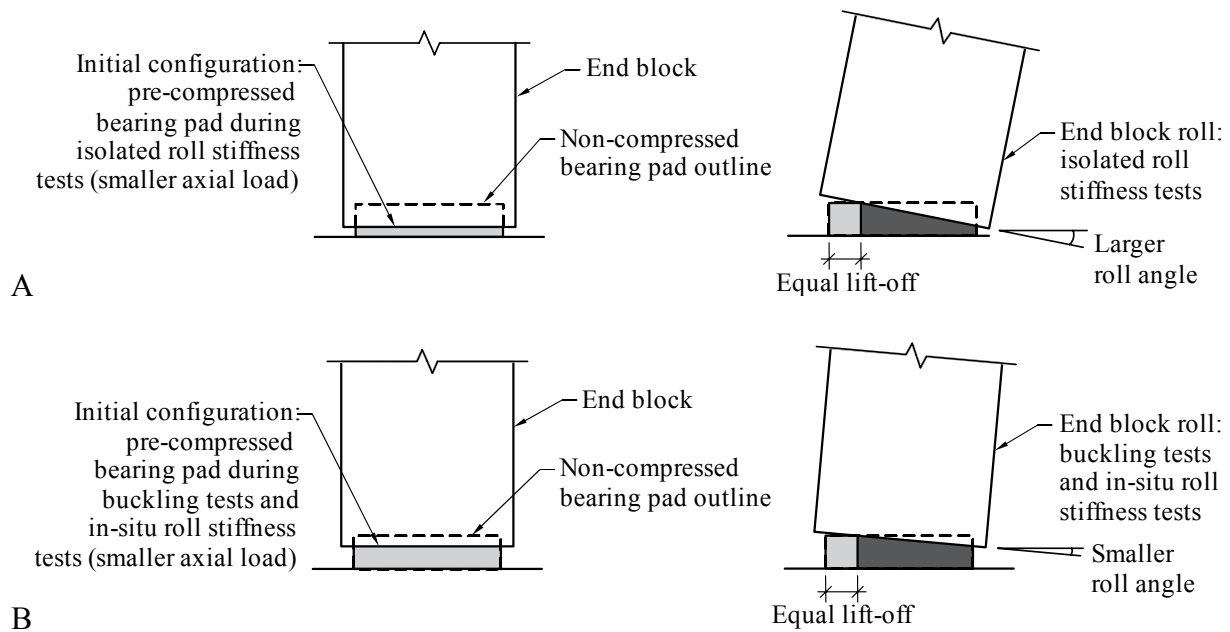


Figure 9-15. Bearing pad contact areas during testing. A) During isolated roll stiffness tests. B) During buckling tests.

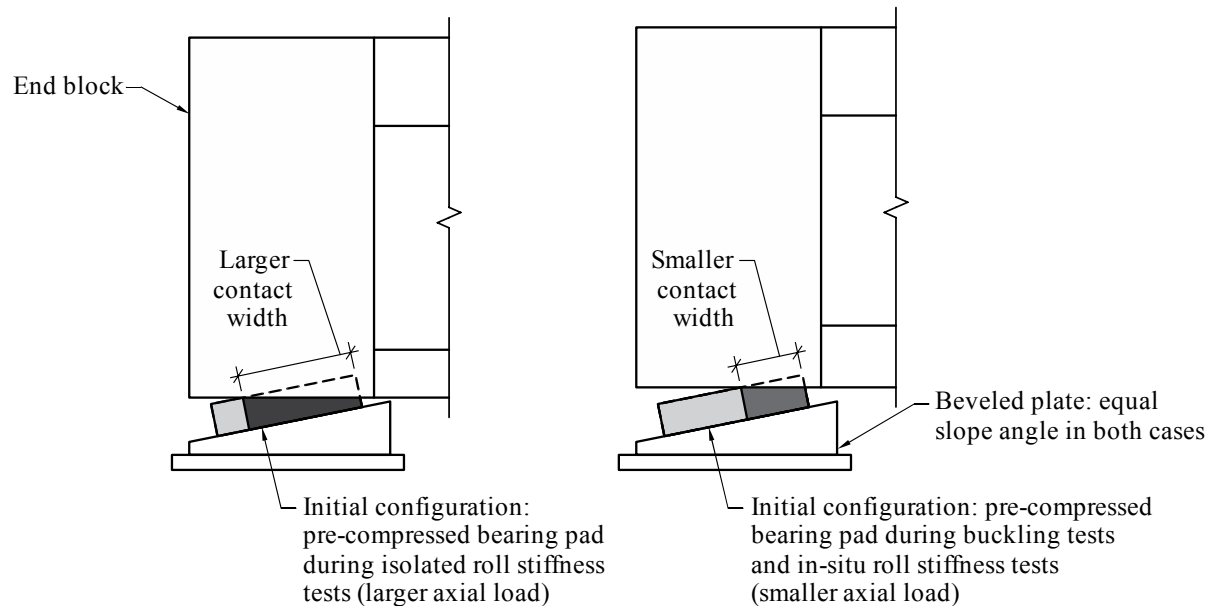
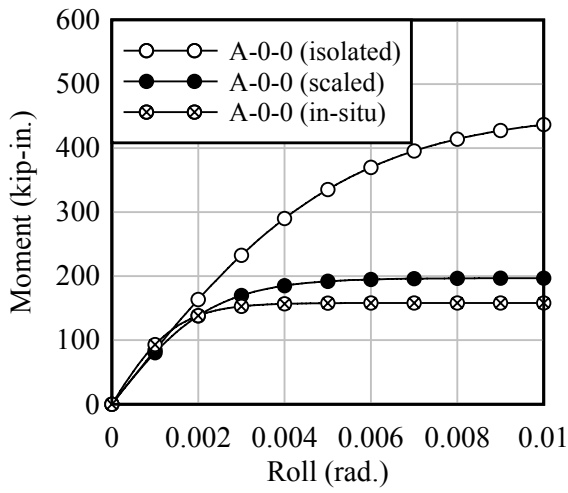
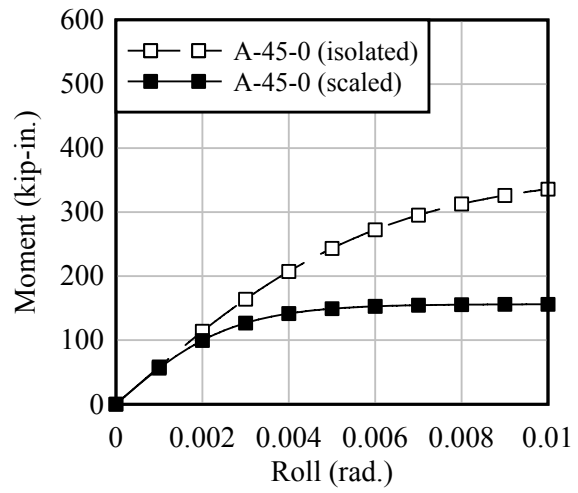


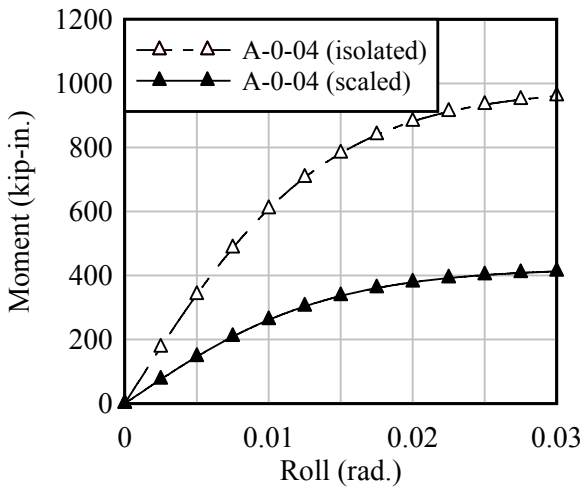
Figure 9-16. Bearing pad contact areas during both isolated roll stiffness tests and buckling tests



A



B



C

Figure 9-17. Moment-rotation curves, from isolated roll stiffness tests (scaled and original) and in-situ roll stiffness tests. A) A-0-0. B) A-45-0. C) A-0-04.

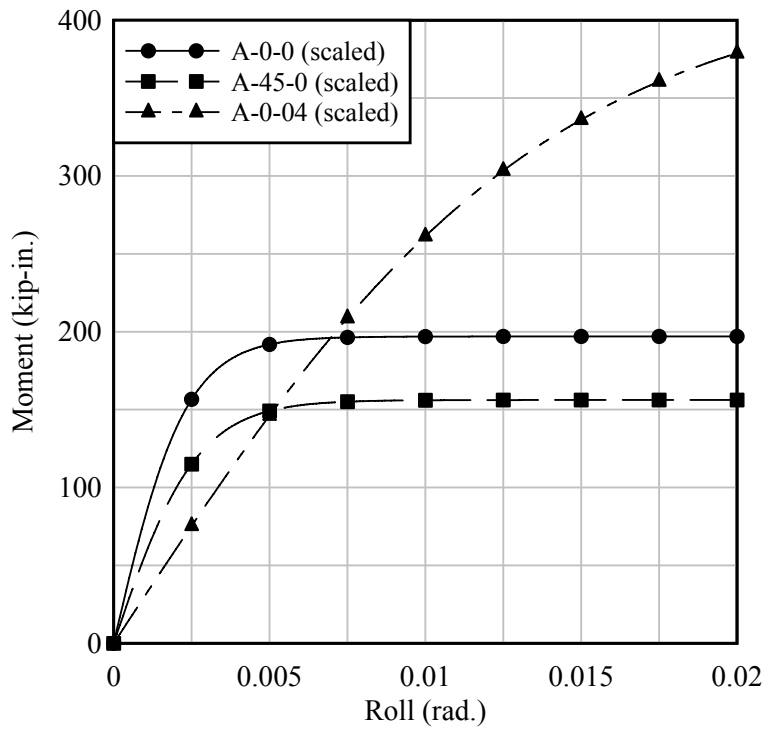


Figure 9-18. Moment-rotation curves, scaled from isolated bearing pad tests

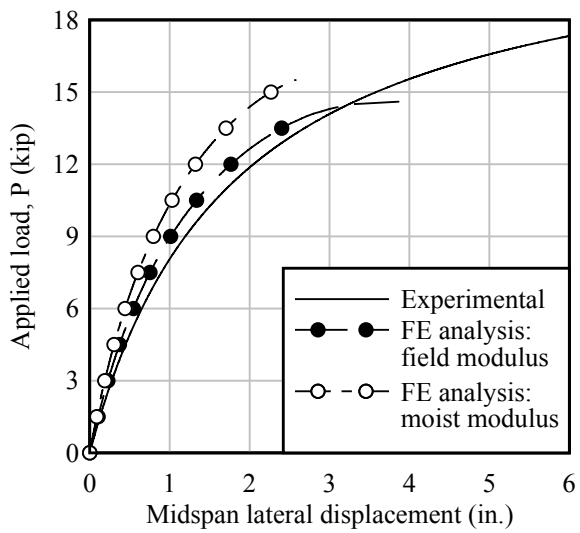


Figure 9-19. Comparison of experimental and FE buckling curves (configuration A-0-0)

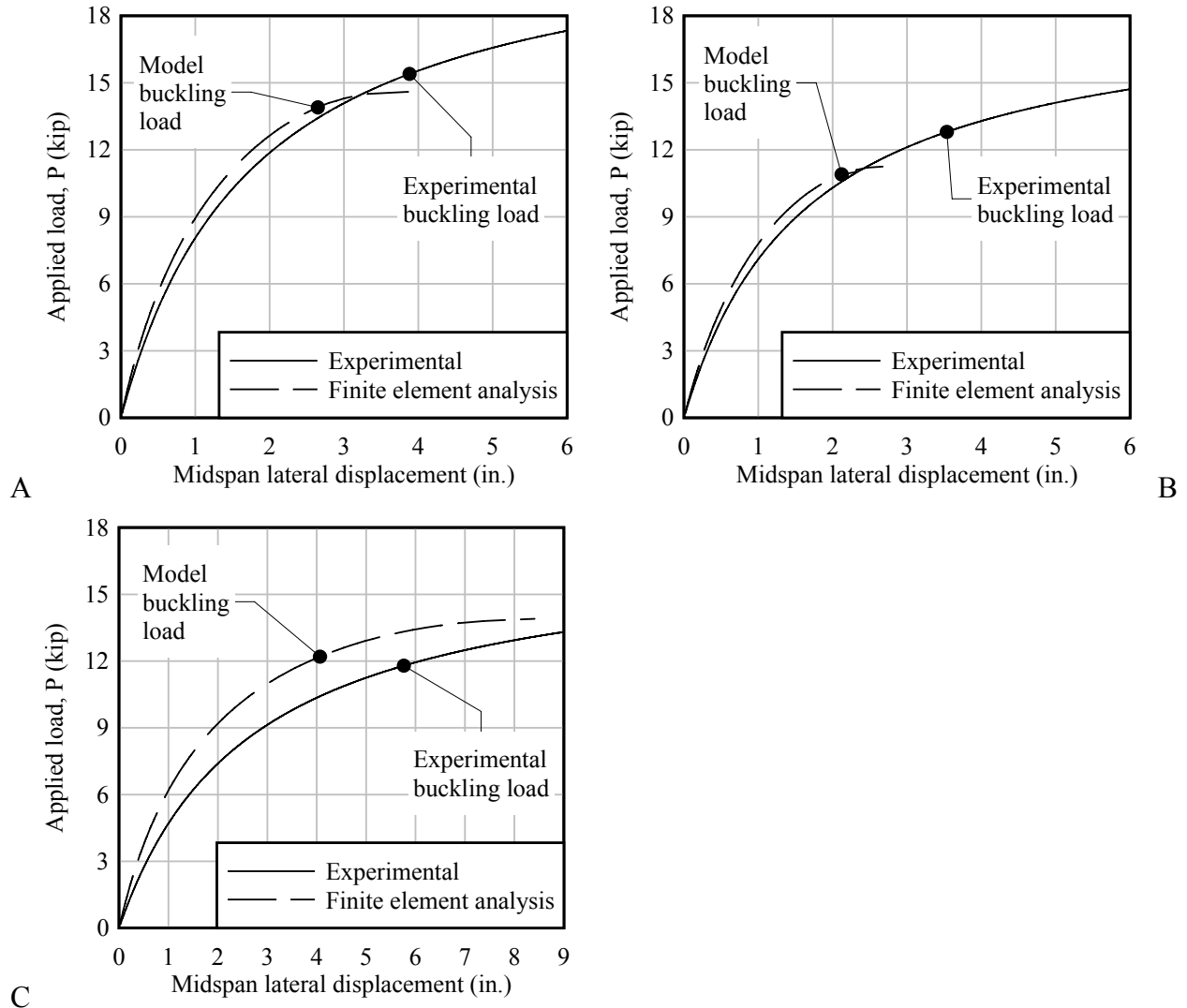


Figure 9-20. Buckling curves from experimental tests and finite element models. A) A-0-0. B) A-45-0. C) A-0-04.

CHAPTER 10 CONCLUSIONS

Roll stiffnesses of various types of standard bearing pads were quantified under the effects of skew angle, slope angle or a combination of skew and slope. A bearing pad test device was designed and fabricated to impose axial load, skew, and slope on bearing pads, and to enable measurement of roll rotation as a function of moment applied. Additionally, girder buckling capacities of a full scale test girder were quantified under the effects of skew angle, slope angle or a combination of skew and slope. The pads used to support each end of the test girder were the same pads previously tested to determine roll stiffness. Gravity load simulators were designed and fabricated to apply vertical load to the test girder without imposing artificial lateral restraint. In both types of testing (bearing pad and girder buckling), multiple test repetitions were performed under identical conditions, to ensure that reasonable repeatability of the data was achieved.

Based on the isolated roll stiffness test results, for all three pad types tested, substantial reductions in roll stiffness arose from the combined effects of skew and slope. Although not as severe as the combination of skew and slope, it was found that skew angle alone significantly reduced the roll stiffness of a bearing pad as well. Regarding the buckling tests, reductions in buckling capacities resulted from the imposition of skew or slope angle alone. A severe reduction was observed in the combination of skew and slope combined, with the most extreme case (A-45-04) causing the test girder to buckle under its own self-weight without any superimposed loads.

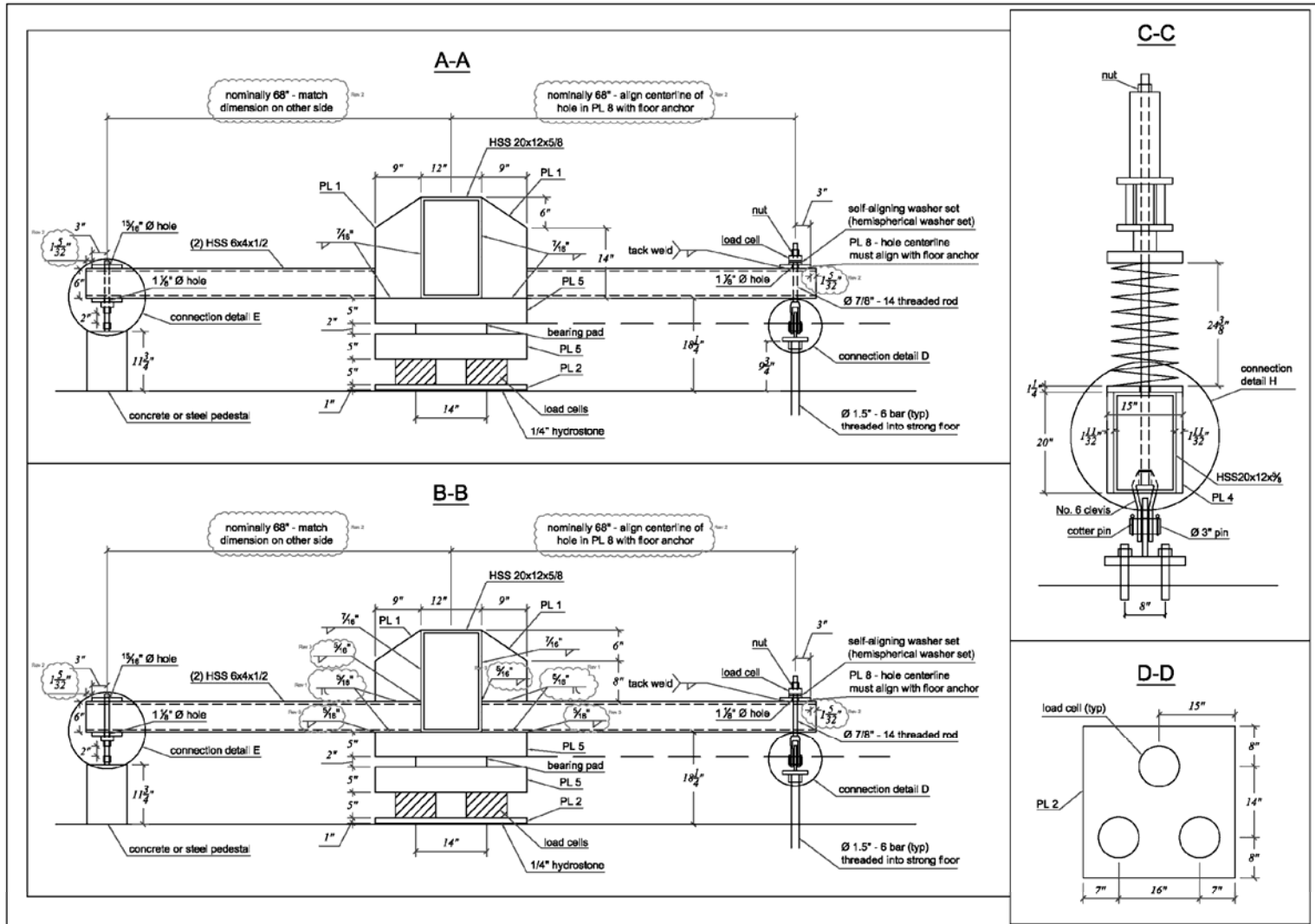
It is therefore recommended that consideration be given to requiring bearing pads to be oriented to match girder alignment (to eliminate skew angle), and also to provide beveled bearing plates such that the bottom of the plate of the unloaded girder is parallel to the beam seat.

These requirements would eliminate the adverse effects of skew and slope, both of which have been experimentally demonstrated to reduce bearing pad roll stiffness and girder buckling capacity.

Further analytical studies should be conducted to examine the effects of roll stiffness on Florida I-Beam (FIB) girders, with typical lengths. Such studies can be executed using the finite element buckling modeling techniques documented in this thesis. The buckling capacity determination rule—in which the buckling load is defined as the point at which the slope of the load-deflection curve drops to below 1/10th of its initial value—should continue to be used in future studies to determine girder buckling capacity.

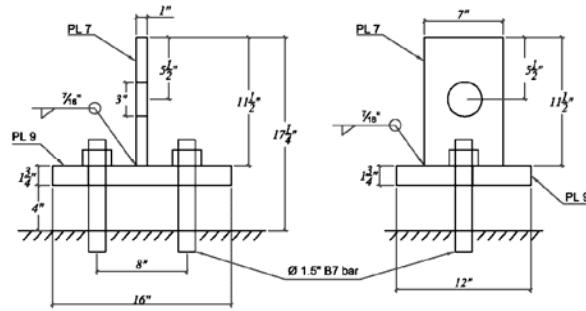
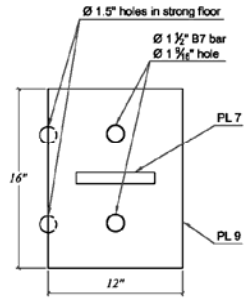
APPENDIX A
BEARING PAD TEST DEVICE FABRICATION PLANS

This appendix includes drawings for the fabrication of the bearing pad test device, used in the isolated roll stiffness tests.

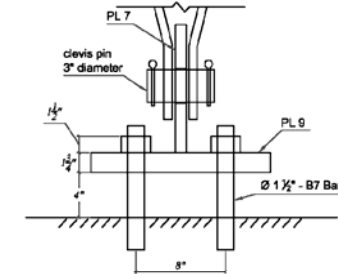


| REVISIONS | | Experimental Validation of Bracing Recommendations for Long-Span Concrete Girders | | |
|------------------------|------------------------|---|-------------------------|--------------|
| Revision 1: 2009-07-29 | Revision 3: 2009-08-06 | University of Florida | Bearing Pad Test Device | Sheet 2 of 5 |
| Revision 2: 2009-08-03 | | | | |

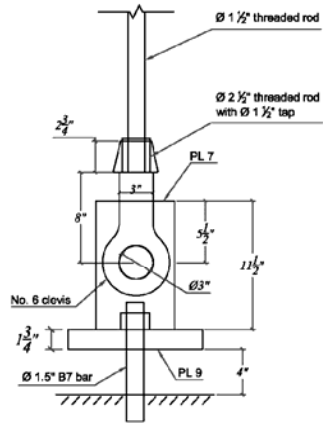
Connection Detail A



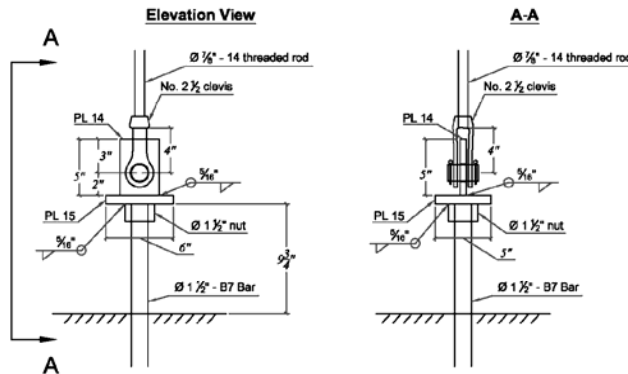
Connection Detail C



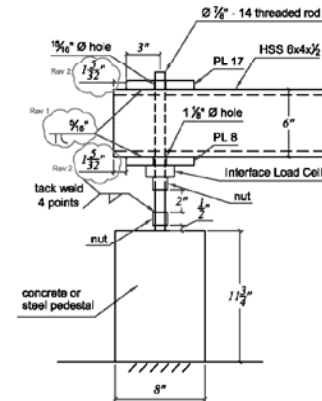
Connection Detail B



Connection Detail D



Connection Detail E



REVISIONS

| | |
|------------------------|------------------------|
| Revision 1: 2009-07-29 | Revision 3: 2009-08-06 |
| Revision 2: 2009-08-03 | |

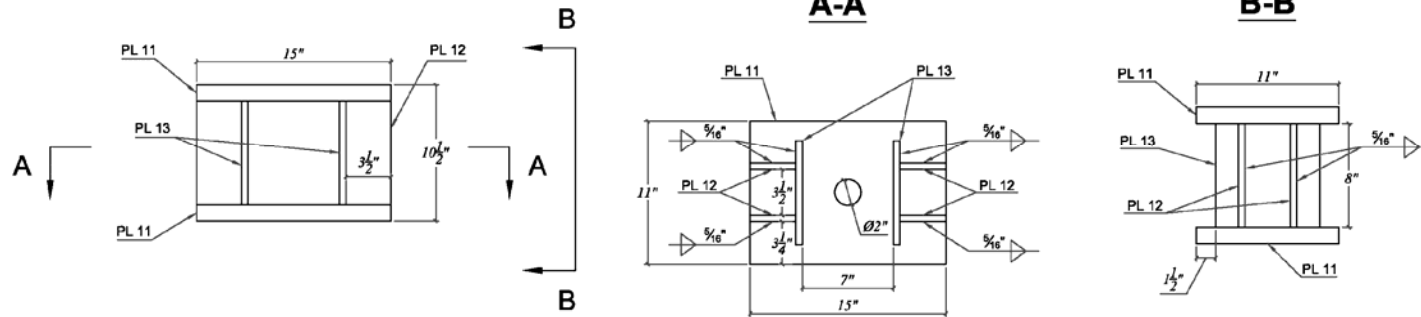
Experimental Validation of Bracing Recommendations for Long-Span Concrete Girders

University of Florida

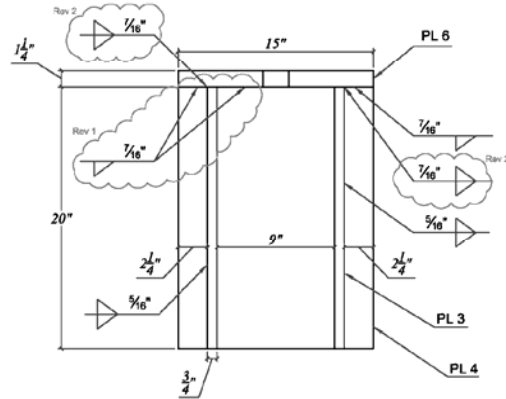
Bearing Pad Test Device

Sheet 3 of 5

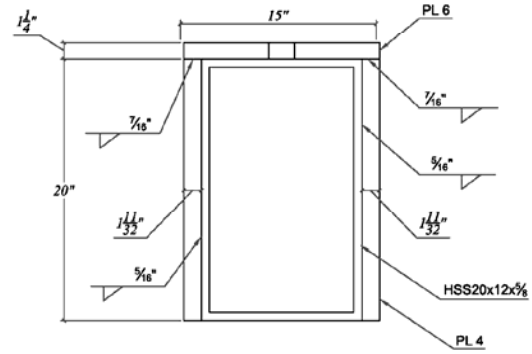
Connection Detail F - JACKING CHAIR



Connection Detail G



Connection Detail H



REVISIONS

| | |
|------------------------|------------------------|
| Revision 1: 2009-07-29 | Revision 3: 2009-08-06 |
| Revision 2: 2009-08-03 | |

Experimental Validation of Bracing Recommendations for Long-Span Concrete Girders

University of Florida

Bearing Pad Test Device

Sheet 4 of 5

PLATE LIST

| | | | | | | |
|------------------------------------|------------------------------------|------------------------------------|------------------------------------|------------------------------------|------------------------------------|------------------------------------|
| <p><u>1</u></p> <p>(4) 36 ksi</p> | <p><u>2</u></p> <p>(1) 36 ksi</p> | <p><u>3</u></p> <p>(4) 36 ksi</p> | <p><u>4</u></p> <p>(2) 36 ksi</p> | <p><u>5</u></p> <p>(2) 36 ksi</p> | | |
| <p><u>6</u></p> <p>(2) 36 ksi</p> | <p><u>7</u></p> <p>(2) 50 ksi</p> | <p><u>8</u></p> <p>(2) 36 ksi</p> | <p><u>9</u></p> <p>(2) 36 ksi</p> | <p><u>10</u></p> <p>(1) 36 ksi</p> | | |
| <p><u>11</u></p> <p>(2) 36 ksi</p> | <p><u>12</u></p> <p>(4) 36 ksi</p> | <p><u>13</u></p> <p>(2) 36 ksi</p> | <p><u>14</u></p> <p>(1) 36 ksi</p> | <p><u>15</u></p> <p>(1) 36 ksi</p> | <p><u>16</u></p> <p>(1) 36 ksi</p> | <p><u>17</u></p> <p>(1) 36 ksi</p> |

| | | | | |
|-------------------------------|-------------------------------|--|---------------------|--|
| <i>REVISIONS</i> | | <i>Experimental Validation of Bracing Recommendations for Long-Span Concrete Girders</i> | | |
| <i>Revision 1: 2009-07-29</i> | <i>Revision 3: 2009-08-06</i> | <i>University of Florida</i> | | |
| <i>Revision 2: 2009-08-03</i> | | <i>Bearing Pad Test Device</i> | <i>Sheet 5 of 5</i> | |

APPENDIX B
FULL SCALE TEST GIRDER FABRICATION PLANS

This appendix includes drawings for the fabrication of the test girder, used in the full scale buckling tests.

General Notes:

Materials

Concrete shall be FDOT class V, mix design number 05-1364
 f'_c (28 day) = 6,500 psi
 f_{ci} (release) = 4,000 ksi

REV 2

The same concrete batch(s) shall be used for all three (3) specimens.

Mild reinforcement shall be ASTM A615 grade 60 (fy 60 ksi).

Prestressing strand shall be ASTM A416 270 ksi Lo-Lax.

Fabricator shall provide data sheets from concrete, strand, and rebar suppliers.

Fabricator shall provide report of strand stressing.

Fabricator shall provide material samples to UF/FDOT as follows:

(8) 6" dia x 12" cylinders from each concrete batch: (4) cylinders cure with girder, (4) lab cure

(8) 36" pieces of prestressing strands free from sand, dust, etc.
 Samples taken directly off of reel

Schedule

Fabrication schedule to be determined.

REV 2

Contact Megan Salvetti at UF at least one (1) week prior to stress, casting, detensioning, and shipping: 561-866-2531 or meg8253@ufl.edu.

Other

Fabricator shall be responsible for fabrication of "precast segments". Fabricator will transport these three (3) segments from the fabrication facility to:
 FDOT Structures Research Center
 2007 East Paul Dirac Drive
 Tallahassee, FL 32310

Delivery time to be coordinated with FDOT.

Upon completion and delivery of "precast segments" by Fabricator, FDOT shall fabricate "closure pours (CP)" and "solid end blocks (EB)".

Unless otherwise noted, fabrication of girders shall follow typical procedures and practices for FDOT bridge girders.

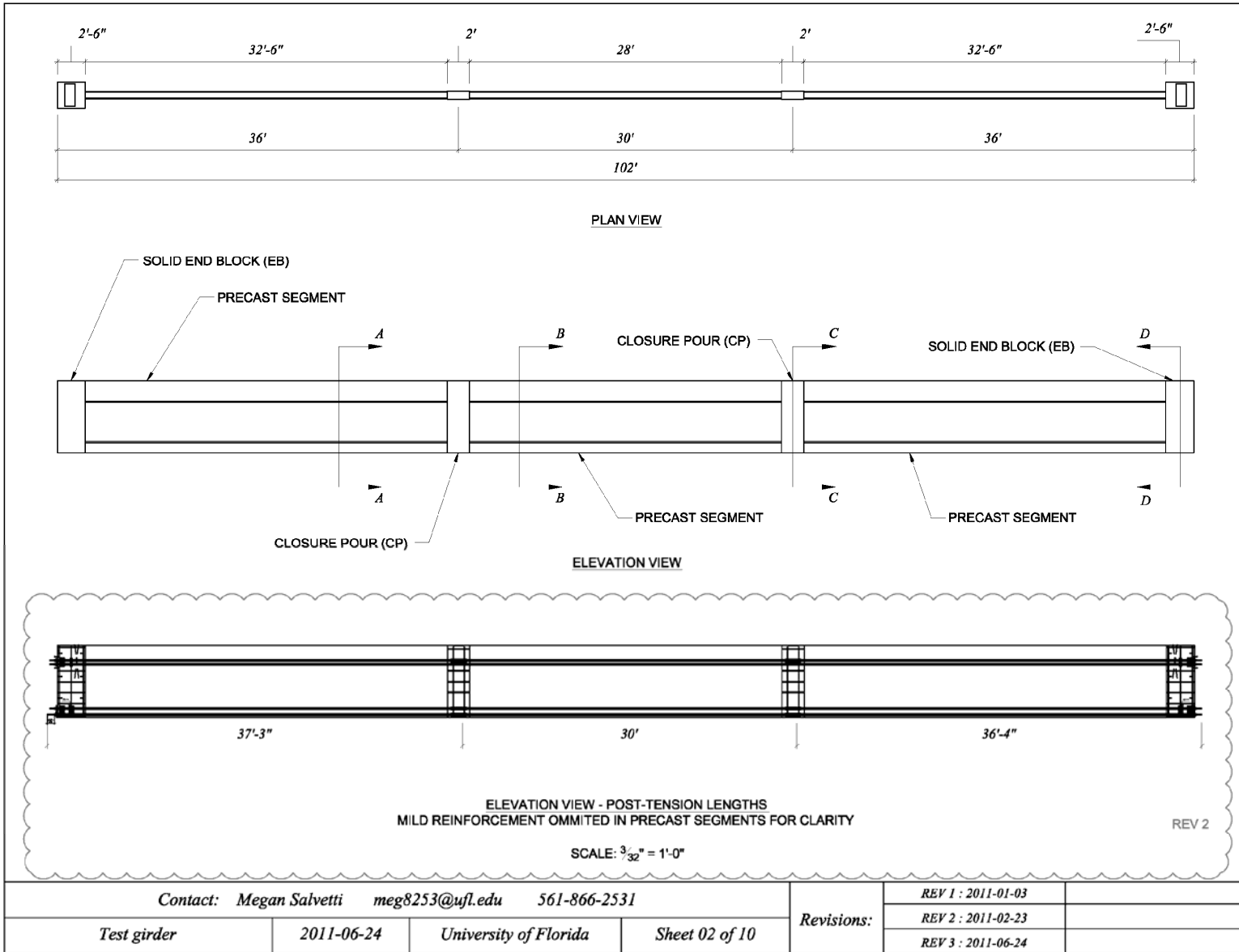
Cover beams with heavy tarp during curing.

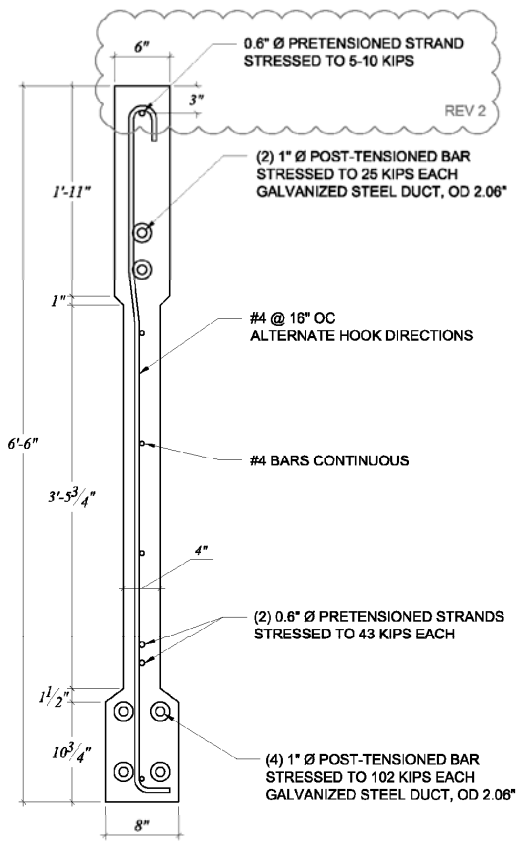
Inspections will be provided by on-site FDOT personnel and by UF.

No patch-work or finishing is required.

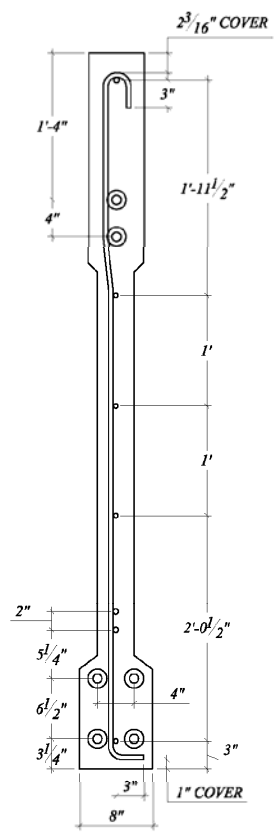
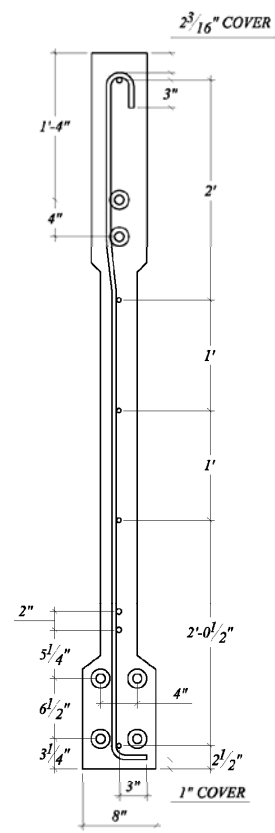
Production:
 Contact Megan Salvetti
 (561) 866-2531
 at least one (1) week prior to
 stressing, casting, detensioning,
 and shipping

| | | | | | | |
|--|-----------------------|----------------|--------------------|------------|--------------------|--|
| Contact: Megan Salvetti meg8253@ufl.edu 561-866-2531 | | | | Revisions: | REV 1 : 2011-01-03 | |
| General notes | | | | | REV 2 : 2011-02-23 | |
| 2011-06-24 | University of Florida | Sheet 01 of 10 | REV 3 : 2011-06-24 | | | |



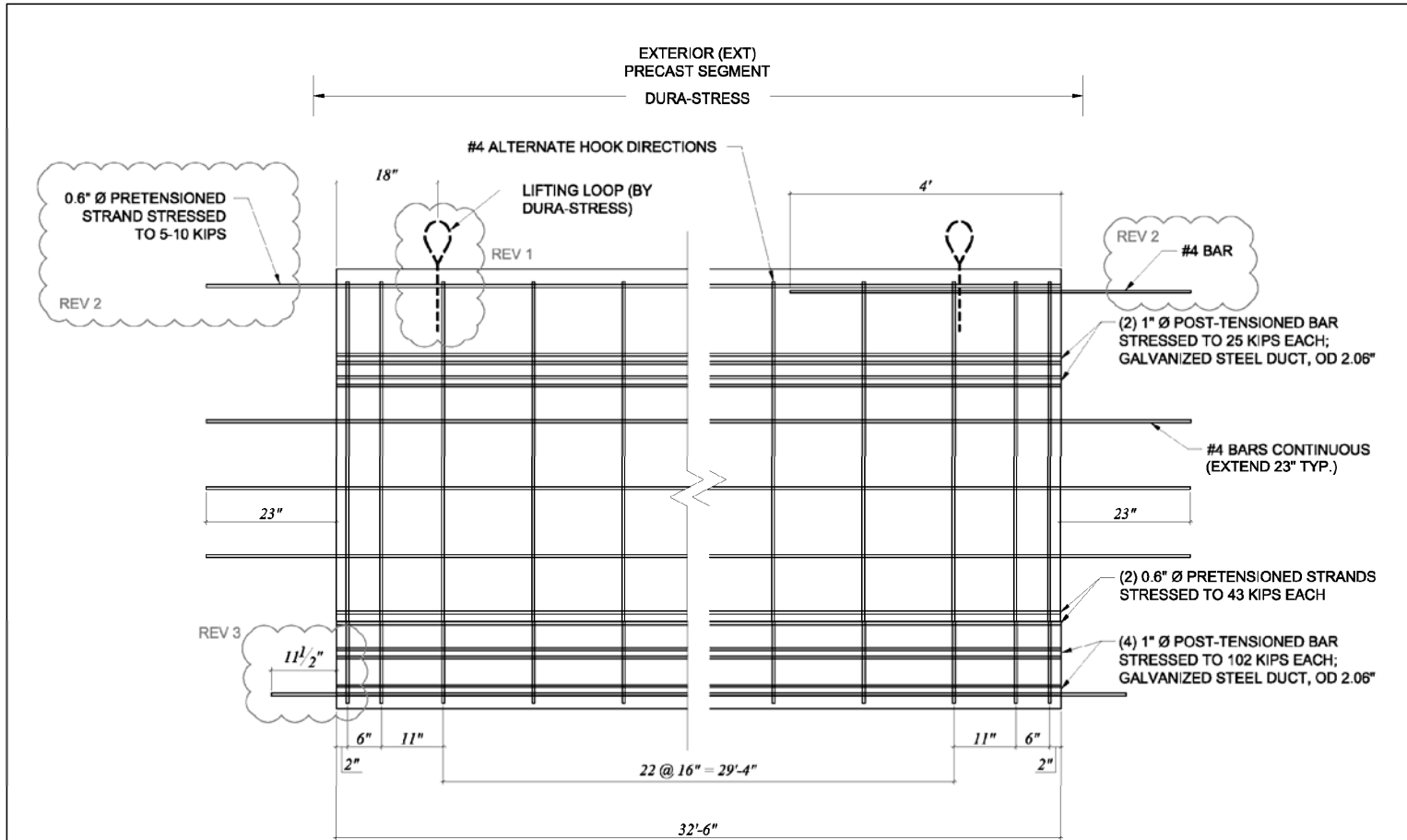


SECTION A-A DETAILS
EXTERIOR PRECAST SEGMENT
SCALE: 3/4"=1'-0"



SECTION B-B DETAILS
INTERIOR PRECAST SEGMENT
SCALE: 3/4"=1'-0"
REV 2

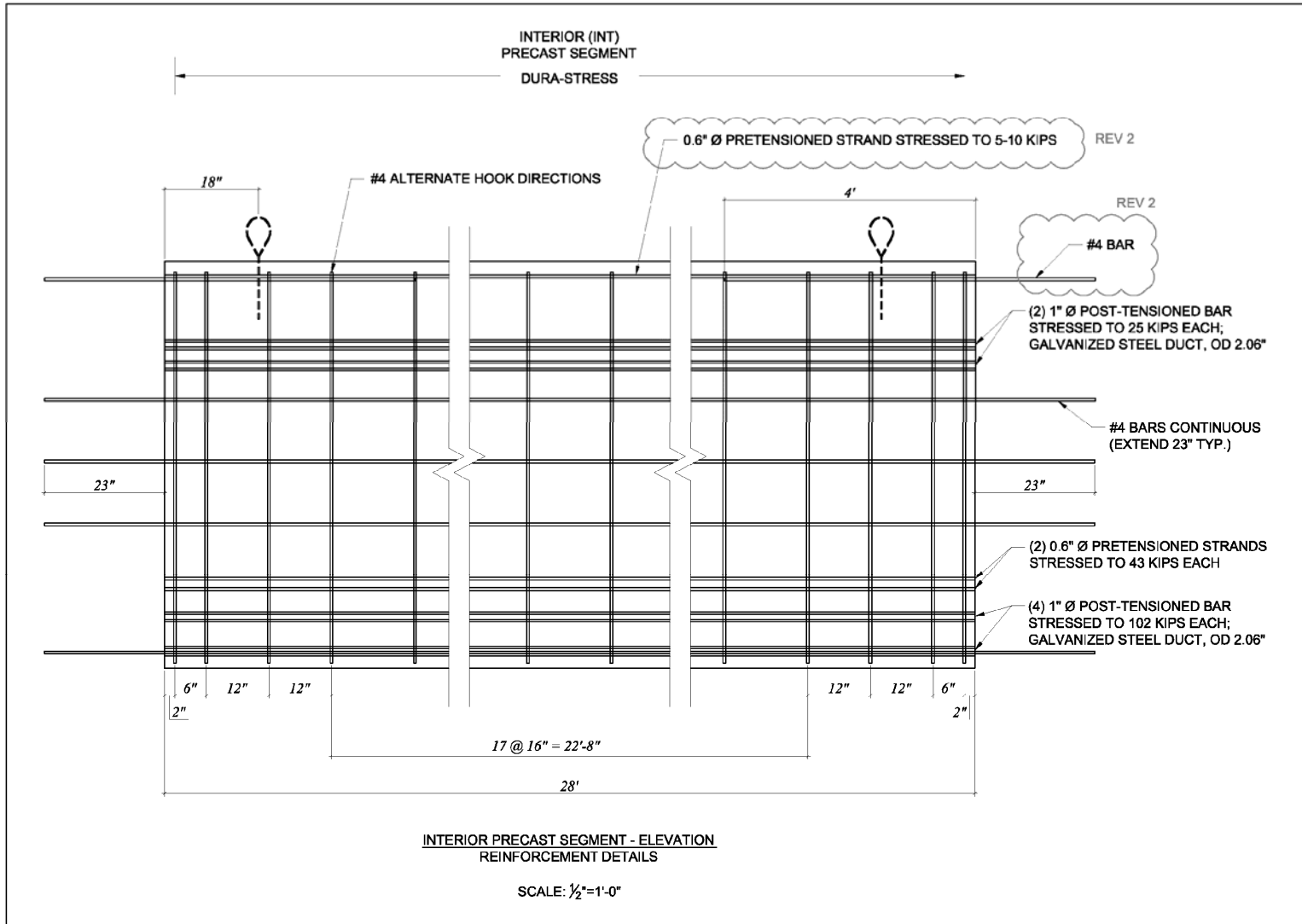
| | | | | | | |
|--|------------|-----------------------|----------------|------------|--------------------|--|
| Contact: Megan Salvetti meg8253@ufl.edu 561-866-2531 | | | | Revisions: | REV 1 : 2011-01-03 | |
| Precast segment details | 2011-06-24 | University of Florida | Sheet 03 of 10 | | REV 2 : 2011-02-23 | |
| | | | | | REV 3 : 2011-06-24 | |



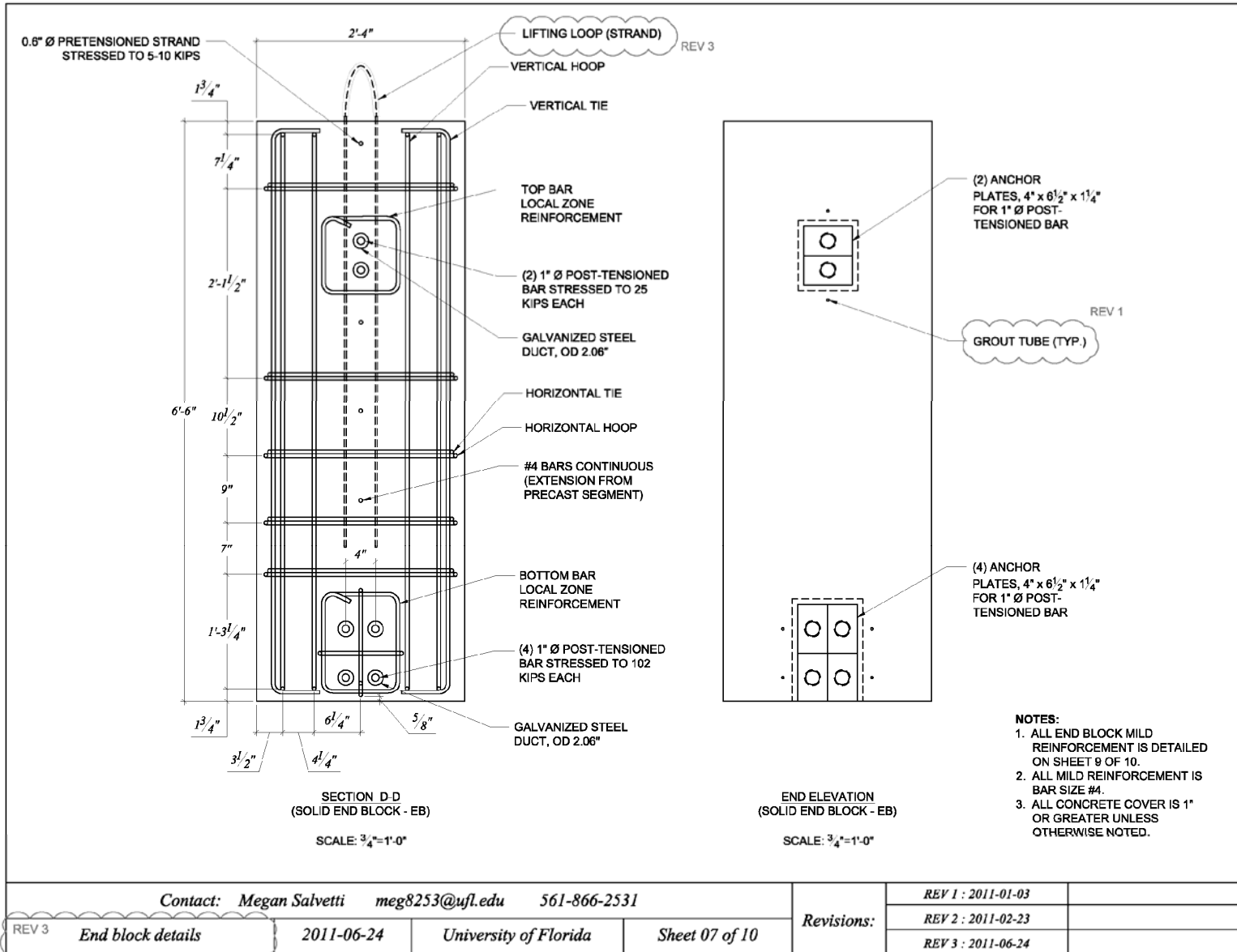
EXTERIOR PRECAST SEGMENT - ELEVATION
REINFORCEMENT DETAILS

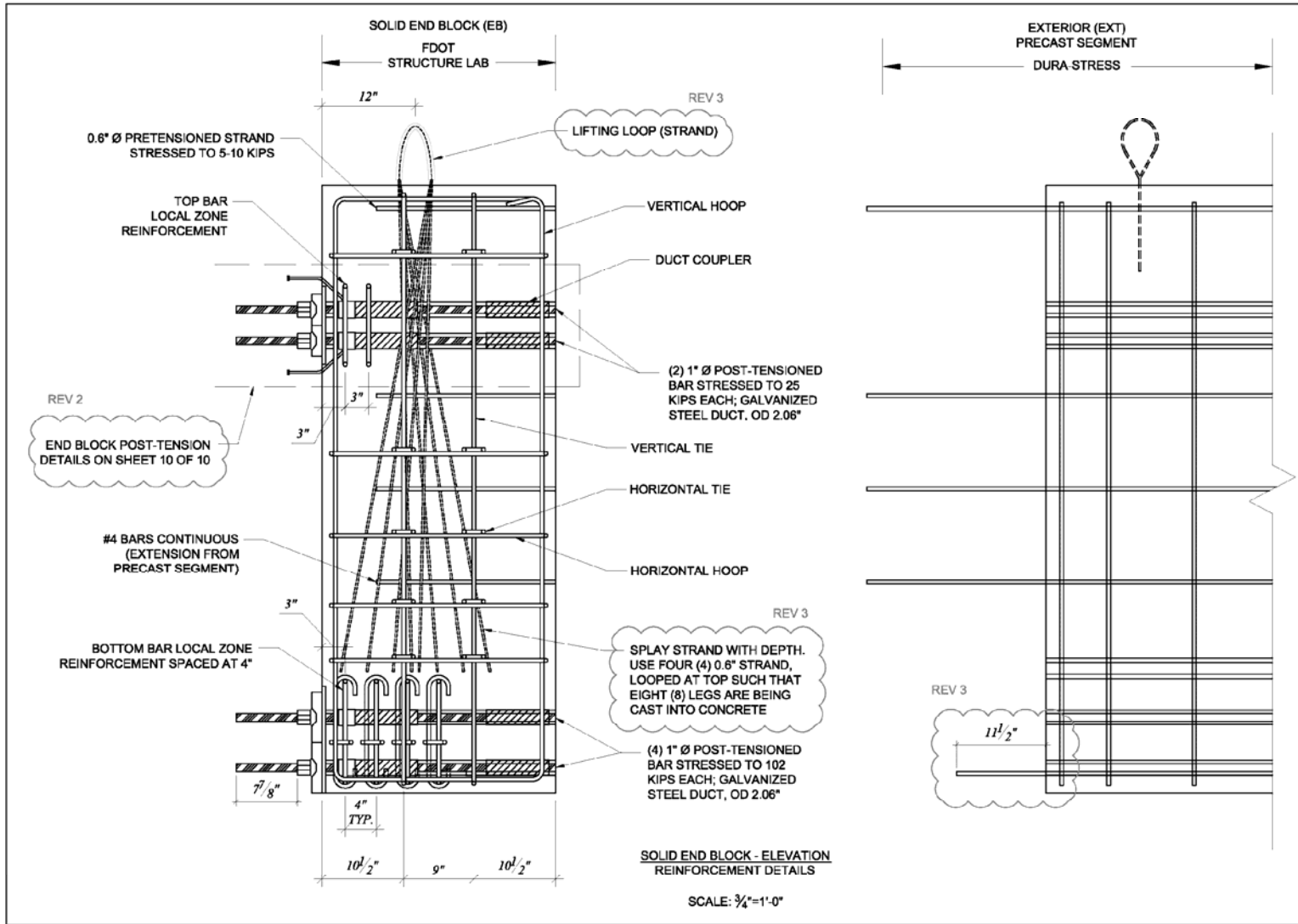
SCALE: 1/2"=1'-0"

| | | | | | | |
|--|-----------------------|----------------|--------------------|------------|--------------------|--|
| Contact: Megan Salvetti meg8253@ufl.edu 561-866-2531 | | | | Revisions: | REV 1 : 2011-01-03 | |
| Exterior precast segment details | | | | | REV 2 : 2011-02-23 | |
| 2011-06-24 | University of Florida | Sheet 04 of 10 | REV 3 : 2011-06-24 | | | |

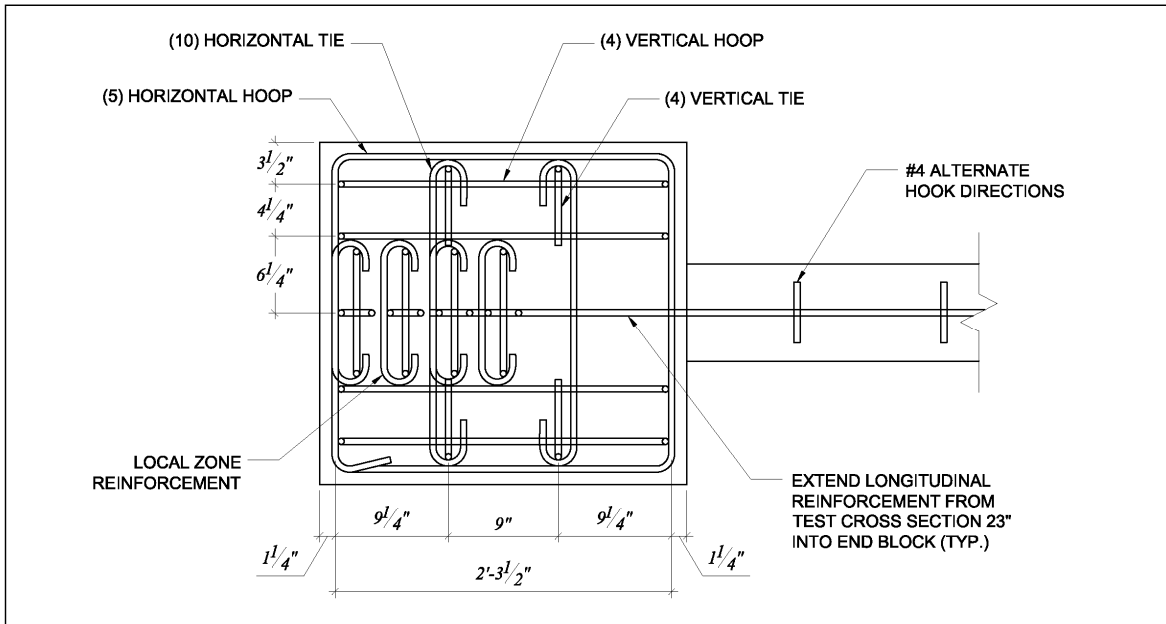


| | | | | | | |
|---|--|--|--|------------|--------------------|--|
| Contact: Megan Salvetti meg8253@ufl.edu 561-866-2531 | | | | Revisions: | REV 1 : 2011-01-03 | |
| Interior precast segment details 2011-06-24 University of Florida Sheet 05 of 10 | | | | | REV 2 : 2011-02-23 | |
| | | | | | REV 3 : 2011-06-24 | |



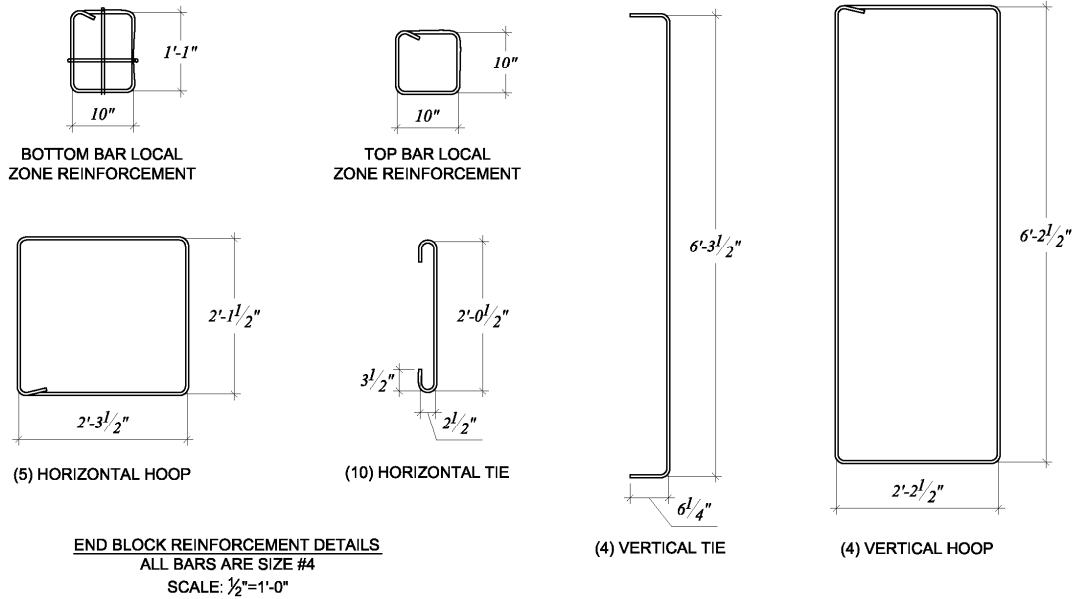


| | | | | | | | |
|--|-------------------|------------|-----------------------|------------|--------------------|--------------------|--------------------|
| Contact: Megan Salvetti meg8253@ufl.edu 561-866-2531 | | | | Revisions: | REV 1 : 2011-01-03 | | |
| REV 3 | End block details | 2011-06-24 | University of Florida | | Sheet 08 of 10 | REV 2 : 2011-02-23 | |
| | | | | | | | REV 3 : 2011-06-24 |



END BLOCK TO PRECAST SEGMENT CONNECTION - PLAN VIEW
 ALL BARS ARE SIZE #4. PRETENSIONED STRANDS AND POST-TENSIONED BARS NOT SHOWN FOR CLARITY.

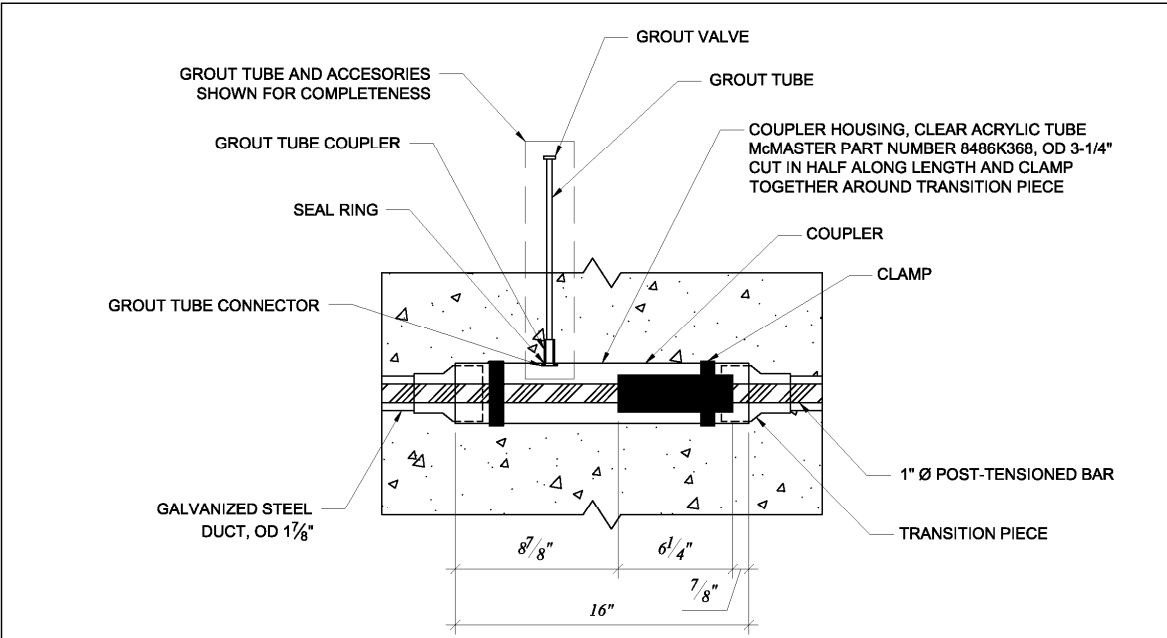
SCALE: 1"=1'-0"



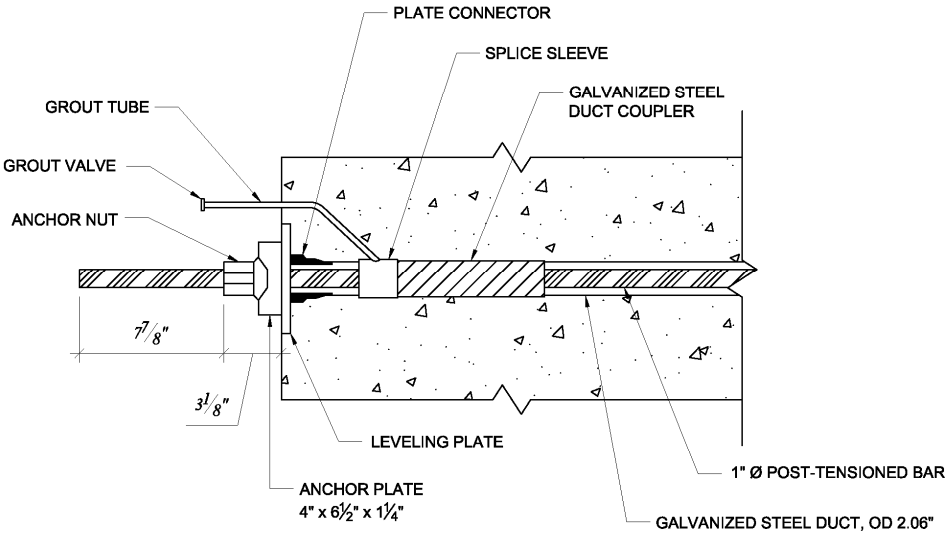
END BLOCK REINFORCEMENT DETAILS
 ALL BARS ARE SIZE #4
 SCALE: 1/2"=1'-0"

Contact: Megan Salvetti meg8253@ufl.edu 561-866-2531

| | | | | |
|------------|---------------------------------|--------------------|-----------------------|---------------|
| REV 3 | End block reinforcement details | 2011-06-22 | University of Florida | Sheet 9 of 10 |
| Revisions: | REV 1 : 2011-01-03 | REV 2 : 2011-02-23 | REV 3 : 2011-06-24 | |



CLOSURE POUR - POST-TENSION DETAILS
 MILD REINFORCEMENT NOT SHOWN FOR CLARITY
 SCALE: 1 1/2"=1'-0"



SOLID END BLOCK - POST-TENSION DETAILS
 MILD REINFORCEMENT NOT SHOWN FOR CLARITY
 SCALE: 1 1/2"=1'-0"

Contact: Megan Salvetti meg8253@ufl.edu 561-866-2531

| | | | |
|---------------------------------|--------------------|-----------------------|--------------------|
| Post-tension connection details | 2011-06-22 | University of Florida | Sheet 10 of 10 |
| Revisions: | REV 1 : 2011-01-03 | REV 2 : 2011-02-23 | REV 3 : 2011-06-24 |

APPENDIX C
COMPRESSIVE STRENGTH AND ELASTIC MODULUS TEST RESULTS

This appendix includes the compressive strength and elastic modulus test results, from cylinders cast from the test girder, used in the full scale buckling tests.

Table C-1. Compressive strength test results performed for each girder component

| Date poured | Batch | Curing | Date tested | Age (days) | Fracture type | Compressive strength (psi) |
|-------------|-----------------------------|--------------|------------------|------------|---------------|----------------------------|
| 5/18/2011 | Precast segment: Exterior A | moist | 28 day | 28 | - | 7540 |
| | | moist | 9/19/2011 | 124 | 1 | 8828 |
| | | moist | 12/8/2011 | 204 | 4 | 7564 |
| | | moist | 12/8/2011 | 204 | 1 | - |
| | | <i>field</i> | <i>12/8/2011</i> | <i>204</i> | <i>4</i> | <i>6368</i> |
| | | <i>field</i> | <i>12/8/2011</i> | <i>204</i> | <i>4</i> | <i>6131</i> |
| | | <i>field</i> | <i>12/8/2011</i> | <i>204</i> | <i>4</i> | <i>6514</i> |
| 5/19/2011 | Precast segment: Exterior B | moist | 28 day | 28 | - | 7720 |
| | | moist | 9/19/2011 | 123 | 1,2 | 9154 |
| | | moist | 12/8/2011 | 203 | 4 | 8160 |
| | | moist | 12/8/2011 | 203 | 1 | 8238 |
| | | <i>field</i> | <i>12/8/2011</i> | <i>203</i> | <i>4</i> | <i>5956</i> |
| | | <i>field</i> | <i>12/8/2011</i> | <i>203</i> | <i>4</i> | <i>5680</i> |
| | | <i>field</i> | <i>12/8/2011</i> | <i>203</i> | <i>1</i> | <i>5858</i> |
| 5/23/2011 | Precast segment: Interior | moist | 28 day | 28 | - | 8070 |
| | | moist | 9/19/2011 | 119 | 1,2 | 9004 |
| | | moist | 12/8/2011 | 199 | irregular | 6646 |
| | | moist | 12/8/2011 | 199 | 4 | 8088 |
| | | <i>field</i> | <i>12/8/2011</i> | <i>199</i> | <i>4</i> | <i>6348</i> |
| | | <i>field</i> | <i>12/8/2011</i> | <i>199</i> | <i>4</i> | <i>7855</i> |
| | | <i>field</i> | <i>12/8/2011</i> | <i>199</i> | <i>4</i> | <i>7223</i> |
| 8/26/2011 | South end block | moist | 9/13/2011 | 18 | 4 | 8812 |
| | | moist | 9/13/2011 | 18 | 4 | 8806 |
| | | moist | 12/8/2011 | 104 | 1 | 9060 |
| | | moist | 12/8/2011 | 104 | 1 | 9514 |
| | | moist | 12/8/2011 | 104 | 4 | 8783 |
| | | <i>field</i> | <i>12/8/2011</i> | <i>104</i> | <i>4</i> | <i>7693</i> |
| | | <i>field</i> | <i>12/8/2011</i> | <i>104</i> | <i>1</i> | <i>7335</i> |
| 8/30/2011 | North end block | moist | 9/13/2011 | 14 | 4 | 8346 |
| | | moist | 9/13/2011 | 14 | 4 | 8154 |
| | | moist | 12/8/2011 | 100 | 1 | 9490 |
| | | moist | 12/8/2011 | 100 | 1 | 8808 |
| | | moist | 12/8/2011 | 100 | 1 | 10016 |
| | | <i>field</i> | <i>12/8/2011</i> | <i>100</i> | <i>1</i> | <i>7082</i> |
| 8/30/2011 | Closure pours | moist | 9/13/2011 | 14 | 4 | 6124 |
| | | moist | 9/13/2011 | 14 | 4 | 6322 |
| | | moist | 12/8/2011 | 100 | 1 | 8292 |
| | | moist | 12/8/2011 | 100 | 4 | 7366 |
| | | moist | 12/8/2011 | 100 | irregular | 7090 |
| | | <i>field</i> | <i>12/8/2011</i> | <i>100</i> | <i>4</i> | <i>5264</i> |

Table C-2. Elastic modulus test results performed for each girder component

| Date poured | Batch | Curing | Date tested | Age (days) | Poisson's ratio | Modulus of Elasticity (ksi) |
|-------------|-----------------------------|--------------|-------------|------------|-----------------|-----------------------------|
| 5/18/2011 | Precast segment: Exterior A | moist | 12/9/2011 | 205 | 0.34 | 5450 |
| | | moist | 12/9/2011 | 205 | 0.31 | 5000 |
| | | moist | 12/9/2011 | 205 | 0.23 | 5000 |
| | | <i>field</i> | 12/9/2011 | 205 | 0.27 | 4550 |
| | | <i>field</i> | 12/9/2011 | 205 | 0.28 | 4750 |
| | | <i>field</i> | 12/9/2011 | 205 | 0.27 | 4550 |
| 5/19/2011 | Precast segment: Exterior B | moist | 12/9/2011 | 205 | 0.32 | 5600 |
| | | moist | 12/9/2011 | 205 | 0.2 | 5000 |
| | | moist | 12/9/2011 | 205 | 0.3 | 5000 |
| | | <i>field</i> | 12/9/2011 | 205 | 0.31 | 4650 |
| | | <i>field</i> | 12/9/2011 | 205 | 0.31 | 4950 |
| | | <i>field</i> | 12/9/2011 | 205 | 0.29 | 4700 |
| 5/23/2011 | Precast segment: Interior | moist | 12/12/2011 | 208 | 0.27 | 5000 |
| | | moist | 12/12/2011 | 208 | 0.27 | 5050 |
| | | moist | 12/12/2011 | 208 | 0.27 | 5150 |
| | | <i>field</i> | 12/9/2011 | 205 | 0.32 | 5050 |
| | | <i>field</i> | 12/9/2011 | 205 | 0.28 | 5000 |
| | | <i>field</i> | 12/9/2011 | 205 | 0.27 | 4750 |
| 8/26/2011 | South end block | moist | 12/12/2011 | 208 | 0.27 | 5500 |
| | | moist | 12/12/2011 | 208 | 0.27 | 5250 |
| | | moist | 12/12/2011 | 208 | 0.28 | 5400 |
| | | <i>field</i> | 12/9/2011 | 205 | 0.25 | 4600 |
| | | <i>field</i> | 12/9/2011 | 205 | 0.25 | 4950 |
| | | <i>field</i> | 12/9/2011 | 205 | 0.27 | 5000 |
| 8/30/2011 | North end block | moist | 12/12/2011 | 208 | 0.27 | 5000 |
| | | moist | 12/12/2011 | 208 | 0.31 | 5050 |
| | | moist | 12/12/2011 | 208 | 0.26 | 5000 |
| | | <i>field</i> | 12/9/2011 | 205 | 0.27 | 4300 |
| | | <i>field</i> | 12/9/2011 | 205 | 0.26 | 4250 |
| | | <i>field</i> | 12/9/2011 | 205 | 0.26 | 4150 |
| 8/30/2011 | Closure pours | moist | 12/12/2011 | 208 | 0.25 | 4600 |
| | | moist | 12/12/2011 | 208 | 0.28 | 5050 |
| | | moist | 12/12/2011 | 208 | 0.31 | 4600 |
| | | <i>field</i> | 12/9/2011 | 205 | 0.27 | 3700 |
| | | <i>field</i> | 12/9/2011 | 205 | 0.26 | 3700 |
| | | <i>field</i> | 12/9/2011 | 205 | 0.25 | 3500 |

APPENDIX D
DYWIDAG JACK CALIBRATION FORM

This appendix includes the DYWIDAG jack calibration form, used to determine the prestress levels in the post-tensioned bars, in the full scale buckling tests.



JACK CALIBRATION FORM

CALIBRATION ID
9931

JACK TYPE: 60Mp SERIES 04
JACK ID: A56

THEO. RAM AREA: 20.50
COMPUTED RAM AREA: 20.82

DATE: 9/2/2011

PRESSURE GAUGES:
MASTER GAUGE: 475

MASTER GAUGE CALIBRATION STANDARD: ANSI 45.2
SERVICE GAUGE CALIBRATION STANDARD: ANSI 40.1

SERVICE GAUGE(S): GAUGE 1: 6-10218 GAUGE 2: GAUGE3: GAUGE 4:

LOADCELL:
TYPE: Slope Indicator I.D. NO. 10158
METER NUMBER: 1280
METER MFG: Slope Indicator

CALIBRATION STANDARD: ASTM E4 AND E74

CONVERSION EQUATION: $AVG. X \cdot 1 + 0$

Temperature: 87 Humidity: 74%

Calibration Location: DYWIDAG SYSTEMS INTERNATIONAL, INC.

Calibrated By: Gary Smith

Calibration Firm: DYWIDAG SYSTEMS INTERNATIONAL, INC.

Verified By: Greg Wilkinson

Verification Firm: DYWIDAG SYSTEMS INTERNATIONAL, INC.

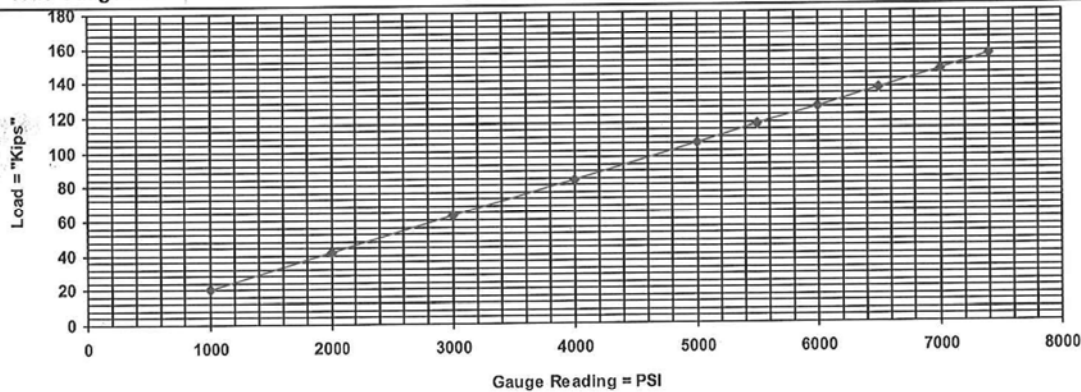
Customer: University of Florida

Job Number: J081583

| MASTER | GAUGE 1 | GAUGE 2 | GAUGE 3 | GAUGE 4 | RUN 1 | RUN 2 | RUN 3 | AVG | ACT KIPS |
|--------|---------|---------|---------|---------|--------|--------|--------|---------|----------|
| 1000 | 1000 | 0 | 0 | 0 | 20.61 | 20.45 | 20.73 | 20.597 | 20.597 |
| 2000 | 2000 | 0 | 0 | 0 | 41.81 | 41.39 | 41.35 | 41.517 | 41.517 |
| 3000 | 3000 | 0 | 0 | 0 | 62.77 | 62.15 | 62.36 | 62.427 | 62.427 |
| 4000 | 4000 | 0 | 0 | 0 | 83.36 | 82.86 | 83.05 | 83.090 | 83.090 |
| 5000 | 5000 | 0 | 0 | 0 | 104.29 | 103.73 | 103.82 | 103.947 | 103.947 |
| 5500 | 5500 | 0 | 0 | 0 | 114.89 | 113.91 | 114.25 | 114.350 | 114.350 |
| 6000 | 6000 | 0 | 0 | 0 | 125.28 | 124.37 | 124.74 | 124.797 | 124.797 |
| 6500 | 6500 | 0 | 0 | 0 | 135.61 | 134.92 | 135.06 | 135.197 | 135.197 |
| 7000 | 7000 | 0 | 0 | 0 | 146.33 | 145.24 | 145.57 | 145.713 | 145.713 |
| 7400 | 7400 | 0 | 0 | 0 | 154.48 | 153.71 | 153.93 | 154.040 | 154.040 |

For Monostrand Use Only Please Refer To; Use Gauge PS

True Gauge PSI: N/A N/A = 80% of U.T.S Use Gauge PSI: N/A



Dywidag Systems International USA Inc.



GAUGE CALIBRATION FORM

GAUGE TYPE: 6" 10000 PSI GAUGE

CAL ID: 11086

GAUGE I.D.#: 6-10218

DATE: 9/2/2011

Special Note:

TEMP: 87

| MASTER | TEST RUN 1 | TEST RUN 2 | TEST RUN 3 | AVG.READING |
|--------|------------|------------|------------|-------------|
| 0 | 0 | 0 | 0 | 0 |
| 1000 | 1000 | 1000 | 1000 | 1000 |
| 2000 | 2000 | 2000 | 2000 | 2000 |
| 3000 | 3000 | 3000 | 3000 | 3000 |
| 4000 | 4000 | 4000 | 4000 | 4000 |
| 5000 | 5000 | 5000 | 5000 | 5000 |
| 6000 | 6000 | 6000 | 6000 | 6000 |
| 7000 | 7000 | 7000 | 7000 | 7000 |
| 8000 | 8000 | 8000 | 8000 | 8000 |
| 9000 | 9000 | 9000 | 9000 | 9000 |

CALIBRATED BY: Gary, Smith

CUSTOMER: University of Florida

JOB NUMBER: J081583

MASTER INSTRUMENT ID No.: 91550

TRACE # 9912-EQ

DESCRIPTION : DEADWEIGHT TESTER

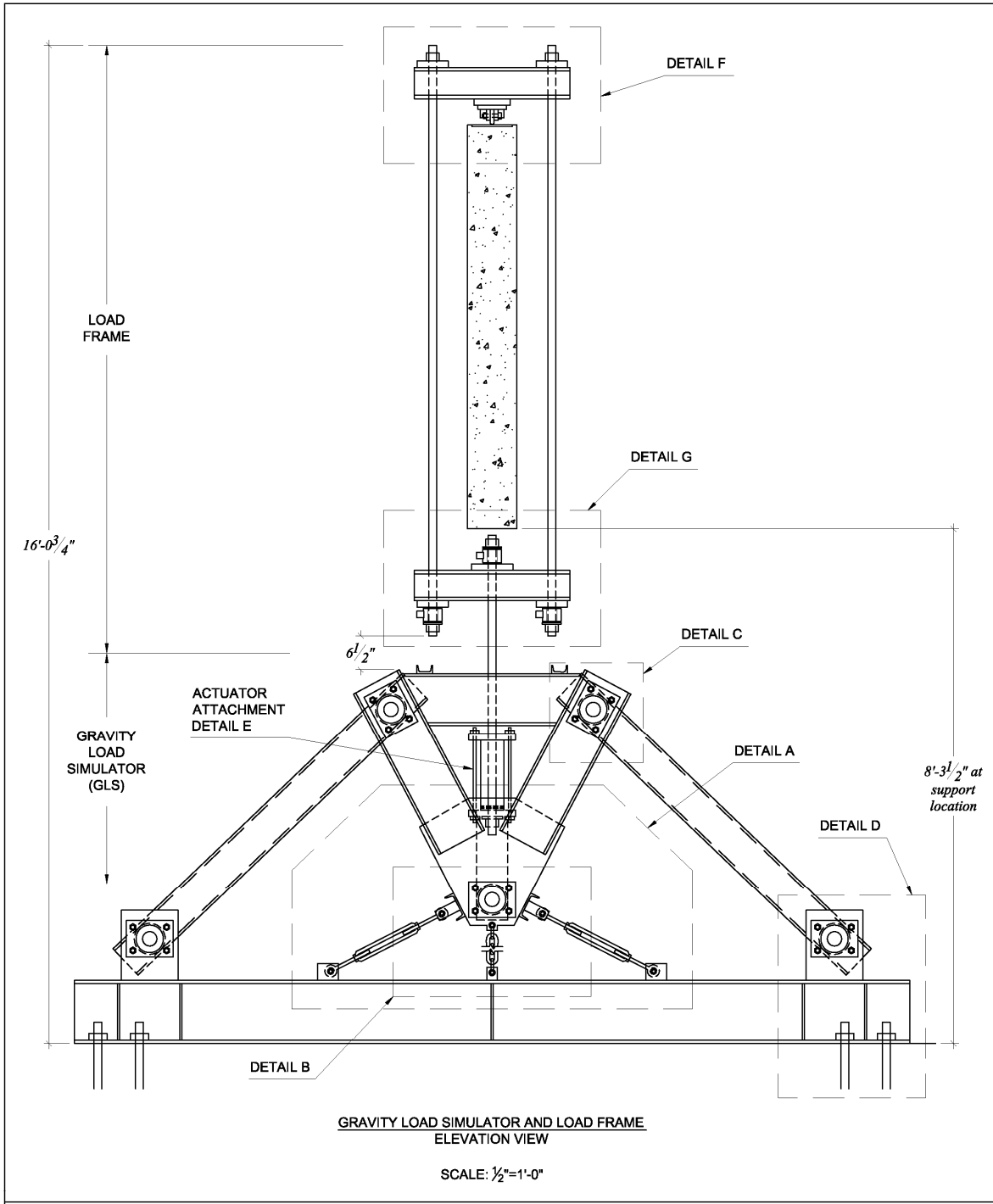
ALTHOUGH RAM/GAUGE COMBINATIONS ARE CALIBRATED AS A UNIT, GAUGES ARE CALIBRATED INDEPENDENTLY, AND ARE USABLE ON OTHER DYWIDAG SYSTEM RAMS, WHEN THIS DOES NOT CONFLICT WITH PROJECT SPECIFICATIONS.

INSTRUCTIONS:

1. Each gauge must be calibrated to a master instrument that has been calibrated and traceable to NIST Standards.
2. Each gauge must be calibrated to meet or exceed ASME STD. 40.1.
3. Each gauge will be calibrated before being used in a jack calibration.
4. Each gauge will be calibrated before being sent to the customer as a replacement gauge.
5. Connect the gauge to the testing machine.
6. Pressurize the gauge in 10 increments throughout it's entire range, 3 times.
7. Record the gauge and test standard readings.
8. If gauge is in need of adjustment, consult the manufacturers product manual contained in the DSI equipment calibration and standards book.
9. Form is to be used by Equipment Dept. staff in the calibration of hydraulic gauges that will be used by the customer.
10. Form is to be completely filled out.
11. Form is to be filled in the gauge calibration file according to it's I.D. No. and with any associated equipment file. One Copy to customer.

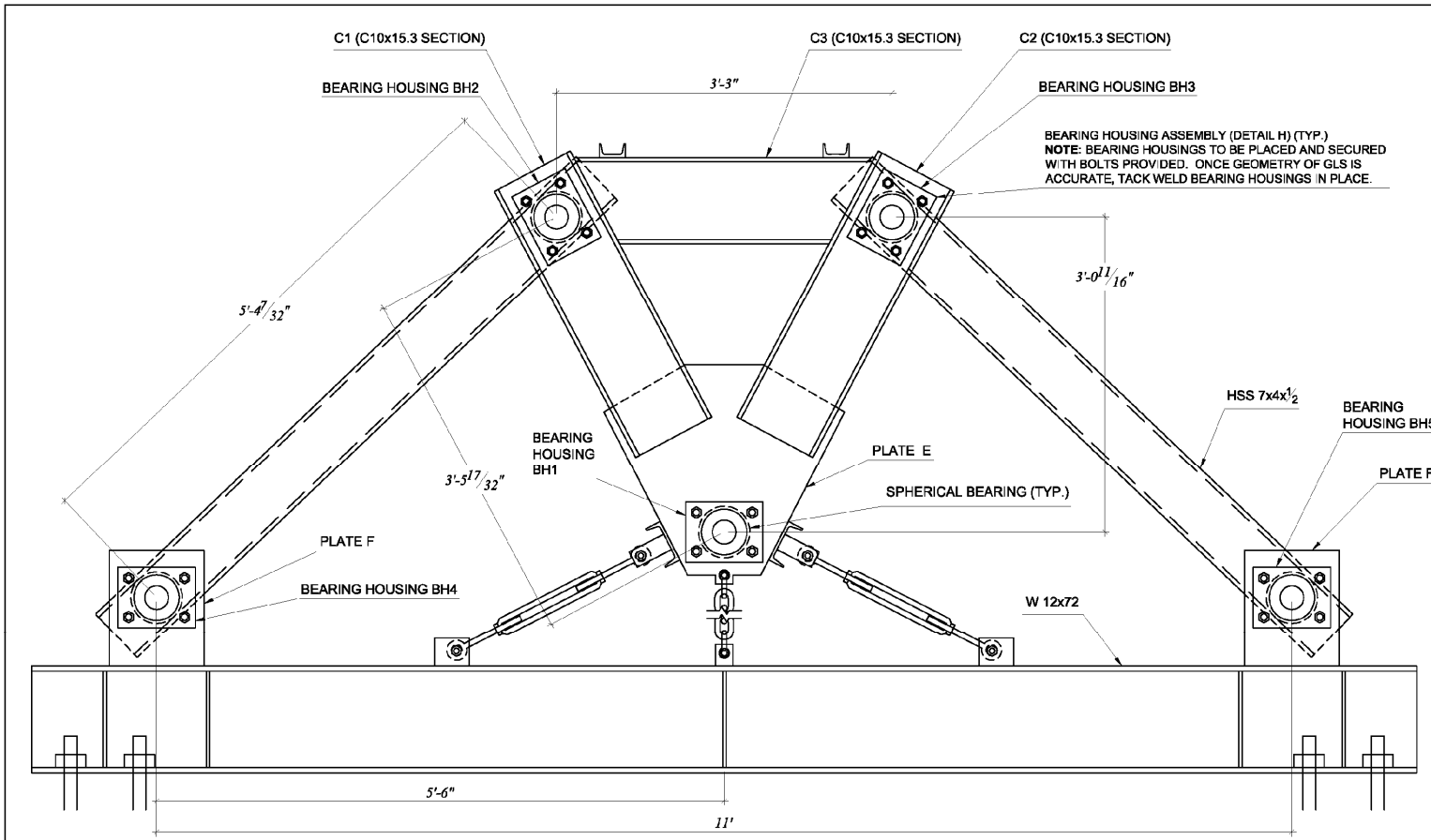
APPENDIX E
GRAVITY LOAD SIMULATOR FABRICATION PLANS

This appendix includes drawings for the fabrication of the gravity load simulators, used in the full scale buckling tests.



Experimental Validation of Bracing Recommendations for Long-Span Concrete Girders

| | | | |
|---------------------------------------|-------------------|------------------------------|-----------------------|
| <i>Overview of GLS and load frame</i> | <i>2011-06-24</i> | <i>University of Florida</i> | <i>Sheet 01 of 16</i> |
| Revisions: | | | |

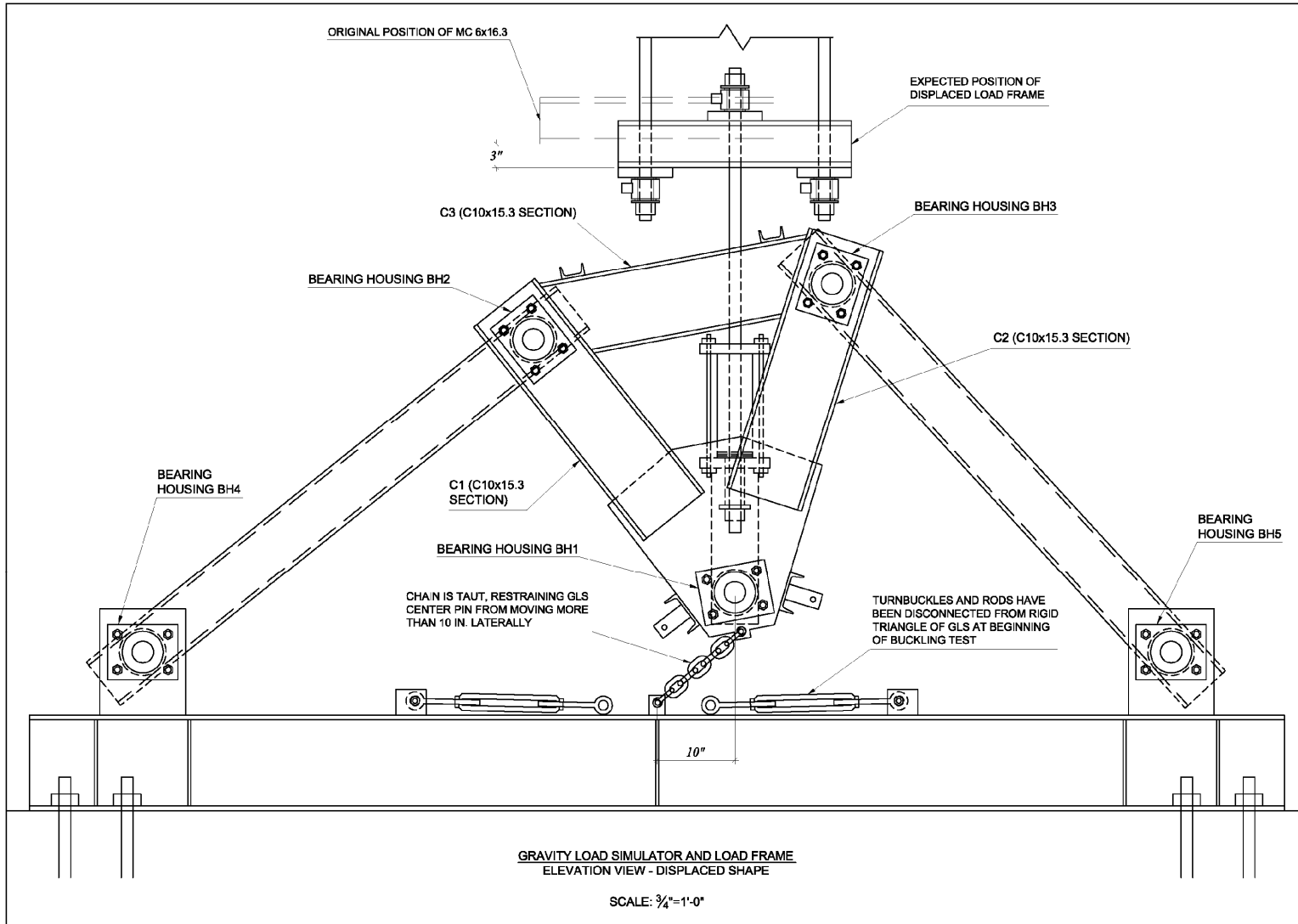


BEARING HOUSING ASSEMBLY (DETAIL H) (TYP.)
NOTE: BEARING HOUSINGS TO BE PLACED AND SECURED WITH BOLTS PROVIDED. ONCE GEOMETRY OF GLS IS ACCURATE, TACK WELD BEARING HOUSINGS IN PLACE.

NOTE: THE GEOMETRY OF THE GRAVITY LOAD SIMULATOR IS THE MOST IMPORTANT ASPECT OF THE DESIGN. ACCURATE DIMENSIONS BETWEEN THE SPHERICAL BEARINGS OF THE GLS TO THOSE SHOWN ON THIS SHEET ARE PIVOTAL TO ENSURE VERTICAL LOAD APPLICATION.

GRAVITY LOAD SIMULATOR
 ELEVATION VIEW
 SCALE: 3/4"=1'-0"

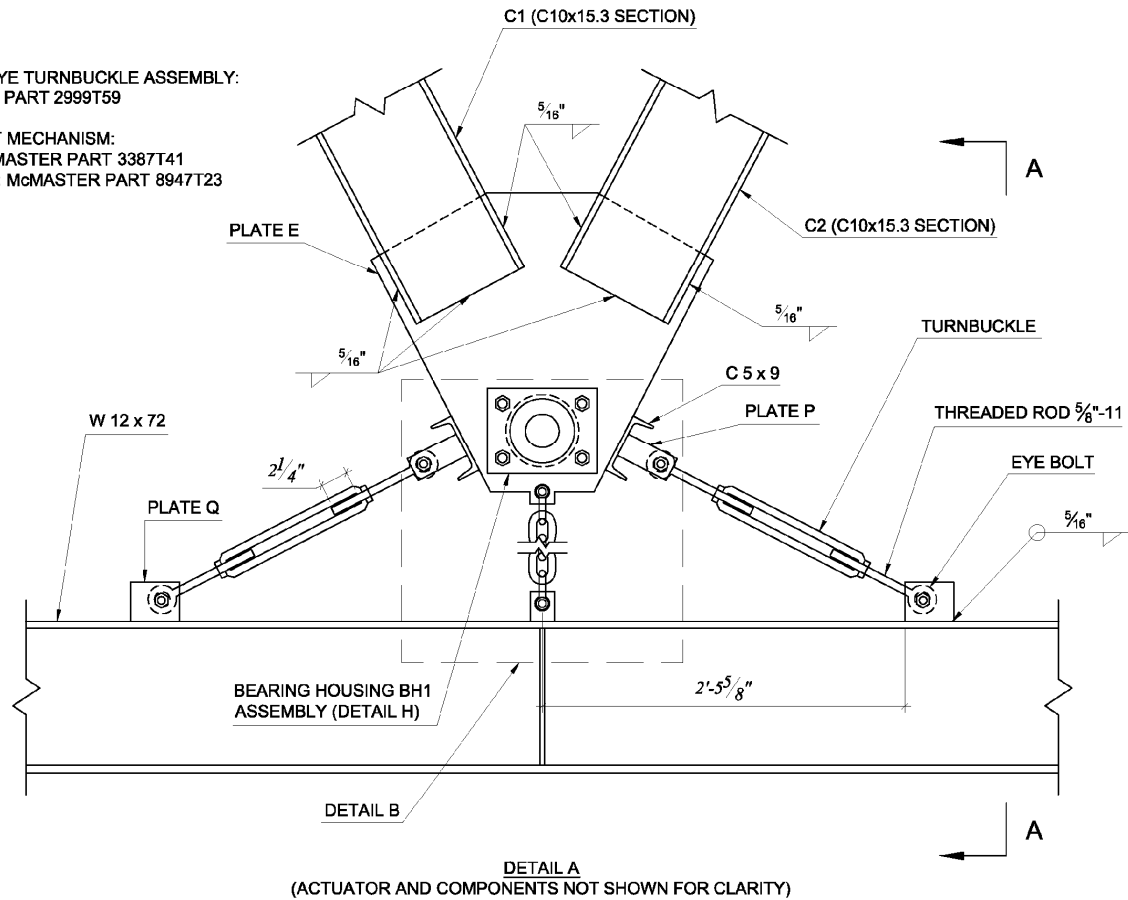
| | | | | | | |
|--|------------|-----------------------|----------------|------------|--|--|
| <i>Experimental Validation of Bracing Recommendations for Long-Span Concrete Girders</i> | | | | Revisions: | | |
| GLS elevation view | 2011-06-24 | University of Florida | Sheet 02 of 16 | | | |



| | | | | | | |
|--|------------|-----------------------|----------------|------------|--|--|
| <i>Experimental Validation of Bracing Recommendations for Long-Span Concrete Girders</i> | | | | Revisions: | | |
| GLS elevation view | 2011-06-24 | University of Florida | Sheet 03 of 16 | | | |

EYE AND EYE TURNBUCKLE ASSEMBLY:
McMASTER PART 2999T59

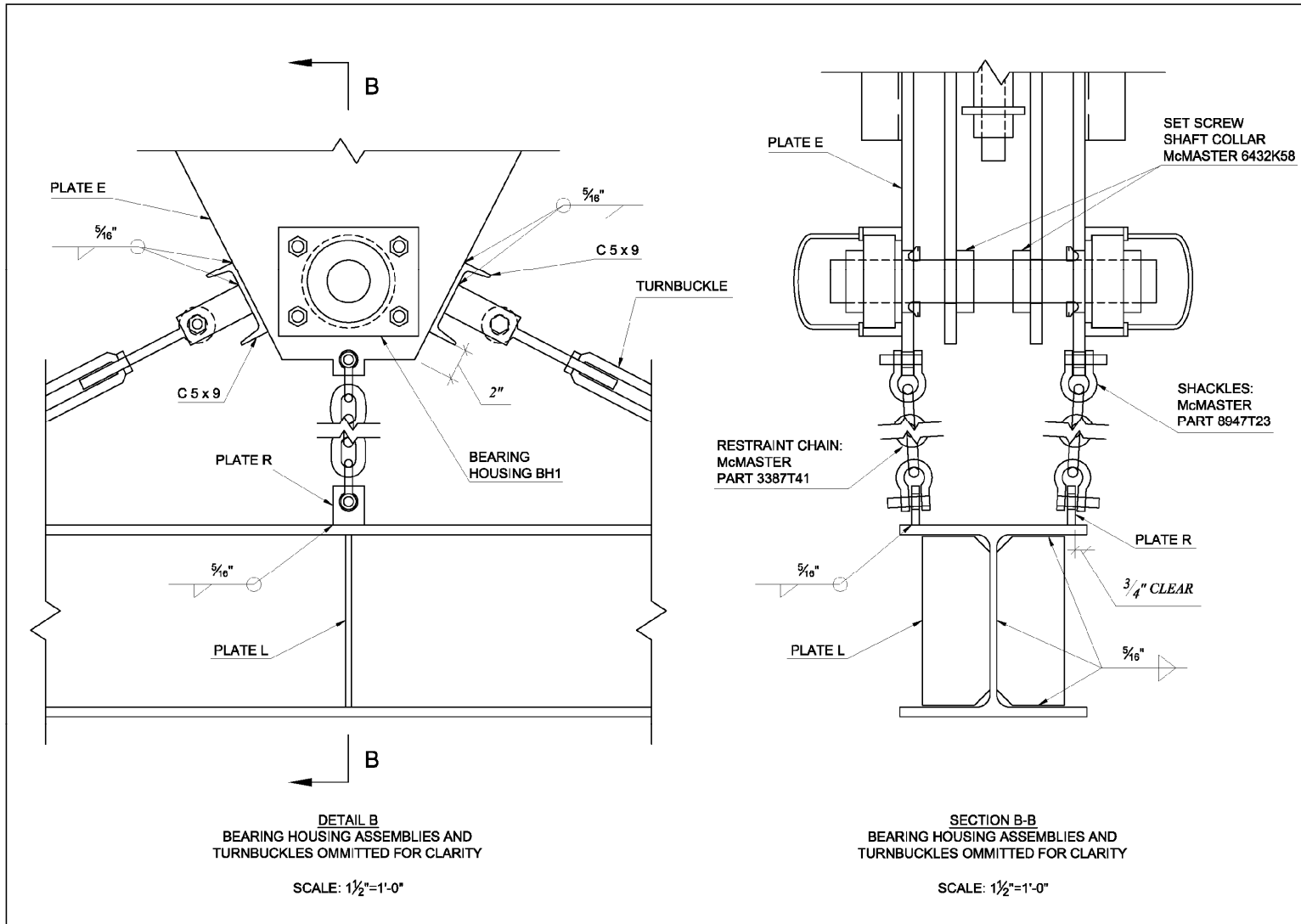
RESTRAINT MECHANISM:
CHAIN: McMASTER PART 3387T41
SHACKLES: McMASTER PART 8947T23



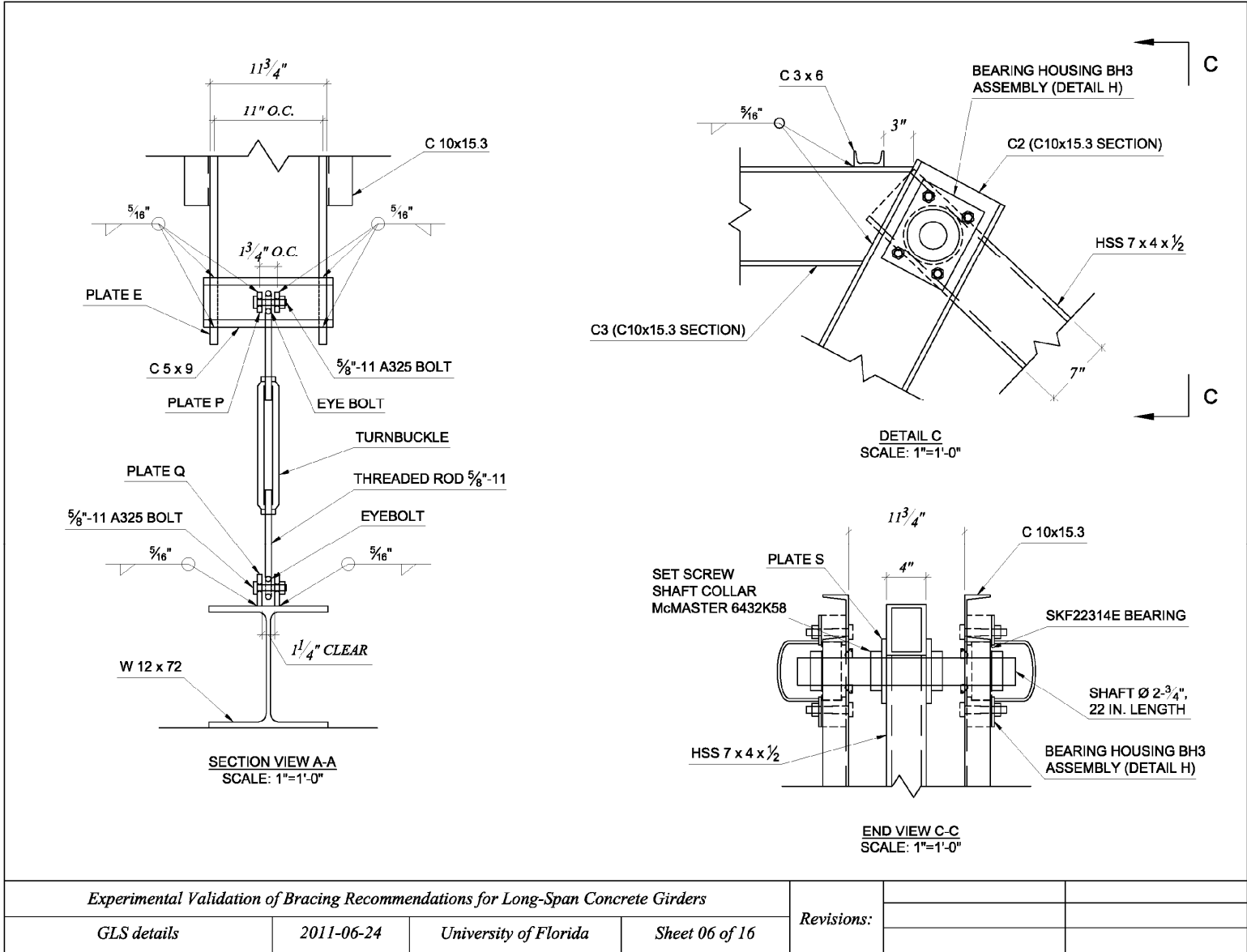
DETAIL A
(ACTUATOR AND COMPONENTS NOT SHOWN FOR CLARITY)

SCALE: 1"=1'-0"

| | | | | | | |
|--|------------|-----------------------|----------------|------------|--|--|
| <i>Experimental Validation of Bracing Recommendations for Long-Span Concrete Girders</i> | | | | Revisions: | | |
| GLS details | 2011-06-24 | University of Florida | Sheet 04 of 16 | | | |

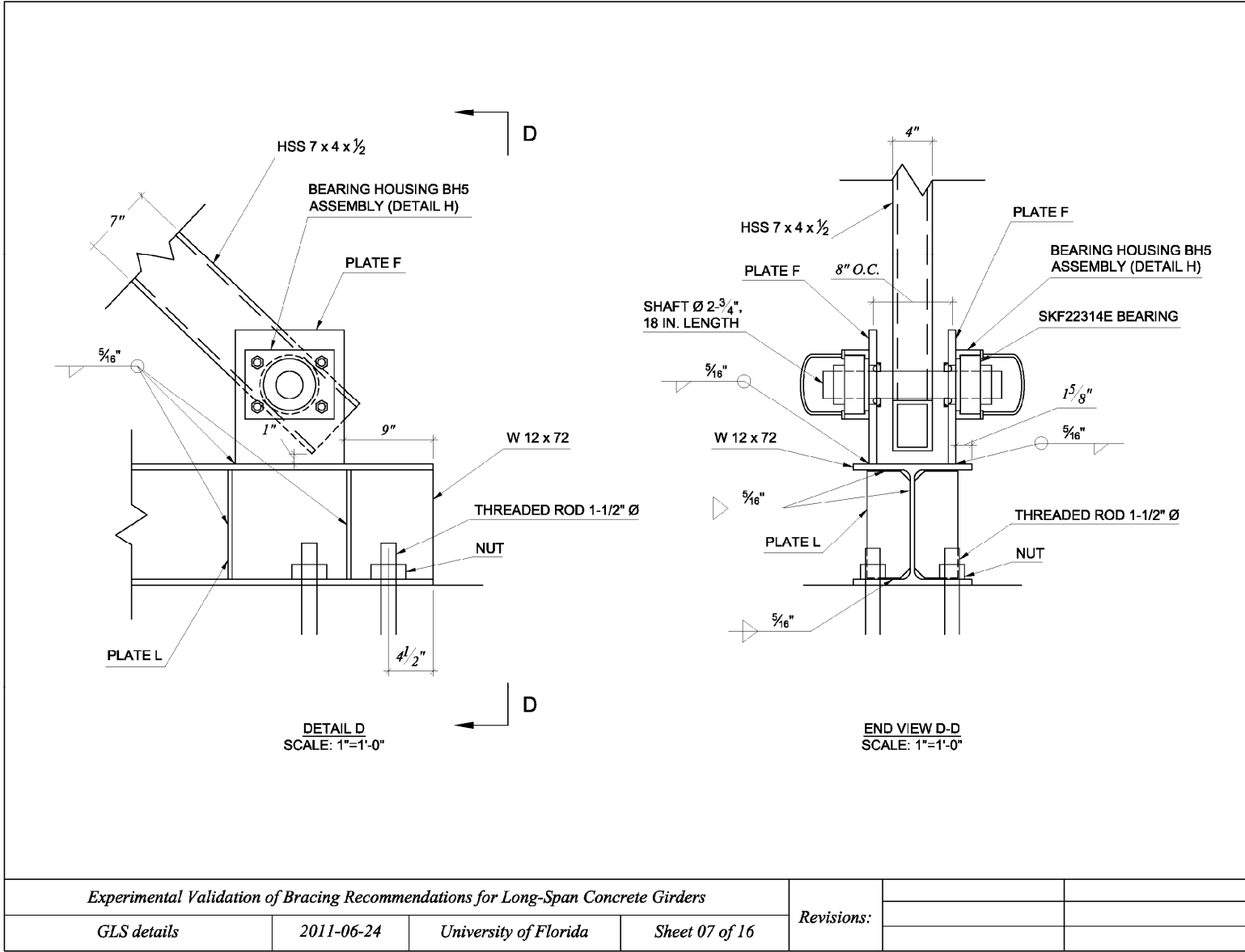


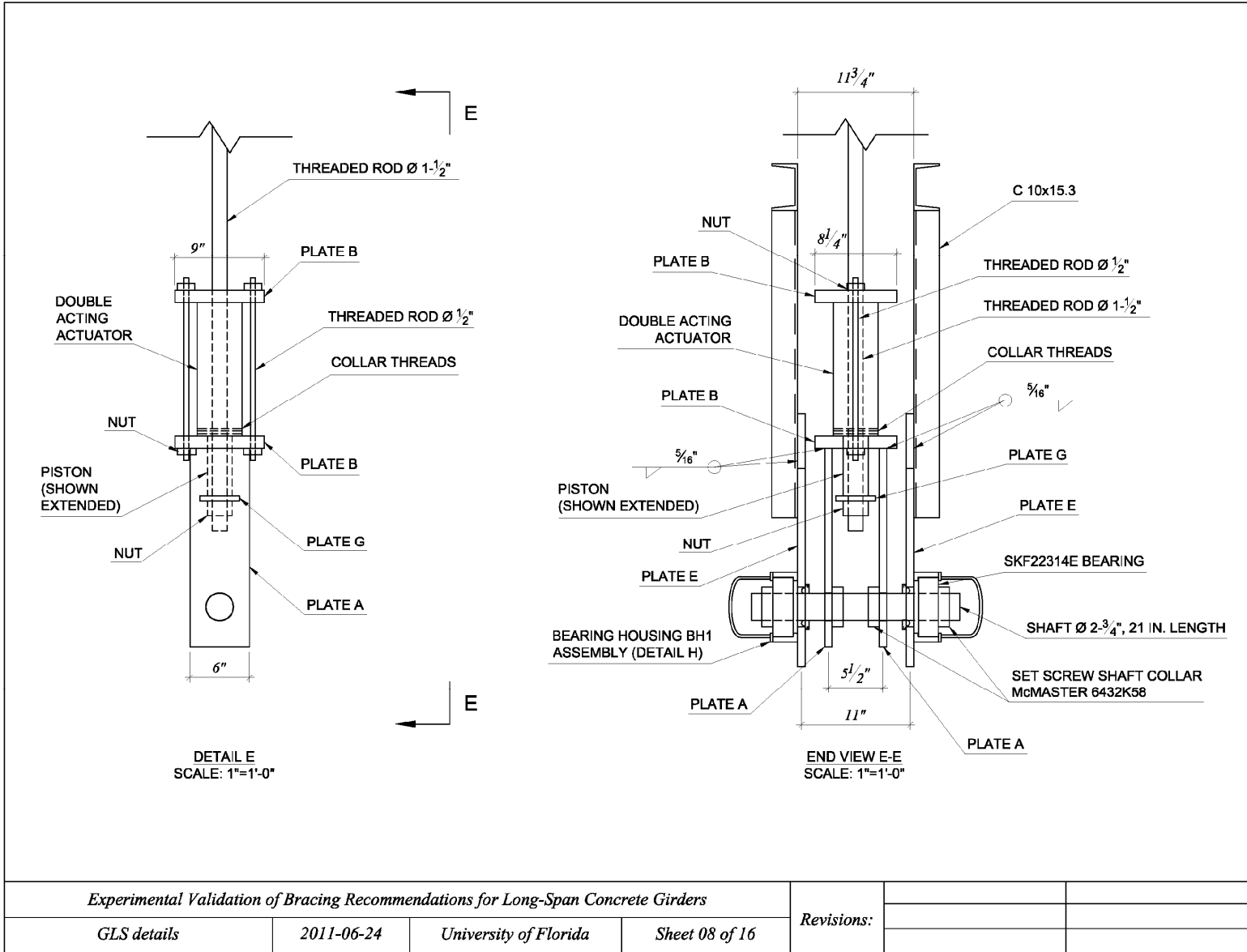
| | | | | | | |
|--|------------|-----------------------|----------------|------------|--|--|
| <i>Experimental Validation of Bracing Recommendations for Long-Span Concrete Girders</i> | | | | Revisions: | | |
| GLS details | 2011-06-24 | University of Florida | Sheet 05 of 16 | | | |



Experimental Validation of Bracing Recommendations for Long-Span Concrete Girders

| | | | | | | |
|-------------|------------|-----------------------|----------------|------------|--|--|
| GLS details | 2011-06-24 | University of Florida | Sheet 06 of 16 | Revisions: | | |
|-------------|------------|-----------------------|----------------|------------|--|--|





Experimental Validation of Bracing Recommendations for Long-Span Concrete Girders

GLS details

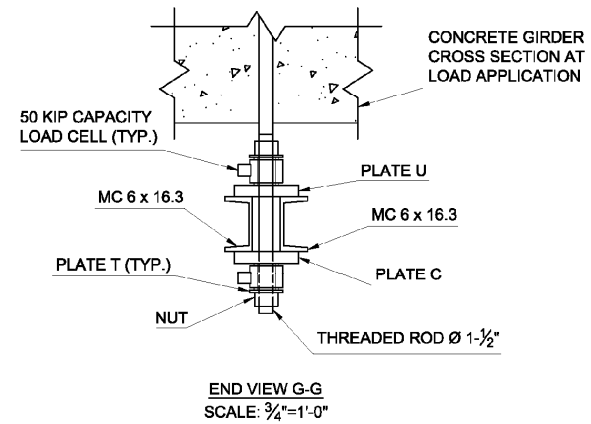
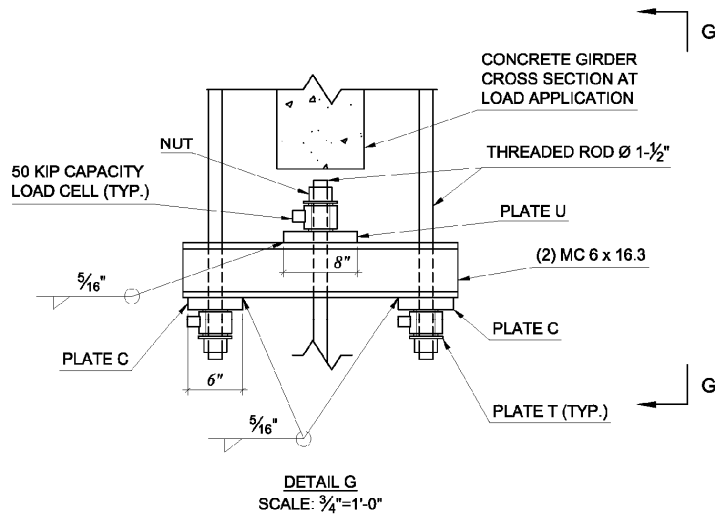
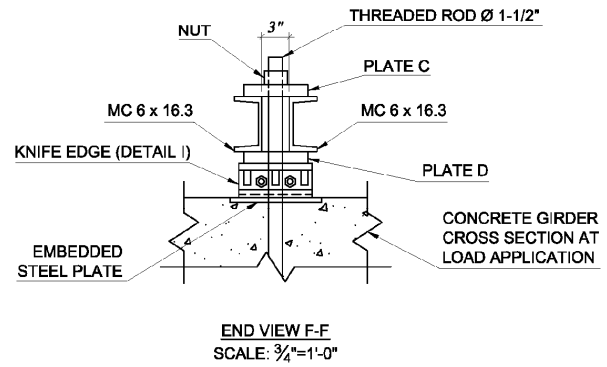
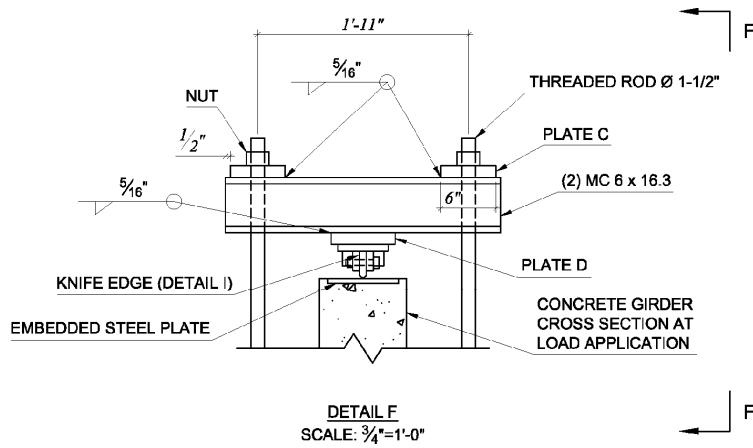
2011-06-24

University of Florida

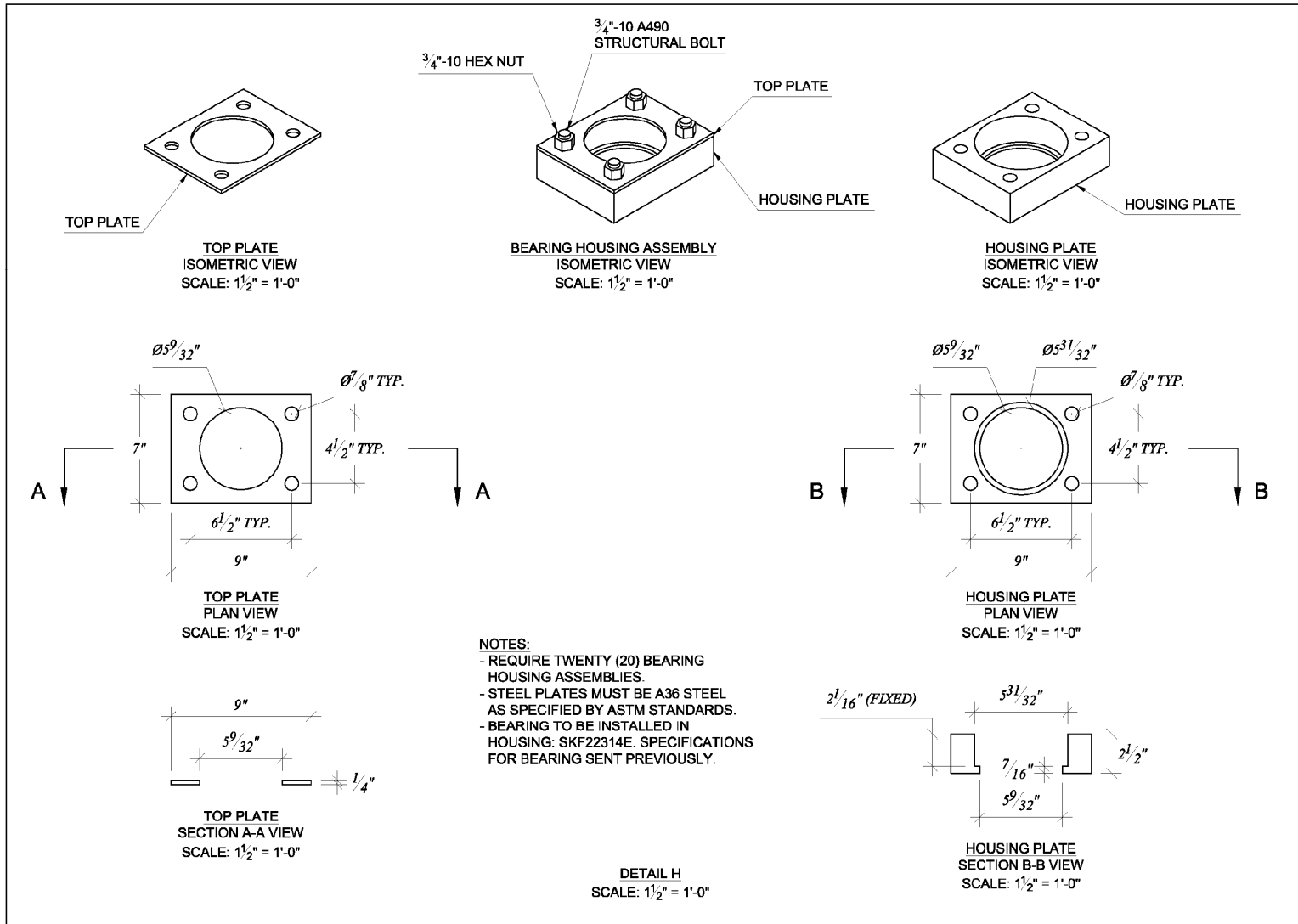
Sheet 08 of 16

Revisions:

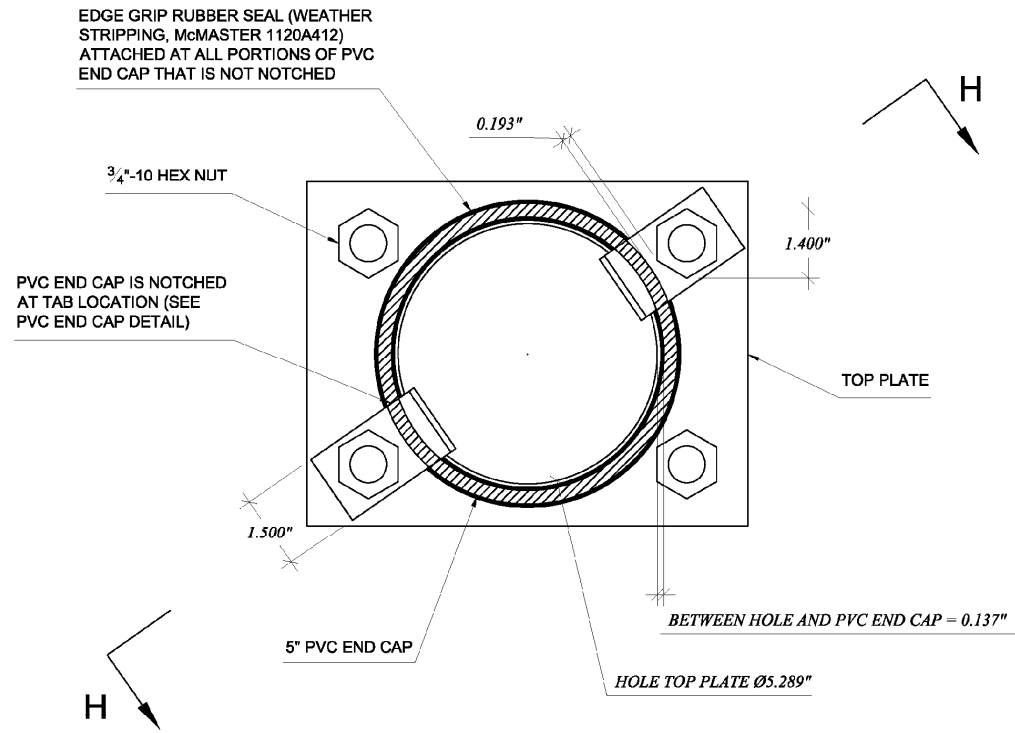
| | | |
|--|--|--|
| | | |
| | | |
| | | |



| | | | | | | |
|--|------------|-----------------------|----------------|------------|--|--|
| <i>Experimental Validation of Bracing Recommendations for Long-Span Concrete Girders</i> | | | | Revisions: | | |
| <i>Load frame details</i> | 2011-06-24 | University of Florida | Sheet 09 of 16 | | | |

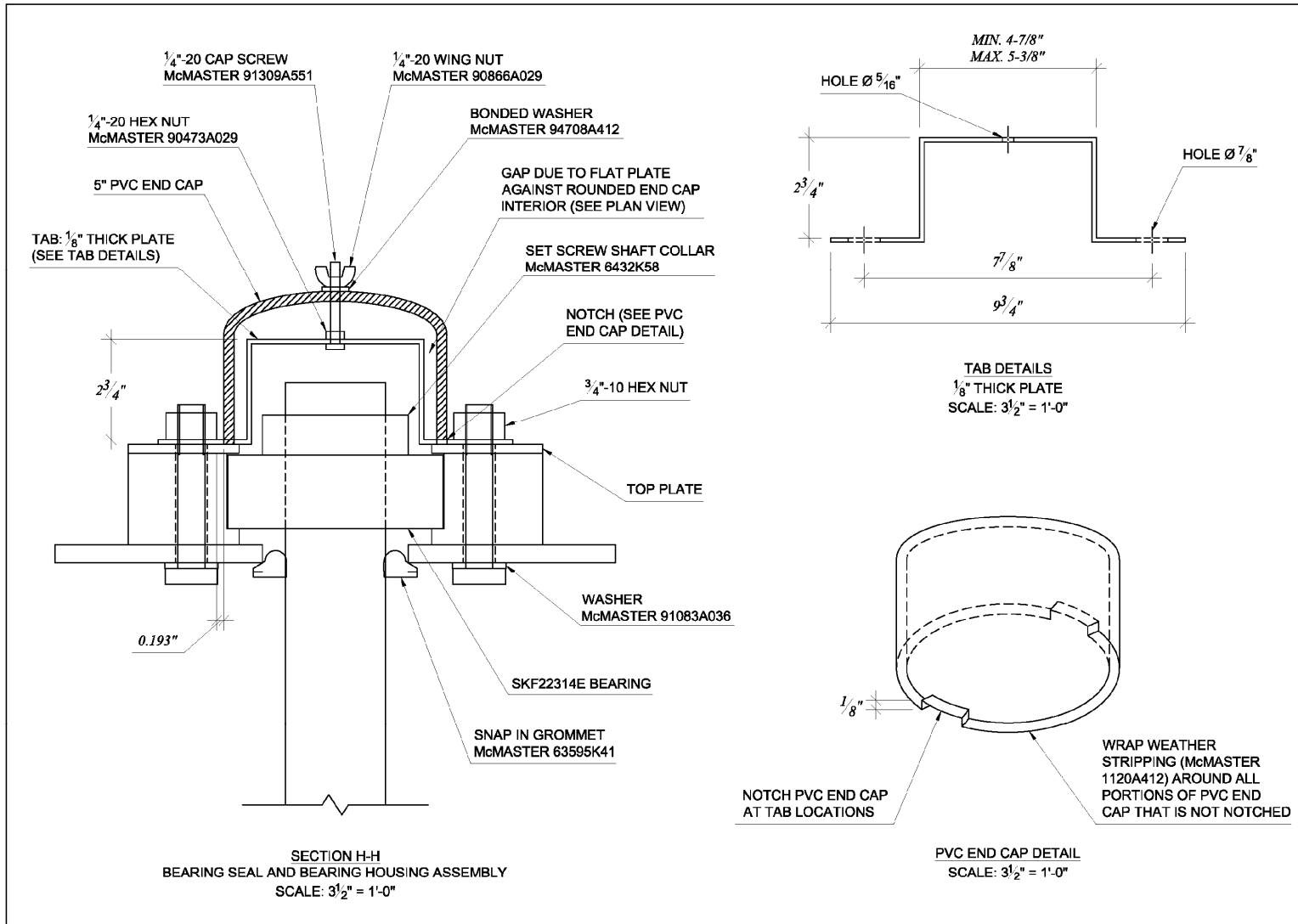


| | | | | | | |
|--|-------------------|------------------------------|-----------------------|------------|--|--|
| <i>Experimental Validation of Bracing Recommendations for Long-Span Concrete Girders</i> | | | | Revisions: | | |
| <i>Detail H: bearing housing assembly</i> | <i>2011-06-24</i> | <i>University of Florida</i> | <i>Sheet 10 of 16</i> | | | |

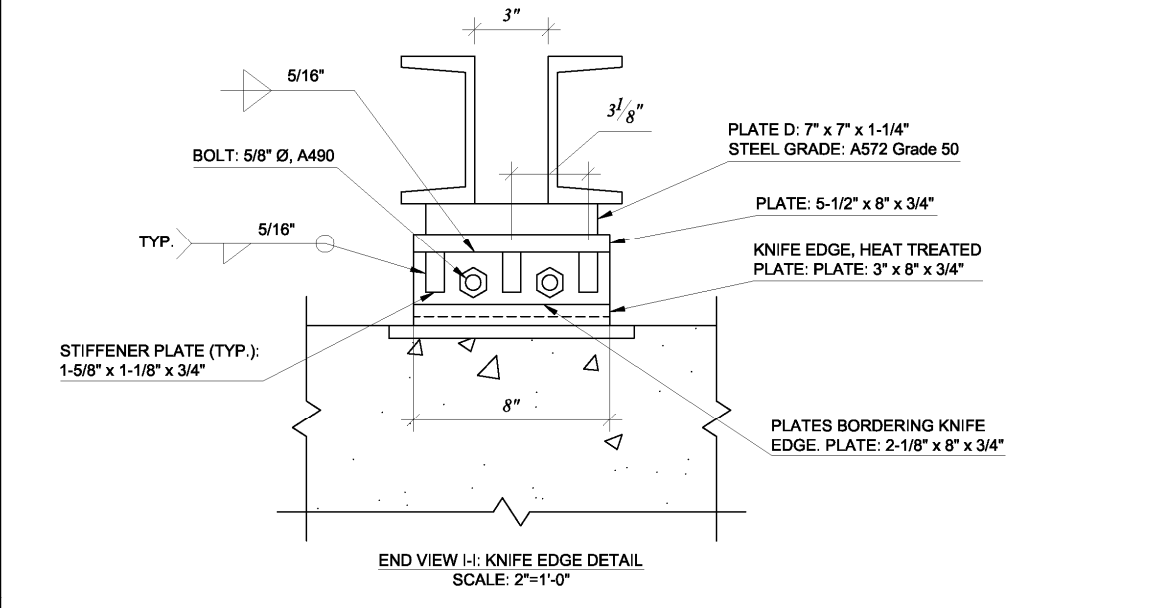
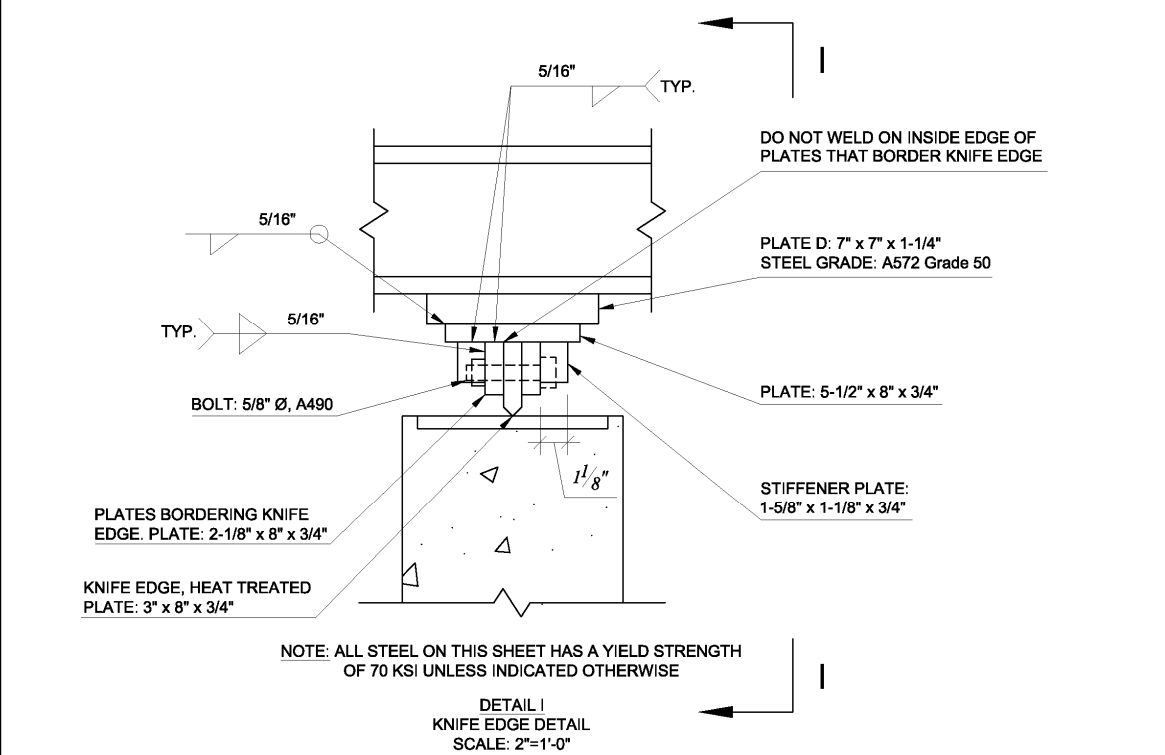


PLAN VIEW OF BEARING HOUSING ASSEMBLY AND BEARING SEAL
SCALE: 4" = 1'-0"

| | | | | | | |
|--|-------------------|------------------------------|-----------------------|------------|--|--|
| <i>Experimental Validation of Bracing Recommendations for Long-Span Concrete Girders</i> | | | | Revisions: | | |
| <i>Detail H: bearing seal</i> | <i>2011-06-24</i> | <i>University of Florida</i> | <i>Sheet 11 of 16</i> | | | |
| | | | | | | |

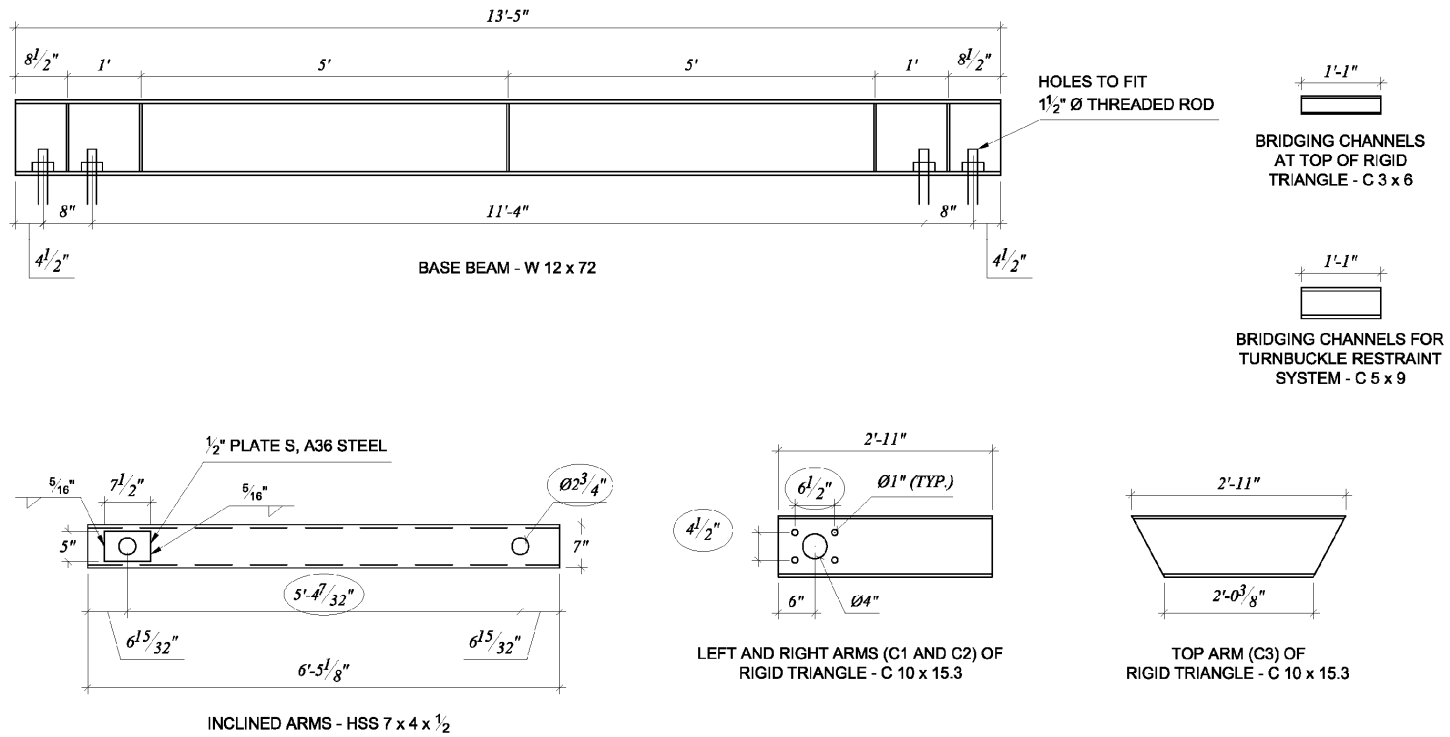


| | | | | | | |
|--|------------|-----------------------|----------------|------------|--|--|
| <i>Experimental Validation of Bracing Recommendations for Long-Span Concrete Girders</i> | | | | Revisions: | | |
| <i>Detail H: bearing seal</i> | 2011-06-24 | University of Florida | Sheet 12 of 16 | | | |



Experimental Validation of Bracing Recommendations for Long-Span Concrete Girders

| | | | |
|-------------------------------------|-------------------|------------------------------|-----------------------|
| <i>Detail I: knife edge details</i> | <i>2011-06-24</i> | <i>University of Florida</i> | <i>Sheet 13 of 16</i> |
| <i>Revisions:</i> | | | |



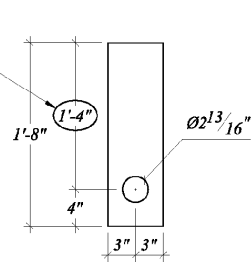
NOTE: KEY DIMENSIONS ASSOCIATED WITH SPHERICAL BEARING LOCATIONS ARE CIRCLED.

GRAVITY LOAD SIMULATOR STEEL MEMBERS
 DETAILS OF HOLE SIZE/LOCATION, STIFFENER LOCATION

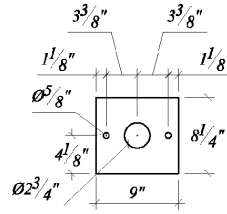
SCALE: 1/2"=1'-0"

| | | | | | | |
|--|------------|-----------------------|----------------|------------|--|--|
| <i>Experimental Validation of Bracing Recommendations for Long-Span Concrete Girders</i> | | | | Revisions: | | |
| <i>GLS steel member list</i> | 2011-06-24 | University of Florida | Sheet 14 of 16 | | | |
| | | | | | | |

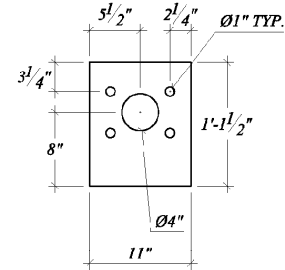
DIMENSION MUST MATCH ON EACH PAIR OF PLATES PER GLS TO MAINTAIN VERTICAL LOAD



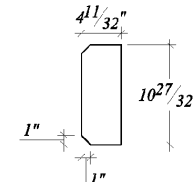
(4) PLATE A
Grade A36, $t = \frac{3}{4}$ in.



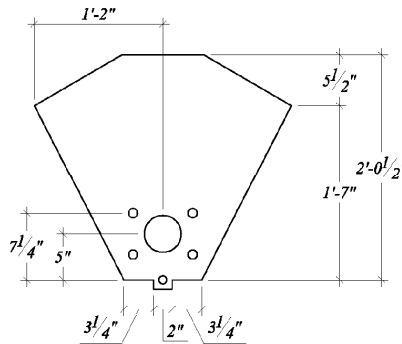
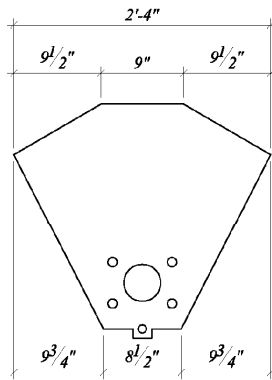
(4) PLATE B
A572 Grade 50
 $t = 1\frac{1}{4}$ in.



(8) PLATE F
Grade A36
 $t = \frac{1}{2}$ in.



(20) PLATE L
Grade A36
 $t = \frac{3}{8}$ in.



(4) PLATE E
Grade A36, $t = \frac{3}{4}$ in.

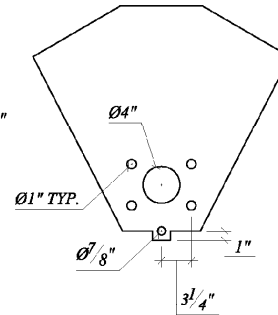
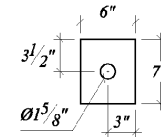
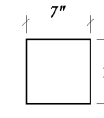


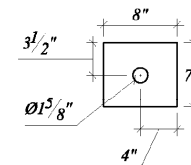
PLATE LIST - GLS
SCALE: $\frac{3}{4}$ "=1'-0"



(8) PLATE C
A572 Grade 50
 $t = 1\frac{1}{4}$ in.

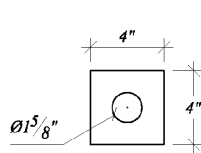


(2) PLATE D
A572 Grade 50
 $t = 1\frac{1}{4}$ in.

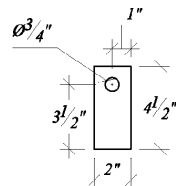


(2) PLATE U
A572 Grade 50
 $t = 1\frac{1}{4}$ in.

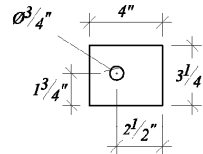
| | | | | | | |
|---|------------|-----------------------|----------------|------------|--|--|
| Experimental Validation of Bracing Recommendations for Long-Span Concrete Girders | | | | Revisions: | | |
| GLS plate list | 2011-06-24 | University of Florida | Sheet 15 of 16 | | | |



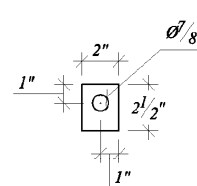
(2) PLATE G
Grade A36
t = 1/2 in.



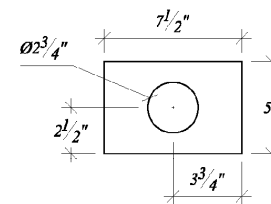
(8) PLATE P
Grade A36
t = 1/2 in.



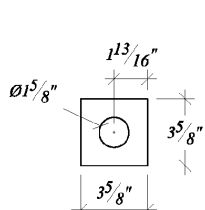
(8) PLATE Q
Grade A36
t = 1/2 in.



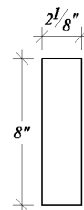
(4) PLATE R
Grade A36
t = 1/2 in.



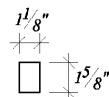
(8) PLATE S
Grade A36
t = 1/2 in.



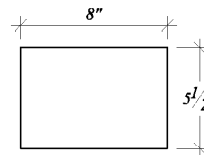
(6) PLATE T
Grade A36
t = 1/4 in.



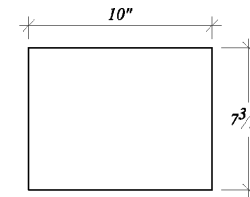
(4) KNIFE EDGE SANDWICH PLATES
70 ksi AT LAB
t = 3/4 in.



(12) KNIFE EDGE STIFFENER
70 ksi AT LAB
t = 3/4 in.



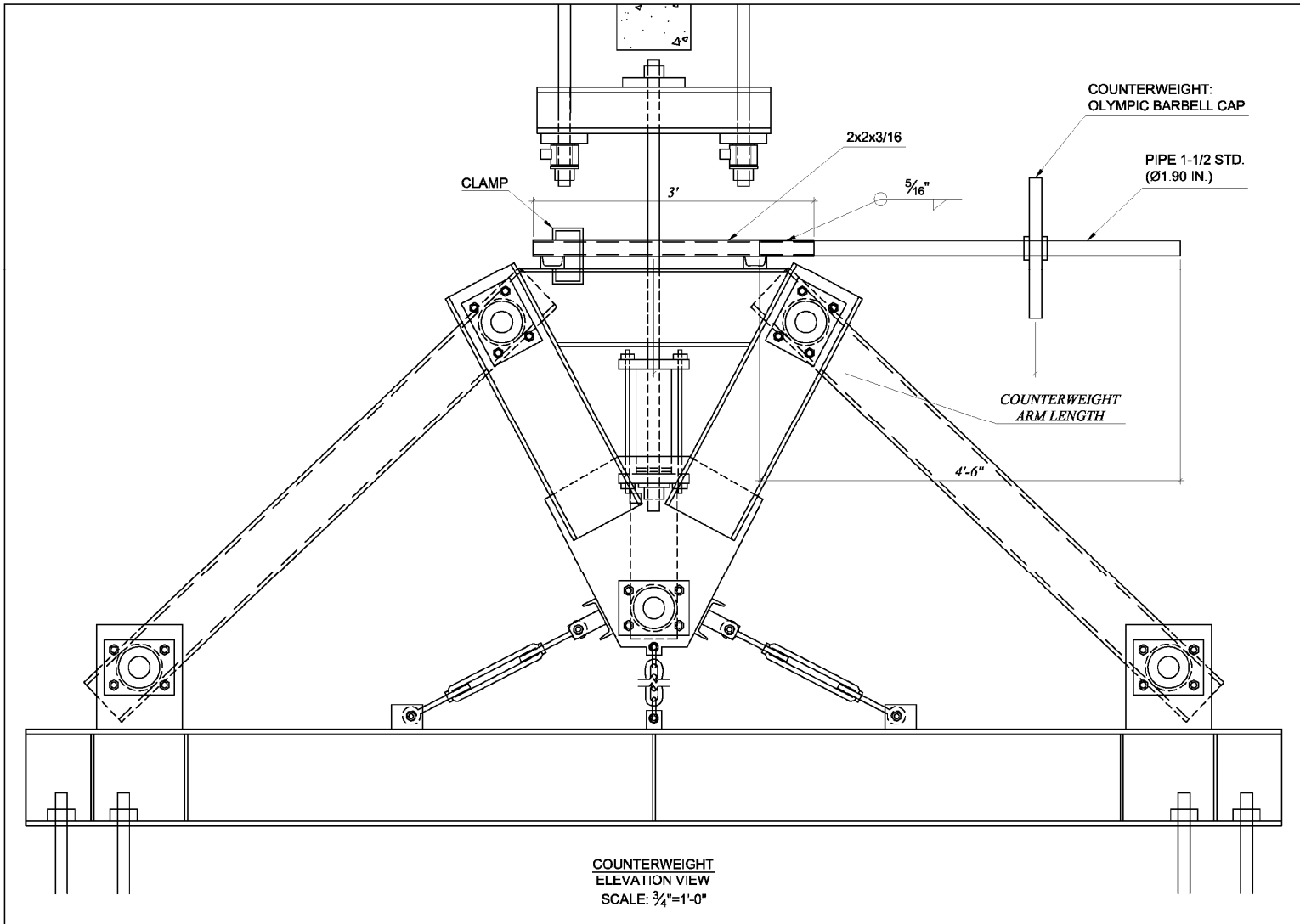
(2) KNIFE EDGE BRIDGING PLATES
70 ksi AT LAB
t = 3/4 in.



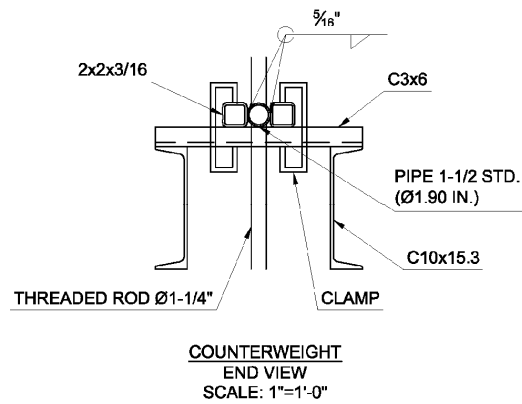
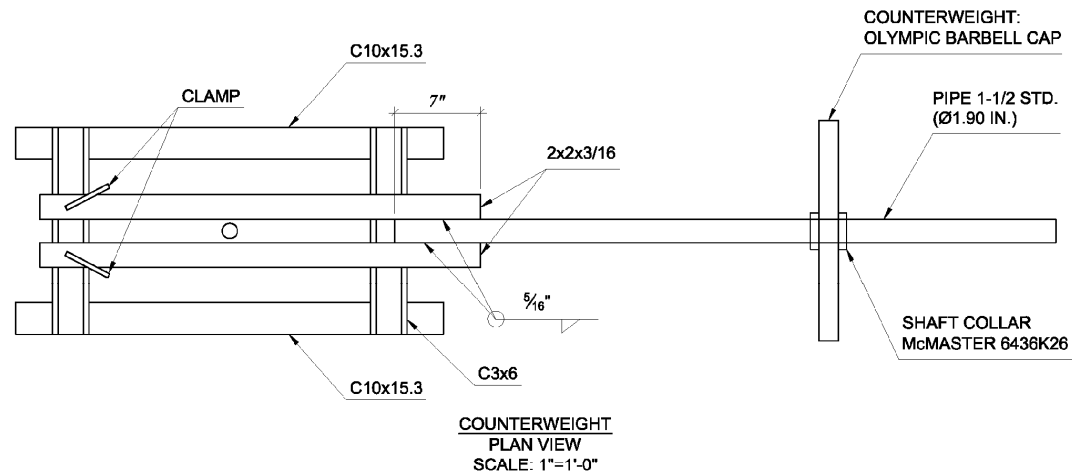
(2) EMBEDDED PLATES
Grade A36
t = 1/2 in.

PLATE LIST - GLS
SCALE: 1-1/2" = 1'-0"

| | | | | | | |
|--|------------|-----------------------|----------------|------------|--|--|
| <i>Experimental Validation of Bracing Recommendations for Long-Span Concrete Girders</i> | | | | Revisions: | | |
| GLS plate list | 2011-06-24 | University of Florida | Sheet 16 of 16 | | | |



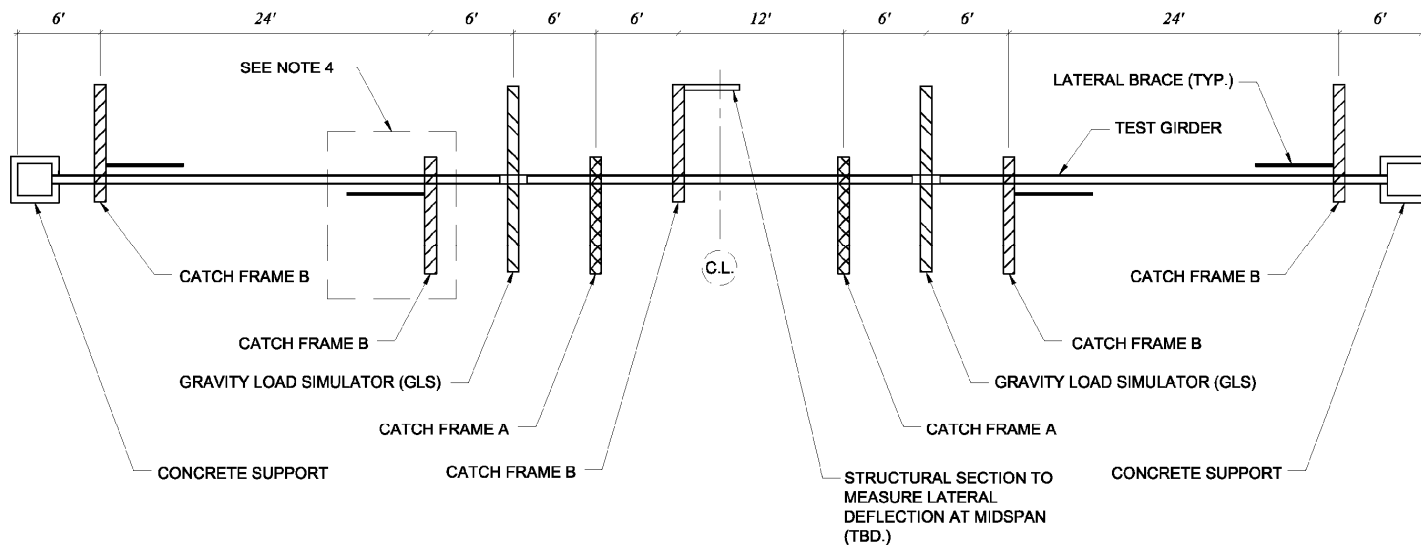
| | | | | | | |
|--|-------------------|------------------------------|-----------------------|-------------------|--|--|
| <i>Experimental Validation of Bracing Recommendations for Long-Span Concrete Girders</i> | | | | <i>Revisions:</i> | | |
| <i>GLS counterweight plans</i> | <i>2011-12-07</i> | <i>University of Florida</i> | <i>Sheet 01 of 02</i> | | | |



| | | | | | | |
|--|-------------------|------------------------------|-----------------------|------------|--|--|
| <i>Experimental Validation of Bracing Recommendations for Long-Span Concrete Girders</i> | | | | Revisions: | | |
| <i>GLS counterweight plans</i> | <i>2011-12-07</i> | <i>University of Florida</i> | <i>Sheet 02 of 02</i> | | | |

APPENDIX F
CATCH FRAMES FABRICATION PLANS

This appendix includes drawings for the fabrication of the gravity load simulators, used in the full scale buckling tests.



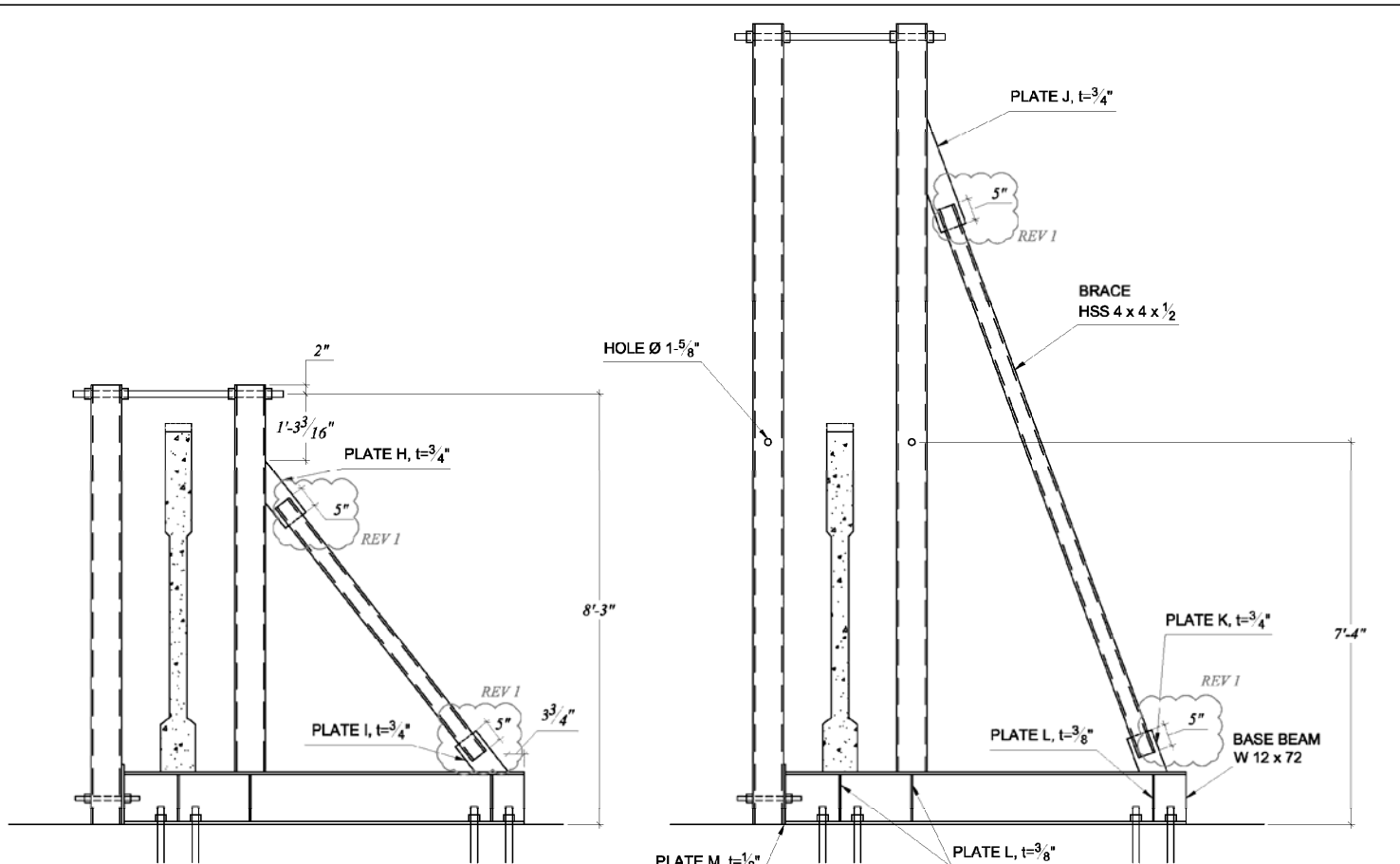
PLAN VIEW
 LOCATIONS OF CATCH FRAMES (A AND B) AND GRAVITY LOAD
 SIMULATORS RELATIVE TO LENGTH OF TEST GIRDER

SCALE: $\frac{3}{32}'' = 1'-0''$

NOTES:

1. TO PREVENT UNACCEPTABLE NEGATIVE MOMENT AT THE ENDS OF THE BEAM, LIFT TEST GIRDER WITH CRANES AT THE ENDS OF THE BEAM ONLY.
2. CRANES SHALL BE LOCKED TOGETHER, SO THAT THERE IS ONE CONTROL FOR BOTH ENDS, WITH A SINGLE OPERATOR AT MIDSPAN.
3. USE FOAMBOARD OR PLYWOOD TO CUSHION COLUMNS OF CATCH FRAMES AS TEST GIRDER IS BEING LIFTED. THIS PREVENTS LATERAL MOVEMENT DURING LIFTING, BUT CAN BE REMOVED TO ALLOW LATERAL DISPLACEMENT DURING A TEST.
4. DETAILED VIEWS OF CATCH FRAME AND LATERAL BRACING ARE SHOWN ON SHEET 05 AND SHEET 06. ORIENTATION OF LATERAL BRACING SHOWN ABOVE.

| | | | | | | |
|--|-------------------|------------------------------|-----------------------|-------------------|---------------------------|--|
| <i>Experimental Validation of Bracing Recommendations for Long-Span Concrete Girders</i> | | | | <i>Revisions:</i> | <i>REV 1 : 2011-03-08</i> | |
| <i>Catch frame and GLS locations</i> | <i>2011-03-08</i> | <i>University of Florida</i> | <i>Sheet 01 of 07</i> | | | |



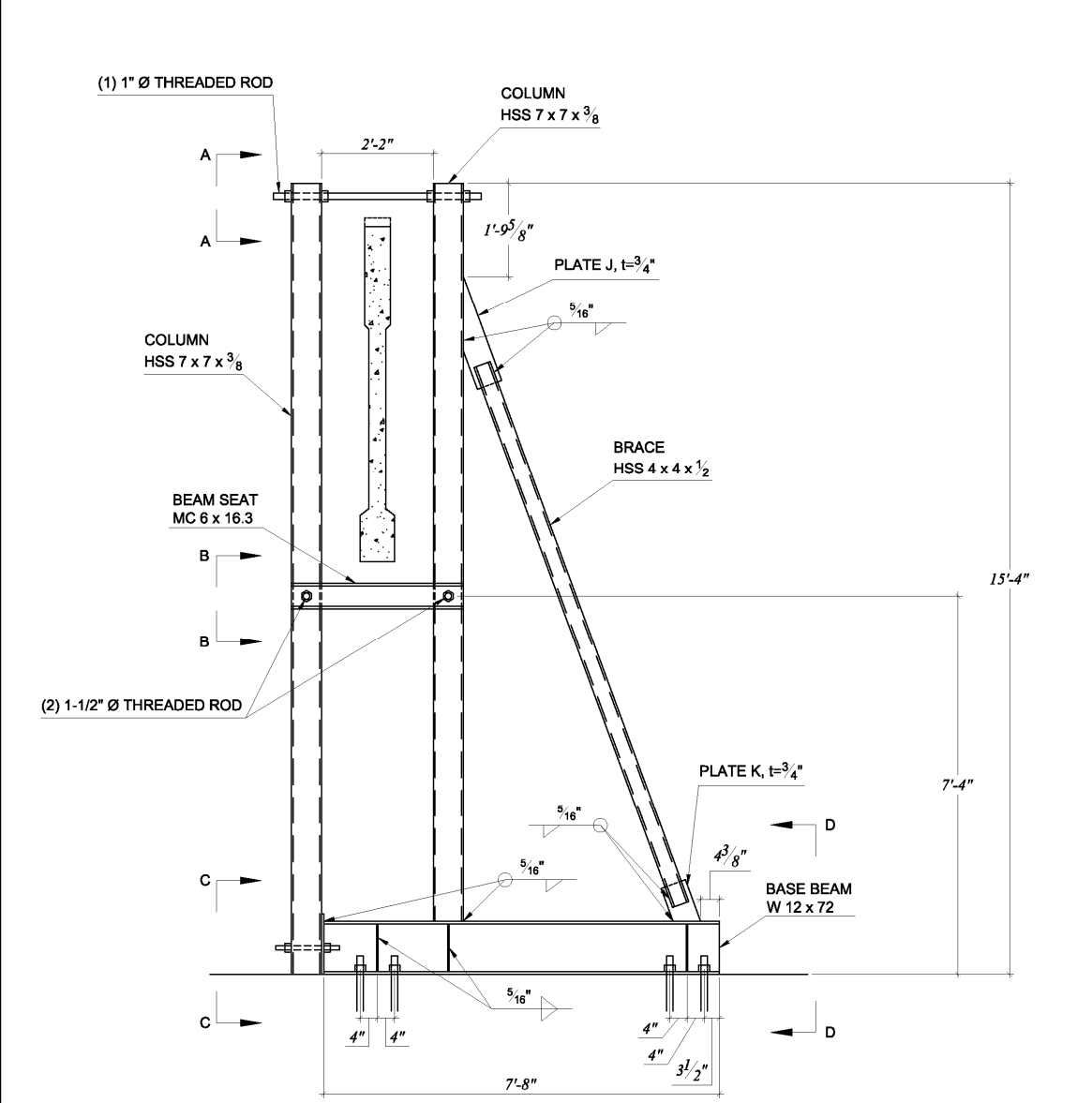
ELEVATION VIEW - CATCH FRAME A
 BEAM SUPPORTED BY CATCH FRAME DURING
 CLOSURE POUR AND END BLOCK CASTING
 (LATERAL BRACING OMITTED FOR CLARITY)

SCALE = 3/8" = 1'-0"

ELEVATION VIEW - CATCH FRAME B
 BEAM SUPPORTED BY CATCH FRAME DURING
 CLOSURE POUR AND END BLOCK CASTING
 (LATERAL BRACING OMITTED FOR CLARITY)

SCALE = 3/8" = 1'-0"

| | | | | | | |
|--|------------|------------------------------|-----------------------|------------|--------------------|--|
| <i>Experimental Validation of Bracing Recommendations for Long-Span Concrete Girders</i> | | | | Revisions: | REV 1 : 2011-03-08 | |
| <i>Catch frames A and B</i> | 2011-03-08 | <i>University of Florida</i> | <i>Sheet 02 of 07</i> | | | |

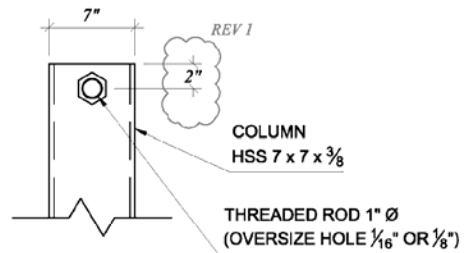


ELEVATION VIEW - CATCH FRAME B
 TEST GIRDER SUSPENDED DURING BUCKLING TEST
 (LATERAL BRACING OMITTED FOR CLARITY)

SCALE = $\frac{3}{8}$ " = 1'-0"

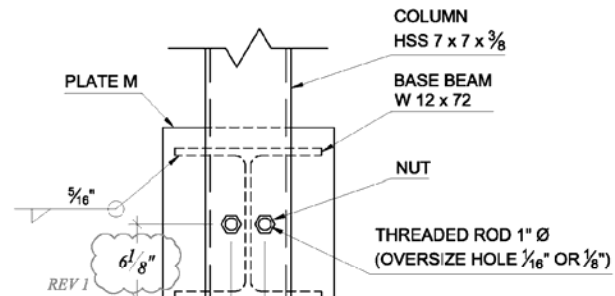
Experimental Validation of Bracing Recommendations for Long-Span Concrete Girders

| | | | |
|-----------------------|--------------------|-----------------------|----------------|
| Catch frame B details | 2011-03-08 | University of Florida | Sheet 03 of 07 |
| Revisions: | REV 1 : 2011-03-08 | | |



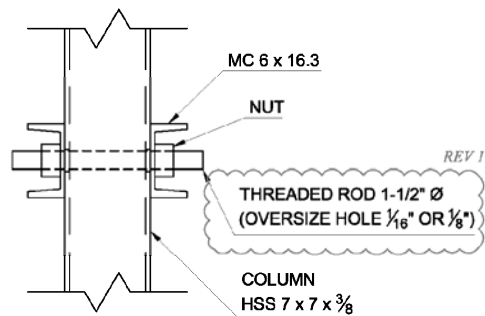
END VIEW A-A

SCALE: 1"=1'-0"



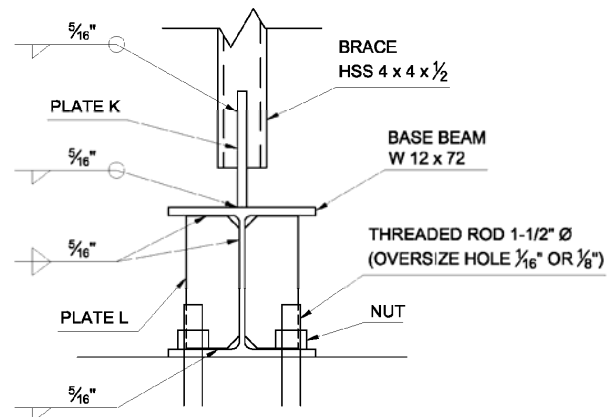
END VIEW C-C

SCALE: 1"=1'-0"



END VIEW B-B

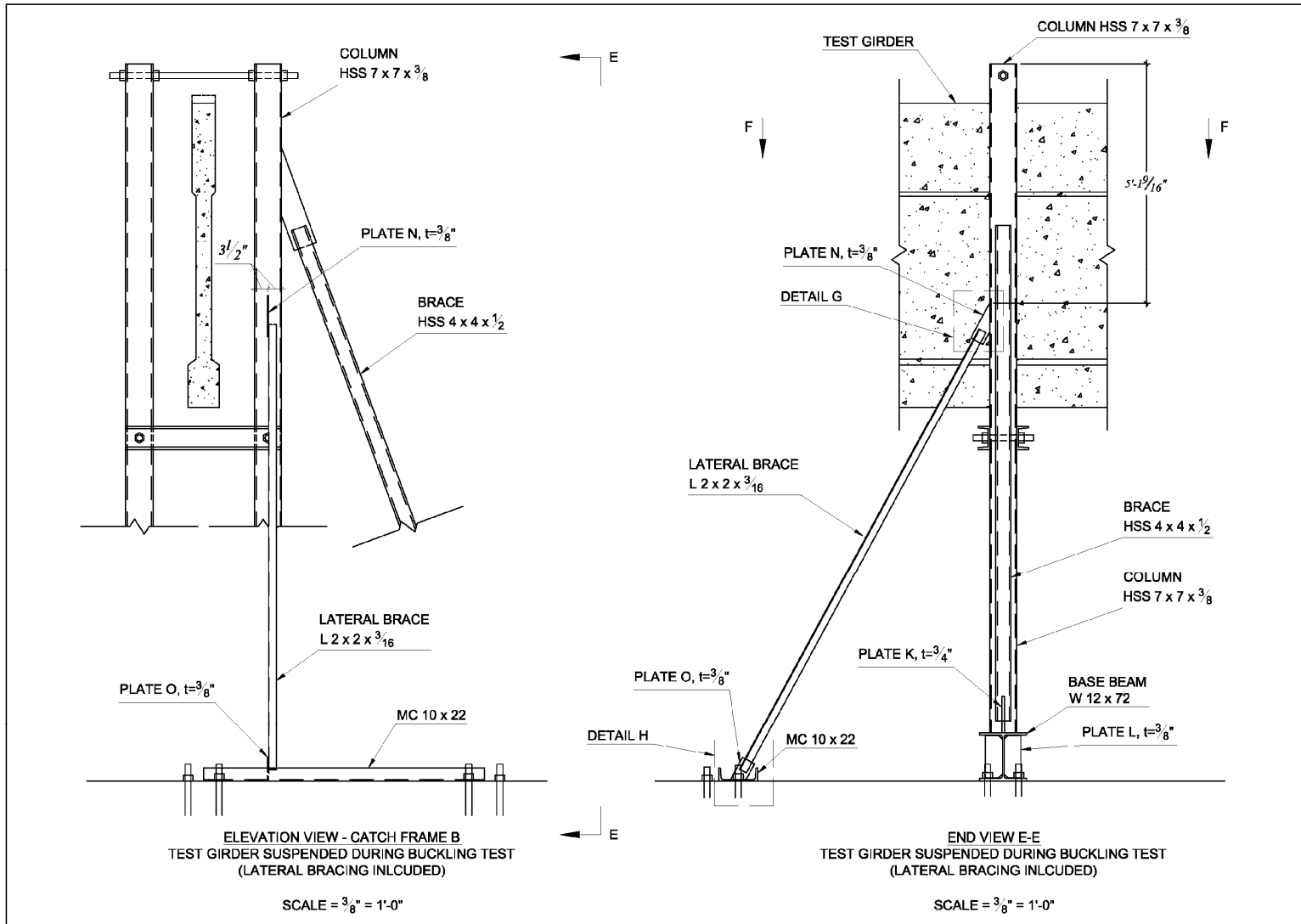
SCALE: 1"=1'-0"



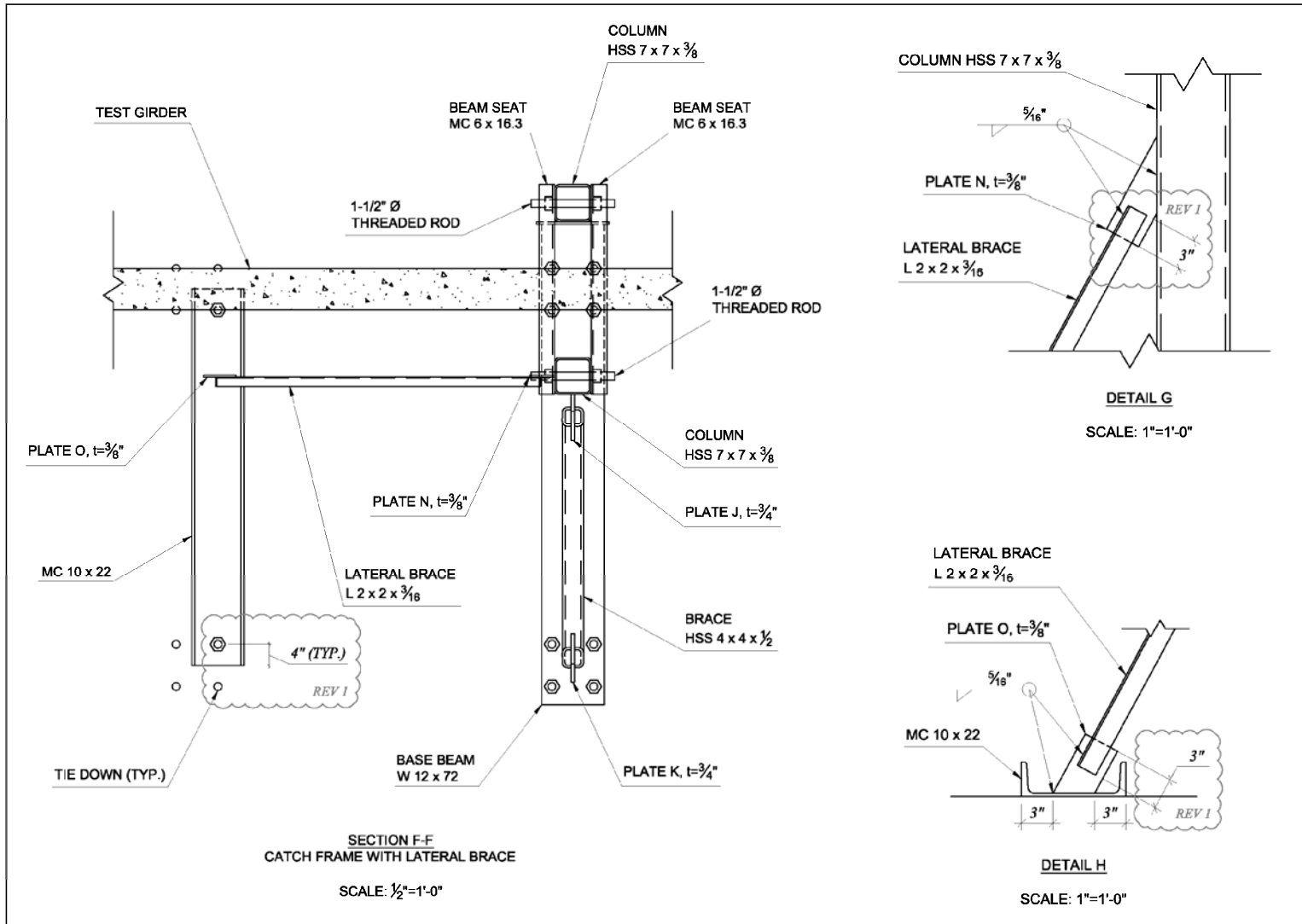
END VIEW D-D

SCALE: 1"=1'-0"

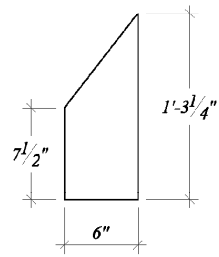
| | | | | | | |
|--|------------|-----------------------|----------------|------------|--------------------|--|
| <i>Experimental Validation of Bracing Recommendations for Long-Span Concrete Girders</i> | | | | Revisions: | REV 1 : 2011-03-08 | |
| Connection details | 2011-03-08 | University of Florida | Sheet 04 of 07 | | | |
| | | | | | | |



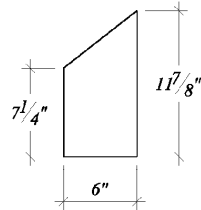
| | | | | | | |
|--|------------|-----------------------|----------------|------------|--------------------|--|
| <i>Experimental Validation of Bracing Recommendations for Long-Span Concrete Girders</i> | | | | Revisions: | REV 1 : 2011-03-08 | |
| Catch frame lateral bracing details | 2011-03-08 | University of Florida | Sheet 05 of 07 | | | |



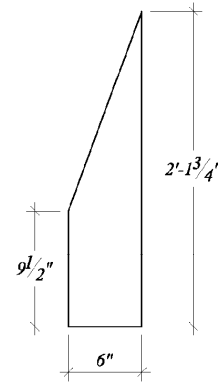
| | | | | | | |
|--|-------------------|------------------------------|-----------------------|-------------------|---------------------------|--|
| <i>Experimental Validation of Bracing Recommendations for Long-Span Concrete Girders</i> | | | | <i>Revisions:</i> | <i>REV 1 : 2011-03-08</i> | |
| <i>Catch frame lateral bracing details</i> | <i>2011-03-08</i> | <i>University of Florida</i> | <i>Sheet 06 of 07</i> | | | |
| | | | | | | |



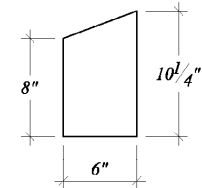
(2) PLATE H
Grade A36, $t = \frac{3}{4}$ in.



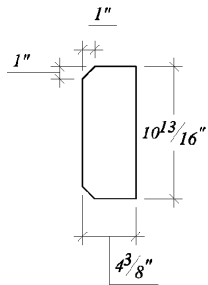
(2) PLATE I
Grade A36, $t = \frac{3}{4}$ in.



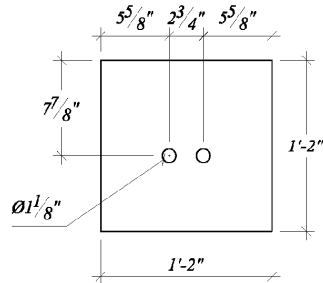
(5) PLATE J
Grade A36, $t = \frac{3}{4}$ in.



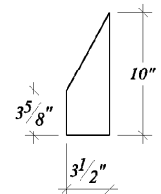
(5) PLATE K
Grade A36, $t = \frac{3}{4}$ in.



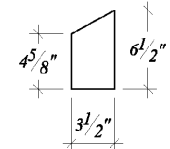
(58) PLATE L
Grade A36, $t = \frac{3}{8}$ in.



(7) PLATE M
Grade A36, $t = \frac{1}{2}$ in.



(4) PLATE N
Grade A36, $t = \frac{3}{8}$ in.



(4) PLATE O
Grade A36, $t = \frac{3}{8}$ in.

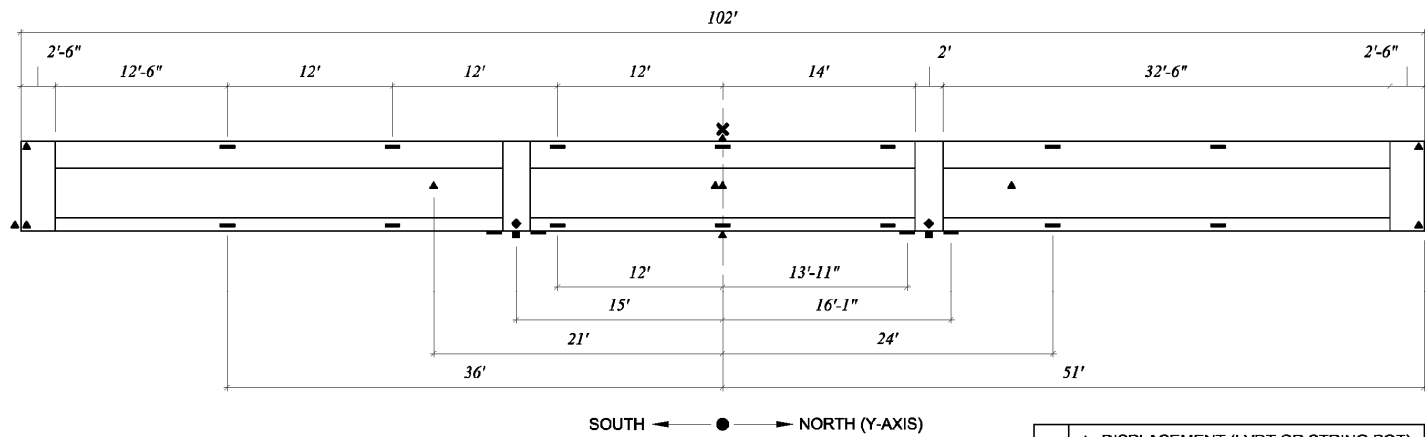
REV 1

PLATE LIST - CATCH FRAMES
ALL PLATES WERE PURCHASED FROM NAMASCO
SCALE: 1"=1'-0"

| | | | | | | |
|--|------------|-----------------------|----------------|------------|--------------------|--|
| <i>Experimental Validation of Bracing Recommendations for Long-Span Concrete Girders</i> | | | | Revisions: | REV 1 : 2011-03-08 | |
| <i>Catch frame plate list</i> | 2011-03-08 | University of Florida | Sheet 07 of 07 | | | |

APPENDIX G
BUCKLING TESTS INSTRUMENTATION PLAN

This appendix includes drawings of the instrumentation used in the full scale buckling tests.



NAMING SYSTEM:

T - LD - F - H, where:

T = type of instrumentation

- Dx, Dy, Dz : displacement transducer along x, y, and z-axis (respectively)
- Sx, Sz : string potentiometer along x, and z-axis (respectively)
- F : force
- VW : vibrating wire strain gage
- SG : strain gage
- Rx, Ry : rotation about x and y-axis (respectively)

LD = longitudinal distance from midspan

- N0 : at midspan
- N21 : 21' North of midspan
- S21 : 21' South of midspan, etc.

F = face of beam

- E : East
- W : West
- C : Center

H = height

- 0 : mount to bottom of beam
- 2 : mount 2" from bottom, etc.

For example, Dx-S21-W-38 : measures displacement along the x-axis, 21' South of midspan, mounted on the West face, 38" from the bottom of the beam.

ELEVATION VIEW
INSTRUMENTATION LOCATIONS
SCALE: $\frac{3}{32}'' = 1'-0''$

| | |
|------------|-------------------------------------|
| KEY | ▲ DISPLACEMENT (LVDT OR STRING POT) |
| | ■ LOAD CELL |
| | — STRAIN GAGE |
| | ◆ VIBRATING WIRE STRAIN GAGE |
| | ✕ INCLINOMETER |

INSTRUMENTATION SUMMARY:

| <u>INCLINOMETER</u> | <u>STRING POTENTIOMETER:</u> | <u>STRAIN GAGE (60 mm):</u> |
|-----------------------------|------------------------------|-----------------------------|
| Rx-N0-C-78 | Sx-N0-C-0 | SG-N0-E-2 |
| Ry-N0-C-78 | Sz-N0-C-0 | SG-N0-E-76 |
| | Sx-N0-C-78 | SG-N0-W-2 |
| <u>LVDT (50mm STROKE):</u> | <u>LOAD CELL</u> | <u>SG-N0-W-76</u> |
| Dx-S51-W-2 | (50 KIP CAPACITY): | SG-S12-E-2 |
| Dx-S51-W-76 | F-S15-E | SG-S12-E-76 |
| Dy-S51-E-2 | F-S15-C | SG-S12-W-2 |
| Dy-S51-W-2 | F-S15-W | SG-S12-W-76 |
| Dz-S51-E-2 | F-N15-E | SG-S14-E-0 |
| Dz-S51-W-2 | F-N15-C | SG-S14-W-0 |
| | F-N15-W | SG-S16-E-0 |
| <u>LVDT (100mm STROKE):</u> | | SG-S16-W-0 |
| Dx-S21-W-38 | <u>VIBRATING WIRE</u> | SG-S24-E-2 |
| Dx-N0-W-38 | <u>STRAIN GAGE</u> | SG-S24-E-76 |
| Dx-N21-W-38 | (CAST IN CONCRETE): | SG-S24-W-2 |
| | VW-S15-E-6.5 | SG-S24-W-76 |
| <u>LVDT (200mm STROKE):</u> | VW-S15-W-6.5 | SG-S36-E-2 |
| Dx-S0-W-38 | VW-N15-E-6.5 | SG-S36-E-76 |
| | VW-N15-W-6.5 | SG-S36-W-2 |
| | | SG-S36-W-76 |
| | | SG-N12-E-2 |
| | | SG-N12-E-76 |
| | | SG-N12-W-2 |
| | | SG-N12-W-76 |
| | | SG-N14-E-0 |
| | | SG-N14-W-0 |
| | | SG-N16-E-0 |
| | | SG-N16-W-0 |
| | | SG-N24-E-2 |
| | | SG-N24-E-76 |
| | | SG-N24-W-2 |
| | | SG-N24-W-76 |
| | | SG-N36-E-2 |
| | | SG-N36-E-76 |
| | | SG-N36-W-2 |
| | | SG-N36-W-76 |

Experimental Validation of Bracing Recommendations for Long-Span Concrete Girders

Instrumentation summary

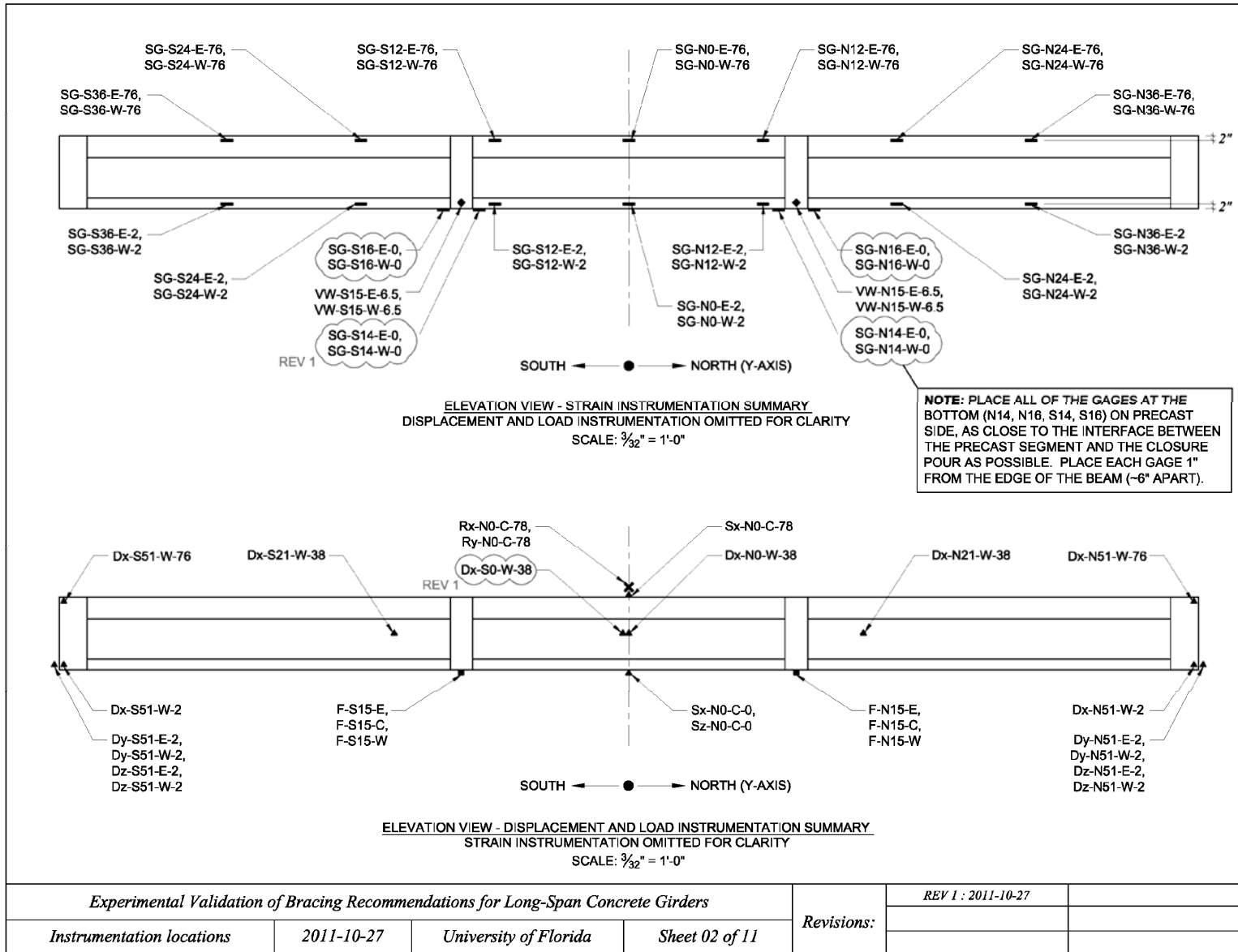
2011-10-27

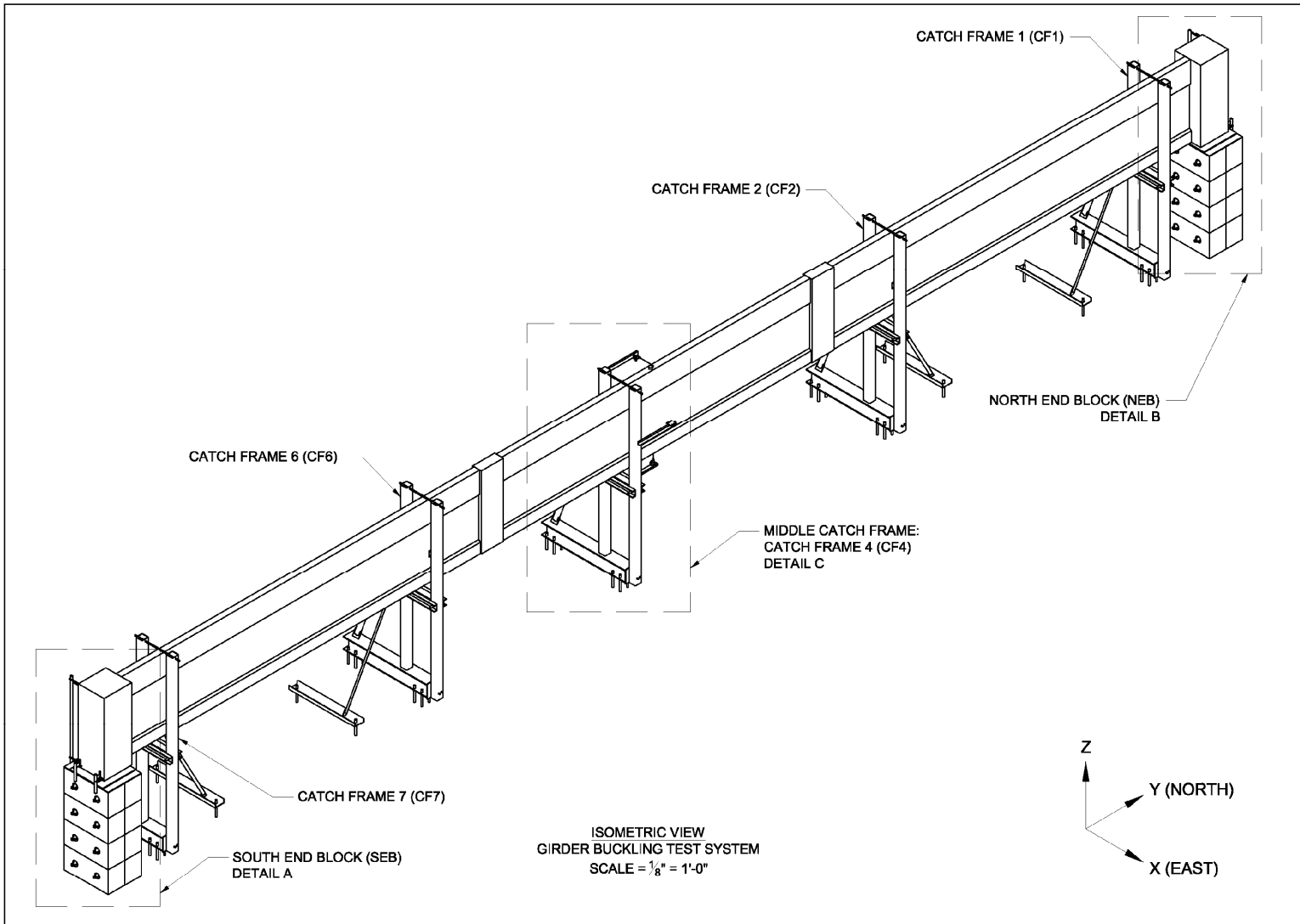
University of Florida

Sheet 01 of 11

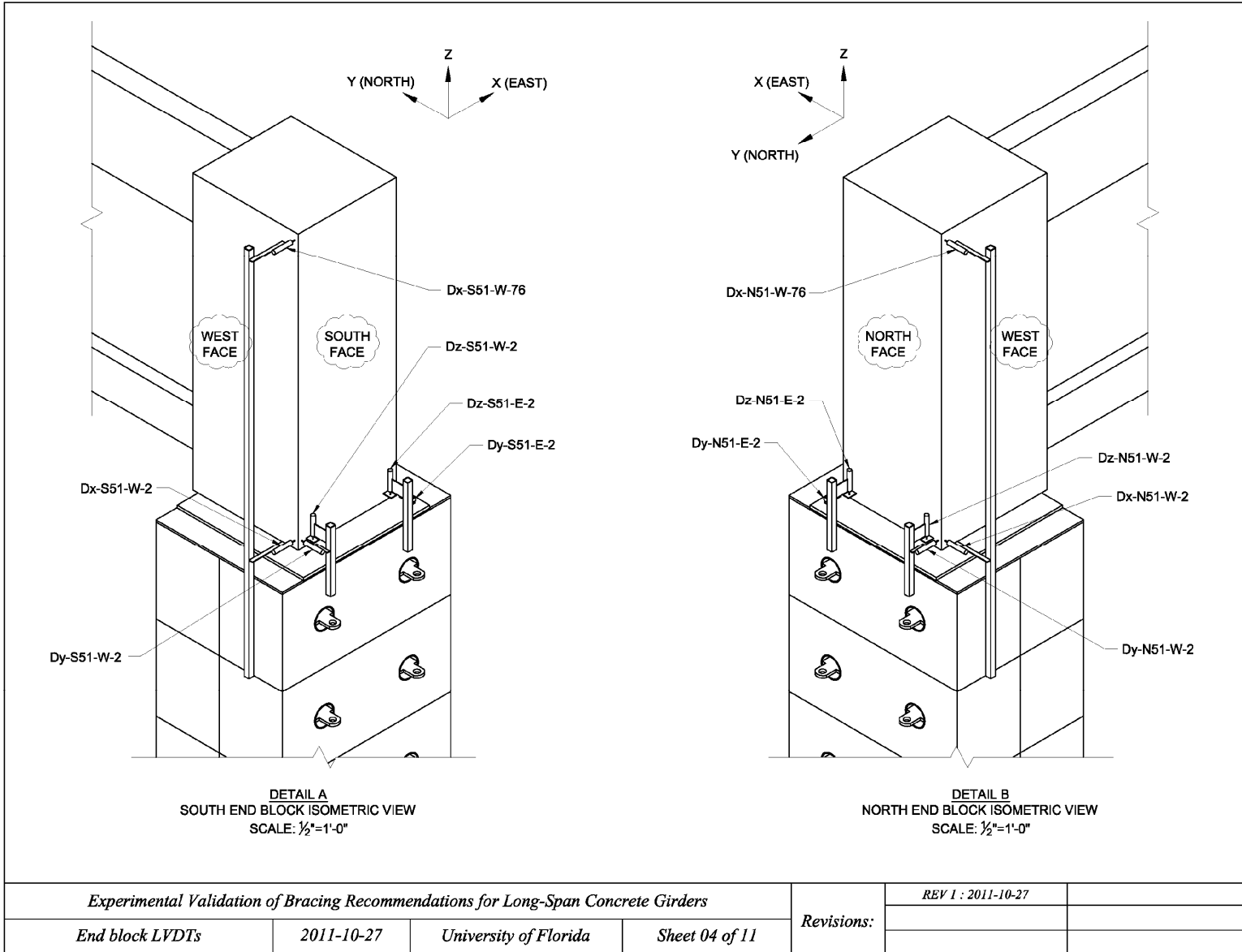
Revisions:

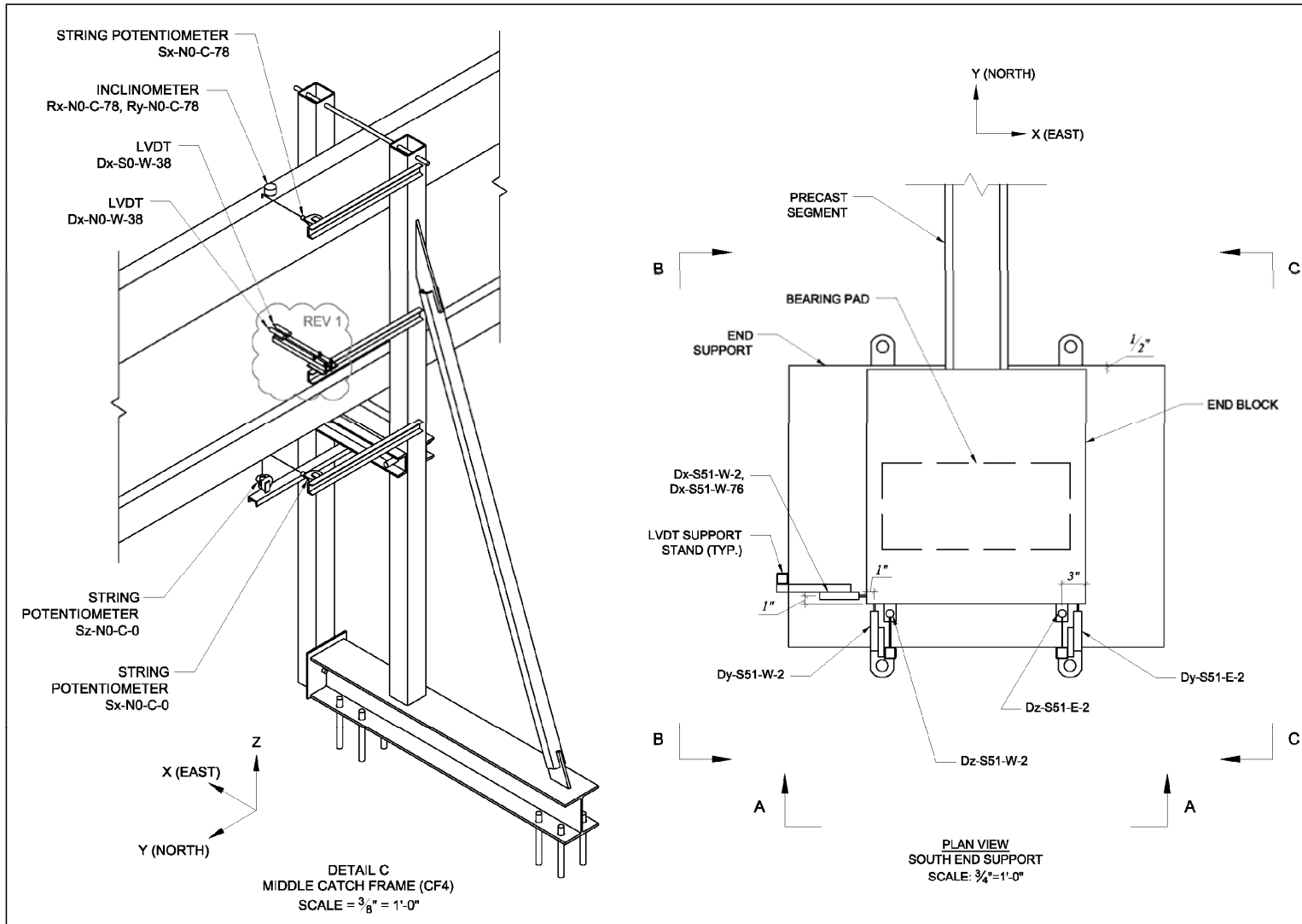
REV 1 : 2011-10-27



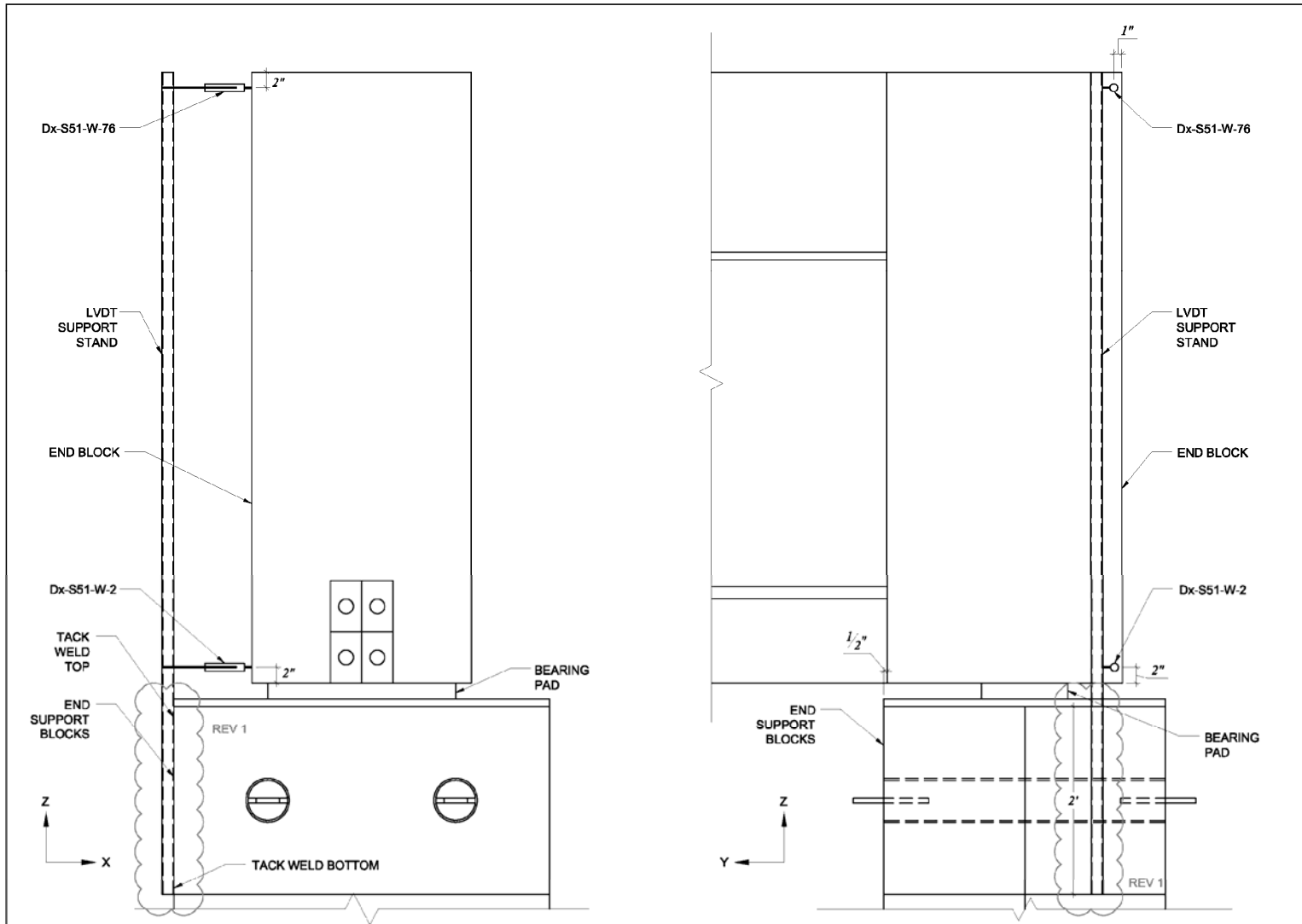


| | | | | | | |
|--|------------|-----------------------|----------------|------------|--------------------|--|
| <i>Experimental Validation of Bracing Recommendations for Long-Span Concrete Girders</i> | | | | Revisions: | REV 1 : 2011-10-27 | |
| <i>Instrumentation plan overview</i> | 2011-10-27 | University of Florida | Sheet 03 of 11 | | | |

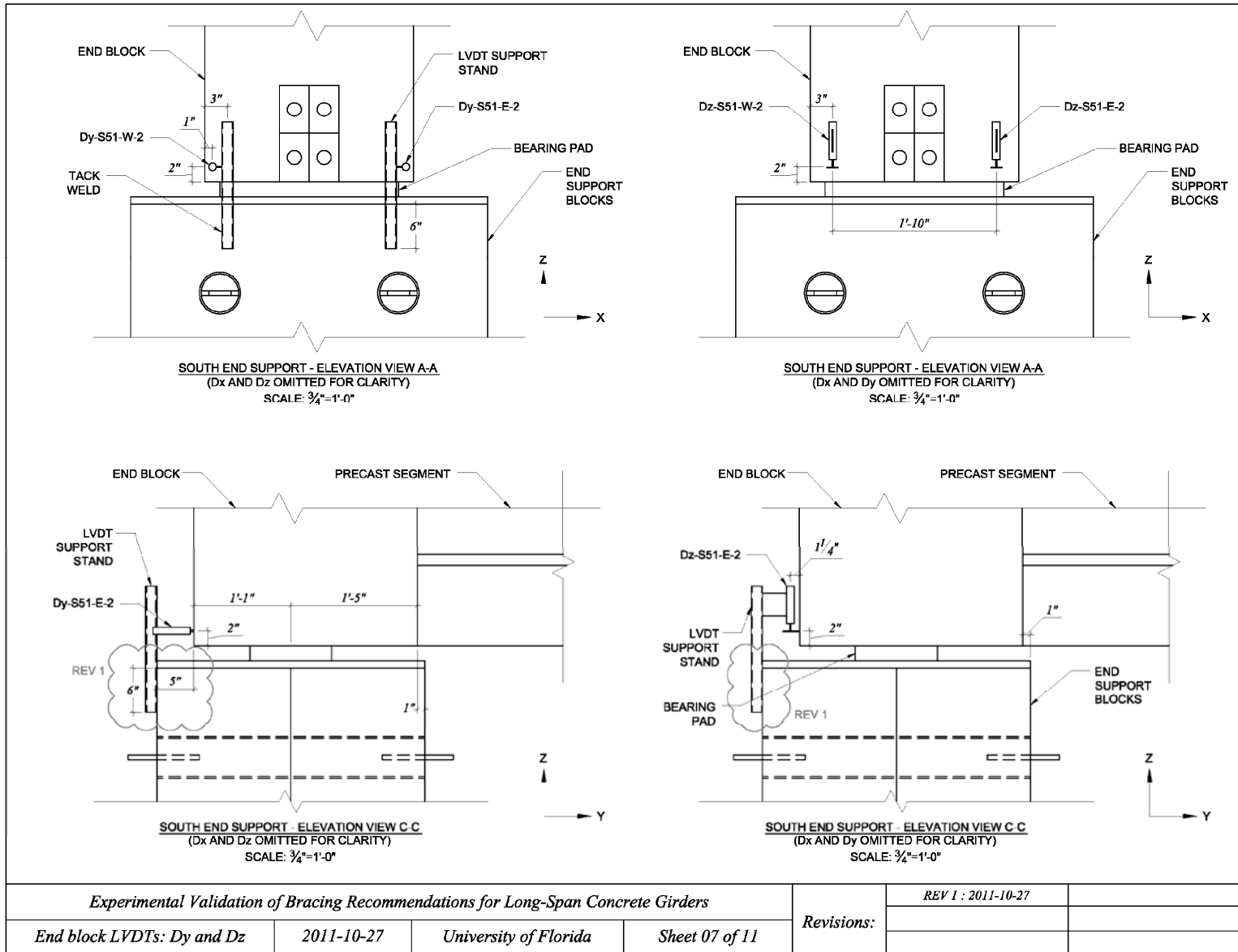




| | | | | | | |
|--|------------|-----------------------|----------------|------------|--------------------|--|
| <i>Experimental Validation of Bracing Recommendations for Long-Span Concrete Girders</i> | | | | Revisions: | REV 1 : 2011-10-27 | |
| <i>Instrumentation plan</i> | 2011-10-27 | University of Florida | Sheet 05 of 11 | | | |



| | | | | | | |
|--|------------|-----------------------|----------------|------------|--------------------|--|
| <i>Experimental Validation of Bracing Recommendations for Long-Span Concrete Girders</i> | | | | Revisions: | REV 1 : 2011-10-27 | |
| <i>End block LVDTs: Dx</i> | 2011-10-27 | University of Florida | Sheet 06 of 11 | | | |



Experimental Validation of Bracing Recommendations for Long-Span Concrete Girders

End block LVDTs: Dy and Dz

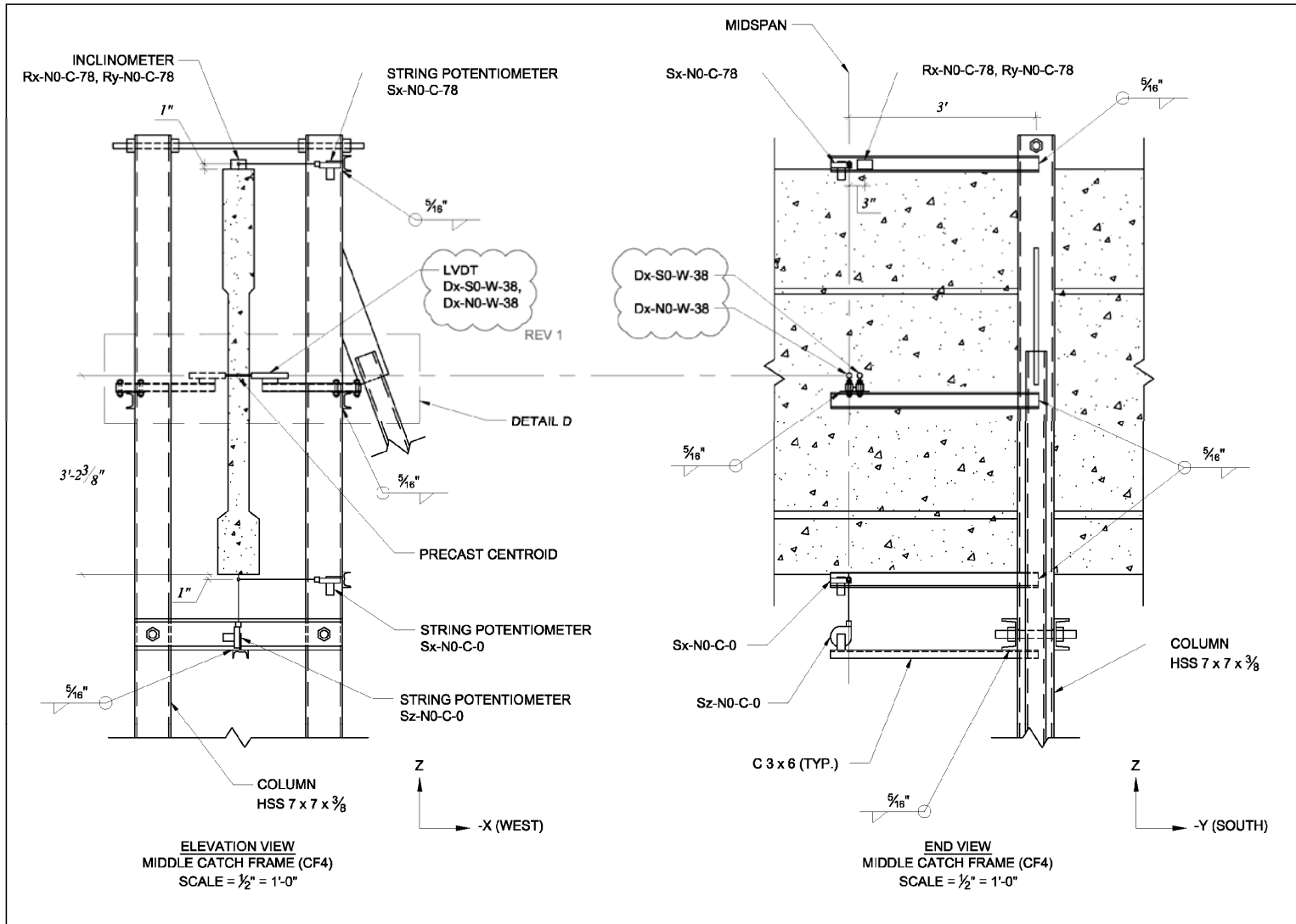
2011-10-27

University of Florida

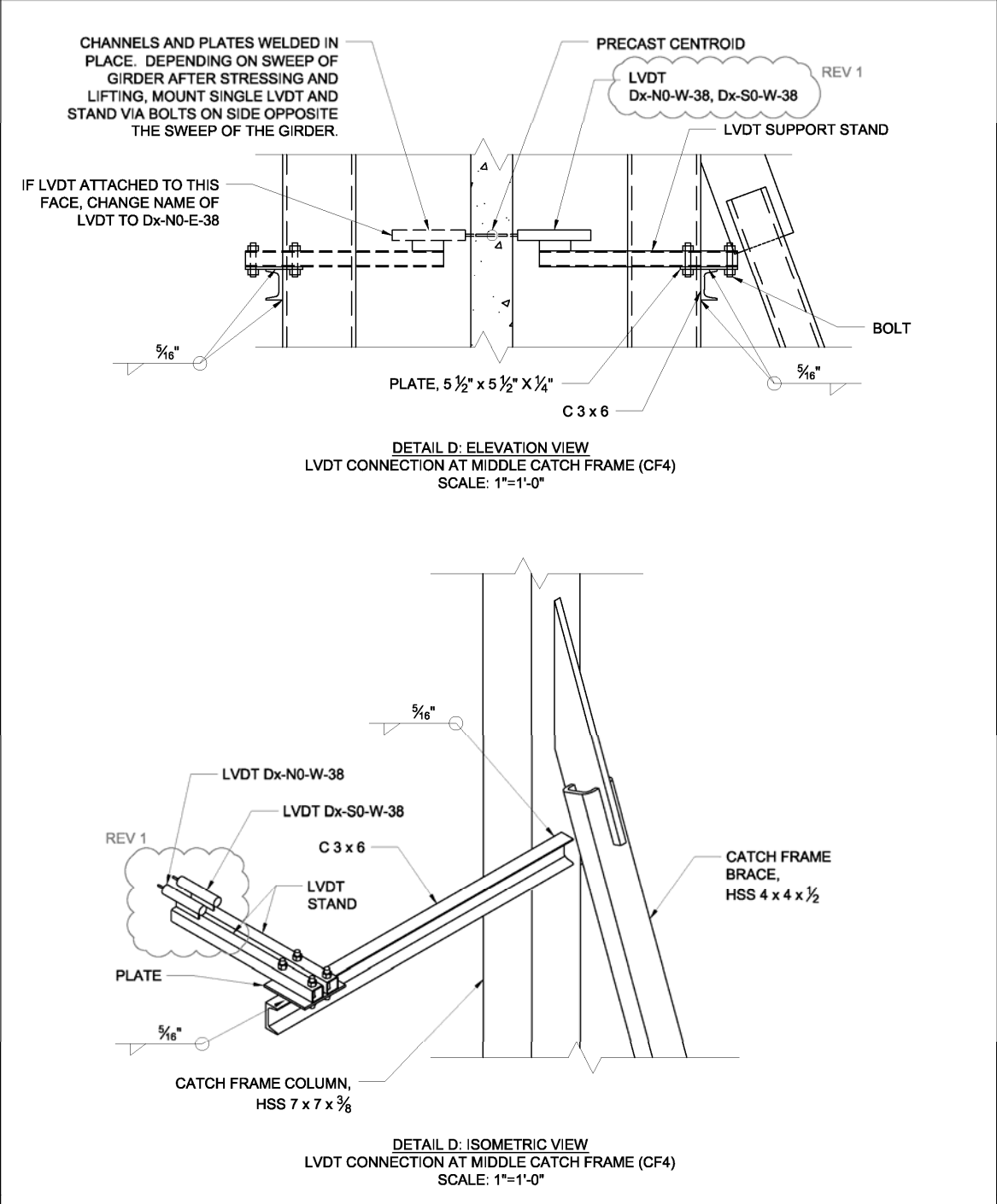
Sheet 07 of 11

Revisions:

REV 1 : 2011-10-27

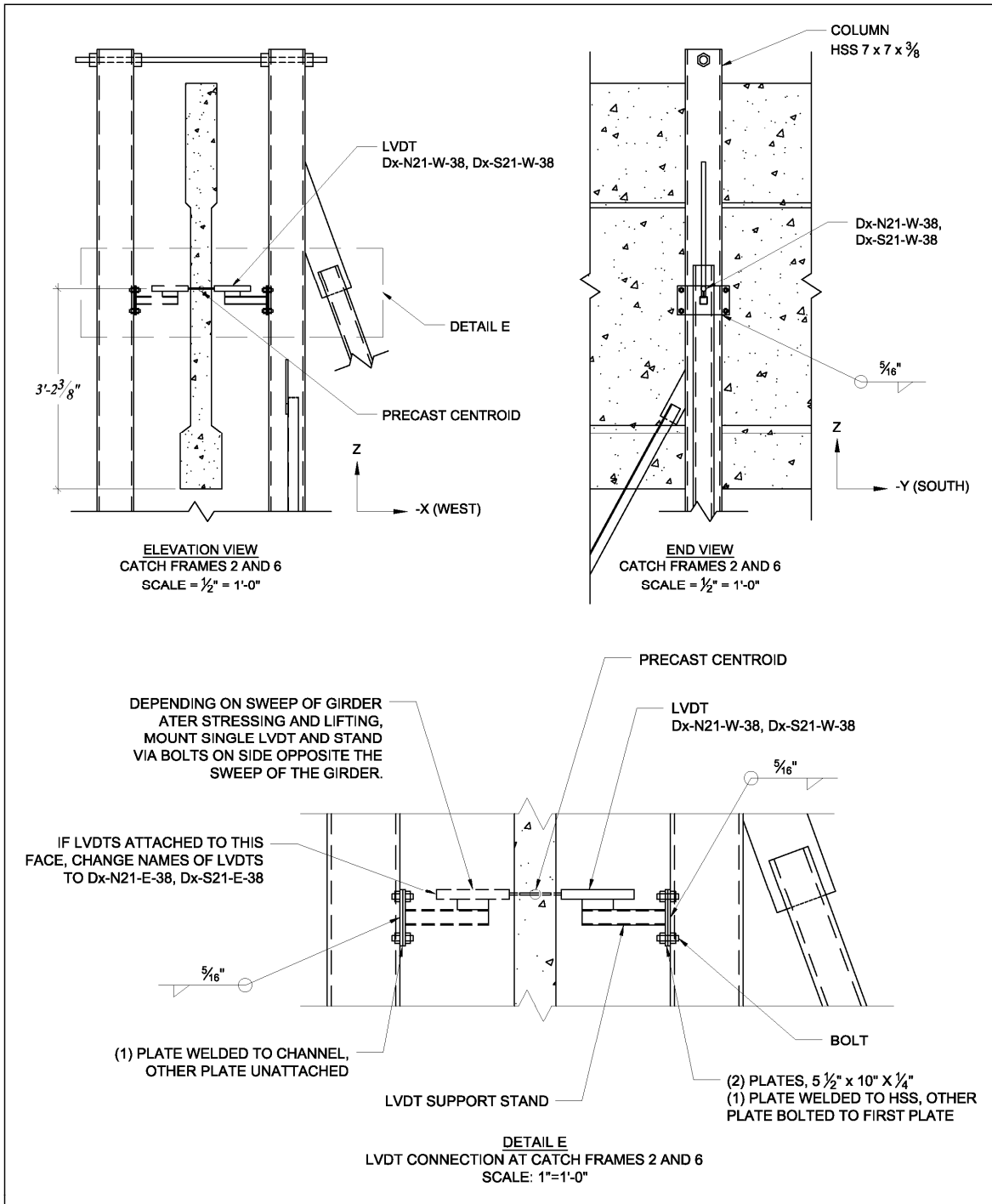


| | | | | | | |
|--|-------------------|------------------------------|-----------------------|-------------------|---------------------------|--|
| <i>Experimental Validation of Bracing Recommendations for Long-Span Concrete Girders</i> | | | | Revisions: | <i>REV 1 : 2011-10-27</i> | |
| <i>Catch frame 4 instrumentation</i> | <i>2011-10-27</i> | <i>University of Florida</i> | <i>Sheet 08 of 11</i> | | | |
| | | | | | | |



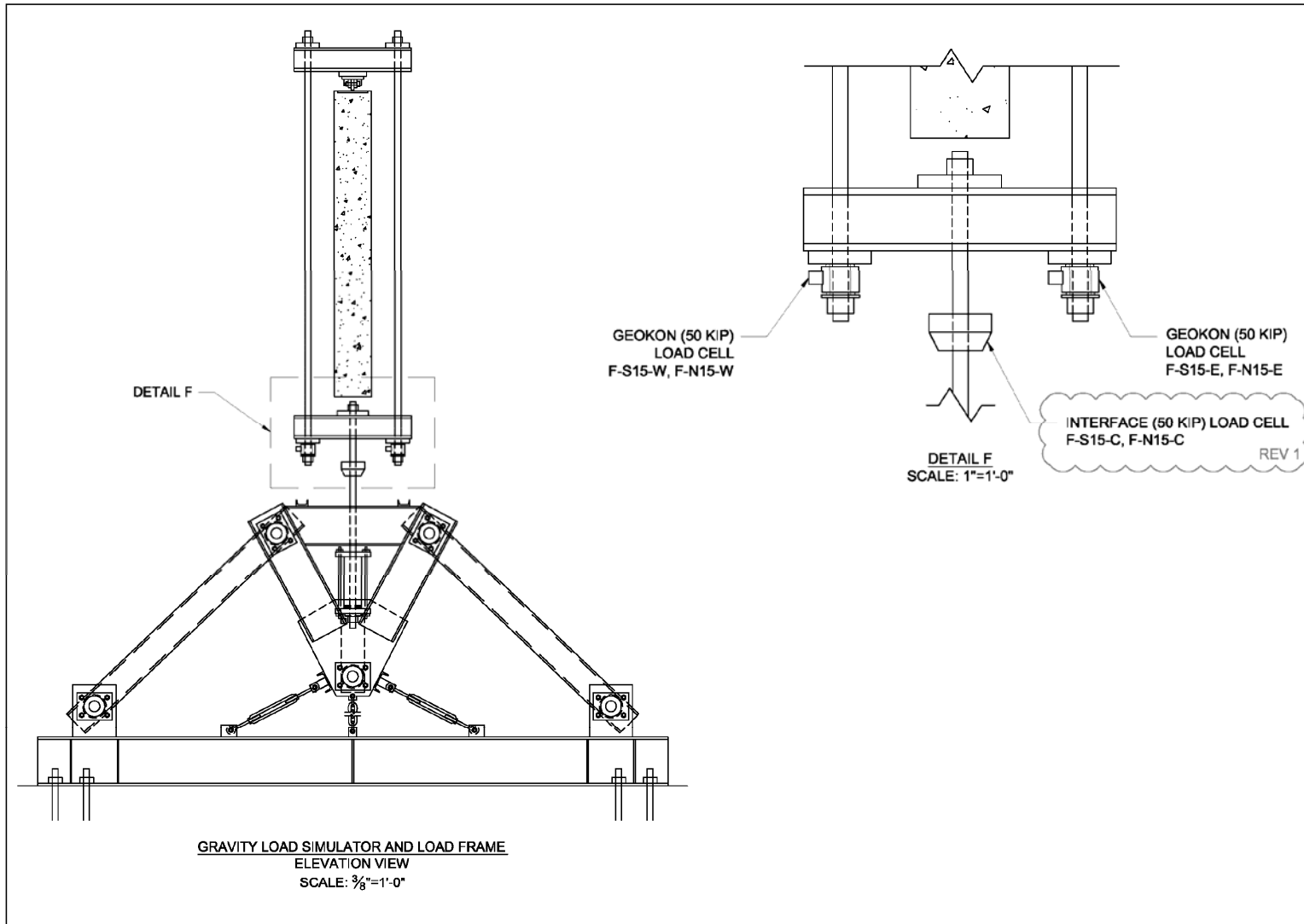
Experimental Validation of Bracing Recommendations for Long-Span Concrete Girders

| | | | |
|---------------------------------------|--------------------|-----------------------|----------------|
| Catch frame 4 instrumentation details | 2011-10-27 | University of Florida | Sheet 09 of 11 |
| Revisions: | REV 1 : 2011-10-27 | | |



Experimental Validation of Bracing Recommendations for Long-Span Concrete Girders

| | | | |
|-----------------------------|--------------------|-----------------------|----------------|
| CF2 and CF4 instrumentation | 2011-10-27 | University of Florida | Sheet 10 of 11 |
| Revisions: | REV 1 : 2011-10-27 | | |



| | | | | | | |
|--|-------------------|------------------------------|-----------------------|-------------------|---------------------------|--|
| <i>Experimental Validation of Bracing Recommendations for Long-Span Concrete Girders</i> | | | | <i>Revisions:</i> | <i>REV 1 : 2011-10-27</i> | |
| <i>Load frame instrumentation</i> | <i>2011-10-27</i> | <i>University of Florida</i> | <i>Sheet 11 of 11</i> | | | |
| | | | | | | |

LIST OF REFERENCES

- AASHTO. (2004). *LRFD Bridge Design Specifications*, 2nd Ed., AASHTO, Washington D.C.
- ADINA System 8.7 [Computer software]. (2010). "Theory and Modeling Guide, Volume I: ADINA." ADINA R&D, Inc.
- Allen, D. T., Cook, R. A., and Ansley, M. H. (2010). "Shear Stiffness of Neoprene Bearing Pads Under Long-Term Loads." *Transportation Research Record: Journal of the Transportation Research Board No. 2172*, Washington, D.C., 38-46.
- ASTM C39. (2001) "Standard Test Method for Compressive Strength of Concrete Cylinders Cast in Place in Cylindrical Molds." American Society of Testing and Materials, ASTM International, West Conshohocken, PA.
- ASTM C109. (2011). "Test Method for Compressive Strength of Hydraulic Cement Mortars (Using 2-in. or [50-mm] Cube Specimens)." American Society for Testing and Materials, ASTM International, West Conshohocken, PA.
- ASTM C469. (1994) "Standard Test Method for Static Modulus of Elasticity and Poisson's Ratio of Concrete in Compression." American Society of Testing and Materials, ASTM International, West Conshohocken, PA.
- ASTM D4014-03. (2003). "Standard Specification for Plain and Steel-Laminated Elastomeric Bearings for Bridges." American Society for Testing and Materials, ASTM International, West Conshohocken, PA.
- Consolazio, G. R., Hamilton III, H. R., Bui L., and Chung J. (2007). "Lateral Bracing of Long-Span Florida Bulb-Tee Girders." *Structures Research Report No. 2007/52290*, Engineering and Industrial Experiment Station, University of Florida, Gainesville, Florida.
- Deaver, J. E. (2003). "Laboratory Tests on Torsional Braces for Steel Bridge Girders with Normal Supports." M.S. Thesis, Department of Civil and Environmental Engineering, University of Houston, Houston, TX.
- Doody, M. E., and Noonan, J. E. (1999). "Long-Term Performance of Elastomeric Bridge TBearings." *Transportation Research Record: Journal of the Transportation Research Board No. 1688*, Washington, D.C., 139-146.
- FDOT. (2010). *FDOT Design Standards Specification*, Structures Design Office, Florida Department of Transportation, Tallahassee, Florida.
- FDOT. (2010). *FDOT Standard Specifications for Road and Bridge Construction*, Florida Department of Transportation, Tallahassee, FL.
- FDOT. (2012). *FDOT Structures Design Guidelines*, Structures Design Office, Florida Department of Transportation, Tallahassee, FL.

- Gent, A. N. (2001). *Engineering with Rubber: How to Design Rubber Components*, 2nd Edition, Hanser Gardner Publications Inc., Cincinnati, Ohio, 312-313.
- Green, T., Yazdani, N., Spainhour, L., and Cai, S. C. (2001). "Effect of Bearing Stiffness and Skew Angle on Performance of Precast Concrete Bridges." *Transportation Research Record: Journal of the Transportation Research Board*. No. 1770, Washington, D.C., 27-33.
- Hurff, J. B. (2010). "Stability of Precast Prestressed Concrete Bridge Girders Considering Imperfections and Thermal Effects." Ph.D. Dissertation, School of Civil and Environmental Engineering, Georgia Institute of Technology, Atlanta, GA.
- Kalkan, I. (2009). "Lateral Torsional Buckling of Rectangular Reinforced Concrete Beams." Ph.D. Dissertation, School of Civil and Environmental Engineering, Georgia Institute of Technology, Atlanta, GA.
- Lehman, D. E., Roeder, C. W., and Larsen, R. A. (2005). "Design of Cotton Duck Bridge Bearing Pads." *J. Bridge Eng.*, 10(5), 555-563.
- Mast, R. F. (1989). "Lateral Stability of Long Prestressed Concrete Beams, Part 1." *PCI Journal*, V. 34, No. 1, Jan-Feb, pp. 34-53.
- Mast, R. F. (1993). "Lateral Stability of Long Prestressed Concrete Beams, Part 2." *PCI Journal*, V. 38, No. 1, Jan-Feb, pp. 70-88.
- Muscarella J. V., and Yura, J. A. (1995). "An Experimental Study of Elastomeric Bridge Bearings with Design Recommendations." *FHWA/TX-98/1304-3*.
- PCI. (2003). *PCI Bridge Design Manual*, Precast/Prestressed Concrete Institute, Chicago, Illinois.
- Stoddard, W. P. (1997). "Lateral-Torsional Buckling Behavior of Polymer Composite I-Shaped Members." Ph.D. Dissertation, School of Civil and Environmental Engineering, Georgia Institute of Technology, Atlanta, GA.
- Vidot-Vega, A. L., Possiel B., Robinson B., Kowalsky M. J., and Gabr M. A. (2009). "Evaluation of Rotational Stiffness of Elastomeric Bearing Pad-Anchor Bolt Connections on Deep Foundation Bents." *J. Bridge Eng.*, 14(6), 487-495.
- Yarimci, E., Yura, J. A., and Lu, L. W. (1967). "Techniques for Testing Structures Permitted to Sway." *Experimental Mechanics*, V. 7, No. 8, Aug., pp. 321-331.
- Yazdani, N., Eddy, S., and Cai, C. (2000). "Effect of Bearing Pads on Precast Prestressed Concrete Bridges." *J. Bridge Eng.*, 5(3), 224-232.

Yura, J.A., Kumar, A., Yakut, A., Topkaya, C., Becker, E., and Collingwood, J. (2001). "Elastomeric Bridge Bearings: Recommended Test Methods." *NCHRP Report No. 449*, Washington D.C.

Yura, J.A., and Phillips, B.A. (1992). "Bracing Requirements for Elastic Steel Beams." *Research Report 1239-1*, Center for Transportation Research, The University of Texas, Austin, TX.

BIOGRAPHICAL SKETCH

The author was born in Boynton Beach, FL. She began attending the University of Florida in the September 2004, where she received the degree of Bachelor of Science in civil engineering in December 2008. She then continued with graduate studies at the University of Florida, where she anticipates receiving a Master of Science degree in civil engineering in May 2012, with an emphasis in civil structures. Upon graduation, the author will pursue a career in bridge design.